Power quality and stability improvement of more-electronics power systems

Fang, Jingyang

2018

Fang, J. (2018). Power quality and stability improvement of more-electronics power systems. Doctoral thesis, Nanyang Technological University, Singapore.

https://hdl.handle.net/10356/89918

https://doi.org/10.32657/10220/47181

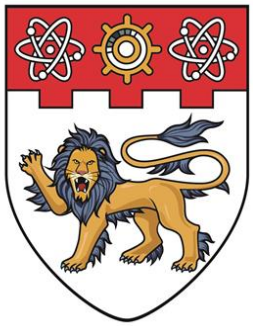

NANYANG TECHNOLOGICAL UNIVERSITY
SINGAPORE

POWER QUALITY AND STABILITY IMPROVEMENT OF MORE-ELECTRONICS POWER SYSTEMS

FANG JINGYANG

SCHOOL OF ELECTRICAL AND ELECTRONIC ENGINEERING

2018

Power Quality and Stability Improvement of More-Electronics Power Systems

Fang Jingyang

School of Electrical and Electronic Engineering

A thesis submitted to the Nanyang Technological University
in partial fulfilment of the requirement for the degree of
Doctor of Philosophy

2018

Acknowledgements

I would like to extend my sincere gratitude to the following people for their help and support during my postgraduate journey.

First and foremost, I will forever beholden to my supervisor, Assistant Professor Tang Yi. As for me, he is both a responsible teacher and a friendly brother. I cherish the time we spent together as well as the knowledge and skills learnt from him. Whenever I encountered research difficulties, Prof Tang would patiently teach me the methodology for finding solutions rather than the solution itself. Moreover, his rigorous attention to details has greatly reshaped my research habits. I always keep in mind the important saying from him, i.e. doing our best like an excellent artisan. Fortunately, through joint efforts, we came up with several ideas and later translated them into high-quality publications. I am really kissed by fortune to be supervised by him.

Also, I thank Professor Wang Peng and Assistant Professor Alessandro Romagnoli. Serving as Thesis Advisory Committee (TAC) members, they provided valuable suggestions on improving the quality of this thesis.

Professor Blaabjerg Frede and Associate Professor Yang Yongheng from Aalborg University, Denmark, have my gratitude. Their inputs greatly improved the archival values of my papers.

I truly appreciate my colleagues, Dr. Li Xiaoqiang, Dr. Li Hongchang, and Dr. Yang Shunfeng. They helped me considerably throughout the postgraduate period in terms of logical reconstruction, formula derivation, and software and hardware designs.

Thanks for the support provided by research technicians Ms. Tan Jennifer and Mr. Tan Peng Chye in Electric Power Research Lab and Water and Energy Research Lab, respectively.

Last but not least, I wish to express my endless gratitude to my beloved parents. Their love is the external source of power for me to move on.

Table of Contents

Acknowledgements ..... **i**
Table of Contents ..... **iii**
Abstract ..... **vii**
List of Figures ..... **xi**
List of Tables ..... **xix**
List of Acronyms ..... **xxi**
Chapter 1 Introduction **1**
1.1 Background **1**
1.2 Motivation and Objectives **6**
1.3 Major Contributions of the Thesis **11**
1.4 Organization of the Thesis **12**
Chapter 2 Fundamentals of More-Electronics Power Systems **15**
2.1 Background and Introduction **15**
2.2 System Configuration **16**
2.3 Power Converters Controlled as AC Voltage Sources **19**
2.3.1 System Modelling 19
2.3.2 Controller Design 22
2.4 Power Converters Controlled as AC Current Sources **32**
2.4.1 System Modelling 33
2.4.2 Controller Design 35
2.5 Grid Support by Power Converters **42**
2.5.1 Virtual Synchronous Generators (VSGs) 42
2.5.2 Power Support by Power Converters 46
2.5.3 Active Power Filters (APFs) 47
2.6 Summary **48**
Chapter 3 Advanced Passive Power Filters for Power Quality Enhancement **51**
3.1 Background and Introduction **51**
3.2 Magnetic Integrated *LLCL* Filters **55**

3.2.1 Fundamental Principle 55
3.2.2 Magnetic Circuit Analysis 57
3.2.3 Core Design and Volume Comparison 60
3.2.4 Experimental Verification 64
3.3 Series-Parallel-Resonant *LCL* (*SPRLCL*) Filters 67
3.3.1 Fundamental Principle 68
3.3.2 Filter Design 71
3.3.3 Experimental Verification 74
3.4 *LT-C-L* Filters 77
3.4.1 Fundamental Principle 78
3.4.2 Magnetic Integrated *LT-C-L* filters 81
3.4.3 Experimental Verification 85
3.5 State of the Art Passive Power Filters 86
3.5.1 Filter Topologies 87
3.5.2 Filtering Performances 90
3.5.3 Filter Robustness 93
3.5.4 Experimental Verification 96
3.6 Summary 99
Chapter 4 Converter-Level Stability Improvement through Impedance Reshaping of Power Converters 101
4.1 Background and Introduction 101
4.1.1 Sources of Instability Issues 102
4.1.2 Solutions to Instability Issues 104
4.2 Phase-Locked-Loops (PLLs) 107
4.2.1 PLL Modelling 108
4.2.2 Effect of PLLs 110
4.3 Instability Issue due to PLLs 114
4.3.1 Introduction of Impedance Criterion 114
4.3.2 Stability Analysis 116
4.4 Stability Improvement through Impedance Reshaping 119
4.4.1 Fundamental Principle 120
4.4.2 Design of Impedance Controller 121

4.4.3 Impedance Reshaping and Stability Improvement 122
4.4.4 Simulation and Experimental Verifications 124
4.5 Summary 128
Chapter 5 System-Level Frequency Stability Improvement by Distributed Virtual Inertia and VSGs 131
5.1 Background and Introduction 131
5.1.1 Challenge of Inertia Reduction 132
5.1.2 Inertia Enhancement Techniques 136
5.2 Influence of Inertia on Frequency Regulation 137
5.2.1 Frequency Regulation Framework 137
5.2.2 Influence of Inertia 138
5.3 Power Converters with Distributed Virtual Inertia 143
5.3.1 Fundamental Principle 143
5.3.2 Analysis of Virtual Inertia 146
5.3.3 Design of Virtual Inertia 150
5.3.4 Simulation and Experimental Verifications 151
5.4 VSGs with Hybrid Energy Storage Systems (HESSs) 159
5.4.1 System Implementation 159
5.4.2 Control Structure 162
5.4.3 Power Management Scheme 163
5.4.4 Experimental Verification 167
5.5 Summary 169
Chapter 6 Conclusion and Future Research 171
6.1 Conclusion 171
6.2 Future Research 173
6.2.1 Grid Support under Adverse Grid Conditions 174
6.2.2 Converter-Level Instability Issues due to Grid Support 175
6.2.3 Virtual Inertia Support by Energy Storage Units 176
Author's Publications 179
References 181

Abstract

Primary drivers behind grid transformations comprise a marriage of the ever-increasing energy demand and a desire for reduction of carbon footprint. As the trend of grid transformations continues, a significantly high penetration level of renewable energy sources (RESs) is to be expected. Since renewables, in parallel with other emerging technologies such as energy storage and electric vehicles (EVs), are normally coupled to power grids through power electronic converters, power systems gradually evolve into more-electronics power systems. Despite its clear efficiency and control benefits, power electronics brings in issues to power systems. For one hand, it is difficult to ensure high-quality power supplies due to the power quality issues introduced by power electronics. For the other hand, power electronics may introduce instability issues. The instability issues should be blamed not only for the improper control of a single power converter but also for the undesirable operation of the entire power system. As power quality and stability are at the core of power system operations, this thesis aims to investigate and overcome several associated issues in the hope of smoothing the transformation towards future smart grids.

First, the fundamentals of more-electronics power systems including system configurations, operating principles, and modelling and control of power converters are described. For the purpose of analysis, a single-area power system consisting of power converter-interfaced energy storage, photovoltaic generation, and virtual synchronous generator (VSG), is selected as the research object. Power converters in more-electronics power systems are basically controlled as either AC voltage sources or AC current sources. Therefore, these two types of power converters are designed in detail. Moreover, since power converters are increasingly being expected to provide grid support functions, e.g. the power support, research efforts along this trajectory are reviewed.

A prominent power quality issue refers to the current harmonic issue, which can be eased through the use of the proposed advanced passive filters. High-order

passive filters allow improved harmonic attenuation with smaller filter sizes. To reap these benefits, the *LCL*-based trap filters containing extra *LC* resonant trap(s), represented by *LLCL* filters, become a hot research topic. In addition, the magnetic integration technique is a parallel research direction for filter size reduction. However, for the integrated *LCL* filter, the coupling effect between the two inductors acts as a major obstacle. To tackle this issue, the coupling is properly designed and used to form the proposed magnetic integrated *LLCL* filter. It combines the advantages of magnetic integration and trap filter, resulting in an approximate 50% inductance reduction. Additionally, the series-parallel-resonant *LCL* (*SPRLCL*) filter containing one series-resonant trap and one parallel-resonant trap is proposed. It enables excellent filtering and robustness against parameter changes. When a parallel-resonant *LC*-trap combines with the *LCL* filter, the *LT-C-L* filter can be obtained. It is concluded that the *LT-C-L* filter can be the most promising trap filter due to the advantages of high robustness, roll-off rate, and reduced converter current distortions.

For individual power converters, the objective of grid synchronization, particularly under weak grid conditions, may introduce the converter-level instability issue, and this issue can be resolved by reshaping the quadrature-axis (*q*-axis) converter impedance. The grid synchronization of grid-connected power converters necessitates phase-locked-loops (PLLs). However, the inclusion of PLLs tends to shape the converter impedance as a negative resistance in the *q*-axis within the control bandwidth of PLLs. Because of this, the interaction between converter impedance and grid impedance may possibly destabilize power conversion systems. To solve this issue, an impedance controller directly relating the *q*-axis voltage to the *q*-axis current reference is proposed. The proposed controller manages to reshape the *q*-axis converter impedance as a positive resistance in the low-frequency band and address the instability concern.

The distributed virtual inertia contributed by grid-connected power converters and virtual synchronous generators (VSGs) allow the improvement of the system-level frequency stability. In more-electronics power systems, as

synchronous generators being gradually replaced by renewable generators, the lack of inertia issue becomes more obvious. One effective approach for inertia enhancement is to employ the proposed grid-connected power converters with the distributed virtual inertia. By proportionally relating the grid frequency and DC-link voltages, the DC-link capacitors of power converters act as energy buffers and inertia suppliers. Another approach for inertia enhancement lies in the use of VSGs. Although the concept has been well-known, the implementation and coordination control of the energy storage systems (ESSs) in VSGs remain untouched. To fill this research gap, the hybrid ESS (HESS) consisting of a battery and an ultracapacitor is proposed. In this HESS, the ultracapacitor tackles the fast-varying power required by inertia emulation while the battery compensates for the long-term power fluctuations required by the remaining parts of VSGs. Through these methods, the significant improvements of frequency nadir and rate of change of frequency (RoCoF) can be expected, thereby improving the system-level frequency stability.

In general, this thesis focuses on and addresses several major power quality and instability issues introduced by power electronics in more-electronics power systems. Specifically, the proposed advanced passive filters are effective solutions to the ever-challenging current harmonic issue. The converter-level instability issue due to PLLs and weak grids is addressed by reshaping the q-axis converter impedance. Moreover, the proposed distributed virtual inertia and VSGs manage to improve the system-level frequency stability.

As the renewable integration trend continues, new challenges and opportunities will emerge in more-electronics power systems. With reference to the power quality, the grid support by power converters under adverse grid conditions is considered to be a challenge. For individual power converters with grid support functions, the grid support under weak grids may cause instability concerns, which should be addressed through further research efforts. With respect to the system-level frequency stability, there is a great opportunity to explore the inertia emulation potentials of energy storage units, such as batteries.

List of Figures

Figure 1.1 Solar PV global capacity and annual additions, 2006−2016 [4]. 2
Figure 1.2 Wind power global capacity and annual additions, 2006−2016 [4]...2
Figure 1.3 Schematic diagrams of renewable generation systems [6]. 3
Figure 1.4 Schematic diagram of energy storage systems [9]. 4
Figure 1.5 Schematic diagram of energy storage systems in electric vehicles [11]. 4
Figure 1.6 Applications of power electronics in more-electronics power systems. 5
Figure 2.1 Schematic diagram of the example more-electronics power system. 17
Figure 2.2 Photo of the experimental prototype. 18
Figure 2.3 Schematic diagram of VCCs. 19
Figure 2.4 Block diagram of the system plant of VCCs. 22
Figure 2.5 Block diagram of the voltage and current controllers of VCCs in the (a) mixed *s*- and *z*-domains and (b) *z*-domain. 24
Figure 2.6 Pole-zero map of $T_{i\text{ref\_}v}(z)$ with various ($K_{gl}K_{gc}$). 25
Figure 2.7 Step responses of $T_{i\text{ref\_}v}(z)$ with various K_{gl} and K_{gc}. 26
Figure 2.8 Bode diagrams of $T_{i\text{ref\_}v}(z)$ with and without the current control. 27
Figure 2.9 Detailed block diagram of the voltage controller of VCCs. 27
Figure 2.10 Bode diagrams of $T_{i\text{ref\_}v}(z)S_{gr}(z)z^{Ngc}$ as a function of N_{gc}. 29
Figure 2.11 Bode diagram of $v_{gf}(z)$ / $\Delta v_{gf}(z)$. 29
Figure 2.12 Nyquist diagram of the voltage controller of VCCs. 30
Figure 2.13 Experimental results of VCCs supplying (a) linear and (b) nonlinear loads. 31
Figure 2.14 Schematic diagram of CCCs. 32
Figure 2.15 Block diagram of the system plants of CCCs. 35
Figure 2.16 Block diagram of the current controller of CCCs in the (a) mixed *s*- and *z*-domains and (b) *z*-domain. 36

Figure 2.17 Bode diagrams of $G_{c\_ol}(z)$ as a function of K_{cp} for the (a) *LCL* filter and (b) *L* filter cases. 38
Figure 2.18 Root loci of $G_{c\_ol}(z)$ for the (a) *LCL* filter and (b) *L* filter cases. 39
Figure 2.19 Pole-zero maps of $G_{c\_cl}(z)$ as a function of K_{ci} for the (a) *LCL* filter and (b) *L* filter cases. 40
Figure 2.20 Experimental results of the *L*-filtered CCC. 41
Figure 2.21 Block diagram of the VSG outer-loop control. 43
Figure 2.22 Comparisons between (a) simulation result of the synchronous generator and (b) experimental result of the VSG with the primary frequency control. 45
Figure 2.23 Comparisons between (a) simulation result of the synchronous generator and (b) experimental result of the VSG with the secondary frequency control. 45
Figure 2.24 Block diagram of the droop control of CCCs. 46
Figure 2.25 Block diagram of the i_d–i_q harmonic detection scheme of APFs. 48
Figure 3.1 Current spectrum of an *L*-filtered power converter. 53
Figure 3.2 Schematic diagram of *LLCL* filters [57]. 54
Figure 3.3 Equivalent circuits of the magnetic integrated *LCL* filters with the (a) positive coupling and (b) negative coupling. 56
Figure 3.4 Bode diagrams of $G_{plant\_LCL}(s)$ and $G_{plant\_LLCL}(s)$. 57
Figure 3.5 (a) Core structure and (b) equivalent magnetic circuit of integrated *LLCL* filters. 58
Figure 3.6 Schematic diagrams of single-phase (a) H-bridge and (b) half-bridge power converters. 60
Figure 3.7 Physical dimensions of (a) integrated inductor core and (b) discrete inductor cores. 63
Figure 3.8 Volume comparison between integrated inductor core and discrete inductor cores. 64
Figure 3.9 Experimental (a) waveforms and (b) spectrum of i_{cga} of the *LCL*-filtered power converter (case I). 65

Figure 3.10 Experimental (a) waveforms and (b) spectrum of i_{cga} of the integrated *LLCL*-filtered power converter. 66
Figure 3.11 Experimental (a) waveforms and (b) spectrum of i_{cga} of the *LCL*-filtered power converter (case II). 67
Figure 3.12 Schematic diagram of (a) *LCCL* filter and (b) *L-TC-L* filters. 68
Figure 3.13 Bode diagrams of $G_{\text{plant\_LCL}}(s)$, $G_{\text{plant\_LLCL}}(s)$, and $G_{\text{plant\_L-TC-L}}(s)$. 70
Figure 3.14 Schematic diagram of *SPRLCL* filters. 70
Figure 3.15 Bode diagrams of $G_{\text{plant\_SPRLCL}}(s)$ wirh the *SPRLCL* filters designed with (a) method I, (b) method II, and (c) method III. 72
Figure 3.16 Bode diagrams of $G_{\text{plant\_SPRLCL}}(s)$ with the *SPRLCL* filters designed with method III and ±20% variations of (a) L_{cf} and (b) L_{cg}. 73
Figure 3.17 Bode diagrams of $G_{\text{plant\_SPRLCL}}(s)$ with the *SPRLCL* filters designed with (a) method I and ±20% variations of L_{cf} and (b) method II and ±20% variations of L_{cg}. 73
Figure 3.18 Experimental waveforms of grid voltage v_{ga}, grid current i_{sa}, and spectrum of i_{sa} before harmonic compensation. 75
Figure 3.19 Experimental waveforms of grid voltage v_{ga}, grid current i_{sa}, and spectrum of i_{sa} after harmonic compensation by the *LCL*-filtered APF. 76
Figure 3.20 Experimental waveforms of grid voltage v_{ga}, grid current i_{sa}, and spectrum of i_{sa} after harmonic compensation by the *LLCL*-filtered APF. 76
Figure 3.21 Experimental waveforms of grid voltage v_{ga}, grid current i_{sa}, and spectrum of i_{sa} after compensation by the method II designed *SPRLCL*-filtered APF. 77
Figure 3.22 Experimental waveforms of the grid voltage v_{ga}, grid current i_{sa}, and spectrum of i_{sa} of (a) *LLCL*- and (b) method III designed *SPRLCL*-filtered APFs with 50% variations of L_f. 78
Figure 3.23 Schematic diagram of *LT-C-L* filters. 79
Figure 3.24 Bode diagrams of $G_{\text{plant\_LCL}}(s)$ and $G_{\text{plant\_LT-C-L}}(s)$. 80
Figure 3.25 (a) Core structure and (b) equivalent magnetic circuit of integrated *LT-C-L* filters. 81

Figure 3.26 (a) Time-domain and (b) *s*-domain circuits of the converter-side branch loop of integrated *LT-C-L* filters. 82
Figure 3.27 Bode diagrams of $G_{plant\_int\_LT\text{-}C\text{-}L}(s)$ as a function of the coupling coefficient k_M. 84
Figure 3.28 Experimental (a) waveforms and (b) spectrum of i_{cga} of the *LCL*-filtered power converter. 86
Figure 3.29 Experimental (a) waveforms and (b) spectrum of i_{cga} of the *LT-C-L*-filtered power converter. 87
Figure 3.30 Schematic diagrams of state of the art passive filters. 88
Figure 3.31 Bode diagrams of $G_{plant}(s)$ of power converters with state of the art passive filters. 91
Figure 3.32 Bode diagrams of the transfer functions from the converter voltage to the converter current of *LCL-LC-*, *L-C-TL-*, and *LT-C-L*-filtered power converters. 92
Figure 3.33 Bode diagrams of $G_{plant\_LCL\text{-}LC}(s)$, $G_{plant\_L\text{-}C\text{-}TL}(s)$, and $G_{plant\_LT\text{-}C\text{-}L}(s)$ under a weak grid with L_s = 3 mH. 94
Figure 3.34 Bode diagrams of $G_{plant\_LCL\text{-}LC}(s)$ and $G_{plant\_LT\text{-}C\text{-}L}(s)$ with series *RC* dampers. 95
Figure 3.35 Bode diagrams of $G_{plant\_LT\text{-}C\text{-}L}(s)$ with the ±40% variations of the trap inductance L_{ct}. 96
Figure 3.36 Experimental spectra of i_{cia} of (a) *LCL-LC-* and (b) *LT-C-L*-filtered power converters. 97
Figure 3.37 Experimental spectra of i_{cia} of (a) *L-C-TL-* and (b) *LT-C-L*-filtered power converters under a weak grid with L_s = 3 mH. 98
Figure 3.38 Experimental spectra of i_{cga} of (a) *L-C-TL-* and (b) *LT-C-L*-filtered power converters under a weak grid with L_s = 3 mH. 98
Figure 4.1 Structure of PLLs. 108
Figure 4.2 Block diagram of the small-signal model of PLLs. 110
Figure 4.3 Block diagram of the *q*-axis current control including the PLL effect. 111

Figure 4.4 Bode diagram of $G_{c\_cl}(z)$ as a function of K_{cp}. 113
Figure 4.5 Bode diagram of $Z_{cq}(z)$ as a function of K_{pll_p}. 114
Figure 4.6 Norton equivalent circuit of power converters. 116
Figure 4.7 Pole-zero maps of $G_{c\_cl}(z)$ as a function of K_{cp} 117
Figure 4.8 Pole-zero maps of 1 / $Z_{cq}(z)$ as a function of K_{pll_p}. 117
Figure 4.9 Bode diagrams of $Z_s(z)$ / $Z_{cq}(z)$ as functions of (a) K_{pll_p}, (b) L_s, and (c) R_s. 119
Figure 4.10 Block diagram of the q-axis current control with the proposed impedance controller. 120
Figure 4.11 Bode diagrams of ideal and simplified impedance controllers $G_{qf}(z)$ and K_{qf}. 122
Figure 4.12 Bode diagrams of $Z_{cq}(z)$ as functions of K_{pll_p} and K_{qf} with the impedance controller. 123
Figure 4.13 Bode diagrams of $Z_s(z)$ / $Z_{cq}(z)$ as functions of K_{pll_p} and K_{qf} with the impedance controller. 124
Figure 4.14 Bode diagrams of $Z_s(z)$ / $Z_{cq}(z)$ including the PLL filter (a) without and (b) with the proposed impedance controller. 125
Figure 4.15 Simulation results of grid currents i_{cgx} ($x = a, b, c$) and PLL q-axis voltage v_{gq_pll} during system dynamics. 126
Figure 4.16 Experimental results of grid currents i_{cgx} ($x = a, b, c$) and PLL q-axis voltage v_{gq_pll} during system dynamics. 127
Figure 4.17 Simulation results of PLL q-axis voltages v_{gq_pll} during system startups with (a) $K_{pll\_p} = 1$ and (b) $K_{pll\_p} = 15$. 128
Figure 4.18 Experimental results of PLL q-axis voltages v_{gq_pll} during system startups with the upper trace $K_{pll\_p} = 1$ and lower trace $K_{pll\_p} = 15$. 129
Figure 5.1 Frequency response curve following a generator tripping event. 133
Figure 5.2 Effect of inertia under a low-frequency event. 135
Figure 5.3 Simplified schematic diagram of a single-area power system (GS: synchronous generators and M: motors). 137
Figure 5.4 Block diagram of the frequency regulation framework. 138

Figure 5.5 Pole-zero map of $G_{Pf}(s)$ as a function of H (H = 5, 10, 20, and 50). 139
Figure 5.6 Responses of $G_{Pf}(s)$ as a function of H (H = 5, 10, 20, and 50) under a 3% step-up load change. 140
Figure 5.7 Frequency regulation performance indices (a) RoCoF, (b) frequency nadir, (c) overshoot, and (d) settling time as a function of H under a 3% step-up load change. 142
Figure 5.8 Inertia mapping between synchronous generators and DC-link capacitors. 144
Figure 5.9 Overall structure of grid-connected power converters with distributed virtual inertia. 145
Figure 5.10 Block diagram of the voltage and current controllers of grid-connected power converters in the s-domain. 146
Figure 5.11 Frequency regulation framework with the virtual inertia control. 147
Figure 5.12 Plots of the virtual inertia coefficient H_p as functions of (a) C_{cdc} and V_{cdc_ref} and (b) ΔV_{cdc_max} and V_{cdc_ref}. 151
Figure 5.13 Design flowchart of virtual inertia. 152
Figure 5.14 Simulation waveforms of (a) frequency f_o and (b) DC-link voltage v_{cdc} with and without the distributed virtual inertia under a 3% step-up load change. 153
Figure 5.15 Simulation waveforms of (a) energy change ΔE_c and (b) power change ΔP_c with and without the distributed virtual inertia under a 3% step-up load change. 154
Figure 5.16 Simulation waveforms of (a) frequency f_o and (b) DC-link voltage v_{cdc} with and without the distributed virtual inertia under a 3% step-down load change. 155
Figure 5.17 Simulation waveforms of (a) energy change ΔE_c and (b) power change ΔP_c with and without the distributed virtual inertia under a 3% step-down load change. 156

Figure 5.18 Experimental waveforms of frequency f_o (top) and DC-link voltage v_{cdc} (bottom) with and without the distributed virtual inertia under a 3% step-up load change. 157
Figure 5.19 Experimental waveforms of energy change ΔE_c (top) and power change ΔP_c (bottom) with and without the distributed virtual inertia under a 3% step-up load change..... 157
Figure 5.20 Experimental waveforms of frequency f_o (top) and DC-link voltage v_{cdc} (bottom) with and without the distributed virtual inertia under a 3% step-down load change. 158
Figure 5.21 Experimental waveforms of energy change ΔE_c (top) and power change ΔP_c (bottom) with and without the distributed virtual inertia under a 3% step-down load change..... 158
Figure 5.22 Schematic diagram of the proposed VSG system (UC: ultracapacitor). 161
Figure 5.23 Block diagram of the DC voltage/current controller of HESSs. .. 162
Figure 5.24 Block diagram of the frequency controller of HESSs. 164
Figure 5.25 Block diagram of the frequency regulation framework of the proposed VSG system..... 164
Figure 5.26 Principle of power allocation according to (5-32)..... 166
Figure 5.27 Steady-state experimental results of the proposed VSG system. . 168
Figure 5.28 Experimental waveforms of frequency f_o and ultracapacitor voltage v_{gdc} of the proposed VSG system under a 3% step-up load change..... 168
Figure 5.29 Experimental waveforms of battery power change ΔP_{bat} and ultracapacitor power change ΔP_{uc} of the proposed VSG system under a 3% step-up load change..... 169
Figure 5.30 Experimental waveforms of the battery power change ΔP_{bat} and ultracapacitor power change ΔP_{uc} of the proposed VSG system under an intermittent RES output. 169

List of Tables

Table 1-1 Current distortion limits for systems rated from 120 V through 69 kV [14]. 7
Table 1-2 Classification of system-level instability issues, mechanisms, and solutions [13]. 9
Table 2-1 Experimental components. 18
Table 2-2 System parameters of VCCs. 23
Table 2-3 Control parameters of VCCs. 31
Table 2-4 System parameters of CCCs. 36
Table 2-5 Control parameters of virtual synchronous generators. 44
Table 3-1 System parameters for testing the integrated *LLCL* filter. 60
Table 3-2 Filter parameters for testing the integrated *LLCL* filter. 61
Table 3-3 Filter parameters for testing the *SPRLCL* filters. 74
Table 3-4 System parameters for testing the *SPRLCL* filters. 74
Table 3-5 System parameters for testing the *LT-C-L* filter. 85
Table 3-6 Filter parameters for testing the *LT-C-L* filter. 85
Table 3-7 Filter parameters of state of the art trap filters. 92
Table 3-8 Main characteristics of state of the art passive power filters. 99
Table 4-1 Classification of the instability sources in more-electronics power systems. 102
Table 4-2 System parameters of power converters for testing the impedance controller. 112
Table 4-3 Control parameters of power converters for testing the impedance controller. 112
Table 5-1 International grid standards on frequency control. 133
Table 5-2 International grid standards on the RoCoF withstand capabilities of generators. 134
Table 5-3 System parameters for testing the distributed virtual inertia. 149
Table 5-4 Control parameters for testing the distributed virtual inertia. 150
Table 5-5 System parameters of the proposed VSG system. 161

Table 5-6 Control parameters of the DC voltage/current controller of HESSs. 163
Table 5-7 Control parameters of the frequency controller of HESSs. 164

List of Acronyms

AC	Alternating Current
APF	Active Power Filter
CCC	Current-Controlled Converter
d-axis	Direct-Axis
DC	Direct Current
DVR	Dynamic Voltage Restorer
ESR	Equivalent Series Resistor
ESS	Energy Storage System
FACTS	Flexible Alternating Current Transmission System
EV	Electric Vehicle
GM	Gain Margin
HESS	Hybrid Energy Storage System
HVAC	High-Voltage Alternating Current
HVDC	High-Voltage Direct Current
KCL	Kirchhoff's Current Law
KVL	Kirchhoff's Voltage Law
LPF	Low-Pass Filter
MPPT	Maximum Power Point Tracking
PI	Proportional Integral
PM	Phase Margin
PLL	Phase-Locked-Loop
PV	Photovoltaic
PWM	Pulse Width Modulation
q-axis	Quadrature-Axis
RES	Renewable Energy Source
RoCoF	Rate of Change of Frequency
STATCOM	Static Compensator
SPRLCL	Series-Parallel-Resonant LCL Filter

SVG	Static Var Generator
TDD	Total Demand Distortion
THD	Total Harmonic Distortion
UC	Ultracapacitor
UPFC	United Power Flow Controller
UPQC	United Power Quality Conditioner
UPS	Uninterruptible Power Supply
VCC	Voltage-Controlled Converter
VSG	Virtual Synchronous Generator
VSM	Virtual Synchronous Machine
ZOH	Zero-Order Hold

Chapter 1 Introduction

In the beginning, this chapter presents the research background of the trend of grid transformations. Following this trend, conventional power systems gradually evolve into more-electronics power systems. However, power electronics brings in issues to power systems. Specifically, the power quality and instability issues introduced by power electronics pose serious threats, and thus solving them becomes the research objectives of this thesis. After elaborating on the research motivation and objectives, this chapter provides a summary of the major contributions of this thesis. Finally, the chapter ends with the thesis organization.

1.1 Background

Presently, there is a global trend of grid transformations. The primary drivers behind this trend include the increase of energy production and environmental protection. The conventional power system suffers from considerable transmission losses, greenhouse gas emissions, and low energy conversion efficiency. As the trend continues, conventional power systems are expected to be replaced by next-generation power systems, or known as smart grids, in the future [1]. The smart grid features a high penetration level of renewable energy sources (RESs), a large-scale deployment of energy storage and grid-connected electric vehicles (EVs), pervasive monitoring and control, and self-healing capability [2]. These features necessitate flexible power conversions and accurate control of various electrical parameters, i.e. voltage, current, power, etc. Such requirements make power electronics an enabling technology for future smart grids, because the core of power electronics lies in the process and conversion of power [3].

Grid transformations already happen and can be evidenced by the worldwide growing penetration levels of RESs, such as solar photovoltaics (PV) and wind power. For demonstration, Figure 1.1 and Figure 1.2 illustrate the global capacity

and annual additions from 2006 to 2016 of solar PV and wind power, respectively [4]. It is clear that the installation capacity of renewable energies continues to increase, particularly for solar PV, whose annual addition even outweighs that of wind power in 2016.

Different from fossil fuel-based generators, renewable generators are normally coupled to power grids through power electronic converters. The employment of power electronics allows smooth power transfers between renewable generators

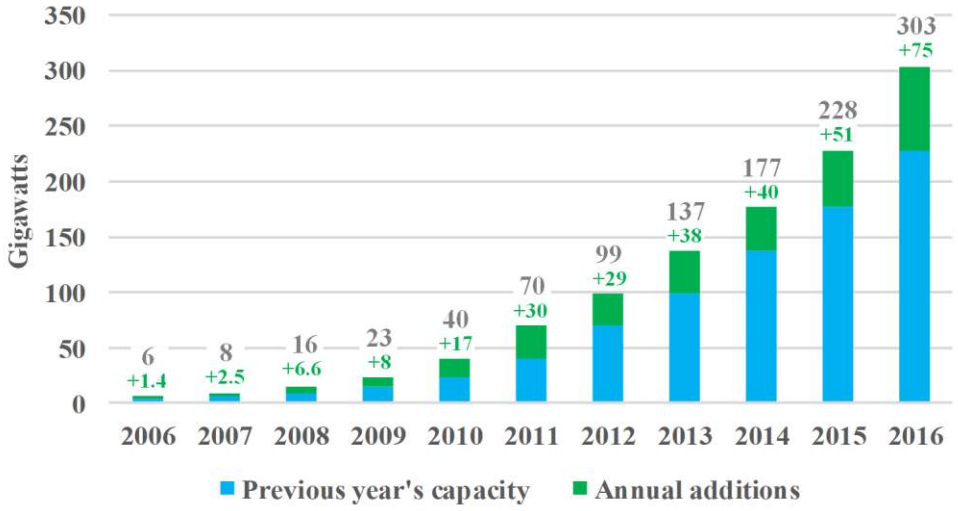

Figure 1.1 Solar PV global capacity and annual additions, 2006−2016 [4].

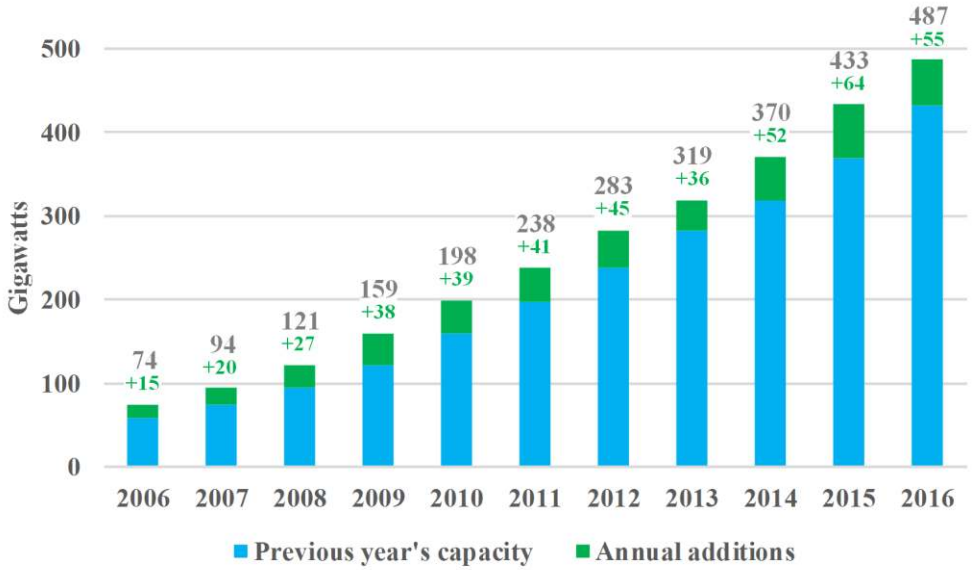

Figure 1.2 Wind power global capacity and annual additions, 2006−2016 [4].

and power grids. For instance, the PV panel generally outputs a DC voltage, which can be boosted up into a higher DC voltage through a DC/DC converter and then inverted into an AC voltage for grid connection, as demonstrated in Figure 1.3(a). Similarly, the wind turbine may be connected to the power grid through a back to back power converter consisting of an AC/DC rectifier and a DC/AC inverter for speed regulation and reactive power support, as shown in Figure 1.3(b). Although it is possible to achieve a direct integration of wind power without the use of power converters, known as the Danish Concept, such a solution leads to a fixed rotor speed, hence low efficiency [5]. As a result, power electronics becomes an essential part in renewable generation systems.

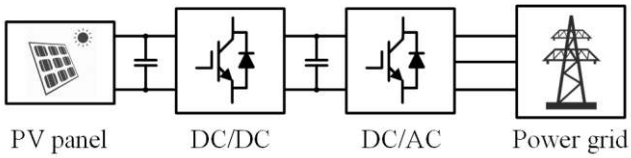

(a) PV generation system

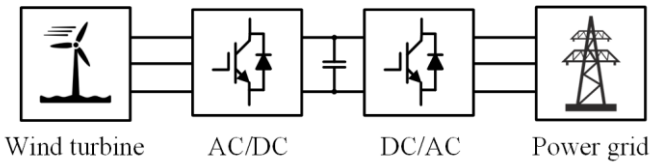

(b) Wind generation system

Figure 1.3 Schematic diagrams of renewable generation systems [6].

One drawback of the power produced by renewable generators lies in its intermittency. That is, the PV output power varies greatly with solar irradiances, and the availability of wind power depends greatly on wind speeds. In order to get rid of the uncertainty due to weather conditions, energy storage devices, such as batteries, ultracapacitors, flywheels, and fuel cells, are increasingly applied to modern power systems [7]. These energy storage devices may either be integrated into renewable generation systems or leveraged as individual energy storage systems (ESSs). For the former case, energy storage devices are usually connected to the DC-links of inverters through DC/DC converters. For the latter case, ESSs may be configured in a variety of ways. One notable example is the battery storage system shown in Figure 1.4, where the battery replaces the PV

panel in Figure 1.3(a) [8]. Power converters in Figure 1.4 should enable bidirectional power transfers so that the charging state of the battery can be managed.

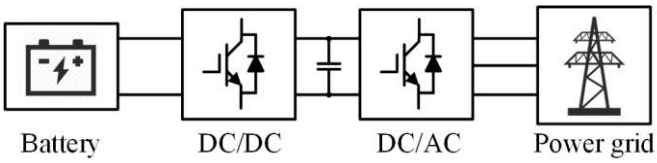

Figure 1.4 Schematic diagram of energy storage systems [9].

Energy storage is also quite necessary in EVs [10]. The development of EVs will materialize the vehicle-to-grid concept, through which EVs are supposed to exchange power with the power grid and provide the grid support whenever necessary. Figure 1.5 details the ESSs in grid-connected EVs, where the adoption of various types of power converters noticeably validates the vital role which power electronics plays.

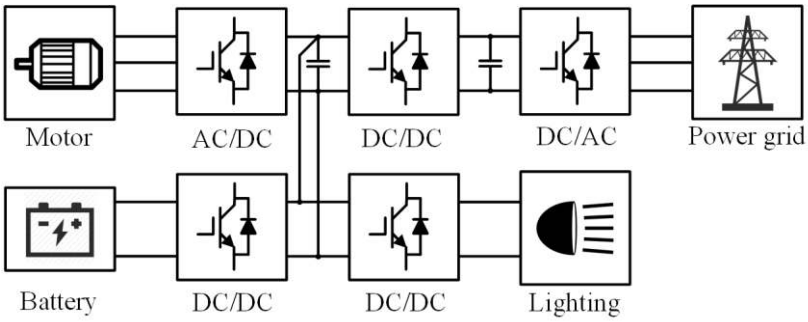

Figure 1.5 Schematic diagram of energy storage systems in electric vehicles [11].

Besides being used in renewable generation and ESSs, power electronics also finds its use in several other grid-connected applications. These applications include power supplies for domestic appliances, telecommunication centers, lighting, industrial electrolyte, and induction heating. In addition, the electric motor drive remains to be one major application field of power electronics. Additionally, the power quality improvement of power systems through power electronics is also showing great promise. To list a few examples, uninterruptable power supplies (UPSs), static var generators (SVGs) or static compensators (STATCOMs), active power filters (APFs), dynamic voltage restorers (DVRs), and unified power flow controllers (UPFCs) or unified power quality

conditioners (UPQCs) are all power electronic converters with dedicated control. In addition to STATCOMs or SVGs, other series and parallel power electronics-based compensation equipment is widely used in flexible AC transmission systems (FACTs) to enhance the controllability and power transfer capability of AC grids. In high-voltage high-power applications, such as high-voltage DC or AC (HVDC or HVAC) transmissions, power converters enabling flexible voltage and current transformations become the primary choice.

The applications of power electronics in modern power systems are summarized graphically in Figure 1.6. It can be safely concluded from Figure 1.6 and the above discussions that modern power systems are essentially more-

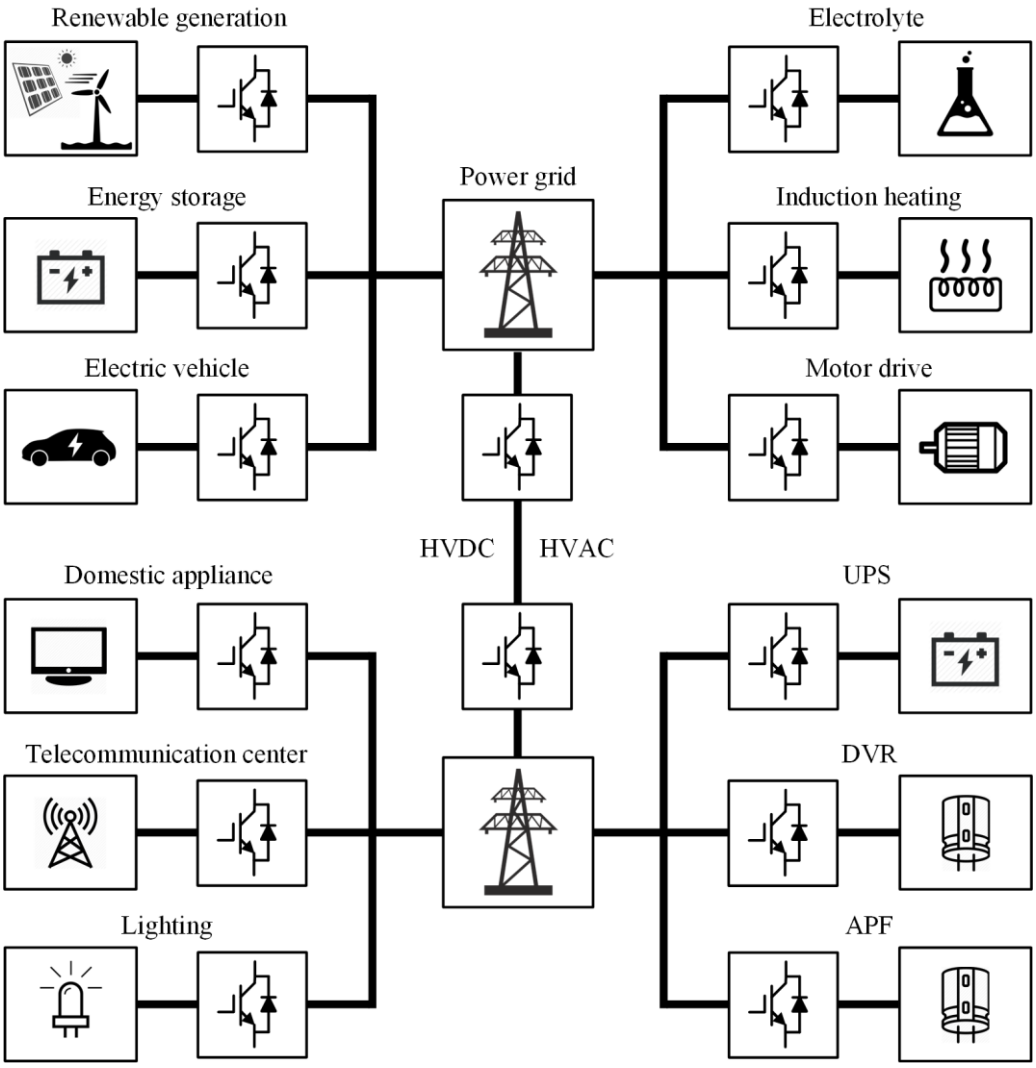

Figure 1.6 Applications of power electronics in more-electronics power systems.

electronics power systems, where the power converters acting as grid interfaces play an important role in matching the voltages/currents between generation and demand, and they are ubiquitous in more-electronics power systems.

1.2 Motivation and Objectives

Despite clear efficiency and control benefits, power electronics also brings in issues to more-electronics power systems and challenges their operations in terms of power quality and stability. Power quality and stability are two important aspects that greatly influence the operations of power systems. By definition, power quality issues refer to voltage and current deviations that cause malfunction or failure of customer equipment [12]. While the stability is defined as the property of a power system to maintain within an equilibrium state after being subjected to a disturbance [13]. Since the power quality and instability issues faced by more-electronics power systems take various forms and have different roots, this thesis only focuses on the major issues, which are caused by and can be resolved by power electronics.

Power quality issues can be largely categorized into two groups, i.e. the issues pertaining to the voltage quality and issues regarding the current quality. Power system operators are supposed to provide high-quality voltages to satisfy customers, while customers should always remember to comply with grid codes and inject (absorb) only clean currents to (from) power grids.

Typical voltage quality issues comprise voltage sags/swells, unbalances, and harmonics [12]. Normally, the grid voltages generated by synchronous generators feature standard voltage amplitudes, frequency, and highly sinusoidal waveforms. However, the voltages seen by end-users could have quality issues. These issues are usually caused by the voltage drops along transmission lines, and the undesirable load currents following through the transmission lines should be blamed for such voltage drops. For this reason, most of the voltage quality issues are caused by the existing current quality issues. Therefore, it is the responsibility of both power system operators and customers to ensure high-quality voltage

supplies [14]. By means of power electronics, the solutions to voltage quality issues include DVRs and UPQCs [15-17].

Since current quality issues may be the roots for voltage quality issues, this thesis mainly focuses on the current quality issues introduced by power electronics. Current harmonics and the reactive current are two common current quality issues. Current harmonics refer to the current components appearing at the multiples of fundamental frequency. Without being properly handled, current harmonics may introduce additional power losses and noises, interferences with communication systems, or even fire hazards. In addition, current harmonics have the risk of being magnified through system resonances, and therefore they must be effectively attenuated. Grid codes prescribe standards, e.g. IEEE Standard 519-2014, on current harmonics, as tabulated in Table 1-1 [14], where the total demand distortion (TDD) is defined as the square root of the sum of harmonic components divided by the maximum load fundamental current [12]. It equals the total harmonic distortion (THD) under maximum load conditions [12].

Table 1-1 Current distortion limits for systems rated from 120 V through 69 kV [14].

Maximum harmonic current distortion in percent of I_L						
Individual harmonic order (odd harmonics)[a,b]						
I_{sc}/I_L	$3 \le h < 11$	$11 \le h < 17$	$17 \le h < 23$	$23 \le h < 35$	$35 \le h < 50$	TDD
< 20[c]	4.0	2.0	1.5	0.6	0.3	5.0
20 < 50	7.0	3.5	2.5	1.0	0.5	8.0
50 < 100	10.0	4.5	4.0	1.5	0.7	12.0
100 < 1000	12.0	5.5	5.0	2.0	1.0	15.0
> 1000	15.0	7.0	6.0	2.5	1.4	20.0

[a]Even harmonics are limited to 25% of the odd harmonic limits above.
[b]Current distortions that result in a DC offset, e.g., half-wave converters, are not allowed.
[c]All power generation equipment is limited to these values of current distortion, regardless of actual I_{sc}/I_L.
where I_{sc} = maximum short-circuit current at PCC
I_L = maximum demand load current (fundamental frequency component) at the PCC under normal load operating conditions.

As observed, more stringent standards are prescribed for weak power grids, which are characterized by a small ratio of the maximum short-circuit current to

the maximum demand load current. This can be understandable, because the weak grid features the larger grid impedance and harmonic voltage drop as compared with those of a stiff grid. Another observation is that requirements become stricter as the harmonic order increases. This is based on the understanding that high-order harmonics have smaller magnitudes and can be better attenuated by passive filters. The reactive current corresponds to the fundamental current component in quadrature with the grid voltage, which will increase the system apparent power and may overload the system. As power electronic solutions, APFs and UPQCs are effective in the compensation of low-order current harmonics, e.g. 5^{th} and 7^{th} order harmonics, as well as the reactive current [18].

The operations of power converters produce high-order harmonics at the switching frequency and its multiples [19]. However, high-order current harmonics, e.g. the harmonics above several kilohertz, are difficult to be actively compensated by power electronic equipment, because such harmonics are often beyond the control bandwidths of power converters. As such, passive filters are always necessary in power converters to cope with high-order harmonics [20]. To sufficiently attenuate switching harmonics and comply with grid codes, passive filters have to incorporate large inductors and/or capacitors. Nevertheless, these passive components are often bulky and expensive as compared with their active counterparts [21]. Hence, there is a strong motivation to attenuate the harmonics introduced by power converters using smaller filter components. This objective can be achieved using advanced passive filters and/or the magnetic integration technique, as will be detailed.

In addition to causing power quality issues, the use of power electronics may challenge the stability of more-electronics power systems. The instability issues can be broadly divided into two categories − converter-level and system-level instability issues. Although being properly designed for normal operating conditions, power converters may become unstable when applied to specific more-electronics power systems. Additionally, even if individual power

converters can operate stably, the entire power system may become unstable. These instability issues as well as the relevant mitigation methods serve as the major research motivation and objectives of this thesis.

Improper controller designs, time-delays, resonances arising from high-order passive filters, interactions among multiple power converters, and weak grids may lead to converter-level instabilities [22-24]. In particular, power converters may become unstable under weak power grids if the grid synchronization through phase-locked-loops (PLLs) do not work well. This issue has already been identified in [25-28]. However, effective measures capable of overcoming this instability issue have so far not been found. Therefore, converter-level instability issues and their solutions are further explored in this thesis.

The grid frequency and voltage amplitude are fundamental health indicators of power systems, and the angles of different buses are another indicator [13]. Specifically, the frequency stands for the degree of the active power balance between generation and demand, while the voltage amplitude indicates the extent of the reactive power balance. Frequency and voltage variations beyond certain acceptable ranges may cause generation and load tripping or even grid collapses [13]. Therefore, the grid frequency and voltages must be well regulated through proper power control. For clarity, Table 1-2 provides a classification of system-level instability issues, their mechanisms, and typical solutions in conventional power systems.

Table 1-2 Classification of system-level instability issues, mechanisms, and solutions [13].

Instability issue		Mechanism	Solution
Frequency	Non-oscillatory small-signal instability	Insufficient synchronizing torque	Synchronous generator
	Oscillatory small-signal instability	Insufficient damping torque or unstable control	Power system stabilizer
	Transient instability	Large disturbance	Power flow control
Voltage	Small-disturbance voltage instability	Reactive power imbalance	Reactive power reserve
	Large-disturbance voltage instability	Large disturbance	Coordination of protection and control

As compared with conventional power systems, more-electronics power systems may exploit the reactive power compensation capability of specific power electronic equipment, e.g. SVGs and APFs, or grid-connected power converters to achieve the voltage support and help balance the reactive power [29, 30]. Grid-connected power converters inherently have the reactive power compensation capability, and this can be achieved using their DC-link capacitors without any additional power source or energy storage unit [29].

However, the frequency support and active power compensation through grid-connected power converters are not very straightforward, as capacitors cannot continuously absorb/output active power. Currently, grid-connected power converters often transfer certain amounts of active power according to the requirements of relevant sources and loads. For example, in renewable generation applications, grid-connected power converters operate in the maximum power point tracking (MPPT) mode to optimize the energy yield regardless of grid conditions. So far, the power electronic equipment without energy storage dedicated to active power compensation has not been reported. In conventional power systems, synchronous generators help balance the active power and frequency. During frequency events and power imbalance conditions, synchronous generators automatically inject or absorb power for frequency support, and this effect is partially caused by the power system inertia. As the power converters featuring no inertia gradually replaces synchronous generators in more-electronics power systems, the frequency regulation becomes a serious concern. To address the concern, this thesis explores the possibility of frequency regulation and frequency stability improvement by use of power electronics. Normally, energy storage is necessary, used in combination with power converters, for flexible active power and frequency control [31, 32]. However, as will be revealed later, it is possible to achieve the frequency stability improvement of more-electronics power systems by means of inertia enhancement without additional energy storage.

From the above discussions, the research motivation and objectives of this thesis are summarized as follows:

- to identify the major power quality and instability issues introduced by power electronics in more-electronics power systems as well as the state of the art solutions;
- to construct a single-area more-electronics power system, through which power quality and instability issues, together with their solutions, can be investigated and verified;
- to address the major power quality issue, viz. the current harmonic issue due to power converters;
- to investigate the converter-level instability issue arising from grid synchronization and PLLs as well as resolve this issue;
- to explore system-level frequency instability issues, particularly for those associated with the lack of inertia, and propose feasible solutions;
- to figure out the potential power quality and instability issues faced by future more-electronics power systems and provide future research directions;

1.3 Major Contributions of the Thesis

This thesis investigates and resolves several power quality and instability issues due to the widespread use of power electronics in more-electronics power systems. Its major contributions can be summarized as follows:

- The major power quality and instability issues introduced by power electronics in more-electronics power systems and their state-of-the-art solutions have been identified.
- A single-area more-electronics power system has been built up in the laboratory. This prototype serves as the research object and is dedicated to investigating power quality and instability issues as well as their solutions.

- Several advanced passive filters, i.e. the magnetic integrated *LLCL* filter, series-parallel-resonant *LCL* (*SPRLCL*) filter, and *LT-C-L* filter, have been proposed to effectively attenuate the switching harmonics generated by grid-connected power converters. These advanced passive filters have attractive features of small filter sizes, strong attenuation, and high robustness;
- The converter-level instability issue arising from grid synchronization and PLLs has been investigated. Furthermore, this issue has been successfully resolved through the modification of converter control and reshaping the quadrature-axis (*q*-axis) impedance of power converters as a positive resistance in the low-frequency band;
- The concept of the distributed virtual inertia by grid-connected power converters has been proposed. Through the proposed virtual inertia control, grid-connected power converters are supposed to generate the virtual inertia and improve the system-level frequency stability. In addition, the frequency stability improvement using virtual synchronous generators (VSGs) has been explored. In particular, the proposed VSG contains a hybrid energy storage system (HESS) for power management;
- The future research directions on the improvement of power quality and stability in more-electronics power systems have been pointed out.

1.4 Organization of the Thesis

This thesis is categorized into six chapters, which are briefly discussed as listed below:

Chapter 1 introduces the ongoing trend of grid transformations. Following this trend, conventional power systems gradually evolve into more-electronics power systems. Along with the benefits of power electronics are power quality and instability issues. The motivation and objectives of this thesis are to investigate and overcome these issues. The analysis and solutions concerning these issues serve as the major contributions of this thesis.

Chapter 2 describes the fundamentals of more-electronics power systems, covering the system configuration, operating principle, mathematic modelling, and controller designs. A single-area more-electronics power system is constructed and used as the research object. In more-electronics power systems, two major types of grid-interfaced power converters, viz. those controlled as AC voltage sources and AC current sources, are analysed in detail. In addition, the grid support functions implemented by power converters are reviewed.

Chapter 3 proposes several advanced passive filters for harmonic filtering and power quality improvement. These filters feature extra *LC* resonant trap(s), tuned at the switching frequency and its multiples. Specifically, the integrated *LLCL* filter is derived from the integrated *LCL* filter by intentionally designing the coupling between the two inductors. It combines the advantages of magnetic integration and trap filter. The series-parallel-resonant *LCL* (*SPRLCL*) filter has one series *LC*-trap and one parallel *LC*-trap. It enables enhanced filtering and robustness. The *LT-C-L* filter is a combination of a parallel-resonant *LC*-trap and an *LCL* filter. It turns out to be the most promising trap filter due to the advantages of high robustness, roll-off rate, and reduced converter current distortions.

Chapter 4 explores the converter-level instability issue due to PLLs under weak grid conditions as well as its solution. To maintain synchronism with the power grid, PLLs are normally necessary in current-controlled or grid-following power converters. However, the employment of PLLs shapes the *q*-axis converter impedance as a negative resistance within its control bandwidth and causes an instability concern. To address this concern, an impedance controller directly relating the *q*-axis voltage to the *q*-axis current reference is proposed. The proposed controller reshapes the *q*-axis converter impedance as a positive resistance in the low-frequency band and stabilizes the power converter control.

Chapter 5 aims to improve the system-level frequency stability of more-electronics power systems by use of the grid-connected power converters with the distributed virtual inertia or operated as VSGs. These solutions tend to

improve the frequency stability by means of inertia enhancement. The distributed virtual inertia can be expected from grid-connected power converters when the grid frequency and DC-link voltages are proportionally related. As a result, the improvements of frequency nadir and rate of change of frequency (RoCoF) can be achieved. An alternative approach for inertia enhancement lies in the employment of VSGs. The proposed VSG contains a HESS consisting of a battery and an ultracapacitor for better power management.

Chapter 6 presents the future research directions concerning the power quality and stability improvement of more-electronics power systems. First, the power converters supporting power grids under adverse grid conditions are considered as a research direction. Another research direction lies in the investigation of the converter-level instability due to the grid support by power converters under weak grids. In addition, there is a great opportunity to explore the inertia emulation capabilities of energy storage units, such as batteries, for system-level frequency stability improvement.

Chapter 2 Fundamentals of More-Electronics Power Systems

This chapter discusses the fundamentals of more-electronics power systems. It begins with the background and introduction. Next, the configuration and fundamental components of more-electronics power systems are described. Special attention is paid to the example more-electronics power system, which is selected as the research object and constructed in the laboratory. This is followed by the detailed descriptions with regards to the modelling and control of two basic types of power converters in more-electronics power systems, viz. power converters controlled as AC voltage sources and those controlled as AC current sources. Finally, the power converters with grid support functions are presented in this chapter.

2.1 Background and Introduction

As the shares of renewable energies continue to grow, along with the developments of other emerging technologies associated with power electronics, e.g. grid-scale energy storage and EVs, modern power systems gradually develop into more-electronics power systems.

Conventionally, power systems operate in a centralized manner [13]. The electricity is generated by gas- or coal-fired synchronous generators and then transformed into high-voltage levels and transmitted along long-distance transmission lines, before being transformed back into low-voltage levels and consumed by end-users.

In contrast, more-electronics power systems operate more flexibly. Specifically, electricity can be generated by a mix of distributed generators, e.g. PV arrays and wind turbines, and then consumed locally with the surplus energy stored in energy storage units, e.g. batteries. Moreover, customers may not always be electrical loads [33]. Instead, they are encouraged to contribute to active and reactive power regulations according to the requirements of power grids. In terms

of system scales, the more-electronics power system can be either a large-scale power system consisting of multiple areas or a small-scale microgrid being able to operate both in grid-connected and islanded modes. Being different from the power electronics-based power system, where all the equipment is connected to power grids via power electronics [34], the more-electronics power system may contain conventional synchronous generators or motor loads. Nonetheless, it is also possible for a more-electronics power system to be a power electronics-based power system.

The most salient feature of more-electronics power systems lies in the widespread use of power electronics. Referring to Figure 1.6, power converters are employed as grid interfaces for a huge amount of equipment. Under this condition, the operations of grid-interfaced power converters may greatly influence the entire power system. Therefore, the major issues brought by power converters in more-electronics power systems should be carefully investigated. More importantly, the solutions to these issues should be seriously pursued.

2.2 System Configuration

Like conventional power systems, more-electronics power systems contain generators and loads, although generators and loads may be interchangeable from time to time. Besides conventional synchronous generators, renewable generators are deployed in a large-scale and play an essential role in more-electronics power systems. Additionally, ESSs capable of balancing the power mismatch between generation and demand are normally involved. It should be highlighted that renewable generators and ESSs are coupled to power grids through grid-interfaced power converters, which serve as the basic units in more-electronics power systems. These power converters manage to convert DC voltages into desirable AC voltages or alternatively from AC voltages into desirable DC voltages. The modelling and control of grid-interfaced power converters will be discussed later in this chapter.

In order to facilitate the analysis of issues and address them in a more intuitive

way, a single-area more-electronics power system consisting of a virtual synchronous generator (VSG), a PV generation system, an energy storage system (ESS), and AC loads has been selected as the research object. It is shown schematically in Figure 2.1, where the DC-links of all the three-phase grid-interfaced power converters can be connected to either DC voltage sources or capacitors, depending on specific operating conditions.

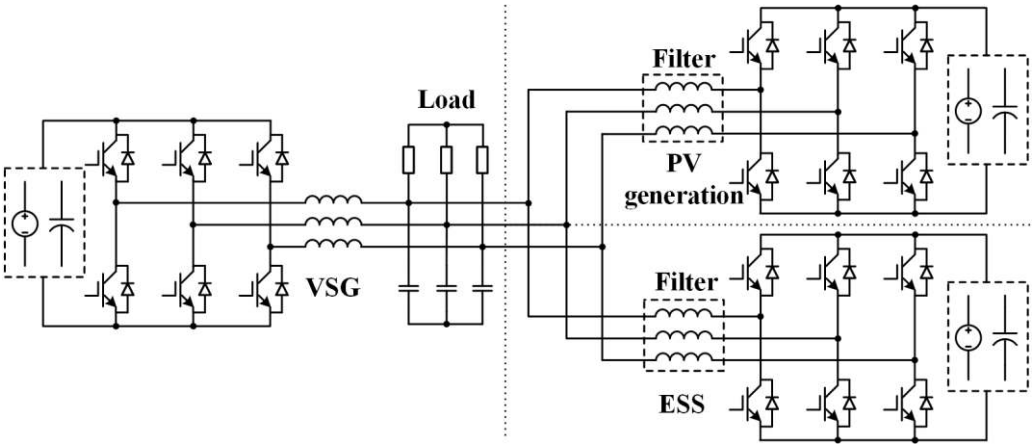

Figure 2.1 Schematic diagram of the example more-electronics power system.

The employment of VSGs allows the regulation of grid voltages and frequency in more-electronics power systems. VSGs are essentially power converters emulating the behaviours of conventional synchronous generators [35, 36]. In Figure 2.1, the VSG aims to operate exactly as the conventional synchronous generator so that power quality and instability issues can be better investigated. It should be remembered that the VSG can be equivalent to a controllable voltage source from the AC side, and therefore it is filtered through an *LC*-filter, where the voltages across the filter capacitors are the AC output voltages [37].

Similar power converters serve as grid interfaces for the PV generation system and ESS, respectively. The differences lie in their DC sides and control schemes. From the AC side, the PV generation system and ESS can be equivalent to controllable AC current sources. As for filters, single inductor *L* filters are the simplest option. However, high-order passive filters, such as the well-known *LCL* filters, may also be selected to improve the filtering capacity and power density of grid-connected converters, as will be detailed in the following sections.

In this system, grid voltages are provided by the VSG. In contrast, the PV generation system and ESS simply inject (absorb) active and reactive powers. Although the power system shown in Figure 2.1 features a small system scale, it incorporates the major components in more-electronics power systems, i.e. the renewable generation, energy storage, and synchronous generator, and can be representative of many other power systems. In accordance to Figure 2.1, a more-electronics power system has been constructed in the laboratory. Figure 2.2 shows its photo, where the key components are listed in Table 2-1.

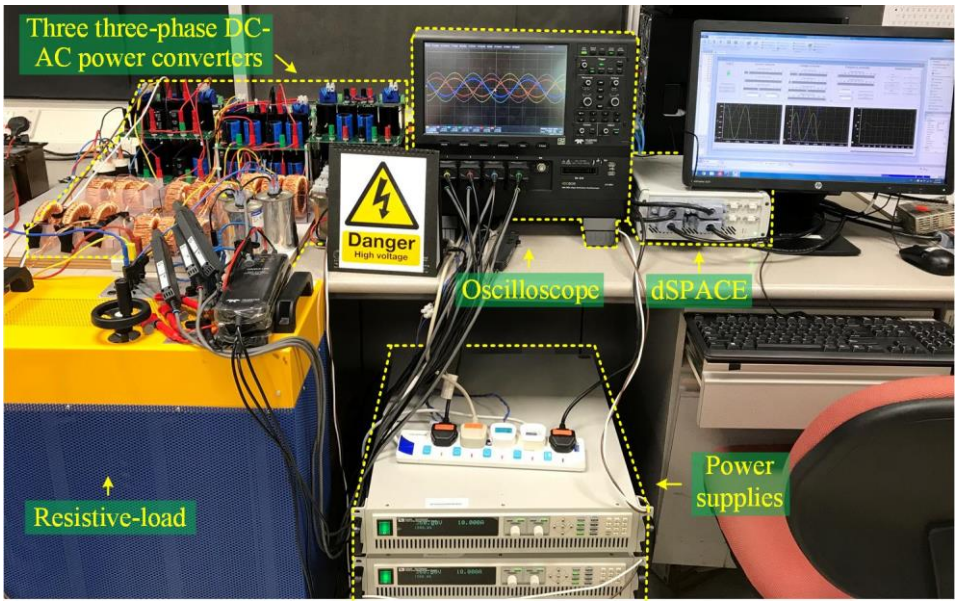

Figure 2.2 Photo of the experimental prototype.

Table 2-1 Experimental components.

Component	Description
Controller	dSPACE Microlabbox
DC power supplies	ITECH IT6500
Oscilloscope	LECROY HDO8038
Switches	CREE C3M0065090D

From the above analysis, there are basically two types of grid-interfaced power converters, viz. power converters controlled as AC voltage sources, e.g. the VSG, and those controlled as AC current sources, e.g. the PV generation system and ESS, in more-electronics power systems [38]. Therefore, the modelling and control of these two types of power converters will be separately discussed.

2.3 Power Converters Controlled as AC Voltage Sources

Figure 2.3 illustrates the schematic diagram of power converters controlled as AC voltage sources, i.e. voltage-controlled converters (VCCs), where the DC-link is connected to a DC voltage source whose voltage is denoted as v_{gdc}. The semiconductor switches $S_{g1} - S_{g6}$ operate at a switching frequency f_{sw}, converting v_{gdc} into AC voltage pulses, before being filtered through the *LC* filter. The basic target of VCCs is to regulate the capacitor voltages v_{gfx} ($x = a, b, c$) following their references – the amplitude v_{gf_ref} and phase angle θ_0.

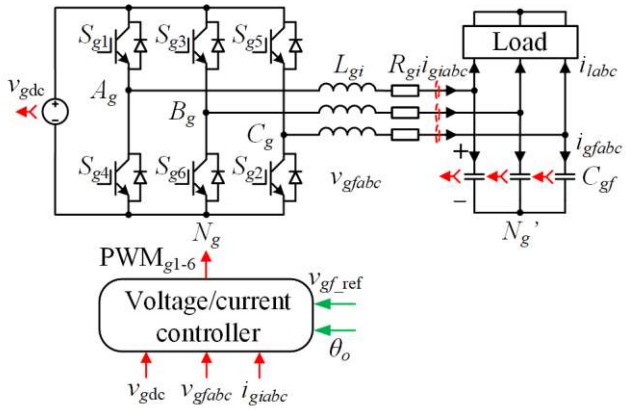

Figure 2.3 Schematic diagram of VCCs.

2.3.1 System Modelling

First, the mathematical model of VCCs is derived, based on which the controller design will then be discussed. Let v_{gxN} ($x = a, b, c$) denote the voltages across the nodes X_g ($X_g = A_g, B_g, C_g$) and N_g, respectively. The following equations can be derived based on the Kirchhoff's voltage law (KVL):

$$\begin{cases} v_{gaN}(t) = v_{gfa}(t) + L_{gi}\dfrac{\mathrm{d}i_{gia}(t)}{\mathrm{d}t} + R_{gi}i_{gia}(t) + v_{gN'N}(t) \\ v_{gbN}(t) = v_{gfb}(t) + L_{gi}\dfrac{\mathrm{d}i_{gib}(t)}{\mathrm{d}t} + R_{gi}i_{gib}(t) + v_{gN'N}(t), \\ v_{gcN}(t) = v_{gfc}(t) + L_{gi}\dfrac{\mathrm{d}i_{gic}(t)}{\mathrm{d}t} + R_{gi}i_{gic}(t) + v_{gN'N}(t) \end{cases} \tag{2-1}$$

where $v_{gN'N}$ represents the voltage between nodes N_g' and N_g.

The capacitor voltages v_{gfx} ($x = a, b, c$) can be further expressed as a function of filter currents i_{gix} ($x = a, b, c$) and load currents i_{lx} ($x = a, b, c$) as:

$$\begin{cases} v_{gfa}(t) = \dfrac{1}{C_{gf}} \int \left[i_{gia}(t) - i_{la}(t) \right] \\ v_{gfb}(t) = \dfrac{1}{C_{gf}} \int \left[i_{gib}(t) - i_{lb}(t) \right] \\ v_{gfc}(t) = \dfrac{1}{C_{gf}} \int \left[i_{gic}(t) - i_{lc}(t) \right] \end{cases}. \tag{2-2}$$

For three-phase three-wire systems, the sum of three-phase currents should always be zero. By summing the three equations in (2-2), it is inferred that three-phase capacitor voltages also amount to zero. With these facts, (2-1) becomes

$$v_{gN'N}(t) = \frac{v_{gaN}(t) + v_{gbN}(t) + v_{gcN}(t)}{3}. \tag{2-3}$$

Inserting (2-3) into (2-1), one obtains

$$\begin{cases} \dfrac{2v_{gaN}(t) - v_{gbN}(t) - v_{gcN}(t)}{3} = v_{gfa}(t) + L_{gi} \dfrac{\mathrm{d}i_{gia}(t)}{\mathrm{d}t} + R_{gi} i_{gia}(t) \\ \dfrac{-v_{gaN}(t) + 2v_{gbN}(t) - v_{gcN}(t)}{3} = v_{gfb}(t) + L_{gi} \dfrac{\mathrm{d}i_{gib}(t)}{\mathrm{d}t} + R_{gi} i_{gib}(t) \\ \dfrac{-v_{gaN}(t) - v_{gbN}(t) + 2v_{gcN}(t)}{3} = v_{gfc}(t) + L_{gi} \dfrac{\mathrm{d}i_{gic}(t)}{\mathrm{d}t} + R_{gi} i_{gic}(t) \end{cases}. \tag{2-4}$$

Define S_{gx} ($x = a, b, c$) as the switch functions. Specifically, the state of $S_{gx} = 1$ corresponds to the on-state of upper switches and off-state of lower switches, and vice versa for the state of $S_{gx} = 0$. Following this definition, $v_{gxN} = S_{gx} v_{g\mathrm{dc}}$ ($x = a, b, c$) can be satisfied, which upon substituted into (2-4) yields

$$\begin{cases} \dfrac{2S_{ga}(t) - S_{gb}(t) - S_{gc}(t)}{3} V_{g\mathrm{dc\_ref}} = v_{gfa}(t) + L_{gi} \dfrac{\mathrm{d}i_{gia}(t)}{\mathrm{d}t} + R_{gi} i_{gia}(t) \\ \dfrac{-S_{ga}(t) + 2S_{gb}(t) - S_{gc}(t)}{3} V_{g\mathrm{dc\_ref}} = v_{gfb}(t) + L_{gi} \dfrac{\mathrm{d}i_{gib}(t)}{\mathrm{d}t} + R_{gi} i_{gib}(t) \\ \dfrac{-S_{ga}(t) - S_{gb}(t) + 2S_{gc}(t)}{3} V_{g\mathrm{dc\_ref}} = v_{gfc}(t) + L_{gi} \dfrac{\mathrm{d}i_{gic}(t)}{\mathrm{d}t} + R_{gi} i_{gic}(t) \end{cases}, \tag{2-5}$$

where $v_{g\mathrm{dc}}$ is replaced by a constant $V_{g\mathrm{dc\_ref}}$. For controller designs, (2-5) can be reorganized in the synchronous $dq0$-frame.

One advantage of the *dq*0-frame is that currents can be easily mapped to active and reactive powers [29]. Moreover, sinusoidal signals are mapped into DC signals, and hence they can be controlled with zero steady-state errors by integrators. The *abc* to *dq*0 transformation consists of two matrices. First, the *abc* to *αβ*0 matrix transforms signals into the stationary *αβ*0-frame, where the *α*-axis aligns the *a*-axis [29]. Also, the *αβ*0-frame control is possible, where integrators should be replaced by resonant controllers [6, 22, 39]. Next, the *αβ*0 to *dq*0 matrix further rotates signals into the synchronous *dq*0-frame. Among various implementations, the matrix mapping positive sequence cosine signals into constants in the *d*-axis has been widely used [40, 41]:

$$T_{dq0/abc} = \frac{2}{3}\begin{bmatrix} \cos\theta_o(t) & \cos\left(\theta_o(t)-\frac{2\pi}{3}\right) & \cos\left(\theta_o(t)+\frac{2\pi}{3}\right) \\ -\sin\theta_o(t) & -\sin\left(\theta_o(t)-\frac{2\pi}{3}\right) & -\sin\left(\theta_o(t)+\frac{2\pi}{3}\right) \\ \frac{1}{2} & \frac{1}{2} & \frac{1}{2} \end{bmatrix}, \tag{2-6}$$

where θ_o is the angle shown in Figure 2.3. After expressing the *abc*-frame signals in the *dq*0-frame signals using the inverse of $T_{dq0/abc}$, (2-5) and (2-2) become

$$\begin{cases} V_{\text{gdc\_ref}} S_{gd}(t) = v_{gfd}(t) + L_{gi}\dfrac{\mathrm{d}i_{gid}(t)}{\mathrm{d}t} + R_{gi}i_{gid}(t) - \omega_o L_{gi} i_{giq}(t) \\ V_{\text{gdc\_ref}} S_{gq}(t) = v_{gfq}(t) + L_{gi}\dfrac{\mathrm{d}i_{giq}(t)}{\mathrm{d}t} + R_{gi}i_{giq}(t) + \omega_o L_{gi} i_{gid}(t) \\ 0 = v_{gf0}(t) + L_{gi}\dfrac{\mathrm{d}i_{gi0}(t)}{\mathrm{d}t} + R_{gi}i_{gi0}(t) \end{cases}, \tag{2-7}$$

$$\begin{cases} C_{gf}\dfrac{\mathrm{d}v_{gfd}(t)}{\mathrm{d}t} - \omega_o C_{gf} v_{gfq}(t) = i_{gid}(t) - i_{ld}(t) \\ C_{gf}\dfrac{\mathrm{d}v_{gfq}(t)}{\mathrm{d}t} + \omega_o C_{gf} v_{gfd}(t) = i_{giq}(t) - i_{lq}(t) \\ C_{gf}\dfrac{\mathrm{d}v_{gf0}(t)}{\mathrm{d}t} = i_{gi0}(t) - i_{l0}(t) \end{cases}, \tag{2-8}$$

where ω_o stands for the fundamental angular frequency, which equals the time derivative of θ_o. The third equations of (2-7) and (2-8) refer to the 0-axis, which

can be ignored henceforth. To facilitate controller designs, (2-7) and (2-8) can be expressed in the complex frequency domain by using the Laplace transformation:

$$\begin{cases} i_{gid}(s) = \dfrac{1}{L_{gi}s + R_{gi}}\left[V_{\text{gdc\_ref}} S_{gd}(s) - v_{gfd}(s) + \omega_o L_{gi} i_{giq}(s)\right] \\ i_{giq}(s) = \dfrac{1}{L_{gi}s + R_{gi}}\left[V_{\text{gdc\_ref}} S_{gq}(s) - v_{gfq}(s) - \omega_o L_{gi} i_{gid}(s)\right] \end{cases}, \tag{2-9}$$

$$\begin{cases} v_{gfd}(s) = \dfrac{1}{C_{gf}s}\left[i_{gid}(s) - i_{ld}(s) + \omega_o C_{gf} v_{gfq}(s)\right] \\ v_{gfq}(s) = \dfrac{1}{C_{gf}s}\left[i_{giq}(s) - i_{lq}(s) - \omega_o C_{gf} v_{gfd}(s)\right] \end{cases}, \tag{2-10}$$

where s denotes the Laplace operator. Equations (2-9) and (2-10) model the system plant, which is further shown schematically in Figure 2.4, where the cross-coupling terms ($-\omega_o L_{gi} i_{gid}$), ($\omega_o L_{gi} i_{giq}$), ($-\omega_o C_{gf} v_{gfd}$), and ($\omega_o C_{gf} v_{gfq}$) introduced by the *abc* to *dq*0 transformations can be observed. It is possible to mitigate the cross-coupling effects by voltage and current feedforward terms [6, 38]. When the cross-coupling effects are ignored, controllers can be designed independently in the *d*-axis and *q*-axis.

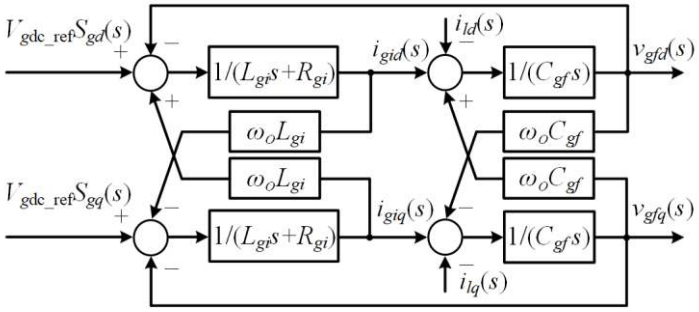

Figure 2.4 Block diagram of the system plant of VCCs.

2.3.2 Controller Design

After modelling the system plant, this subsection aims to design the voltage and current controllers according to the system parameters listed in Table 2-2, where a switching frequency f_{sw} of 10 kHz is a typical choice for kW-level power converters. Despite that the plant has been modelled in the continuous *s*-domain, it should be emphasized that control algorithms are implemented by digital

controllers, and therefore the associated voltage and current controllers should be designed in the discrete z-domain. This section follows the author's work in [42].

Table 2-2 System parameters of VCCs.

Description	Symbol	Value
Filter capacitance	C_{gf}	50 μF
Filter inductance	L_{gi}	1 mH
DC-link voltage reference	$V_{g\mathrm{dc\_ref}}$	400 V
AC voltage reference (rms)	V_{gf_ref}	110 V
Fundamental frequency	f_{ref}	50 Hz
Switching/sampling frequency	$f_{\mathrm{sw}}/f_{\mathrm{s}}$	10 kHz

Figure 2.5(a) details the block diagram of the voltage and current controllers in the mixed s- and z-domains, where $G_{gv}(z)$ and K_{gf} denote the voltage regulator and voltage feedforward compensator, respectively. The voltage regulator can be implemented as a proportional integral (PI) controller. To further improve the voltage quality, a repetitive controller is also employed, as will be discussed. K_{gc} and K_{gl} represent the current regulator and current feedback compensator, respectively. Since they are both implemented as proportional (P) controllers, K_{gc} and K_{gl} can be used to represent the relevant proportional gains.

z^{-1} and the ZOH (zero-order-hold) aim to model the pulse width modulated (PWM) generator. To be specific, the one sampling period delay z^{-1} is caused by the calculations and updates of modulation reference signals, because new references will not be active until calculations are finished and updated in the next sampling period [43]. After modulation signals are updated, they should compare with carrier signals and generate driving pulses. This process can be approximately modelled by the ZOH, which introduces a half sampling period delay [44]. However, note that this approximation only holds true in low-frequency bands, where frequencies are far below the switching frequency.

The plant in Figure 2.5(a) is the simplified version of that in Figure 2.4, where the coupling effect and resistance R_{gi} are ignored. Since it is applicable to both the d- and q-axes, the subscripts d and q are removed. Note that the gain $V_{g\mathrm{dc\_ref}}$ can be incorporated in controllers, and hence it is not explicitly shown here.

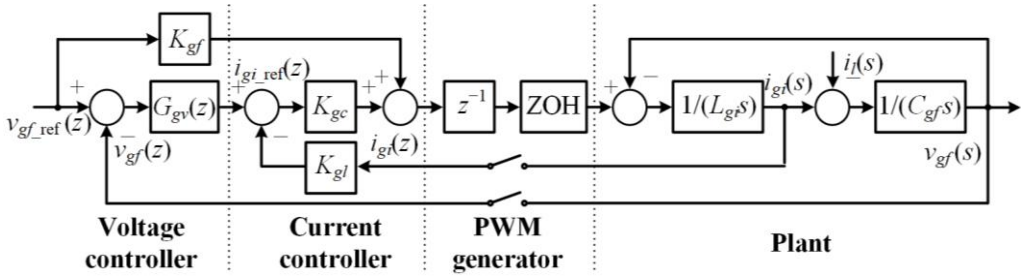

(a) Controller in the mixed *s*- and *z*-domains

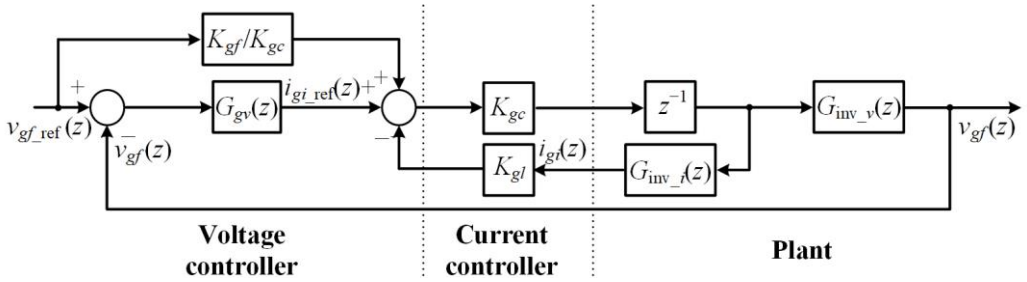

(b) Controller in the *z*-domain

Figure 2.5 Block diagram of the voltage and current controllers of VCCs in the (a) mixed *s*- and *z*-domains and (b) *z*-domain.

The transfer functions from the output of the ZOH to i_{gi} and v_{gf} are derived as

$$G_{\text{inv}\_i}(s) = \frac{C_{gf}s}{L_{gi}C_{gf}s^2+1}, \tag{2-11}$$

$$G_{\text{inv}\_v}(s) = \frac{1}{L_{gi}C_{gf}s^2+1}. \tag{2-12}$$

Through the ZOH *z* transformations, (2-11) and (2-12) change into

$$G_{\text{inv}\_i}(z) = \frac{\sin(\omega_{gr}T_s)(z-1)}{L_{gi}\omega_{gr}\left[z^2-2\cos(\omega_{gr}T_s)z+1\right]}, \tag{2-13}$$

$$G_{\text{inv}\_v}(z) = \frac{\left[1-\cos(\omega_{gr}T_s)\right](z+1)}{z^2-2\cos(\omega_{gr}T_s)z+1}, \tag{2-14}$$

where T_s (i.e. $1 / f_s$) stands for the sampling period. ω_{gr} denotes the resonance angular frequency of the *LC* filter, which is given by

$$\omega_{gr} = \frac{1}{\sqrt{L_{gi}C_{gf}}}. \tag{2-15}$$

With the help of (2-13) and (2-14), the voltage and current controllers can be expressed in the *z*-domain, as depicted in Figure 2.5(b). In what follows, the

design procedures of current controller and voltage controller will be provided sequentially. It should be mentioned that, except for limiting converter currents, the major objective of the current controller is to reshape the system plant, in particular to damp the *LC* resonance, so that the voltage controller can be designed more easily. Therefore, the transfer function from the current reference i_{gi_ref} to the capacitor voltage v_{gf} is more of concern. This transfer function can be derived from Figure 2.5(b) as

$$T_{iref\_v}(z) = \frac{v_{gf}(z)}{i_{gi\_ref}(z)} = \frac{K_{gc}G_{inv\_v}(z)}{z + K_{gl}K_{gc}G_{inv\_i}(z)}, \tag{2-16}$$

where $G_{inv\_i}(z)$ and $G_{inv\_v}(z)$ are expressed in (2-13) and (2-14), respectively. It is apparent from (2-16) that the product of K_{gl} and K_{gc} determines the denominator of $T_{iref\_v}(z)$. Therefore, the poles of $T_{iref\_v}(z)$ are possible to be tuned by changing $(K_{gl}K_{gc})$. This statement can be validated by the pole-zero map of $T_{iref\_v}(z)$, as illustrated in Figure 2.6. As noted, the increase of $(K_{gl}K_{gc})$ gradually stabilizes $T_{iref\_v}(z)$ by shifting one pair of its conjugate poles inside the unit circle and then shifts the poles outside the unit circle and makes $T_{iref\_v}(z)$ unstable again. To yield the maximum stability margin and fastest dynamics, the conjugate poles should be located as close as possible to the origin of the unit circle, which can be achieved with the case of $(K_{gl}K_{gc}) = 4$.

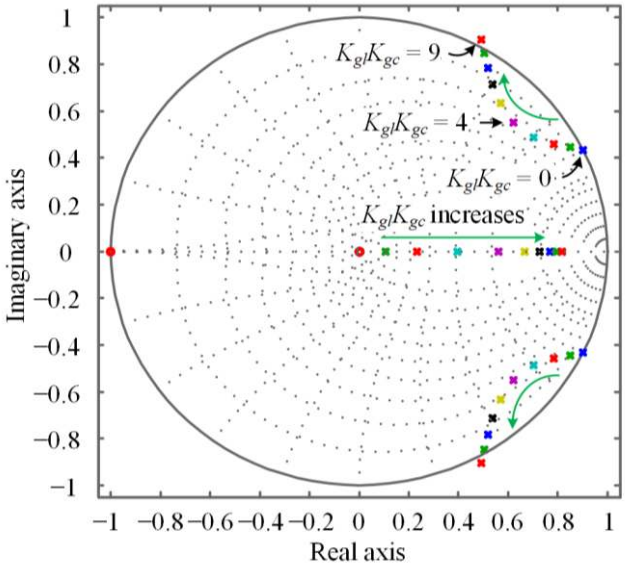

Figure 2.6 Pole-zero map of $T_{iref\_v}(z)$ with various $(K_{gl}K_{gc})$.

After ($K_{gl}K_{gc}$) has been determined, the next step is to design K_{gl} or K_{gc} individually. This can be done through the selection of the steady-state gain of $T_{i\text{ref\_}v}(z)$. In steady state, $z = 1$ is satisfied. Substitution of $z = 1$ into (2-13), it is derived that the steady state value of $G_{\text{inv\_}i}(z)$ is 0. Under this condition, it can be further inferred from (2-16) that the steady-state value of $T_{i\text{ref\_}v}(z)$ is only influenced by K_{gc} regardless of K_{gl}, as verified by the step responses of $T_{i\text{ref\_}v}(z)$ in Figure 2.7. To obtain a unity steady-state gain, K_{gc} is designed to be 1.

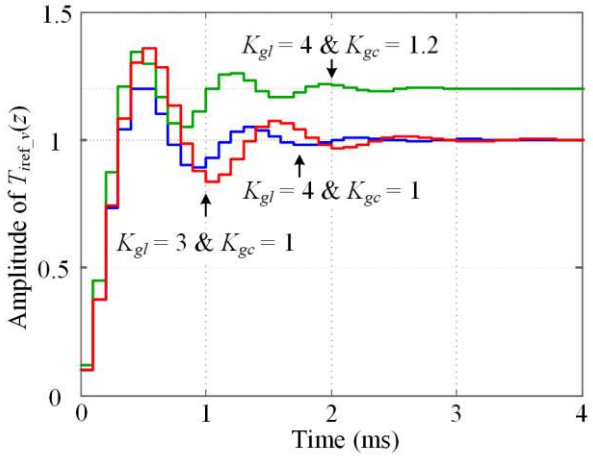

Figure 2.7 Step responses of $T_{i\text{ref\_}v}(z)$ with various K_{gl} and K_{gc}.

The effect of the current control on reshaping $T_{i\text{ref\_}v}(z)$ can be clearly verified by the Bode diagrams of $T_{i\text{ref\_}v}(z)$ drawn in Figure 2.8. Without the current control, i.e. $K_{gl} = 0$ and $K_{gc} = 1$, there is an observable resonant peak introduced by the *LC* filter. After employing the current control, i.e. $K_{gl} = 4$ and $K_{gc} = 1$, the resonant peak can be well attenuated. Moreover, the magnitude of $T_{i\text{ref\_}v}(z)$ is reshaped as around 0 dB until the frequency reaches 1.3 kHz. This feature facilitates the voltage controller design, as will be detailed later. In the following analysis, the current controller, together with the system plant, is lumped into $T_{i\text{ref\_}v}(z)$.

The objective of the voltage controller lies in the elimination of voltage tracking errors and the rejection of disturbances. Since the voltage reference v_{gf_ref} is a constant V_{gf_ref} in the *d*-axis and zero in the *q*-axis, the PI controller will be sufficient for voltage tracking without errors. Additionally, to ensure high-quality grid voltage supplies, a repetitive controller may be further incorporated to reject harmonic disturbances [45, 46].

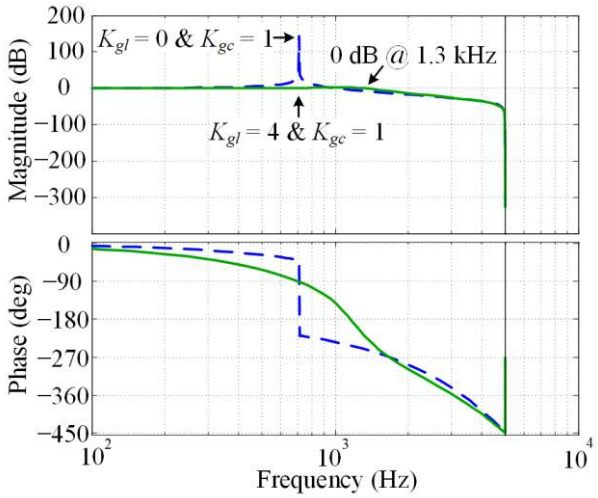

Figure 2.8 Bode diagrams of $T_{iref\_v}(z)$ with and without the current control.

Figure 2.9 details the voltage controller, where the voltage regulator $G_{gv}(z)$ in Figure 2.5 is further implemented as a parallel connection of a PI controller $G_{gv\_pi}(z)$ and a repetitive controller consisting of a fundamental period delay unit $z^{-N_{gr}}$, a constant around one Q_{gr}, a low-pass filter $S_{gr}(z)$, a phase compensation unit $z^{N_{gc}}$, and a proportional gain K_{gr} [47]. In Figure 2.9, the voltage feedforward compensator K_{gf} remains unchanged. As $T_{iref\_v}(z)$ features a unity gain in the low-frequency band (see Figure 2.8), K_{gf} is designed to be K_{gc} so that the feedforward gain from v_{gf_ref} to v_{gf} is unity. This feedforward control helps accelerate the voltage tracking and disturbance rejection.

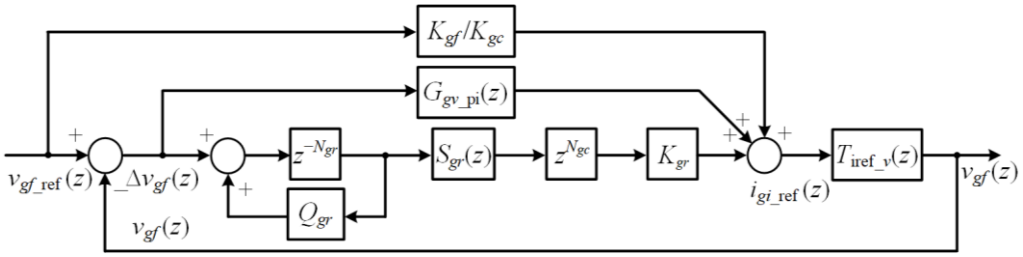

Figure 2.9 Detailed block diagram of the voltage controller of VCCs.

First, the repetitive controller is designed to reject disturbances due to nonlinear loads, while the PI controller is disabled. In order to obtain a fundamental period time-delay, N_{gr} is designed as the ratio of the sampling frequency f_s to the fundamental frequency f_{ref}, i.e. $N_{gr} = f_s / f_{ref} = 200$ [45-47]. Next, the voltage error Δv_{gf} as a function of the voltage reference v_{gf_ref} can be derived as

$$\Delta v_{gf}(z) = \frac{v_{gf\_\mathrm{ref}}(z)(z^{N_{gr}} - Q_{gr})\left[1 - T_{i\mathrm{ref}\_v}(z)\right]}{(z^{N_{gr}} - Q_{gr}) + S_{gr}(z) z^{N_{gc}} K_{gr} T_{i\mathrm{ref}\_v}(z)}. \tag{2-17}$$

Let the denominator of Δv_{gf} equal zero, the characteristic equation of the voltage controller can be obtained as

$$z^{N_{gr}} - Q_{gr} + S_{gr}(z) z^{N_{gc}} K_{gr} T_{i\mathrm{ref}\_v}(z) = 0. \tag{2-18}$$

To guarantee the stable voltage control, all the roots of (2-18) should be located inside the unity circle. Under this condition, $|z| < 1$ and $|z|^{N_{gr}} < 1$ should always be satisfied for each root. Consequently, a sufficient condition for ensuring the stable voltage control can be derived by rearranging (2-18) as

$$\left| S_{gr}(z) z^{N_{gc}} K_{gr} T_{i\mathrm{ref}\_v}(z) - Q_{gr} \right| < 1. \tag{2-19}$$

Upon inserting $z = e^{j(2k\pi / N_{gr})}$ (k = 1, 2, 3… N_{gr} / 2) into (2-17), where k denotes the harmonic order, it is possible to derive the errors of voltage amplitudes at harmonic frequencies as

$$\left| \Delta v_{gf}(e^{j2k\pi/N_{gr}}) \right| = \frac{v_{gf\_\mathrm{ref}}(e^{j2k\pi/N_{gr}})(1 - Q_{gr})\left[1 - T_{i\mathrm{ref}\_v}(e^{j2k\pi/N_{gr}})\right]}{1 - \left[Q_{gr} - S_{gr}(e^{j2k\pi/N_{gr}}) e^{j2k\pi N_{gc}/N_{gr}} K_{gr} T_{i\mathrm{ref}\_v}(e^{j2k\pi/N_{gr}}) \right]}. \tag{2-20}$$

It can be inferred from the numerator of (2-20) that there are two conditions for ensuring zero harmonic errors. The first condition is $Q_{gr} = 1$, and this is the reason for Q_{gr} to be selected as a constant around one, e.g. 0.95. However, it should be noted that Q_{gr} cannot be equal to or greater than one, otherwise the voltage control will become unstable, because the roots of (2-18) move close to the unity circle as Q_{gr} approaches one. Therefore, the first condition is ideal. The second condition refers to $T_{i\mathrm{ref}\_v}(z) = 1$. This condition can be satisfied in the low-frequency band through a well-designed current controller, as detailed previously and shown in Figure 2.8. Additionally, it is desirable for the denominator of (2-20) to stay away from zero to avoid harmonic amplifications.

The low-pass filter $S_{gr}(z)$ serves to sufficiently attenuate high-frequency noises. The design of its cut-off frequency is a trade-off between control bandwidth and harmonic attenuation. Here, $S_{gr}(z)$ is selected as a second-order Butterworth low-

pass filter having a cut-off frequency of 500 Hz. Implementations of $S_{gr}(z)$ as other types of filters, such as notch filters, are also possible [45].

Once $S_{gr}(z)$ has been selected, N_{gc} and K_{gr} should be designed to compensate the phase and amplitude deviations of $T_{iref\_v}(z)S_{gr}(z)$, respectively. The purpose is to keep the left-hand side of (2-19) close to zero, thereby improving the stability margin. Since the magnitude of $T_{iref\_v}(z)S_{gr}(z)$ is already one and significantly close to Q_{gr} in the low-frequency band, it is unnecessary for the amplitude compensation. Therefore, K_{gr} is chosen as 1. Figure 2.10 plots the Bode diagrams of $T_{iref\_v}(z)S_{gr}(z)z^{N_{gc}}$ as a function of N_{gc}, where the case of N_{gc} = 6 yields the widest frequency range of a zero-phase shift, and hence it is being selected.

So far, the design of the repetitive controller is finished. With the designed repetitive controller, the magnitude plot of the system loop gain v_{gf} / Δv_{gf} is depicted in Figure 2.11, where large gains at harmonic frequencies are observed as expected.

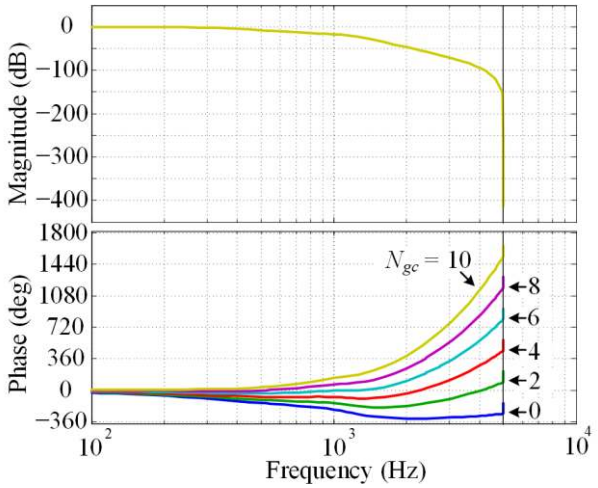

Figure 2.10 Bode diagrams of $T_{iref\_v}(z)S_{gr}(z)z^{N_{gc}}$ as a function of N_{gc}.

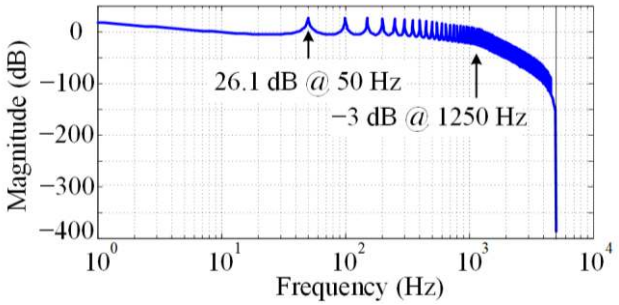

Figure 2.11 Bode diagram of $v_{gf}(z)$ / $\Delta v_{gf}(z)$.

After the repetitive controller is designed, the influence of the PI controller on the stability of the voltage control should further be evaluated. Taking the PI controller into consideration, the expression of the voltage error Δv_{gf} becomes

$$\Delta v_{gf}(z) = \frac{v_{gf\_\mathrm{ref}}(z)(z^{N_{gr}} - Q_{gr})\left[1 - T_{i\mathrm{ref}\_v}(z)\right]}{(z^{N_{gr}} - Q_{gr})\left[1 + T_{i\mathrm{ref}\_v}(z)G_{gv\_\mathrm{pi}}(z)\right] + S_{gr}(z)z^{N_{gc}}K_{gr}T_{i\mathrm{ref}\_v}(z)}. \quad (2\text{-}21)$$

The sufficient condition for the stable voltage control can be further derived as

$$\left| \frac{S_{gr}(z)z^{N_{gc}}K_{gr}T_{i\mathrm{ref}\_v}(z)}{1 + T_{i\mathrm{ref}\_v}(z)G_{gv\_\mathrm{pi}}(z)} - Q_{gr} \right| < 1, \quad (2\text{-}22)$$

where the PI controller $G_{gv\_\mathrm{pi}}(z)$ is discretized from the continuous PI controller through the bilinear z transformation [48]. As the repetitive controller can be modified as a P controller, only the case where $G_{gv\_\mathrm{pi}}(z)$ is implemented as a pure integrator will be analyzed. In this case, $G_{gv\_\mathrm{pi}}(z)$ takes the form of

$$G_{gv\_\mathrm{pi}}(z) = \frac{K_{gv}T_s(z+1)}{2(z-1)}, \quad (2\text{-}23)$$

where K_{gv} represents the integral gain. Under the condition that K_{gv} = 70, the Nyquist diagram of the left-hand side of (2-22) inside the absolute operator is plotted in Figure 2.12. where the trace is always located inside the unit circle centered at the point (0.95, 0), thereby indicating the stable voltage control.

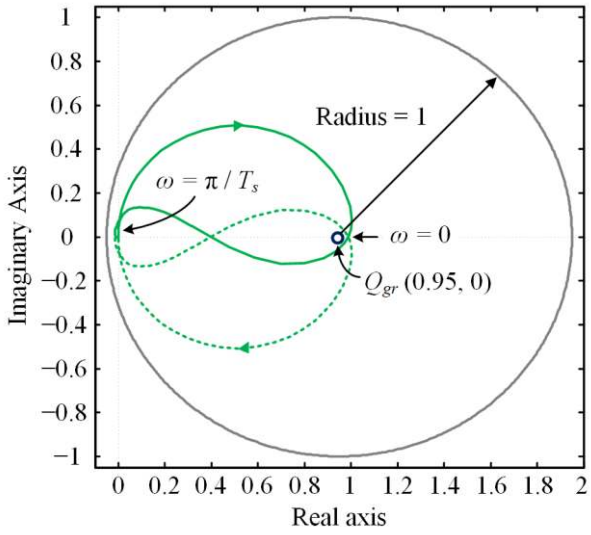

Figure 2.12 Nyquist diagram of the voltage controller of VCCs.

Table 2-3 summarizes the control parameters of VCCs. Based on Table 2-2 and Table 2-3, the experimental results of VCCs are given in Figure 2.13, where the results include both a linear load case and a case of a nonlinear load composed of an inductor-filtered three-phase diode rectifier loaded with a resistor in parallel

Table 2-3 Control parameters of VCCs.

Description	Symbol	Value
Current feedback gain	K_{gl}	4
Current regulator gain	K_{gc}	1
Voltage feedforward gain	K_{gf}	1
Fundamental period delay number	N_{gr}	200
Stabilization factor	Q_{gr}	0.95
Cut-off frequency of low-pass filter	f_{gr_cut}	500 Hz
Phase compensation number	N_{gc}	6
Magnitude compensation gain	K_{gr}	1
Voltage integral gain	K_{gv}	70

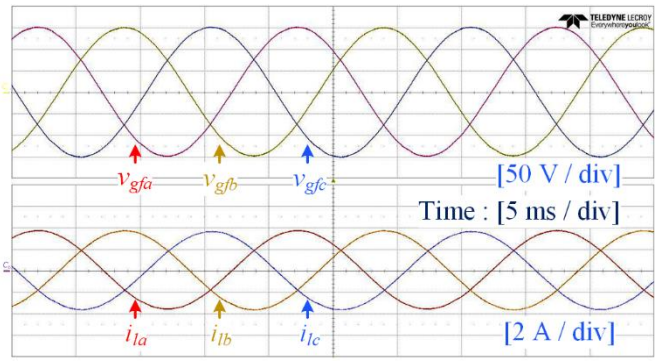

(a) Supplying a linear load

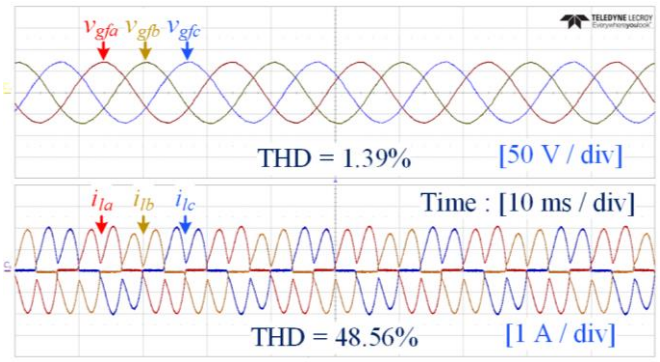

(b) Supplying a nonlinear load

Figure 2.13 Experimental results of VCCs supplying (a) linear and (b) nonlinear loads.

with a capacitor. As observed, the capacitor voltage waveforms are highly sinusoidal regardless of load conditions. In the case of the nonlinear load featuring a THD of 48.56%, power converters manage to maintain the THD of capacitor voltages as low as 1.39%, thereby justifying the effectiveness of the proposed voltage and current controllers. In the experiment, the voltage/current waveforms were exported from an oscilloscope and then analyzed by the Matlab/Simulink Powergui FFT Analyze Tool to yield the THD values.

2.4 Power Converters Controlled as AC Current Sources

Figure 2.14 shows the schematic diagram of power converters controlled as AC current sources, which are defined as current-controlled converters (CCCs) in this thesis. For simplification of analysis, the DC-link is assumed to be fed by a DC voltage source with an output voltage v_{cdc}. However, it is also possible for the DC-link to be fed by a capacitor. In this case, the capacitor voltage should be well regulated.

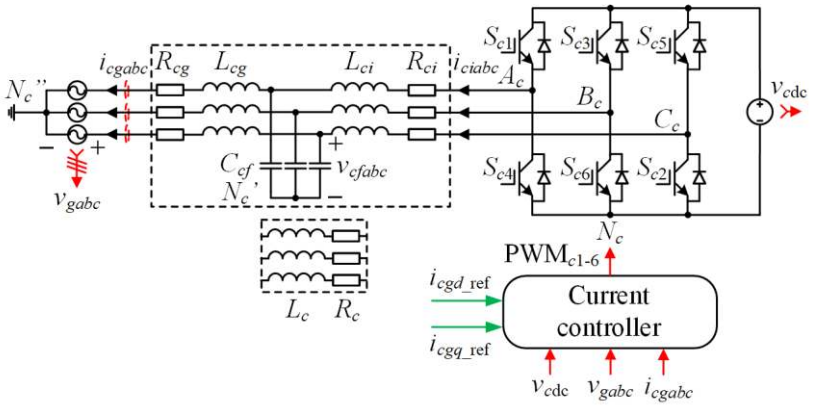

Figure 2.14 Schematic diagram of CCCs.

Ideally, the power grid is modelled to be a three-phase AC voltage source, whose voltages are represented as v_{gx} ($x = a, b, c$). However, remember that grid impedances must be considered under weak grid conditions, as will be analyzed in detail in Chapter 4. Between power grid and semiconductor switches is the passive filter. Its major objective lies in the attenuation of switching harmonics introduced by the modulation of power converters. In this section, the models and controllers of CCCs employing two groups of commonly used passive filters, i.e.

the *L* filter and *LCL* filter, will be detailed. For power converters using other passive filters, system models and controller designs can be investigated in a similar way. Note that CCCs aim to regulate the grid-injected currents i_{cgx} ($x = a$, b, c) according to their *d*- and *q*-axis references i_{cgd_ref} and i_{cgq_ref}.

2.4.1 System Modelling

Once again, the mathematical models of power converters should be derived before controller designs are elaborated. Let v_{cxN} (x = a, b, c) stand for the voltages between nodes X_c ($X_c = A_c$, B_c, C_c) and node N_c, respectively. For *LCL*-filtered power converters, the system plant can be described by the differential equations from (2-24) to (2-26):

$$\begin{cases} v_{caN}(t) = v_{cfa}(t) + L_{ci}\dfrac{\mathrm{d}i_{cia}(t)}{\mathrm{d}t} + R_{ci}i_{cia}(t) + v_{cN'N}(t) \\ v_{cbN}(t) = v_{cfb}(t) + L_{ci}\dfrac{\mathrm{d}i_{cib}(t)}{\mathrm{d}t} + R_{ci}i_{cib}(t) + v_{cN'N}(t), \\ v_{ccN}(t) = v_{cfc}(t) + L_{ci}\dfrac{\mathrm{d}i_{cic}(t)}{\mathrm{d}t} + R_{ci}i_{cic}(t) + v_{cN'N}(t) \end{cases} \tag{2-24}$$

where $v_{cN'N}$ represents the voltage between nodes N_c' and N_c.

$$\begin{cases} v_{cfa}(t) = v_{ga}(t) + L_{cg}\dfrac{\mathrm{d}i_{cga}(t)}{\mathrm{d}t} + R_{cg}i_{cga}(t) + v_{cN''N'}(t) \\ v_{cfb}(t) = v_{gb}(t) + L_{cg}\dfrac{\mathrm{d}i_{cgb}(t)}{\mathrm{d}t} + R_{cg}i_{cgb}(t) + v_{cN''N'}(t), \\ v_{cfc}(t) = v_{gc}(t) + L_{cg}\dfrac{\mathrm{d}i_{cgc}(t)}{\mathrm{d}t} + R_{cg}i_{cgc}(t) + v_{cN''N'}(t) \end{cases} \tag{2-25}$$

where $v_{cN''N'}$ represents the voltage between nodes N_c'' and N_c'.

$$\begin{cases} C_{cf}\dfrac{\mathrm{d}v_{cfa}(t)}{\mathrm{d}t} = i_{cia}(t) - i_{cga}(t) \\ C_{cf}\dfrac{\mathrm{d}v_{cfb}(t)}{\mathrm{d}t} = i_{cib}(t) - i_{cgb}(t). \\ C_{cf}\dfrac{\mathrm{d}v_{cfc}(t)}{\mathrm{d}t} = i_{cic}(t) - i_{cgc}(t) \end{cases} \tag{2-26}$$

In the case of *L*-filtered power converters, (2-24) can be used to model the system plant provided that v_{cfx} (x = a, b, c), L_{ci}, R_{ci}, i_{cix}, and $v_{cN'N}$ are replaced by

v_{gx}, L_c, R_c, i_{cgx}, and $v_{cN"N}$, respectively, where $v_{cN"N}$ represents the voltage between nodes N_c" and N_c. It can be inferred that the models of *LCL*-filtered and *L*-filtered power converters are the same in the low-frequency band if the capacitors are treated as open circuits and all equations in (2-26) are equal to zero. Under these assumptions, L_c and R_c denote the total inductance and resistance, respectively.

Following the same derivation process for the model of VCCs, the complex frequency domain model of *LCL*-filtered CCCs can be derived in the *dq*-frame as

$$\begin{cases} i_{cid}(s) = \dfrac{1}{L_{ci}s + R_{ci}}\left[V_{\text{cdc\_ref}} S_{cd}(s) - v_{cfd}(s) + \omega_o L_{ci} i_{ciq}(s)\right] \\ i_{ciq}(s) = \dfrac{1}{L_{ci}s + R_{ci}}\left[V_{\text{cdc\_ref}} S_{cq}(s) - v_{cfq}(s) - \omega_o L_{ci} i_{cid}(s)\right] \end{cases}, \tag{2-27}$$

$$\begin{cases} i_{cgd}(s) = \dfrac{1}{L_{cg}s + R_{cg}}\left[v_{cfd}(s) - v_{gd}(s) + \omega_o L_{cg} i_{cgq}(s)\right] \\ i_{cgq}(s) = \dfrac{1}{L_{cg}s + R_{cg}}\left[v_{cfq}(s) - v_{gq}(s) - \omega_o L_{cg} i_{cgd}(s)\right] \end{cases}, \tag{2-28}$$

$$\begin{cases} v_{cfd}(s) = \dfrac{1}{C_{cf}s}\left[i_{cid}(s) - i_{cgd}(s) + \omega_o C_{cf} v_{cfq}(s)\right] \\ v_{cfq}(s) = \dfrac{1}{C_{cf}s}\left[i_{ciq}(s) - i_{cgq}(s) - \omega_o C_{cf} v_{cfd}(s)\right] \end{cases}, \tag{2-29}$$

where S_{cd} and S_{cq} denote the switch functions. The complex frequency model of *L*-filtered CCCs can also be described by (2-27) with v_{cfy} ($y = d, q$), L_{ci}, R_{ci}, and i_{ciy} being replaced by v_{gy}, L_c, R_c, and i_{cgy}, respectively.

The block diagram of plant models is shown in Figure 2.15, where the models of *LC*-filtered and *L*-filtered power converters constitute the model of *LCL*-filtered power converters. The right-hand side of the dotted line models *L*-filtered power converters, where v_{cfy} ($y = d, q$), L_{cg}, and R_{cg} should be replaced by $V_{\text{cdc\_ref}}S_{cy}$, L_c, and R_c, respectively. Once again, the cross-coupling terms can be partially mitigated by current and voltage feedforward compensators, and hence the cross-coupling effects are ignored henceforth.

It should be emphasized that the *abc* to *dq*0 transformation requires the phase angle θ_o. However, different from VCCs, CCCs do not generate θ_o internally. Instead, they detect the phase angle from grid voltages. The objective of phase angle detection is normally achieved by phase-locked-loops (PLLs) [49-51]. The effect of PLLs on the power converter control will be elaborated in Chapter 4.

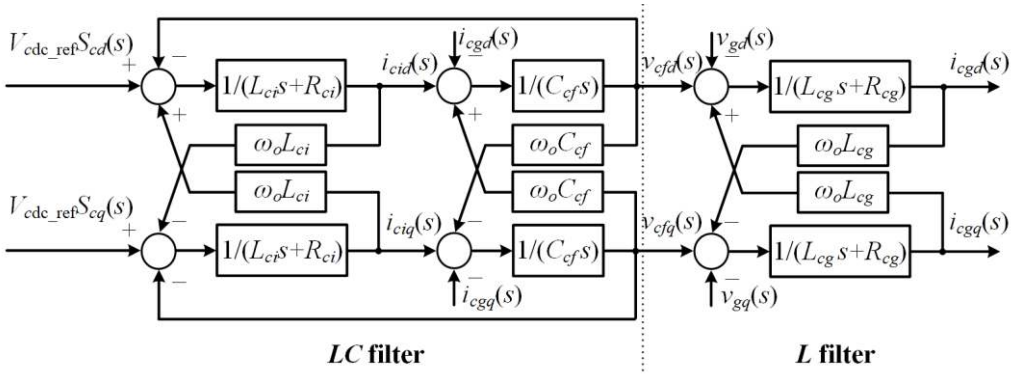

Figure 2.15 Block diagram of the system plants of CCCs.

2.4.2 Controller Design

With the plant models, the current controller can be designed according to the system parameters given in Table 2-4, where the *LCL* filter parameters give rise to a resonance frequency f_{cr} greater than 1 / 6 of the sampling frequency f_s. Under this condition, the resonance damping of grid-current-feedback controlled power converters is unnecessary, as has been investigated and verified in [52-54]. Remember that the conditions for the stable current control of converter-current-feedback controlled power converters become different, i.e. $f_{cr} < f_s / 6$ [52, 55]. The design of *LCL* filters has been covered in many references [56-61], and thus it is excluded here. Instead, this subsection focuses on the current controller design. This part can be partially found in the author's research work [62].

Figure 2.16 details the current controller, where $G_{cc}(z)$ denotes the current regulator. It can be implemented as a PI controller for tracking constant current references or a repetitive controller for harmonic compensation. The PWM generator is again modelled as z^{-1} and the ZOH. Note that the current control is applicable to both the *d*- and *q*-axes, and the resistances R_{ci} and R_{cg} are ignored.

Table 2-4 System parameters of CCCs.

Description	Symbol	Value
Filter capacitance	C_{cf}	5 μF
Grid filter inductance	L_{cg}	1 mH
Converter filter inductance	L_{ci}	1 mH
Total inductance	L_c	2 mH
DC-link voltage reference	V_{cdc_ref}	360 V
Grid voltage reference (rms)	V_{g_ref}	110 V
Fundamental frequency	f_{ref}	50 Hz
Resonance frequency	f_{cr}	3.18 kHz
Switching/sampling frequency	f_{sw}/f_s	10 kHz

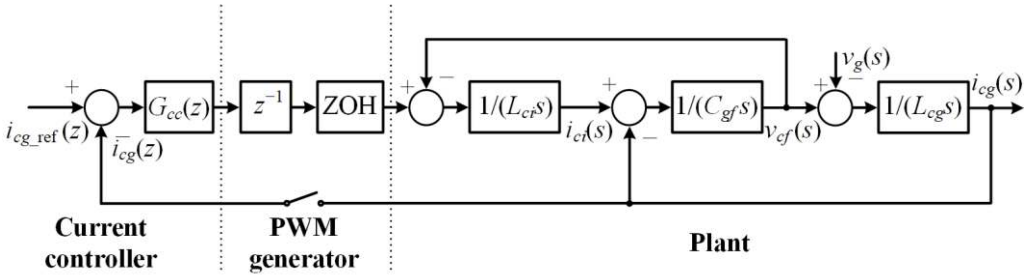

(a) Controller in the mixed *s*- and *z*-domains

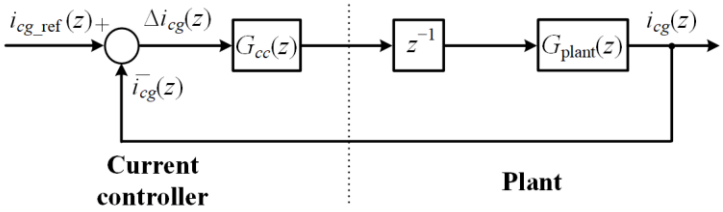

(b) Controller in the *z*-domain

Figure 2.16 Block diagram of the current controller of CCCs in the (a) mixed *s*- and *z*-domains and (b) *z*-domain.

The transfer function from the output of the ZOH to the grid-injected current i_{cg} can be derived from Figure 2.16(a) as

$$G_{\text{plant}}(s) = \begin{cases} \dfrac{\omega_{cr}^{\ 2}}{(L_{ci}+L_{cg})s(s^2+\omega_{cr}^{\ 2})} : & LCL \\ 1/(L_c s) \quad : & L \end{cases}, \tag{2-30}$$

where ω_{cr} stands for the resonance angular frequency of the *LCL* filter, which can be expressed as

$$\omega_{cr} = \sqrt{\frac{L_{ci} + L_{cg}}{L_{ci} L_{cg} C_{cf}}}. \tag{2-31}$$

Through the ZOH z transformation, (2-30) becomes

$$G_{\text{plant}}(z) = \begin{cases} \dfrac{T_s}{(L_{ci} + L_{cg})(z-1)} - \dfrac{\sin(\omega_{cr} T_s)(z-1)/(L_{ci} + L_{cg})}{\omega_{cr}\left[z^2 - 2\cos(\omega_{cr} T_s) z + 1\right]} & : LCL \\ \dfrac{T_s}{L_c(z-1)} & : L \end{cases}, \tag{2-32}$$

where T_s denotes the sampling period. Figure 2.16(b) illustrates the block diagram of the z-domain current controller, from which the loop gain $G_{c\_ol}(z)$ and closed-loop current control transfer function $G_{c\_cl}(z)$ can be derived as

$$G_{c\_ol}(z) = \frac{i_{cg}(z)}{\Delta i_{cg}(z)} = G_{cc}(z) z^{-1} G_{\text{plant}}(z), \tag{2-33}$$

$$G_{c\_cl}(z) = \frac{i_{cg}(z)}{i_{cg\_ref}(z)} = \frac{G_{cc}(z) z^{-1} G_{\text{plant}}(z)}{1 + G_{cc}(z) z^{-1} G_{\text{plant}}(z)}. \tag{2-34}$$

The current controller is first designed as a P controller, i.e. $G_{cc}(z) = K_{cp}$. Under this condition, the Bode diagrams of the loop gain $G_{c\_ol}(z)$ as a function of K_{cp} for *LCL*-filtered and *L*-filtered power converters are drawn in Figure 2.17(a) and (b), respectively, where the gain margin (GM) and phase margin (PM) are used as performance metrices, and the positive values of both metrices indicate the stable current control.

In the *LCL*-filter case, there is an observable magnitude peak introduced by the *LCL* resonance. Around the resonant peak, two magnitude zero-crossings can be observed. Fortunately, the phases are located between −180 and −540 degrees at the zero-crossing frequencies, leading to positive phase margins. As a result, the stability of the current control can be evaluated by the remaining zero-crossing frequency. As the proportional gain K_{cp} increases, both the GM and PM decrease, thereby indicating that the stability margin reduces. To guarantee the stable current control and fair dynamics, a GM > 3 dB and a PM around or greater than 45˚ will be desirable. Note that the case of K_{cp} = 10 gives rise to a GM of 4.1 dB and PM of 44.4 ˚, and therefore this choice will be followed here.

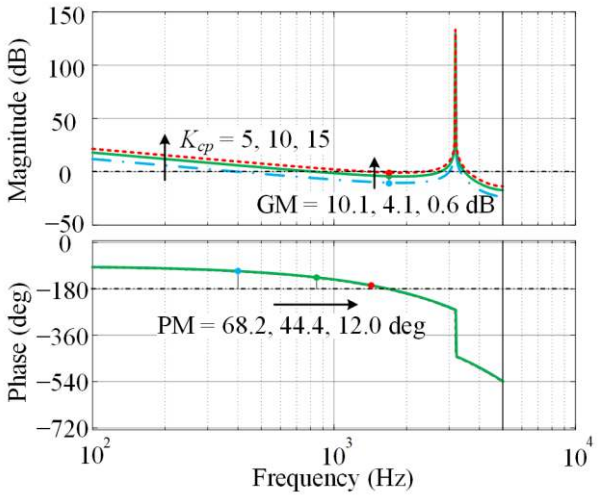

(a) *LCL* filter

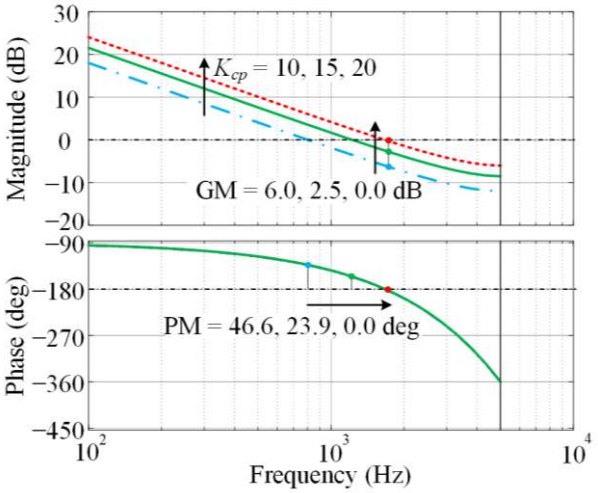

(b) *L* filter

Figure 2.17 Bode diagrams of $G_{c\_ol}(z)$ as a function of K_{cp} for the (a) *LCL* filter and (b) *L* filter cases.

As compared to Figure 2.17(a), Figure 2.17(b) shows that the resonant peak disappears in the *L* filter case. Moreover, the enlarged stability margin allows K_{cp} to be designed more flexibly. Nevertheless, the relationship between stability margin, represented by the GM and PM, and K_{cp} remains unchanged. Specifically, the stability margin shrinks as K_{cp} increases. When K_{cp} = 20, the current control becomes critically stable, which translates into the unstable current control in practice, and hence it must be avoided. It should be recognized that increasing L_c and decreasing K_{cp} have the same effect on the Bode diagram of $G_{c\_ol}(z)$. In this

sense, K_{cp} can be increased accordingly as L_c increases. For example, the case of K_{cp} = 25 ensures fair PM and GM when L_c = 5 mH. Remember that to achieve sufficient attenuation, L filters normally require much larger filter inductances than those of LCL filters. Finally, K_{cp} is designed to be 15 for L-filtered power converters.

The root loci of $G_{c\_ol}(z)$ are depicted in Figure 2.18, where the maximum

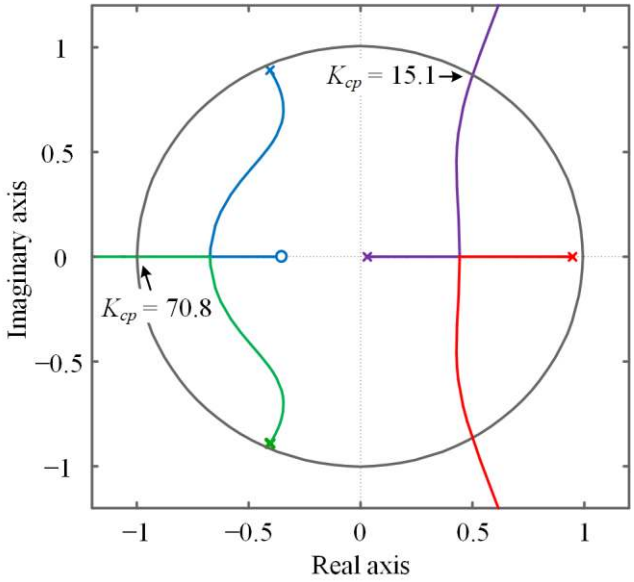

(a) LCL filter

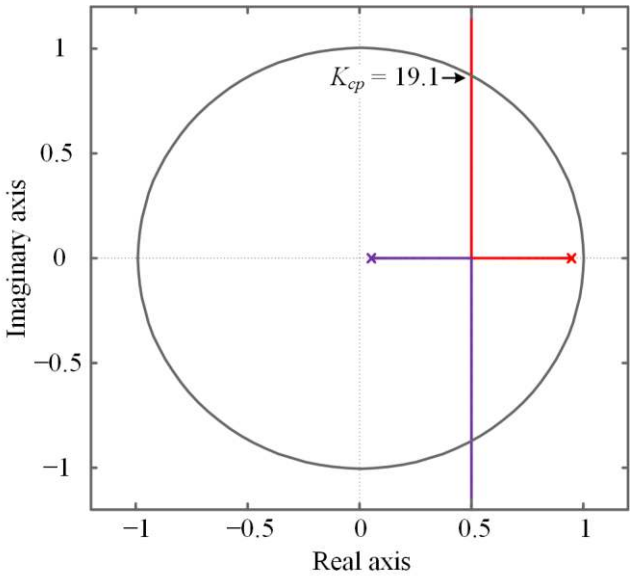

(b) L filter

Figure 2.18 Root loci of $G_{c\_ol}(z)$ for the (a) LCL filter and (b) L filter cases.

acceptable values of K_{cp} for the stable current control can be identified. To be specific, 15.1 and 19.1 are the maximum values of K_{cp} for the *LCL* filter and *L* filter cases, respectively.

Afterwards, the integrator can be incorporated into the current controller. Figure 2.19 shows the pole-zero maps of the closed-loop current control $G_{c\_cl}(z)$ as a function of the integral gain K_{ci}. It is identified that the change of K_{ci} only

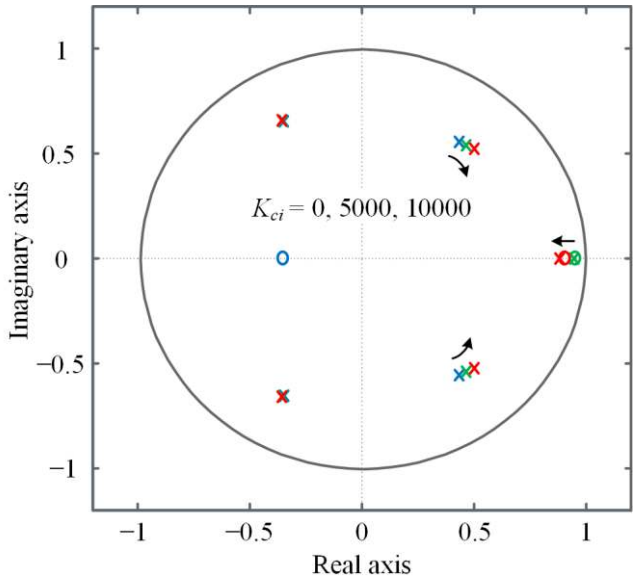

(a) *LCL* filter

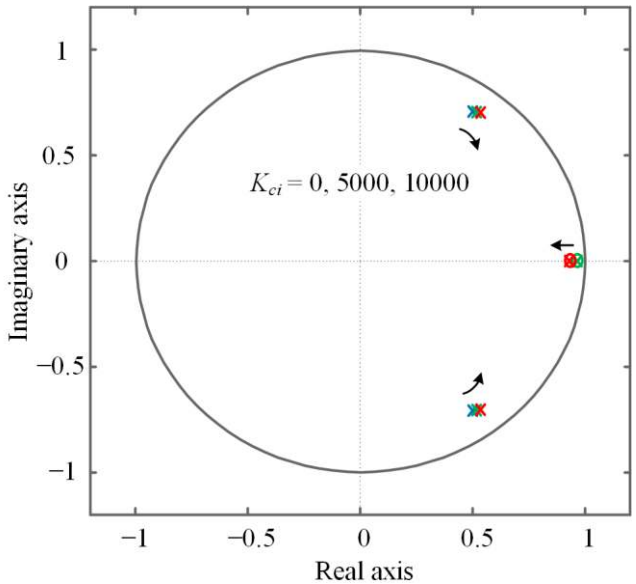

(b) *L* filter

Figure 2.19 Pole-zero maps of $G_{c\_cl}(z)$ as a function of K_{ci} for the (a) *LCL* filter and (b) *L* filter cases.

slightly shifts the locations of closed-loop poles. Therefore, the integrator can be designed with almost no threat on the stability of the current control. It should be noted that the integrator brings in another pair of zero and pole. Additionally, when harmonics are required to be compensated, the repetitive controller should also be incorporated. It can be designed following the same design process as that provided in the previous section, and hence not repeated here.

Based on the system parameters listed in Table 2-4 and control parameters of K_{cp} = 15 and K_{ci} = 300, the experimental results of the *L*-filtered power converter are shown in Figure 2.20, where the filter inductance L_c is increased to 7 mH to attenuate switching harmonics more effectively. Although being highly sinusoidal and in phase with the grid voltages, the current waveforms still contain observable switching harmonics. This means that even a large filter inductor of 7 mH will be insufficient for switching harmonic attenuation. To this end, the switching harmonics become an important power quality issue. Solutions to this issue mainly lie in the modifications of passive filters, and the *LCL* filter in replacement of the *L* filter is one such attempt. However, even the *LCL* filter may be incapable of sufficient harmonic attenuation under certain circumstances. Therefore, more advanced passive filters featuring better attenuation and smaller sizes will be desirable. The performances of the proposed advanced passive filters will be detailed in Chapter 3. In addition, the power grid is assumed to be an ideal power grid modelled as a voltage source in this section. In practice, power converters may encounter instability issues under weak grid conditions, and this will be discussed in Chapter 4.

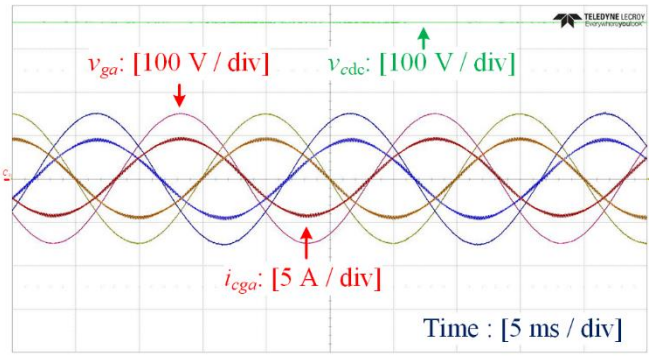

Figure 2.20 Experimental results of the *L*-filtered CCC.

2.5 Grid Support by Power Converters

Sections 2.3 and 2.4 discuss the basic control schemes and controller designs of grid-interfaced power converters. Specifically, the objectives of VCCs and CCCs are the AC voltage regulation and AC current tracking, respectively. In addition to these basic control objectives, power converters are increasingly expected to provide additional grid support functions in more-electronics power systems. This section presents the grid support functions implemented by power converters.

2.5.1 Virtual Synchronous Generators (VSGs)

In power systems, the grid frequency and voltage must be regulated within certain acceptable levels. Otherwise, undesirable load shedding, cascaded failures, or even grid collapses may occur. As mentioned, the grid frequency and voltage amplitude are the indicators of the degrees of active power balance and reactive power balance, respectively. Therefore, active and reactive power balances are at the core of the power system control [13]. Conventionally, the tasks of power balances are mainly performed by synchronous generators. In more-electronics power systems, power converters have replaced synchronous generators in a large-scale. Therefore, power converters are supposed to carry on the responsibility of frequency and voltage regulation, i.e. active and reactive power balances.

One promising approach being able to achieve such objectives is to control power converters as synchronous generators, known as virtual synchronous generators (VSGs) or virtual synchronous machines (VSMs) [35, 36, 42, 63]. Duplicating the functions of synchronous generators, VSGs aim to form grid voltages, and therefore VSGs should be basically implemented as VCCs, where the AC output voltages are tightly controlled. Moreover, VSGs also regulate the grid frequency and voltage amplitude when active and reactive power imbalances occur. In this way, VSGs help balance active and reactive powers as conventional

synchronous generators do. In the following paragraphs, the VSG control will be detailed based on the author's paper [42].

Figure 2.21 presents the block diagram of the VSG outer-loop control, where R_{gd} and R_{gq} denote the frequency and reactive power droop coefficients, respectively. $G_{gs}(s)$ stands for the transfer function of the secondary frequency controller. $G_{gt}(s)$ represents the lumped transfer function of speed governor and reheat turbine. H designates the inertia coefficient. D refers to the damping coefficient of frequency-dependent loads. These transfer functions are employed to model the frequency regulation framework of conventional power systems [13]. It should be mentioned that only the outer control-loop of VSGs, which has not been included in Figure 2.5, is shown here. Normally, the secondary frequency controller $G_{gs}(s)$ is implemented as an integrator. It is optional and only applied to specific generators [33, 64]. Additionally, the reactive power control can be disabled, leading to the direct voltage control. The model of speed governor and reheat turbine $G_{gt}(s)$ can be expressed as [13]

$$G_{gt}(s) = \frac{1}{(T_G s + 1)} \cdot \frac{F_{\mathrm{HP}} T_{\mathrm{RH}} s + 1}{(T_{CH} s + 1)(T_{RH} s + 1)}, \tag{2-35}$$

where T_G and F_{HP} are speed governor and turbine HP coefficients, respectively. T_{CH} and T_{RH} denote the time constants of main inlet volumes and reheater, respectively. Typical values of these parameters can be found in Table 2-5. The influence of the inertia coefficient H on the frequency regulation will be detailed in Chapter 5. More detailed models of generators and loads can be found in [13].

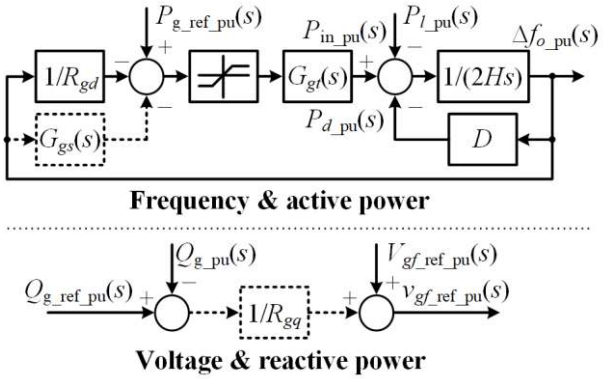

Figure 2.21 Block diagram of the VSG outer-loop control.

Table 2-5 Control parameters of virtual synchronous generators.

Description	Symbol	Value
Frequency droop coefficient	R_{gd}	0.05
Reactive power droop coefficient	R_{gq}	20
Speed governor coefficient	T_G	0.1 s
Turbine HP coefficient	F_{HP}	0.3 s
Time constant of main inlet volumes	T_{CH}	0.2 s
Time constant of reheater	T_{RH}	7.0 s
Inertia coefficient	H	5 s
Damping coefficient	D	1
Secondary control integral gain	K_{gs}	1

In Figure 2.21, the subscripts ref and pu stand for the reference and per unit notations of relevant variables, respectively. P_g and Q_g denote the active and reactive power outputs of generators, respectively. As observed, there are two outputs of the VSG control, namely the change of grid frequency Δf_{o_pu} and AC voltage reference $v_{gf\_\mathrm{ref\_pu}}$. After being transformed into real variables, Δf_o can be used to further calculate the phase angle θ_o through an integrator and a gain of 2π, which are not shown in Figure 2.21. θ_o and v_{gf_ref} will be the references of voltage and current controllers in Figure 2.3. In this sense, VSGs are VCCs with the adjustable phase angle and voltage amplitude such that they operate in a similar manner as synchronous generators do. It should be emphasized that VSGs may not necessarily be exactly the same as synchronous generators, since power converters feature more flexible control and faster responding speeds as compared with synchronous generators [65]. Moreover, the parameters of VSGs can be dynamically changed to improve their performances [66, 67]. Detailed discussions regarding the implementations and control of VSGs will be given in Chapter 5. In the presented more-electronics power system, the VSG is exactly emulating the operations of synchronous generators.

Figure 2.22 illustrates the comparisons between synchronous generator and VSG with the primary frequency control, where the frequency event of a 5% step-down load change occurs at t_1 and disappears at t_2. It is clear that the synchronous

generator and VSG simultaneously raise the grid frequency when the step load changes occur. After the frequency event, they decrease the frequency in the same way, thereby validating the effectiveness of the VSG control.

Figure 2.23 further demonstrates the effect of the secondary frequency control. Upon activating, the secondary frequency control restores the frequency back to its nominal value. Note that the restoration speed can be flexibly adjusted with the change of the integral gain K_{gs}. However, it should be remembered that the activation of the secondary frequency controller means that the VSGs should increase their outputs as long as the frequency deviation exists, and hence it requires a large amount of energy.

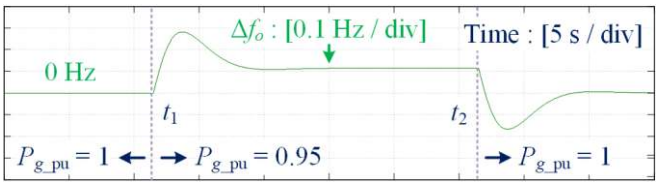

(a) Simulation result of the synchronous generator

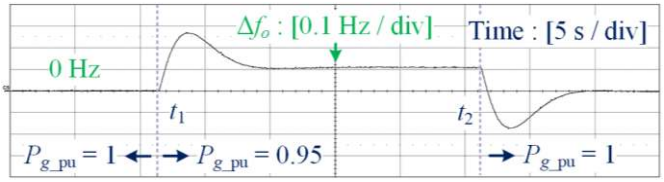

(b) Experimental result of the VSG

Figure 2.22 Comparisons between (a) simulation result of the synchronous generator and (b) experimental result of the VSG with the primary frequency control.

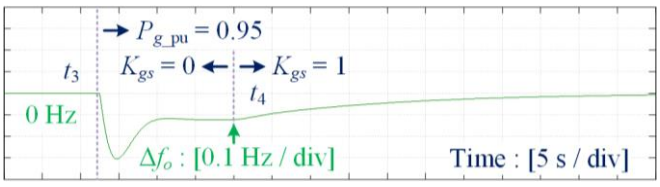

(a) Simulation result of the synchronous generator

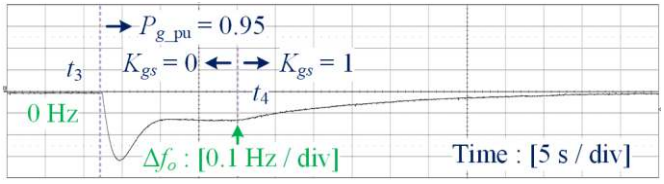

(b) Experimental result of the VSG

Figure 2.23 Comparisons between (a) simulation result of the synchronous generator and (b) experimental result of the VSG with the secondary frequency control.

2.5.2 Power Support by Power Converters

Although not being able to form the power grid, CCCs may also contribute to active and reactive power balances through the dedicated control. One well-proven approach is the droop control, where the output active and reactive powers of CCCs change inversely proportional to the grid frequency and voltage amplitude, respectively. The droop control can be considered as a special case and simplified version of VSG control.

Figure 2.24 illustrates the block diagram of the frequency and voltage droop control of CCCs, where R_{cd} and R_{cq} denote the frequency and voltage droop coefficients, respectively. f_{g_pu} and V_{g_pu} are the measured grid frequency and voltage amplitude, respectively. When f_{g_pu} and V_{g_pu} are less than their corresponding references f_{ref_pu} and $V_{g\_ref\_pu}$, power converters increase their active power reference $p_{c\_ref\_pu}$ and reactive power reference $q_{c\_ref\_pu}$, respectively. $p_{c\_ref\_pu}$ and $q_{c\_ref\_pu}$ are then transformed into the relevant real variables, before yielding the current references through the following equations [38]:

$$i_{cgd\_ref} = \frac{2(p_{c\_ref} v_{gd} + q_{c\_ref} v_{gq})}{3({v_{gd}}^2 + {v_{gq}}^2)}, \tag{2-36}$$

$$i_{cgq\_ref} = \frac{2(p_{c\_ref} v_{gq} - q_{c\_ref} v_{gd})}{3({v_{gd}}^2 + {v_{gq}}^2)}, \tag{2-37}$$

where $v_{gd} = V_{g\_ref}$ and $v_{gq} = 0$ are satisfied in steady state. With i_{cgd_ref} and i_{cgq_ref} obtained, they will serve as the current references in Figure 2.14. Therefore, the droop control acts as the outer control loop of the current controller.

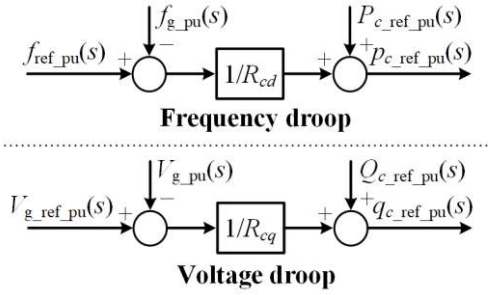

Figure 2.24 Block diagram of the droop control of CCCs.

It should be remembered that the above analysis is only applicable to the cases of inductive converter impedances. In other cases, e.g. resistive converter impedances, the strong interrelationships between frequency and active power as well as voltage and reactive power may change. Research works concerning the influence of impedances on the frequency and voltage droop control can be found in [38, 68-70]. Furthermore, the concept of the virtual impedance has been introduced to help flexibly design line impedances for achieving the accurate droop control [71-73].

Although the droop control is a widely used power support function of CCCs for improving the power system stability, other power support schemes exist and may have great potentials. Note that the droop control only emulates one basic function of synchronous generators for frequency and voltage regulation, and other functions, such as the inertia emulation, may also be implemented and exploited. Chapter 5 will discuss the power support through the virtual inertia control.

2.5.3 Active Power Filters (APFs)

In addition to providing the active and reactive power support, power converters may also support the power quality of more-electronics power systems. An effective solution to multiple power quality issues is known as UPQCs in distribution grids or UPFCs in transmission grids [18, 74, 75]. There is no doubt that UPQCs and UPFCs are very versatile and capable of overcoming a variety of voltage quality and current quality issues [17, 76]. However, UPQCs or UPFCs are dedicated power electronic equipment, and their functions cannot be easily implemented as additional control functions of grid-interfaced power converters.

The UPQC is composed of a dynamic voltage restorer (DVR) and a shunt active power filter (APF) sharing a common DC-link. The DVR aims to overcome voltage quality issues, and it is configured similarly to a VCC. However, the output capacitor of the DVR is often connected in series (instead of in parallel) with the loads, thus making its configuration different from the

configuration of VCCs [17]. As such, the functions of DVRs cannot be implemented by commonly used VCCs.

In contrast, the shunt APF focuses only on current quality issues, e.g. current harmonics and the reactive current. Moreover, the shunt APF has the same configuration as that of CCCs. As a result, harmonic and reactive power compensations may be added as additional functions of CCCs. It should be mentioned that static var generators (SVGs), or known as distributed static compensators (DSTATCOMs) in distribution networks and static compensators (STATCOMs) in transmission networks, target at the reactive current rather than current harmonics [77-79], and therefore the functions of SVGs may also be transplanted into grid support functions of CCCs. Figure 2.25 shows the block diagram of a typical harmonic detection scheme, i.e. the i_d–i_q harmonic detection scheme, of APFs implemented by CCCs, where the measured load currents i_{ld} and i_{lq} subtract their respective fundamental components, and then act as the current references in Figure 2.14. The harmonic detection scheme shown in Figure 2.25 allows only the detection, and hence the compensation, of current harmonics. In order to simultaneously compensate current harmonics and the reactive current, i_{cgq_ref} should be selected as i_{lq}. The performances of APFs will be demonstrated in Chapter 3.

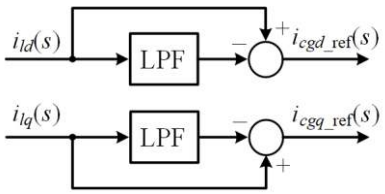

Figure 2.25 Block diagram of the i_d–i_q harmonic detection scheme of APFs.

2.6 Summary

In this chapter, the system configuration, operating principle, and modelling and control of more electronics power systems have been discussed. As an example, a single-area more-electronics power system consisting of a VSG, a PV generation system, and an ESS has been introduced. In general, power converters in more-electronics power systems are categorized into two types, viz. power

converters controlled as AC voltage sources and AC current sources. The mathematical models and controller designs of these two types of power converters are detailed. In addition to basic control objectives, additional grid support functions – the grid support by VSGs, power support by CCCs, and power quality support by APFs, have been presented in this chapter.

Chapter 3 Advanced Passive Power Filters for Power Quality Enhancement

This chapter starts with the introduction of one major power quality issue in more-electronics power systems, viz. the current harmonics introduced by power converters, as well as its state of the art solutions. As switching harmonics are located beyond the control bandwidths of power converters, they have to be attenuated by passive power filters. As compared to the single inductor *L* filter, the high-order *LCL* filter features better harmonic attenuation and a smaller filter size. However, even the *LCL* filter is undesirable in terms of its attenuation capacity, size, and cost, as the requirements of customers and power grids become increasingly demanding. To further improve the filtering performance and power density of passive filters, this chapter proposes several advanced passive filters, including the magnetic integrated *LLCL* filter, series-parallel-resonant *LCL* (*SPRLCL*) filter, and *LT-C-L* filter, i.e. the *LCL* filter in combination with a parallel-resonant *LC*-trap. These filters combine the benefits of several emerging techniques, such as the magnetic integration and/or *LC*-traps, leading to the inductance saving and improvement of harmonic filtering. Finally, it is concluded in this chapter that the *LT-C-L* filter can be the most promising trap filter in terms of filter topology, filtering performance, and robustness.

3.1 Background and Introduction

Power quality issues in more-electronics power systems can be mainly categorized into voltage and current quality issues. As mentioned, current quality issues may further cause voltage quality issues, such as voltage sags/swells, unbalances, and harmonics, in the presence of large grid impedances [12]. Moreover, most of the current quality issues should be blamed for the use of power electronics. Therefore, this chapter focuses predominantly on current quality issues, including current harmonics and the reactive current, and their power electronic solutions. Current harmonics may cause additional noises and

losses along the transmission lines, pulsed motor torques, and interferences to communication systems [12]. The reactive current increases losses and power ratings of power equipment. Therefore, it is desirable to alleviate current harmonics and the unnecessary reactive current.

The operations of power converters give rise to both low-order harmonics, e.g. 5^{th} and 7^{th} order harmonics, and high-order harmonics, such as switching harmonics. Although low-order current harmonics, together with the reactive current, can be well compensated by APFs, as discussed in Chapter 2 [47]. High-order harmonics, mainly appearing around the switching frequency and its multiples, can only be attenuated passively by the output filters of power converters, such as the *LC* filter in Figure 2.3 and *L*/*LCL* filters in Figure 2.14, because switching harmonics are beyond current control bandwidths.

In grid-connected applications, grid-injected current harmonics should be maintained below the limits prescribed by grid codes, e.g. the IEEE Standard 519-2014 listed in Table 1-1. Therefore, passive filters must enable effective harmonic attenuation to comply with grid codes. It is worth to note that voltage-controlled power converters, filtered by *LC* filters, are mainly employed to form the power grid, and therefore they do not subject to the IEEE Standard 519-2014. When they are connected to power grids, additional inductors, either physical inductors or the inductors emulated by control, should be inserted between power converters and power grids, and thus their output *LC* filters become *LCL* filters [63, 69, 80]. In this sense, VCCs and CCCs are the same in terms of harmonic filtering. As a result, only the passive filters of CCCs will be analyzed in the following sections.

According to Table 1-1, high-order (above 35^{th}) current harmonics should be attenuated to be less than the 0.3% maximum demand load current under the condition that the short circuit ratio $I_{sc} / I_L < 20$. Moreover, the current THD under rated load conditions must be less than 5%. These requirements are relaxed as the short circuit ratio increases. The primary reason is that current harmonics generated by power converters predominantly exist in distribution networks.

Despite being simple and reliable, the single inductor *L* filter often exhibits insufficient attenuation at the switching frequency and its multiples. To illustrate this point, Figure 3.1 visualizes the current spectrum of an *L*-filtered power converter, where f_{sw} denotes the switching frequency, and current harmonic magnitudes are plotted on a per unit basis. It can be confirmed that the current harmonics mainly appear around the switching frequency f_{sw} and its multiples $2f_{sw}$, $3f_{sw}$, etc. As observed, the case shown in Figure 3.1 fails to comply with grid codes because of the excessive harmonic magnitudes. To comply with grid codes, large, bulky, and expensive inductors may be incorporated. In addition to the drawbacks in terms of size and cost, a large filter inductor translates into more power losses and a large voltage drop. Further on, a large voltage drop necessitates a high DC-link voltage and overrated components, otherwise the over modulation issue may occur [19]. Another issue caused by the large inductor is the reduced current control bandwidth. As mentioned in Section 2.3, the effect of increasing the inductance is essentially reducing the control bandwidth. For these reasons, except for high-power or high-voltage applications where multiple converters are interleaved or cascaded with shifted phases to cancel out the dominating harmonics, the single inductor *L* filter is increasingly being replaced by the third-order *LCL* filter [81, 82].

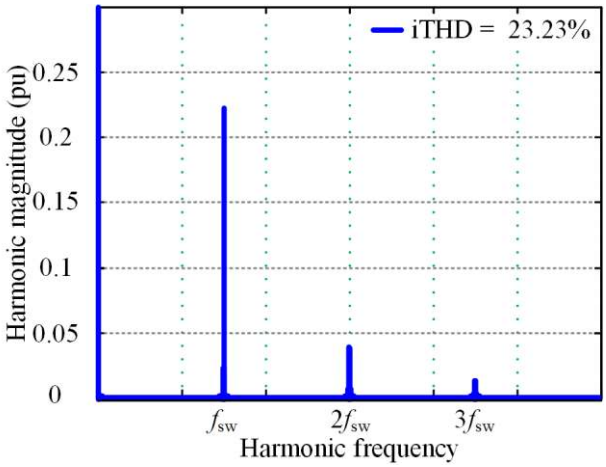

Figure 3.1 Current spectrum of an *L*-filtered power converter.

As compared with the *L* filter, the *LCL* filter features a higher filter order, more filter components, better attenuation, and a smaller size. However, even the *LCL*

filter is unacceptable in certain applications, for instance half-bridge APFs, where high control bandwidths and strong attenuation ability are simultaneously required [61]. Additionally, the filter components of *LCL* filters, particularly for filter inductors, are still very bulky and costly, when compared with active semiconductor devices. As such, there is a strong motivation to further reduce the size and cost of these filter components. Research efforts along this direction can be broadly categorized into two branches, i.e. the modified *LCL* filters and magnetic integration technique.

Among the modified *LCL* filters, the *LLCL* filter enjoys a growing popularity [57, 83-85]. Figure 3.2 illustrates the schematic diagram of *LLCL* filters, where an additional inductor L_{cf} is added to the *LCL* filter [57]. The inductor L_{cf} is connected in series with the filter capacitor C_{cf} to form a series *LC* resonant trap, which is tuned at the switching frequency f_{sw}. By doing so, this resonant trap exhibits extremely low impedances around f_{sw}, and therefore harmonics appearing around f_{sw} can be bypassed by the resonant trap and removed from the grid-side. As a result, the *LLCL* filter with smaller filter inductors can perform even better filtering than the *LCL* filter [57]. To further reap the advantages of *LC* resonant traps, several advanced passive filters are proposed. These passive filters feature *LC* resonant traps, and thus they can be collectively referred to as trap filters, as will be detailed in the following sections.

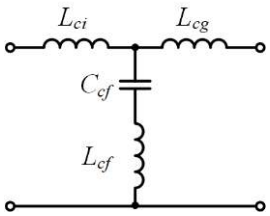

Figure 3.2 Schematic diagram of *LLCL* filters [57].

In parallel to the modified *LCL* filters, the magnetic integration of *LCL* filters is attracting growing attentions [21, 86-89]. The objective of the magnetic integration technique is to improve the power density of passive filters through winding several inductors on a common magnetic core. The idea of the magnetic integration of *LCL* filters is first introduced in [21], where a common I magnetic

core is shared by both the converter-side inductor and grid-side inductor, and the two inductors are separately winded on their respective E cores. The magnetic fluxes generated by two inductor windings tend to cancel out with each other in the common I core, thus leading to size reduction. However, the common core introduces a coupling between the two inductors. This coupling effect is concluded to be an obstacle for harmonic filtering and difficult to be eliminated in the literature [21, 89]. In consequence, great efforts have been attached to the minimization of coupling effects for magnetic integrated *LCL* filters.

3.2 Magnetic Integrated *LLCL* Filters

Rather than trying to minimize the coupling effect, this section intentionally leverages the coupling between the two inductors of the *LCL* filter. As a result, an equivalent magnetic integrated *LLCL* filter can be derived from a properly designed magnetic integrated *LCL* filter. The integrated *LLCL* filter possesses the benefits of both magnetic integration and *LLCL* filter, i.e. high-power density and strong attenuation. Moreover, the additional inductor L_{cf} depicted in Figure 3.2 can be further saved. Therefore, the integrated *LLCL* filter consisting of only one integrated inductor and one filter capacitor can be very simple in terms of its filter structure. This section mainly includes the author's work in [87].

3.2.1 Fundamental Principle

Figure 3.3 depicts the equivalent circuits of magnetic integrated *LCL* filters, where the coupling effect between grid-side inductor and converter-side inductor is represented by the mutual inductance M_{gi}, and the dots stand for identical terminals. It is apparent from Figure 3.3 that there are two possible coupling modes between the two inductors. The first coupling mode, defined as the positive coupling in Figure 3.3(a), introduces an equivalent negative inductor with its inductance $-M_{gi}$, into the filter capacitor branch loop. In contrast, as shown in Figure 3.3(b), the second coupling mode or negative coupling imports a positive inductor in series with the filter capacitor. In this case, it can be

observed that the equivalent circuit of the integrated *LCL* filter is the same as that of the *LLCL* filter shown in Figure 3.2. This interesting observation implies that the integrated *LCL* filter may be designed as an integrated *LLCL* filter. Additionally, the filter inductances L_{cg} and L_{ci} should add or subtract M_{gi} in the cases of positive and negative couplings, respectively. The mutual inductance M_{gi} can be expressed in terms of L_{cg} and L_{ci} as

$$M_{gi} = k_M \sqrt{L_{cg} L_{ci}}, \tag{3-1}$$

where k_M denotes the coupling coefficient, and a large value of k_M indicates a strong coupling case.

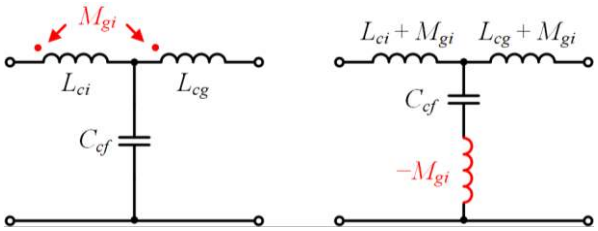

(a) Positive coupling

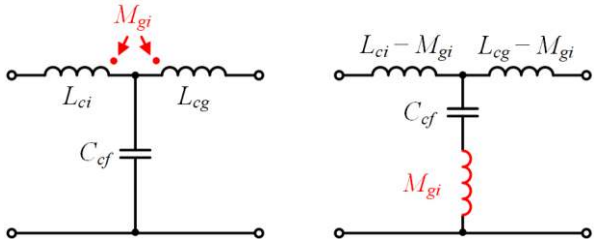

(b) Negative coupling

Figure 3.3 Equivalent circuits of the magnetic integrated *LCL* filters with the (a) positive coupling and (b) negative coupling.

In the case of the negative coupling, the plant model can be derived as

$$G_{\text{plant\_LLCL}}(s) = \frac{(M_{gi} C_{cf} s^2 + 1)\omega_{cr\_\text{LLCL}}{}^2}{(L_{ci} + L_{cg} - 2M_{gi}) s (s^2 + \omega_{cr\_\text{LLCL}}{}^2)}, \tag{3-2}$$

where ω_{cr_LLCL} denotes the resonance angular frequency and can be expressed as

$$\omega_{cr\_\text{LLCL}} = 2\pi f_{cr\_\text{LLCL}} = \sqrt{\frac{L_{ci} + L_{cg} - 2M_{gi}}{L_{ci} L_{cg} C_{cf} - M_{gi}{}^2 C_{cf}}}. \tag{3-3}$$

When the coupling effect is not considered, i.e. M_{gi} = 0, the plant model and resonance angular frequency of integrated *LCL* filters in (3-2) and (3-3) change

into those of conventional *LCL* filters in (2-30) and (2-31), respectively. In addition to the resonance frequency, the integrated *LCL* filter also features a trap frequency, which can be derived by setting the numerator of (3-2) to zero. Note that this trap frequency is essentially the resonance frequency of C_{cf} and M_{gi}, i.e.

$$\omega_{ct\_LLCL} = 2\pi f_{ct\_LLCL} = \sqrt{\frac{1}{M_{gi}C_{cf}}}. \tag{3-4}$$

The integrated *LCL* filter becomes the integrated *LLCL* filter provided that the trap frequency is tuned at the switching frequency, i.e. $f_{ct\_LLCL} = f_{sw}$. Figure 3.4 illustrates the Bode diagrams of the plant models of *LCL*-filtered and integrated *LLCL*-filtered power converters, where the filter inductances and capacitance of the two cases are chosen to be identical. Notice that the integrated *LLCL* filter exhibits strong attenuation around the switching frequency f_{sw}, which is also the major advantage of conventional *LLCL* filters. However, similar to conventional *LLCL* filters, the integrated *LLCL* filter is inferior to the *LCL* filter in terms of attenuation at higher frequency bands. This drawback will be further discussed and addressed in the next section.

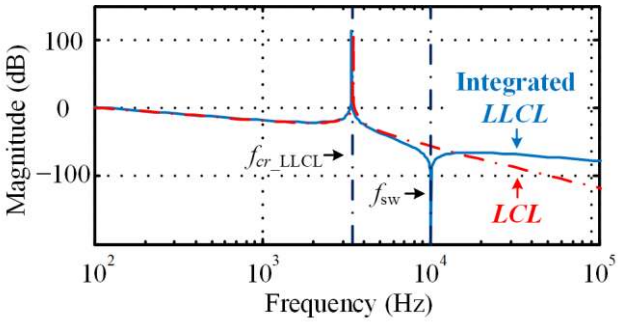

Figure 3.4 Bode diagrams of $G_{plant\_LCL}(s)$ and $G_{plant\_LLCL}(s)$.

3.2.2 Magnetic Circuit Analysis

This subsection focuses on the magnetic circuit analysis and lays the foundation for the core design. Various magnetic cores can be employed for implementing the proposed integrated inductor. One example is the EE magnetic core demonstrated in Figure 3.5. It is clear from the core structure shown in Figure 3.5(a) that the two inductor windings are separately winded on the side

limbs of the EE core with winding turns N_{ci} and N_{cg}, respectively. As the arrows indicate, the fluxes generated by two inductor windings partially cancel out in the side limbs to create a negative coupling effect, and they superimpose in the central limb. At the middle part of the EE core, the air gaps with lengths l_{gs} and l_{gc} are intentionally leaved to avoid magnetic saturation. In Figure 3.5(b), the air gap reluctances are denoted as R_{gs} and R_{gc}, and the reluctances of central limb, side limbs, and yokes are represented as R_c, R_s, and R_{sc}, respectively.

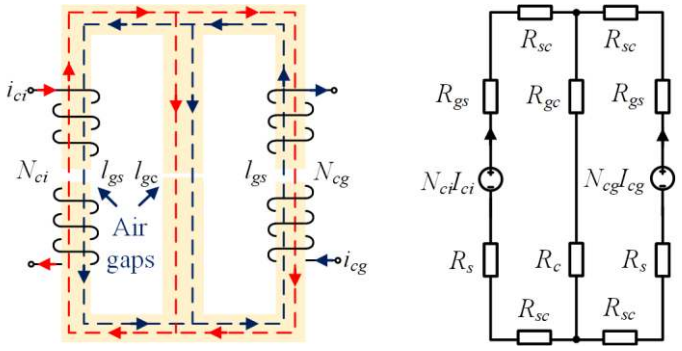

(a) Core structure (b) Equivalent magnetic circuit

Figure 3.5 (a) Core structure and (b) equivalent magnetic circuit of integrated *LLCL* filters.

The self- and mutual reluctances can be derived from Figure 3.5 as

$$R_{ii} = R_{gg} \approx \frac{(R_{gs} + 2R_{gc})R_{gs}}{R_{gc} + R_{gs}}, \tag{3-5}$$

$$R_{ig} = R_{gi} \approx \frac{(R_{gs} + 2R_{gc})R_{gs}}{R_{gc}}, \tag{3-6}$$

where R_{ii} and R_{gg} refer to the self-reluctances while R_{ig} and R_{gi} correspond to the mutual reluctances. Equations (3-5) and (3-6) are satisfied under the assumptions that the air gap reluctances are far greater than the limb and yoke reluctances. Furthermore, the air gap reluctances R_{gs} and R_{gc} are given by

$$R_{gs} \approx \frac{l_{gs}}{A_s \mu_0}, \tag{3-7}$$

$$R_{gc} \approx \frac{l_{gc}}{A_c \mu_0}, \tag{3-8}$$

where A_s and A_c designate the cross-section areas of side limbs and central limb,

respectively. For E cores, $A_c = 2A_s$ is normally satisfied [90]. The constant μ_0 denotes the permeability of air, which equals $4\pi \times 10^{-7}$ N/A^2 [20]. Upon knowing the self-reluctances and mutual reluctances in (3-5) and (3-6), the self-inductances and mutual inductance can be further derived as follows:

$$L_{ci} = \frac{N_{ci}^{\ 2}}{R_{ii}} = \frac{N_{ci}^{\ 2}\mu_0 A_s (l_{gc}A_s + l_{gs}A_c)}{l_{gs}(2l_{gc}A_s + l_{gs}A_c)}, \tag{3-9}$$

$$L_{cg} = \frac{N_{cg}^{\ 2}}{R_{gg}} = \frac{N_{cg}^{\ 2}\mu_0 A_s (l_{gc}A_s + l_{gs}A_c)}{l_{gs}(2l_{gc}A_s + l_{gs}A_c)}, \tag{3-10}$$

$$M_{gi} = \frac{N_{cg}N_{ci}}{R_{gi}} = \frac{N_{ci}N_{cg}l_{gc}\mu_0 A_s^{\ 2}}{l_{gs}(2l_{gc}A_s + l_{gs}A_c)}. \tag{3-11}$$

Substitution of (3-9) − (3-11) into (3-1) yields

$$k_M = \frac{l_{gc}A_s}{l_{gc}A_s + l_{gs}A_c}. \tag{3-12}$$

It can be inferred from (3-12) that k_M can be flexibly designed by the change of air gap lengths l_{gs} and l_{gc}.

It is apparent from Figure 3.4 that the trap frequency f_{ct_LLCL} or switching frequency f_{sw} is much higher than the resonance frequency f_{cr_LLCL}. As a result, the mutual inductance M_{gi} should be much less than the self-inductances L_{ci} and L_{cg}. That is, the coupling coefficient k_M is of a significantly small value. This statement remains valid in the case of conventional *LLCL* filters [57]. According to (3-12), the small value of k_M means that the length of the side limbs l_{gs} is far greater than the length of the central limb l_{gc}. Under this assumption, the self-inductances L_{ci} and L_{cg} are predominantly determined by l_{gs} regardless of l_{gc}. Therefore, in the first step, the self-inductances are tuned by changing their respective winding turns N_{ci} and N_{cg} as well as l_{gs}. After self-inductances are designed, the mutual inductance M_{gi} can be further adjusted by changing l_{gc}. This simplification greatly facilitates the core design. It should be mentioned that the change of l_{gc} may slightly shifts the values of self-inductances in practice, and the relevant deviations can be compensated by the change of winding turns.

3.2.3 Core Design and Volume Comparison

For simplification of analysis, the performance evaluations of passive filters in this chapter are carried out on single-phase power converters. Figure 3.6 depicts the schematic diagrams of two single-phase CCCs, i.e. H-bridge and half-bridge power converters, where C_{cdc} , C_{cdc1}, and C_{cdc2} represent the DC-link capacitances, which are designed to ensure acceptable voltage ripples. Note that single-phase power converters and three-phase power converters can be modelled in a similar way if the decoupling between *d*- and *q*-axes is achieved (see Figure 2.16). In this section, the H-bridge topology in Figure 3.6(a) is adopted. The system parameters for testing the integrated *LLCL* filter are listed in Table 3-1, where the DC-link resistance R_{cdc} indicates that the power converter is operated as a rectifier in this case. For the integrated *LLCL* filter, the design procedure is largely the same as that of conventional *LLCL* filters. The major design criterions can be summarized as the 40% converter ripple current, less than 5% reactive power absorption by the filter capacitor, and compliance with the IEEE standard 519-2014 [14, 57].

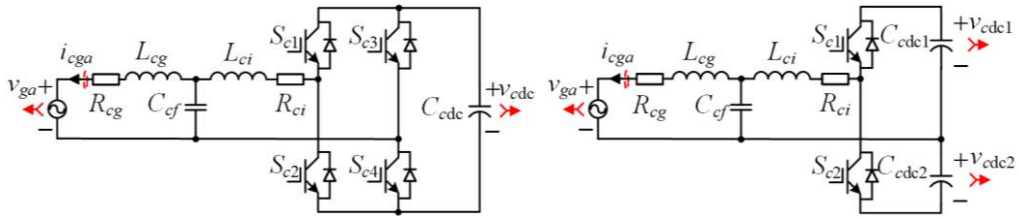

(a) H-bridge (b) Half-bridge

Figure 3.6 Schematic diagrams of single-phase (a) H-bridge and (b) half-bridge power converters.

Table 3-1 System parameters for testing the integrated *LLCL* filter.

Description	Symbol	Value
DC-link capacitance	C_{cdc}	940 μF
DC-link resistance	R_{cdc}	80 Ω
DC-link voltage reference	V_{cdc_ref}	190 V
Grid voltage reference (rms)	V_{g_ref}	110 V
Active power reference	P_{c_ref}	450 W
Fundamental frequency	f_{ref}	50 Hz
Switching/sampling frequency	f_{sw}/f_s	10 kHz

After being designed, the filter parameters are formulated in Table 3-2, where two *LCL* filters are fabricated in the laboratory and denoted as case I and case II , respectively. The mutual inductance M_{gi} can be derived by letting (3-4) equal the switching frequency f_{sw}. Furthermore, the coupling coefficient k_M can be calculated as 0.05 by using (3-1). Substituting k_M = 0.05 into (3-12) and considering that $A_c = 2A_s$, one can derive the ratio l_{gs} / l_{gc} as 9.5, thereby validating that l_{gs} is much greater than l_{gc}.

Table 3-2 Filter parameters for testing the integrated *LLCL* filter.

Description and symbol	Values of *LCL* filter (case I)	Values of *LCL* filter (case II)	Values of integrated *LLCL* filter
Converter inductance L_{ci} (mH)	0.8	1.7	0.8
Grid inductance L_{cg} (mH)	0.8	1.6	0.8
Filter capacitance C_{cf} (μF)	6.0	6.0	6.0
Mutual inductance M_{gi} (μH)	–	–	40.0

To reduce the core losses of the integrated inductor, Litz wires featuring low equivalent series resistors (ESRs) are employed as inductor windings. The cross-section area of Litz wires is denoted as S_{cw}. According to Table 3-2, both the converter inductance L_{ci} and grid inductance L_{cg} of the integrated *LLCL* filter are known, and they are equivalent, i.e. $L_{ci} = L_{cg}$. Moreover, if the maximum inductor currents $I_{ci\_max} = I_{cg\_max}$, maximum flux density B_{c_max}, and utilization efficient of the window area K_{cu} are given, the size of the EE core can be determined by the area-product method through the following equation:

$$A_p = \frac{S_{cw} L_{cg} I_{cg\_max}}{K_{cu} B_{c\_max}}, \tag{3-13}$$

where A_p is defined as the area product of the window area A_w and central limb cross-section area A_s of EE magnetic cores [20]. Substitution of S_{cw} = 0.5 π mm^2, L_{cg} = 0.8 mH, I_{cg_max} = 12 A, K_{cu} = 0.5, and B_{c_max} = 0.3 T into (3-13) yields A_p = 1.01×10^{-7} m^4.

According to the product catalog of TDK [90], one pair of E 70/33/32 magnetic cores with a window area A_w of 5.46×10^{-4} m^2 and a cross-section area A_s of 3.52

$\times 10^{-4}$ m^2 are selected. The resultant area product is 1.92×10^{-7} m^4, which is approximately doubled as compared with the required value of A_p, and hence a sufficient size margin is left. Once the cross-section area A_s is fixed, it is possible to calculate the inductor winding turns from

$$N_{ci} = N_{cg} = \frac{L_{cg} I_{cg\_\max}}{A_s B_{c\_\max}}, \tag{3-14}$$

where $N_{ci} = N_{cg} = 91$ turns can be derived upon substituting the relevant parameters. Under the assumptions that the self-reluctances are approximated to the air gap reluctances of side limbs, i.e. $R_{ii} \approx R_{gg} \approx R_{gs}$, insertion of (3-7) into (3-10) yields

$$l_{gs} = \frac{N_{cg}{}^2 A_s \mu_0}{L_{cg}}. \tag{3-15}$$

It can be derived from (3-15) that $l_{gs} = 4.6$ mm. Recapping that l_{gs} / l_{gc} is 9.5, one can obtain the length of the central limb air gap as $l_{gc} = 0.48$ mm. The adjustments of the lengths of side limb air gaps and central limb air gap can be achieved by inserting small I cores into the air gap of the central limb.

It is of importance to compare the volumes between integrated inductor and discrete inductors. For the conventional *LCL* filter with discrete inductors, the inductors can be winded on the central limbs of two pairs of EE cores, respectively. As the cross-section area of the central limb equals two times of that of the side limbs, the inductors winded on the central limbs are less likely to saturate. As a result, two smaller cores can be used as the cores for discrete inductors. However, remember that the comparison should be carried out between total core volume of discrete inductors and that of the integrated inductor. Moreover, to guarantee a fair comparison, the filter inductances of conventional *LCL* filter (case I) and integrated *LLCL* filter are designed to be identical. Using the area-product method, a pair of E 65/32/27 cores are selected for the converter-side inductor, which yields an area product of 2.94×10^{-7} m^4. For the grid-side inductor, the area product requirement can be relaxed by 40% to 6.06×10^{-8} m^4 due to the removal of ripple currents. Consequently, a pair of E 55/28/21 cores

having an area product of 13.60×10^{-8} m^4 are chosen. Note that the resultant area products are greater than or approximately equal to $2A_p$.

Figure 3.7 illustrates the physical dimensions of the cores of integrated inductor and discrete inductors, where the core volume of the integrated inductor is calculated to be $V_{E70} = 1.13 \times 10^{-4}$ m^3, and the total volume of discrete inductors are derived as $V_{E65} + V_{E55} = 1.36 \times 10^{-4}$ m^3. In comparison, the integrated inductor allows a 16.9% volume reduction as compared with the discrete inductors. In terms of costs, the two cases obtained from the website of Digikey are 8.79 USD/unit (E 70/33/32) and 9.67 USD/unit (E 65/32/27: 5.92 USD/unit and E 55/28/21: 3.75 USD/unit), respectively [91]. It can be concluded that the cost reduction of the integrated inductor case is around 10%.

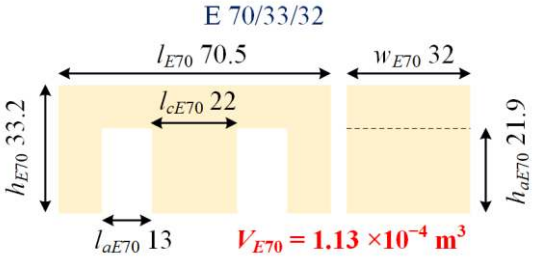

(a) Integrated inductor core

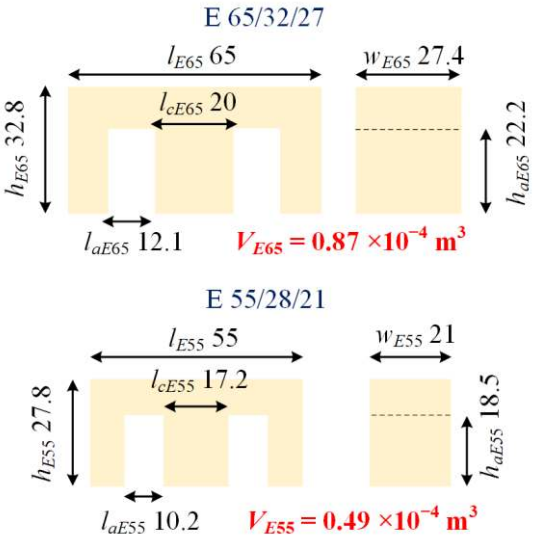

(b) Discrete inductor cores

Figure 3.7 Physical dimensions of (a) integrated inductor core and (b) discrete inductor cores.

Previously, the volume comparison between integrated inductor core and discrete inductor cores is carried out under a specific condition. However, it is desirable to generalize the comparison to various operating conditions of power converters, e.g. with different filter inductances and current ratings. It would be fair that the shapes of all the cores are designed to be the same as that of E 70/33/32, but the core size is scaled accordingly to maintain the same A_p margin among all the cores. Figure 3.8 illustrates the volume comparison between integrated inductor core and discrete inductor cores under various operating conditions of power converters, where the length ratio k_s is used as a scalable factor and is defined as the ratio l_{E70_var} / l_{E70}, in which l_{E70_var} denotes the side length of the integrated inductor core under various conditions. Therefore, a large k_s translates into a large filter inductance or a higher current rating. It is obvious from Figure 3.8 that the integrated inductor allows the reduction of core volumes as compared with the discrete inductors, thereby indicating the effectiveness of the magnetic integration technique in improving the power density of passive filters.

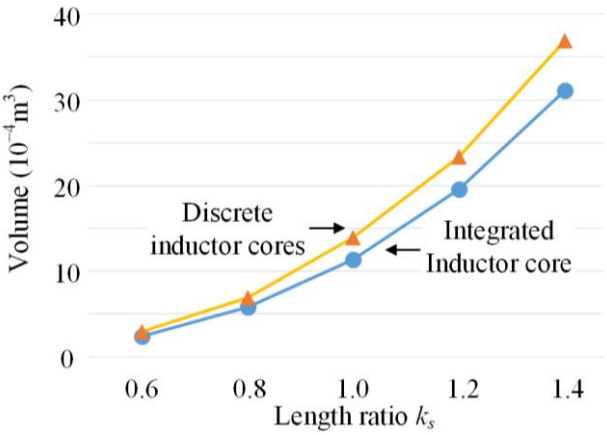

Figure 3.8 Volume comparison between integrated inductor core and discrete inductor cores.

3.2.4 Experimental Verification

To further verify the benefit of the proposed integrated *LLCL* filter in terms of harmonic attenuation, the experimental testing of the power converters filtered by *LCL* and integrated *LLCL* filters was conducted. In the experiments, the

current spectra were derived from current waveforms, which were captured from a digital oscilloscope and then imported into the MATLAB software and analyzed through its Powergui FFT Analyze Tool. Figure 3.9 shows the experimental results of the *LCL*-filtered power converter (case I), where the waveform of the grid-injected current i_{cga} is shaped as a sinusoidal and in phase with the grid voltage v_{ga}. However, there is an observable current spike around the switching frequency 10 kHz or the 200th harmonic frequency, which obviously goes beyond the harmonic limit, i.e. the 0.3% fundamental current magnitude. Small filter inductances and capacitance should be responsible for the insufficient harmonic attenuation. Additionally, it should be mentioned that the double line-frequency voltage ripple in v_{cdc} can be attenuated by a larger DC-link capacitor.

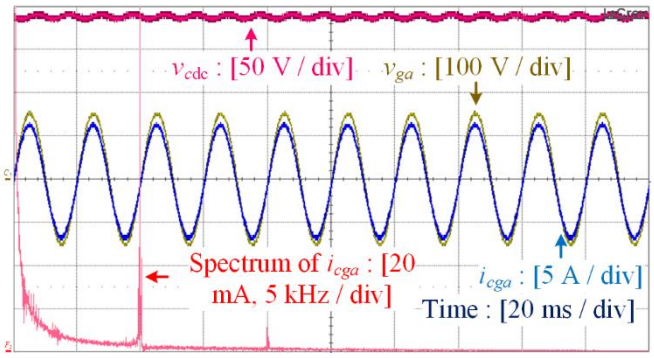

(a) Waveforms

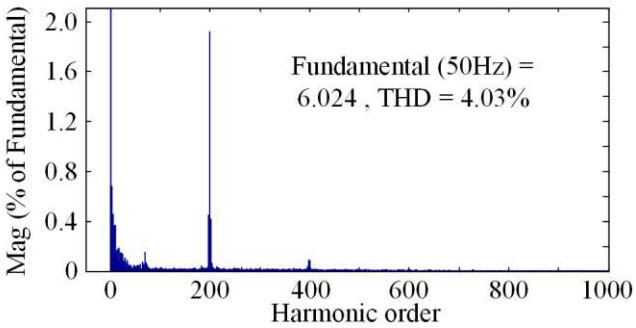

(b) Spectrum of i_{cga}

Figure 3.9 Experimental (a) waveforms and (b) spectrum of i_{cga} of the *LCL*-filtered power converter (case I).

The experimental results of the integrated *LLCL*-filtered power converter are demonstrated in Figure 3.10, where the current spike around the switching

frequency is greatly attenuated as compared with Figure 3.9. It can be observed from Figure 3.10(b) that the integrated *LLCL* filter enables the grid-injected current to comply with grid codes, although the switching frequency harmonics can hardly be fully removed due to component tolerances. However, the higher-frequency harmonics are magnified by the integrated *LLCL* filter. This is because the *LLCL* filter features a weak attenuation ability at frequencies higher than the switching frequency, particularly for the double switching frequency, as evidenced by Figure 3.4. Overall, the integrated *LLCL* filter shows a much better filtering performance than the *LCL* filter.

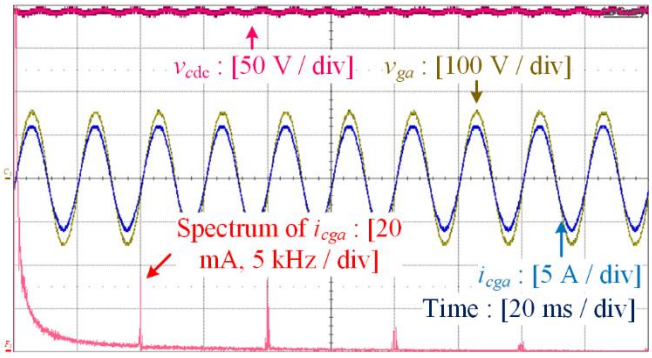

(a) Waveforms

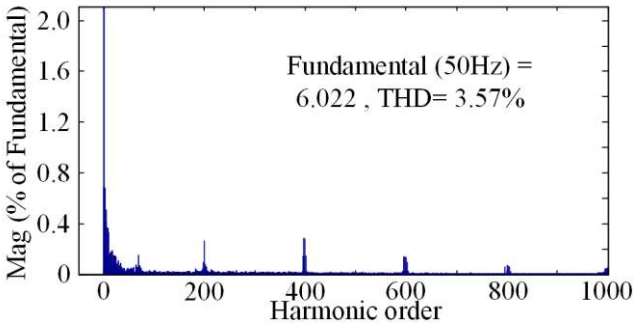

(b) Spectrum of i_{cga}

Figure 3.10 Experimental (a) waveforms and (b) spectrum of i_{cga} of the integrated *LLCL*-filtered power converter.

To effectively attenuate the switching frequency harmonics, another *LCL* filter is designed with the filter inductances doubled (case II). The filtering performance of the case II *LCL* filter can be visualized from Figure 3.11, where the current spike around the switching frequency can be effectively suppressed similarly to Figure 3.10. However, it should be highlighted that the filter

inductances are doubled, resulting in a larger filter size and a higher cost. In other words, with the filtering performance unchanged, the integrated *LLCL* filter allows a 50% inductance reduction as compared with the *LCL* filter.

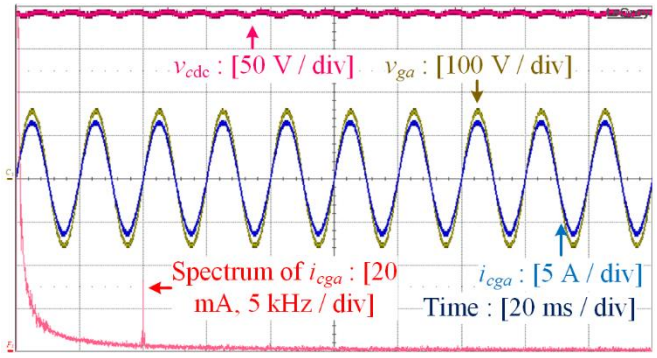

(a) Waveforms

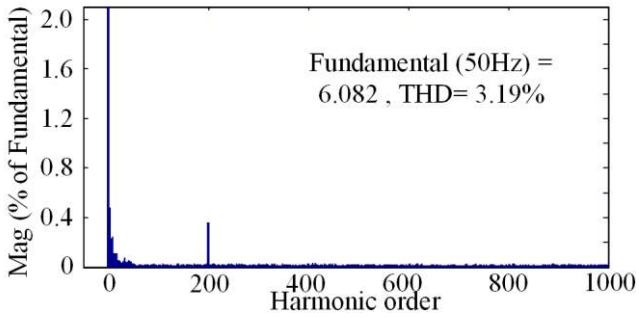

(b) Spectrum of i_{cga}

Figure 3.11 Experimental (a) waveforms and (b) spectrum of i_{cga} of the *LCL*-filtered power converter (case II).

It is safe to conclude from the experimental results that the proposed integrated *LLCL* filter yields both the benefits of magnetic integration (a more than 10% volume reduction) and *LLCL* filter (a 50% reduction of filter inductances). Moreover, the additional filter inductor in the *LLCL* filter is saved. However, the integrated *LLCL* filter also inherits the drawback of poor attenuation at frequencies above the switching frequency from *LLCL* filters. This issue will be solved by other advanced passive filters.

3.3 Series-Parallel-Resonant *LCL* (*SPRLCL*) Filters

In this section, another advanced passive filter consisting of a series-resonant trap and a parallel-resonant trap, i.e. the series-parallel-resonant *LCL* (*SPRLCL*)

filter, is proposed. As the *SPRLCL* filter features two resonant traps, it can be flexibly designed to either simultaneously provide strong attenuation to both the switching frequency and double switching frequency harmonics, and thus overcoming the drawback of *LLCL* filters, or to exhibit high robustness against filter parameter variations. This section mainly summarizes the author's work in [61].

3.3.1 Fundamental Principle

As mentioned earlier, the series *LC*-trap allows the *LLCL* filter to exhibit strong attenuation around the switching frequency, and hence reducing the filter size required for compliance of grid codes. Due to the clear advantages of *LC*-traps, many attempts of incorporating them into *LCL* filters have been made, which will be disclosed as follows [84, 92]. According to the duality relationship between series resonance and parallel resonance, a parallel *LC*-trap consisting of grid-side inductor and an additional capacitor may be employed to modify the *LCL* filter into the *LCCL* filter, as presented in Figure 3.12(a) and detailed in the author's paper [93].

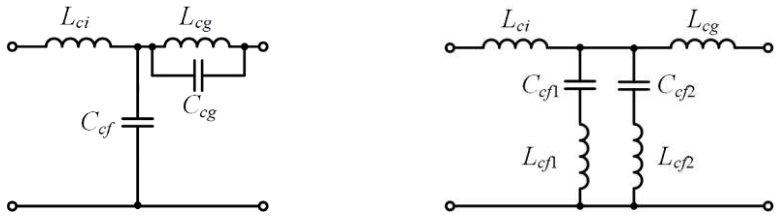

(a) *LCCL* filter (b) *L-TC-L* filter

Figure 3.12 Schematic diagram of (a) *LCCL* filter and (b) *L-TC-L* filters.

The parallel-resonant *LC*-trap features an infinite large impedance at its resonance frequency. Therefore, the parallel-resonant *LC*-trap can be used to block the switching frequency harmonics from entering the power grid when it is tuned at the switching frequency. In this case, the switching frequency harmonics will flow through the filter capacitor. The Bode diagram of the plant model of *LCCL*-filtered power converters is almost identical to that of *LLCL*-filtered power converters under stiff grid conditions [93]. However, the *LCCL* filter

allows better attenuation than the *LLCL* filter in the high-frequency domain when the grid impedance is considered under weak grid conditions.

For half-bridge power converters shown in Figure 3.6(b), switching harmonics are difficult to be sufficiently attenuated [19]. Moreover, a wide control bandwidth is also necessary when half-bridge converters are controlled as APFs to compensate low-frequency harmonics [58]. These requirements necessitate an extremely high attenuation capacity of passive filters. To further improve the filtering ability of the *LLCL* filter, more than one series-resonant *LC*-traps can be employed to perform strong attenuation at the switching frequency and its multiples, and such a filter is named as the *L-TC-L* filter, in which the dashes differentiate filter branch loops and *T* stands for traps [83]. Figure 3.12(b) provides the schematic diagram of an *L-TC-L* filter with two *LC*-traps, in which the *LC*-traps are tuned at the switching frequency and double switching frequency, respectively [83]. An additional filter capacitor may also be included and connected in parallel with the *LC*-traps to further improve the high-frequency attenuation of the *L-TC-L* filter, which is not shown for simplicity [83].

Figure 3.13 shows the Bode diagrams of *LCL*-, *LLCL*-, and *L-TC-L*-filtered power converter plant models, where the total capacitance in each filter is identical. As noticed, the *L-TC-L* filter provides strong attenuation at f_{sw} and $2f_{sw}$. However, the system is noted to have a new resonant peak appearing at the resonance frequency f_{cr2}, and this resonant peak cannot be well damped by the grid resistance. In addition, as compared with the *LLCL* filter, the *L-TC-L* filter contains one more *LC*-trap − a trap inductor and a trap capacitor, which complicates the filter structure. Note that both *LLCL* and *L-TC-L* filters are sensitive to filter parameter variations, and their strong attenuation at the switching frequency will be deteriorated accordingly.

When the additional capacitor of the *LCCL* filter is employed in the *LLCL* filter and paralleled with its grid-side inductor to form a parallel-resonant *LC*-trap, the *SPRLCL* filter can be obtained, as illustrated in Figure 3.14. Similar to the *L-TC-L* filter, the *SPRLCL* filter also contains two *LC*-traps, and thus it can provide

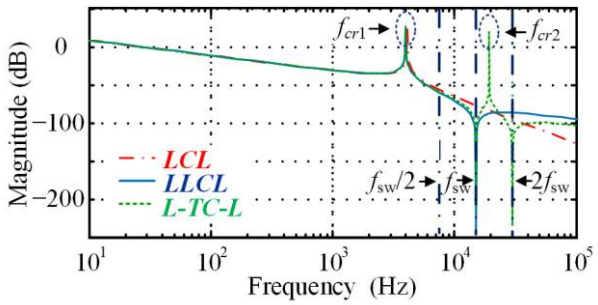

Figure 3.13 Bode diagrams of $G_{\text{plant\_LCL}}(s)$, $G_{\text{plant\_LLCL}}(s)$, and $G_{\text{plant\_L-TC-L}}(s)$.

strong attenuation to the first and second dominant switching harmonics when designed properly. As the parallel trap of *SPRLCL* filters replaces the series trap of *L-TC-L* filters, one trap inductor can be saved, leading to a simplified filter structure. The plant model of *SPRLCL*-filtered power converters, i.e. the transfer function from the converter voltage to the grid-injected current, is derived as

$$G_{\text{plant\_SPRLCL}}(s)=\frac{a_4 s^4+a_2 s^2+1}{b_5 s^5+b_4 s^4+b_3 s^3+b_2 s^2+b_1 s+b_0}, \tag{3-16}$$

where the coefficients are expressed as

$$\begin{cases} a_4 = L_{cg}L_{cf}C_{cg}C_{cf} \\ a_2 = L_{cg}C_{cg}+L_{cf}C_{cf} \\ b_5 = L_{ci}L_{cg}L_{cf}C_{cg}C_{cf}+L_{ci}L_{cg}L_sC_{cg}C_{cf}+L_{cg}L_sL_{cf}C_{cg}C_{cf} \\ b_4 = L_{ci}L_{cg}C_{cg}C_{cf}R_s+L_{cg}L_{cf}C_{cg}C_{cf}R_s \\ b_3 = L_{ci}L_{cg}C_{cf}+L_{ci}L_{cg}C_{cg}+L_{ci}L_sC_{cf}+L_{cg}L_sC_{cg} \\ +L_{cf}C_{cf}L_{ci}+L_{cf}C_{cf}L_{cg}+L_{cf}C_{cf}L_s \\ b_2 = L_{ci}C_{cf}R_s+L_{cg}C_{cg}R_s+L_{cf}C_{cf}R_s \\ b_1 = L_{ci}+L_{cg}+L_s \\ b_0 = R_s, \end{cases} \tag{3-17}$$

in which L_s and R_s denote the grid inductance and resistance, respectively, which are not depicted in Figure 3.14 for simplicity.

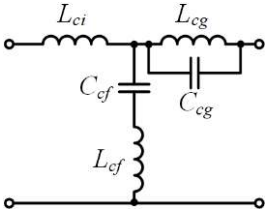

Figure 3.14 Schematic diagram of *SPRLCL* filters.

Let the numerator of $G_{\text{plant\_SPRLCL}}$ equal zero, the resonance frequencies of series and parallel *LC*-traps can be derived as

$$\omega_{cts\_\text{SPRLCL}} = 2\pi f_{cts\_\text{SPRLCL}} = \sqrt{\frac{1}{L_{cf}C_{cf}}}, \tag{3-18}$$

$$\omega_{ctp\_\text{SPRLCL}} = 2\pi f_{ctp\_\text{SPRLCL}} = \sqrt{\frac{1}{L_{cg}C_{cg}}}, \tag{3-19}$$

where f_{cts_SPRLCL} and f_{ctp_SPRLCL} denote the series and parallel resonance frequencies of *LC*-traps, respectively.

3.3.2 Filter Design

For *SPRLCL* filters, there are mainly three design methods to determine the resonance frequencies of *LC*-traps. The first method, i.e. method I, is to place the series resonance frequency at the switching frequency f_{sw}, while the parallel resonance frequency is allocated at the double switching frequency $2f_{\text{sw}}$. Alternatively, the two resonance frequencies can be exchanged with method II. Method III assigns both the series and parallel resonance frequencies at f_{sw} so that the *SPRLCL* filter maintains strong attenuation around the switching frequency even if filter parameters are drifted.

Figure 3.15 draws the Bode diagrams of *SPRLCL*-filtered power converter plant models. It is clear that the *SPRLCL* filters designed with methods I and II perform very sharp attenuation around the switching frequency f_{sw} and double switching frequency $2f_{\text{sw}}$. In contrast, the method III designed *SPRLCL* filter provides extremely high attenuation at f_{sw} at the expense of its attenuation at $2f_{\text{sw}}$. In all the cases, the second resonant peaks can be attenuated well below 0 dB by the grid resistance. This is because the second resonance frequencies are higher than $2f_{\text{sw}}$, and thus the relevant resonant peaks can be better attenuated.

Figure 3.16 plots the Bode diagrams of *SPRLCL*-filtered power converter plant models with parameter variations, where *SPRLCL* filters are designed with method III. It is not surprising to note that *SPRLCL* filters maintain good attenuation around the switching frequency f_{sw} regardless of parameter variations,

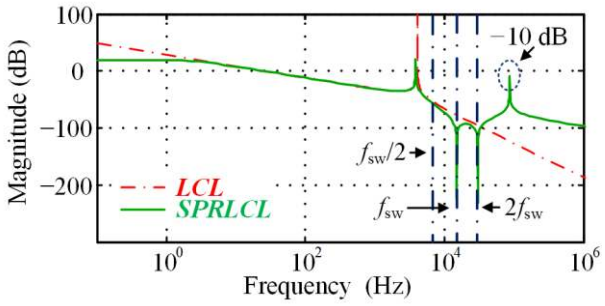

(a) Method I

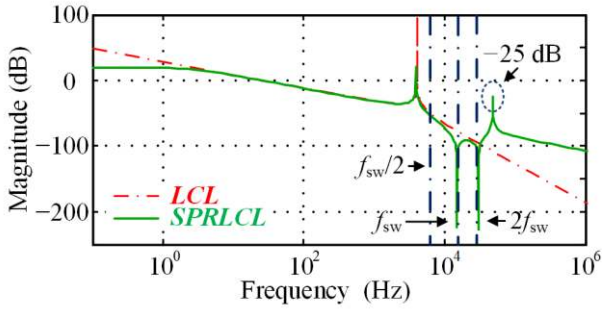

(b) Method II

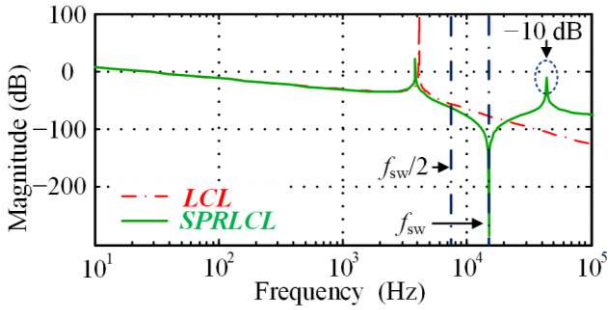

(c) Method III

Figure 3.15 Bode diagrams of $G_{plant\_SPRLCL}(s)$ wirh the *SPRLCL* filters designed with (a) method I, (b) method II, and (c) method III.

i.e. the 20% variations of L_{cf} and L_{cg}, thus validating the high robustness of method III designed *SPRLCL* filters. Note that the variations of capacitances C_{cf} and C_{cg} yield similar results, and hence not shown here. When the same parameter variations are faced by method I and II designed *SPRLCL* filters, they lose their strong attenuation around f_{sw}, as verified by Figure 3.17. However, the high attenuation at the double switching frequency $2f_{sw}$ remains unchanged.

A comprehensive parameter design procedure of *SPRLCL* filters can be found in [61]. Following the design procedure, *SPRLCL* filters can be designed with the

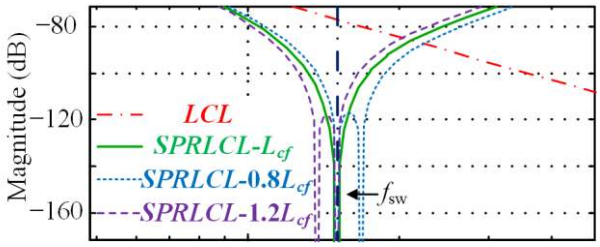

(a) Method III with ±20% variations of L_{cf}

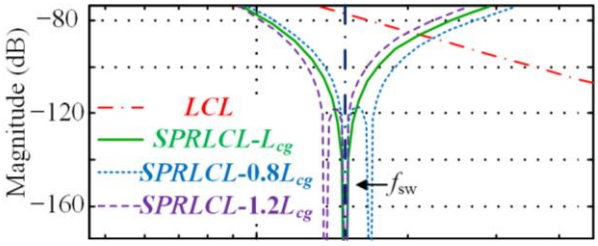

(b) Method III with ±20% variations of L_{cg}

Figure 3.16 Bode diagrams of $G_{plant\_SPRLCL}(s)$ with the *SPRLCL* filters designed with method III and ±20% variations of (a) L_{cf} and (b) L_{cg}.

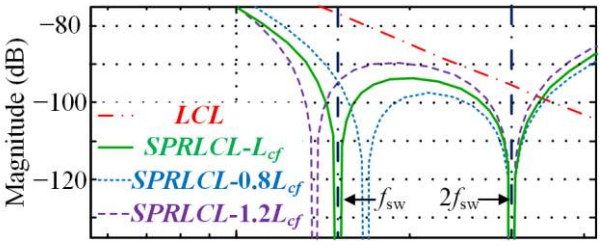

(a) Method I with ±20% variations of L_{cf}

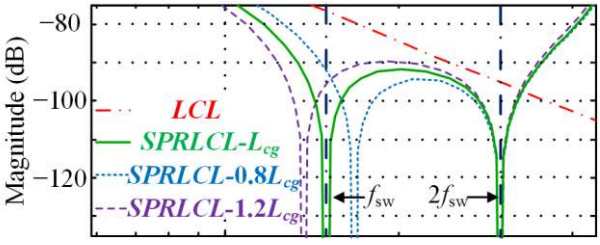

(b) Method II with ±20% variations of L_{cg}

Figure 3.17 Bode diagrams of $G_{plant\_SPRLCL}(s)$ with the *SPRLCL* filters designed with (a) method I and ±20% variations of L_{cf} and (b) method II and ±20% variations of L_{cg}.

aforementioned three design methods, and the resultant filter parameters are listed in Table 3-3, where the first resonance frequencies of all the passive filters are deigned to be f_{sw} / 3 (5 kHz) in order to maximize the damping effect and facilitate the controller design [61].

3.3.3 Experimental Verification

The proposed *SPRLCL* filters were experimentally tested on a half-bridge APF prototype based on the filter and system parameters in Table 3-3 and Table 3-4, respectively. The additional capacitor is implemented by a 100-V metallized polypropylene film capacitor with the capability of handling high ripple currents. Since the experimental results of the APFs filtered by the method I and method II designed *SPRLCL* filters are very similar, only the experimental results concerning method II are provided.

Table 3-3 Filter parameters for testing the *SPRLCL* filters.

Symbol	Values of *LLCL* filter	Values of *SPRLCL* filter (method I)	Values of *SPRLCL* filter (method II)	Values of *SPRLCL* filter (method III)
L_{ci} (mH)	1.5	1.0	1.0	1.5
C_{cf} (μF)	1.7	3.0	3.0	1.7
L_{cg} (mH)	1.0	0.5	0.5	1.0
L_{cf} (μH)	66.7	37.0	9.3	66.7
C_{cg} (nF)	–	56.3	225.2	112.6

Table 3-4 System parameters for testing the *SPRLCL* filters.

Description	Symbol	Value
DC-link capacitances	C_{cdc1}/C_{cdc2}	4700 μF
DC-link voltage references	$V_{cdc\_ref1}/V_{cdc\_ref\,2}$	200 V
Grid voltage reference (rms)	V_{g_ref}	150 V
Fundamental frequency	f_{ref}	50 Hz
Switching/sampling frequency	f_{sw}/f_s	15 kHz

Figure 3.18 shows the experimental waveforms of grid voltage v_{ga}, grid current i_{sa}, and spectrum of i_{sa} before harmonic compensation, where i_{sa} refers to the total APF current and load current. Before the APF is put into operation, i_{sa} is essentially the load current i_{la} featuring a distorted waveform and a THD of 33.1%. It is noted that i_{sa} contains basically negligible switching harmonics around the switching frequency f_{sw} and double switching frequency $2f_{sw}$. However, considerable low-frequency harmonics can be observed.

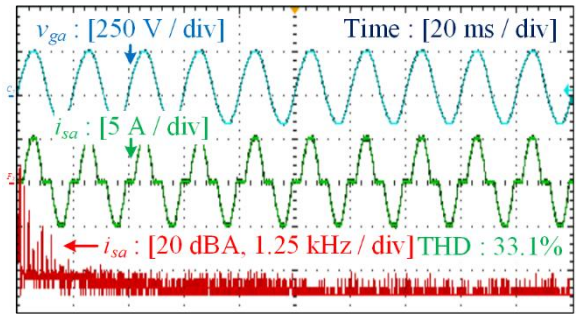

(a) Overall view

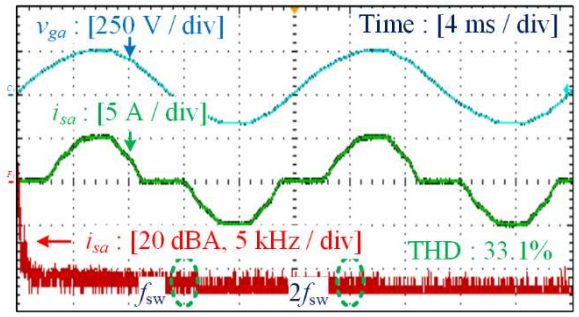

(b) Zoom-in view

Figure 3.18 Experimental waveforms of grid voltage v_{ga}, grid current i_{sa}, and spectrum of i_{sa} before harmonic compensation.

The low-frequency harmonics in i_{sa} can be well compensated by the *LCL*-filtered APF, as validated by Figure 3.19, where the *LCL* filter parameters are designed to be identical as those of the *LLCL* filter in Table 3-3 except for L_{cf}. As observed, along with the compensation of low-frequency harmonics is a low current THD of 4.1%. However, a current spike around the switching frequency f_{sw} can be clearly identified. This current spike prevents the APF from complying with grid codes. Consequently, advanced passive filters are necessary in this case for sufficient high-frequency harmonic attenuation.

Figure 3.20 presents the experimental results of the *LLCL*-filtered APF. As seen, in this case, the dominant switching harmonics around f_{sw} are removed, leading to a reduced current THD of 3.5%. Nevertheless, the double switching frequency harmonics around $2f_{sw}$ are increased. This is due to the poor attenuation ability of *LLCL* filters at $2f_{sw}$, which is in consistence with Figure 3.4.

To further attenuate the double switching frequency harmonics, the method II designed *SPRLCL* filter is employed, and its filtering performance can be

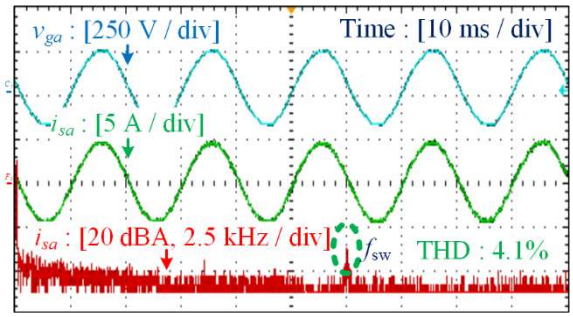

(a) Overall view

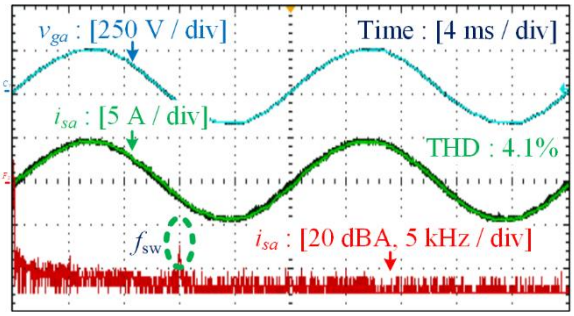

(b) Zoom-in view

Figure 3.19 Experimental waveforms of grid voltage v_{ga}, grid current i_{sa}, and spectrum of i_{sa} after harmonic compensation by the *LCL*-filtered APF.

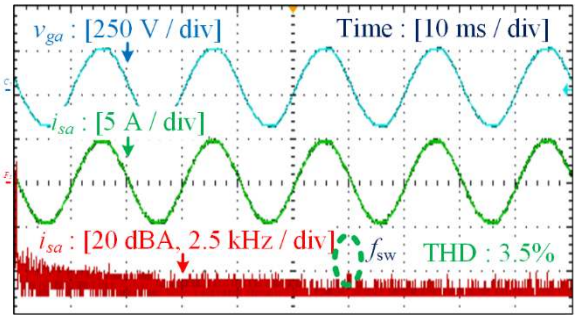

(a) Overall view

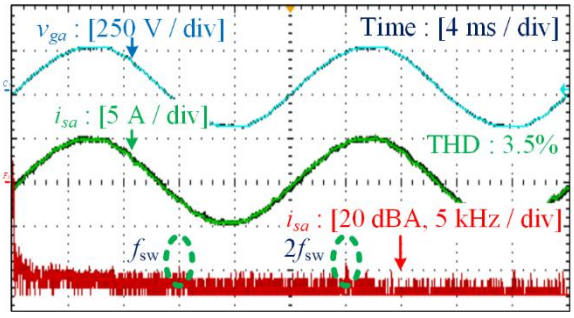

(b) Zoom-in view

Figure 3.20 Experimental waveforms of grid voltage v_{ga}, grid current i_{sa}, and spectrum of i_{sa} after harmonic compensation by the *LLCL*-filtered APF.

visualized in Figure 3.21. It is observed that both the switching frequency and double switching frequency harmonics are sufficiently attenuated, resulting in a current THD as low as 3.3%, which is the lowest one among all the cases.

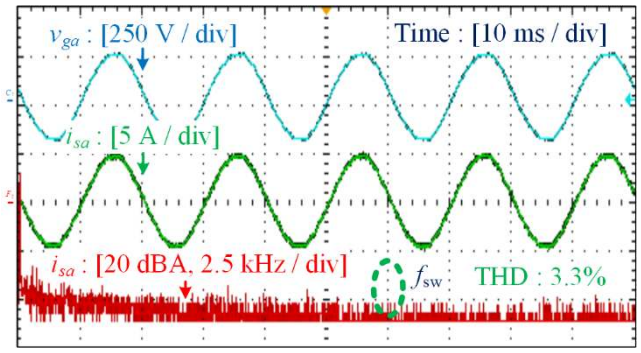

(a) Overall view

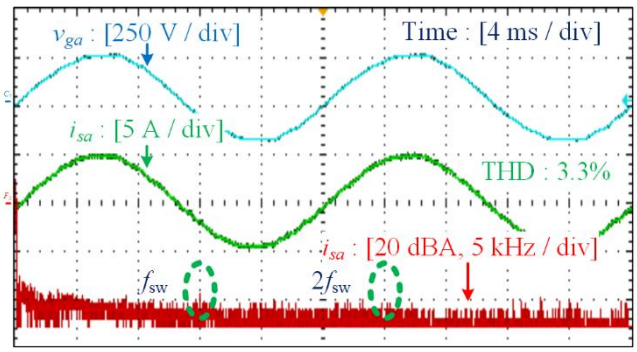

(b) Zoom-in view

Figure 3.21 Experimental waveforms of grid voltage v_{ga}, grid current i_{sa}, and spectrum of i_{sa} after compensation by the method II designed *SPRLCL*-filtered APF.

Figure 3.22 compares the filtering performances of *LLCL* and method III designed *SPRLCL* filters under parameter variations. With a 50% variation of L_f, the *LLCL* filter loses its strong attenuation at the switching frequency, as can be verified by the large current spike in Figure 3.22(a). In contrast, Figure 3.22(b) demonstrates that the method III designed *SPRLCL* filter maintains a high attenuation ability at f_{sw} regardless of parameter variations, thereby indicating the high robustness of *SPRLCL* filters. These experimental results are in good agreement with the theoretical analysis.

3.4 *LT-C-L* Filters

As discussed in the previous section, the *SPRLCL* filter allows strong

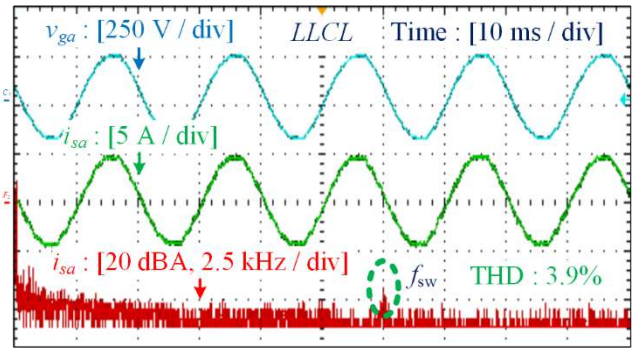

(a) *LLCL*-filtered APF with a 50% variation of L_{cf}

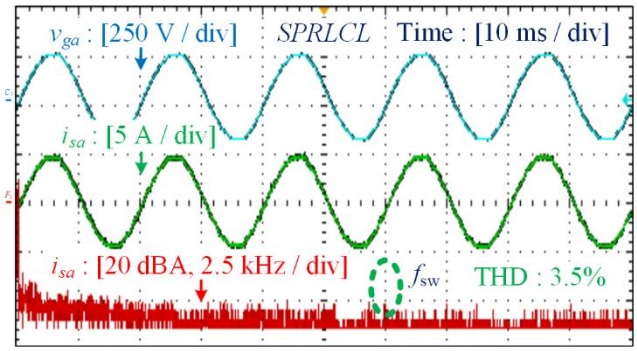

(b) Method III designed *SPRLCL*-filtered APF with a 50% variation of L_f

Figure 3.22 Experimental waveforms of the grid voltage v_{ga}, grid current i_{sa}, and spectrum of i_{sa} of (a) *LLCL*- and (b) method III designed *SPRLCL*-filtered APFs with 50% variations of L_f.

attenuation at both the switching frequency and double switching frequency. However, the *SPRLCL* filter features a complicated filter structure due to two additional *LC*-traps. Moreover, its high-frequency attenuation ability deteriorates as the frequency goes beyond the double switching frequency. Considering these drawbacks, it is desirable to employ the proposed *LT-C-L* filter, which features only one parallel-resonant *LC*-trap and strong attenuation in the high-frequency range as well as the flexibility of filter designs introduced by the magnetic integration technique. This section covers the principle of *LT-C-L* filters included the author's work [92, 94]. More advantages of *LT-C-L* filters will be revealed in the next section.

3.4.1 Fundamental Principle

Similar to the *SPRLCL* filter, the *LT-C-L* filter also contains a parallel-resonant *LC*-trap. The difference lies in that the *LC*-trap of the *LT-C-L* filter is located in

the converter-side rather than the grid-side. Besides the *LC*-trap, an *LCL* filter is included in the *LT-C-L* filter. In this regard, the *LT-C-L* filter can be deemed as a combination of an *LC*-trap and an *LCL* filter, as depicted in Figure 3.23, where L_{ct} and C_{ct} denote the trap inductance and capacitance, respectively.

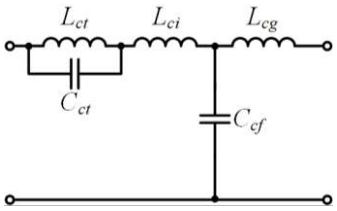

Figure 3.23 Schematic diagram of *LT-C-L* filters.

When the trap frequency is designed at the switching frequency f_{sw}, the *LC*-trap exhibits an infinite large impedance at f_{sw}. Therefore, the *LC*-trap will block the switching frequency harmonics and prevent such harmonics from entering the power grid. The plant model of *LT-C-L*-filtered power converters can be derived from Figure 3.23 as

$$G_{\text{plant\_LT-C-L}}(s) = \frac{a_2 s^2 + 1}{b_5 s^5 + b_3 s^3 + b_1 s}, \tag{3-20}$$

where the coefficients are given by

$$\begin{cases} a_2 = L_{ct} C_{ct} \\ b_5 = L_{ci} L_{cg} L_{ct} C_{cf} C_{ct} + L_{ci} L_s L_{ct} C_{cf} C_{ct} \\ b_3 = L_{ci} L_{cg} C_{cf} + L_{ci} L_s C_{cf} + L_{cg} L_{ct} C_{cf} \\ + L_s L_{ct} C_{cf} + L_{ci} L_{ct} C_{ct} + L_{cg} L_{ct} C_{ct} + L_s L_{ct} C_{ct} \\ b_1 = L_{ci} + L_{cg} + L_s + L_{ct}, \end{cases} \tag{3-21}$$

in which L_s denotes the grid inductance.

Once again, the expression of the trap frequency of *LT-C-L* filters can be easily obtained by setting the numerator of $G_{\text{plant\_L-TC-L}}(s)$ to zero:

$$\omega_{ct\_\text{LT-C-L}} = 2\pi f_{ct\_\text{LT-C-L}} = \sqrt{\frac{1}{L_{ct} C_{ct}}}, \tag{3-22}$$

where $\omega_{ct\_\text{LT-C-L}}$ and $f_{ct\_\text{LT-C-L}}$ stand for the trap angular frequency and trap frequency of *LT-C-L* filters, respectively. Moreover, the resonance frequencies of *LT-C-L* filters can be derived by letting the denominator of $G_{\text{plant\_LT-C-L}}(s)$ equal zero:

$$\omega_{cr1\_\text{LT-C-L}} = 2\pi f_{cr1\_\text{LT-C-L}} = \sqrt{\frac{b_3 - \sqrt{b_3^{\,2} - 4b_5 b_1}}{2b_5}}, \tag{3-23}$$

$$\omega_{cr2\_\text{LT-C-L}} = 2\pi f_{cr2\_\text{LT-C-L}} = \sqrt{\frac{b_3 + \sqrt{b_3^{\,2} - 4b_5 b_1}}{2b_5}}, \tag{3-24}$$

where $\omega_{cr1\_\text{LT-C-L}}$ and $f_{cr1\_\text{LT-C-L}}$ stand for the first or the dominant resonance angular frequency and resonance frequency, respectively, while $\omega_{cr2\_\text{LT-C-L}}$ and $f_{cr2\_\text{LT-C-L}}$ denote the second resonance angular frequency and resonance frequency, respectively.

Figure 3.24 plots the Bode diagrams of *LCL*- and *LT-C-L*-filtered power converter plant models. Obviously, the *LT-C-L* filter shows strong attenuation around the switching frequency f_{sw}. In addition, the high-frequency roll-off rates of *LCL* and *LT-C-L* filters are noted to be identical, and such a high roll-off rate clearly demonstrates the superior attenuation ability of the *LT-C-L*-filter. More comparisons will be given in the next section.

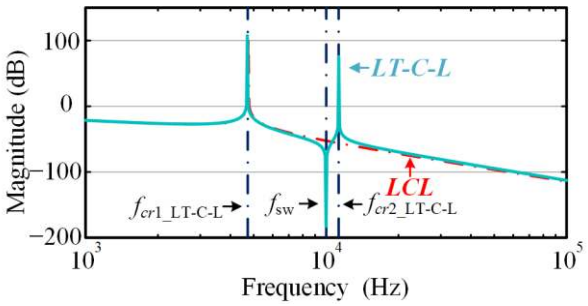

Figure 3.24 Bode diagrams of $G_{\text{plant\_LCL}}(s)$ and $G_{\text{plant\_LT-C-L}}(s)$.

It is obvious from Figure 3.24 that the first resonance frequency of the *LT-C-L*-filter $f_{cr1\_\text{LT-C-L}}$ and the resonance frequency of the *LCL* filter almost overlap. Therefore, $f_{cr1\_\text{LT-C-L}}$ can be approximated into

$$f_{cr1\_\text{LT-C-L}} \approx \frac{1}{2\pi}\sqrt{\frac{L_{ci} + L_{ct} + L_{cg} + L_s}{(L_{ci} + L_{ct})(L_{cg} + L_s)C_{cf}}}, \tag{3-25}$$

where $(L_{ci} + L_{ct})$ and $(L_{cg} + L_s)$ represent the total converter and grid inductances, respectively. The satisfaction of (3-25) is due to the relatively large impedance of the trap capacitor C_{ct} (which is considered to be an open circuit) at $f_{cr1\_\text{LT-C-L}}$. On the contrary, the small impedance of C_{cf} at the second resonance frequency

$f_{cr2\_LT\text{-}C\text{-}L}$ (which is considered to be a short circuit) implies that $f_{cr2\_LT\text{-}C\text{-}L}$ is determined by the converter-side branch loop through the following expression:

$$f_{cr2\_LT\text{-}C\text{-}L} \approx \frac{1}{2\pi}\sqrt{\frac{L_{ct}+L_{ci}}{L_{ct}L_{ci}C_{cf}}}. \tag{3-26}$$

3.4.2 Magnetic Integrated *LT-C-L* filters

As shown in Figure 3.24, the frequency response with regards to the *LT-C-L* filter features the second resonant peak. It is desirable if the frequency of this additional resonant peak can be flexibly designed, and thus avoiding the amplification of switching harmonics. Moreover, in addition to an *LCL* filter, the *LT-C-L* filter contains a trap inductor and a trap capacitor, which complicates the filter structure, and therefore it is preferable to reduce the number of filter components for simplicity. To achieve these objectives, this subsection explores the feasibility of the magnetic integrated *LT-C-L* filter, where the trap inductor and converter inductor are winded on a single magnetic core.

The EE magnetic core is employed as an example and shown schematically in Figure 3.25, where N_{ct} and i_{clt} denote the number of winding turns and the trap inductor current, respectively. The definitions of other notations can be found in Figure 3.5.

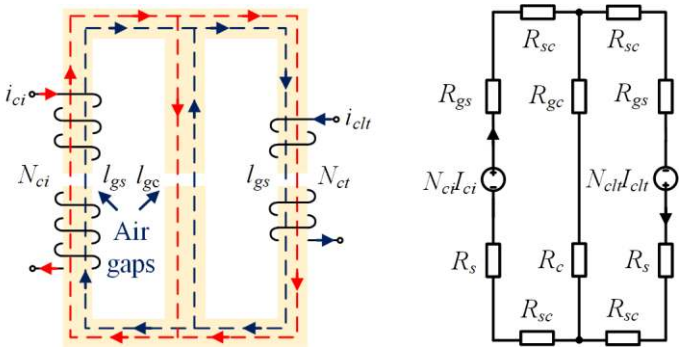

(a) Core structure (b) Equivalent magnetic circuit

Figure 3.25 (a) Core structure and (b) equivalent magnetic circuit of integrated *LT-C-L* filters.

Note that the windings in the right-hand side of Figure 3.5(a) and Figure 3.25(a) have different directions. That is, the trap inductor and converter inductor are coupled positively in the case of the integrated *LT-C-L* filter in Figure 3.25.

The magnetic circuit of integrated *LT-C-L* filters can be analyzed in a similar manner as that of integrated *LLCL* filters. Referring to Section 3.2.2, (3-5) − (3-9) still remain valid. Additionally, the trap inductance can be derived by replacing L_{cg} and N_{cg} with L_{ct} and N_{ct} as

$$L_{ct} = \frac{N_{ct}^{\ 2}}{R_{gg}} = \frac{N_{ct}^{\ 2}\mu_0 A_s (l_{gc}A_s + l_{gs}A_c)}{l_{gs}(2l_{gc}A_s + l_{gs}A_c)}, \tag{3-27}$$

where A_s and A_c stand for the cross-section areas of side limbs and central limb, respectively. Furthermore, replacing N_{cg} in (3-11) by N_{ct}, one obtains

$$M_{ti} = \frac{N_{ct}N_{ci}}{R_{gi}} = \frac{N_{ct}N_{ci}l_{gc}\mu_0 A_s^{\ 2}}{l_{gs}(2l_{gc}A_s + l_{gs}A_c)}, \tag{3-28}$$

where M_{ti} denotes the mutual inductance. The coupling coefficient k_M is defined as the ratio of M_{ti} to the square root of the self-inductance product ($L_{ct}L_{ci}$):

$$k_M = \frac{M_{ti}}{\sqrt{L_{ct}L_{ci}}} = \frac{l_{gc}A_s}{l_{gc}A_s + l_{gs}A_c}. \tag{3-29}$$

To examine the influence of the coupling on the filtering performance of integrated *LT-C-L* filters, the converter-side circuit diagrams are shown in Figure 3.26, where v_{inv} stands for the converter voltage, and i_{cct} and i_{clt} designate the currents following through the trap capacitor and inductor, respectively. The coupling is emulated by two additional current controlled voltage sources in the complex frequency domain, whose voltages are denoted as ($M_{ti}i_{ci}s$) and ($M_{ti}i_{clt}s$), respectively, as shown in Figure 3.26(b).

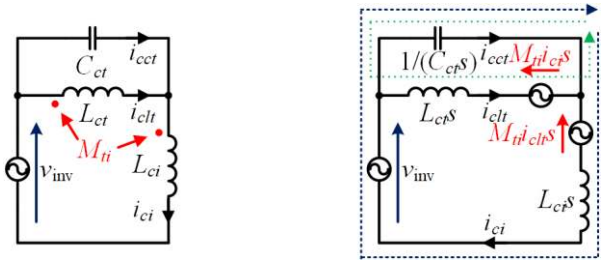

(a) Time-domain circuit (b) *s*-domain circuit

Figure 3.26 (a) Time-domain and (b) *s*-domain circuits of the converter-side branch loop of integrated *LT-C-L* filters.

Applying the KVL to the two loops depicted in Figure 3.26(b) and Kirchhoff's Current Law (KCL) to one of the two nodes in Figure 3.26(a), one obtains

$$\begin{cases} v_{\text{inv}}(s) = M_{ti} i_{clt}(s)s + L_{ci} i_{ci}(s)s + i_{cct}(s)/(C_{ct}s) \\ i_{cct}(s)/(C_{ct}s) = L_{ct} i_{clt}(s)s + M_{ti} i_{ci}(s)s \\ i_{ci}(s) = i_{clt}(s) + i_{cct}(s) \end{cases}. \tag{3-30}$$

Solving (3-30) for v_{inv} and i_{ci}, it gives

$$\frac{i_{ci}(s)}{v_{\text{inv}}(s)} = \frac{L_{ct}C_{ct}s^2 + 1}{(L_{ci}L_{ct} - M_{ti}^{\ 2})C_{ct}s^3 + (L_{ci} + L_{ct} + 2M_{ti})s}, \tag{3-31}$$

from which the relationship between v_{inv} and i_{ci} of the *LT-C-L* filters without the magnetic integration can be derived by letting $M_{ti} = 0$. With (3-31), the plant model of integrated *LT-C-L*-filtered power converters is further derived as

$$G_{\text{plant\_int\_LT-C-L}}(s) = \frac{a_2 s^2 + 1}{b_5 s^5 + b_3 s^3 + b_1 s}, \tag{3-32}$$

where the coefficients are expressed as

$$\begin{cases} a_2 = L_{ct}C_{ct} \\ b_5 = L_{ci}L_{cg}L_{ct}C_{ct}C_{cf} + L_{ci}L_sL_{ct}C_{ct}C_{cf} - L_{cg}M_{ti}^{\ 2}C_{ct}C_{cf} \\ b_3 = L_{ci}L_{cg}C_{cf} + L_{ci}L_sC_{cf} + L_{ci}L_{ct}C_{ct} + L_{cg}L_{ct}C_{cf} + L_{cg}L_{ct}C_{ct} \\ +2L_{cg}M_{ti}C_{cf} + L_sL_{ct}C_{cf} + L_sL_{ct}C_{ct} + 2L_{cs}M_{ti}C_{cf} - M_{ti}^{\ 2}C_{ct} \\ b_1 = L_{ci} + L_{cg} + L_s + L_{ct} + 2M_{ti}. \end{cases} \tag{3-33}$$

It is noted from the numerator of (3-32) that the trap frequencies of integrated *LT-C-L* and conventional *LT-C-L* filters are the same, which is expressed in (3-22). However, the second resonance frequency of *LT-C-L* filters can be shifted through the magnetic integration technique, as indicated by the denominator coefficients in (3-32). Under the assumption that the second resonance frequency $f_{cr2\_\text{int\_LT-C-L}}$ of integrated *LT-C-L* filters is determined by the converter-side branch loop, it is then feasible to derive $f_{cr2\_\text{int\_LT-C-L}}$ by setting the denominator of (3-31) to be zero as

$$f_{cr2\_\text{int\_LT-C-L}} \approx \frac{1}{2\pi}\sqrt{\frac{L_{ci} + L_{ct} + 2M_{ti}}{(L_{ci}L_{ct} - M_{ti}^{\ 2})C_{ct}}}. \tag{3-34}$$

According to (3-34), with the increase of M_{ti}, the second resonance frequency $f_{cr2\_\text{int\_LT-C-L}}$ will also increase, because the numerator of the expression inside the square root operation is positively proportional to M_{ti}, while the denominator is

negatively related to M_{ti}. In this regard, $f_{cr2\_int\_LT\text{-}C\text{-}L}$ can be flexibly designed through the change of M_{ti}, or equivalently, by tuning the coupling coefficient k_M. The Bode diagrams of $G_{plant\_int\_LT\text{-}C\text{-}L}(s)$ as a function of k_M are plotted in Figure 3.27, where the case of $k_M = 0.3$ gives rise to $f_{cr2\_int\_LT\text{-}C\text{-}L} \approx 1.5 f_{sw}$, and this case is desirable as it avoids the amplification of switching harmonics. Notice that the resonant peaks are well damped by the series *RC* damper, and this part will be detailed in the next section. Considering that $A_c = 2A_s$, the ratio of air gap lengths l_{gc} and l_{gs} can be designed as 1 according to (3-29), which yields a k_M of 0.33. The reason for designing (l_{gc} / l_{gs}) as 1 is to facilitate the core design, because the additional I cores for the adjustments of air gaps are no longer necessary in this case. Moreover, it is obvious that integrated *LT-C-L* filters remain their strong attenuation at f_{sw}, which agrees with (3-31).

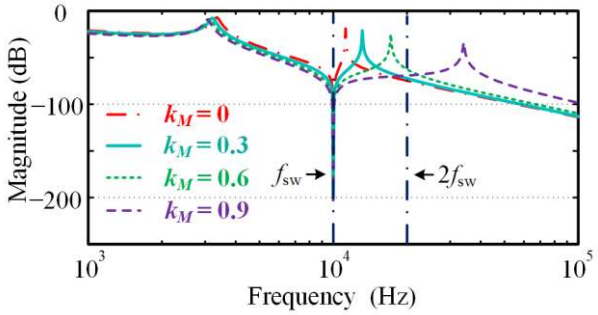

Figure 3.27 Bode diagrams of $G_{plant\_int\_LT\text{-}C\text{-}L}(s)$ as a function of the coupling coefficient k_M.

The design procedure of *LT-C-L* filters basically follows that of *LCL* and *LLCL* filters [57, 61, 94]. According to the system parameters given in Table 3-5, the filters are designed with their parameters tabulated in Table 3-6.

Once again, Litz wires with low ESRs were utilized as inductor windings to reduce the power losses of inductors. For the integrated inductor, its magnetic core is mainly selected according to the A_p requirement of L_{ci}, as L_{ci} is much greater than L_{ct}. Substitution of $S_{cw} = 0.5\ \pi$ mm^2, $L_{ci} = 1$ mH, $I_{ci\_max} = 15$ A, $K_{cu} = 0.5$, and $B_{c\_max} = 0.3$ T into (3-13), the required area product A_p can be calculated as 1.56×10^{-7} m^4. Referring to the product list of TDK [90], one pair of E cores (EE 70/33/32) featuring an area product of 1.92×10^{-7} m^4 is selected.

Table 3-5 System parameters for testing the *LT-C-L* filter.

Description	Symbol	Value
DC-link capacitance	C_{cdc}	940 μF
DC-link voltage reference	V_{cdc_ref}	200 V
DC-link resistance	R_{cdc}	80 Ω
Grid voltage reference (rms)	V_{g_ref}	110 V
Active power reference	P_{c_ref}	500 W
Fundamental frequency	f_{ref}	50 Hz
Switching/sampling frequency	f_{sw}/f_s	10 kHz

Table 3-6 Filter parameters for testing the *LT-C-L* filter.

Symbol	Values of *LCL* filter	Values of *LT-C-L* filter
L_{ci} (mH)	1.25	1.0
C_{cf} (μF)	2.5	2.5
L_{cg} (mH)	0.7	0.7
L_{ct} (mH)	–	0.25
C_{ct} (μF)	–	1.0
k_M	–	1/3

3.4.3 Experimental Verification

The experiments regarding the *LT-C-L* filter were carried out in this subsection. Figure 3.28 provides the experimental results of a conventional *LCL*-filtered power converter, where the spectrum of i_{cga} is highlighted in Figure 3.28(b). As observed, the large current spike around the switching frequency f_{sw} obviously violates the 0.3% fundamental current requirement. In addition, the THD of the grid-injected current i_{cga} is found to be 2.71%. Note that the waveform of the converter current i_{cia} is also given in Figure 3.28, which will be further analyzed in the next section.

After the *LCL* filter is replaced by the *LT-C-L* filter, the switching frequency harmonics around f_{sw} can be greatly attenuated, as evidenced by the experimental results of the *LT-C-L* filter shown in Figure 3.29, where v_{ct} denotes the voltage

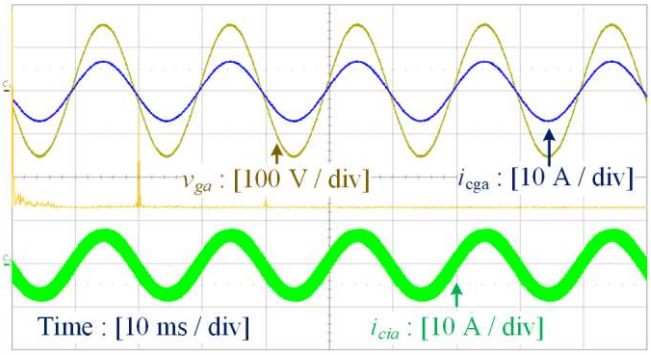

(a) Waveforms

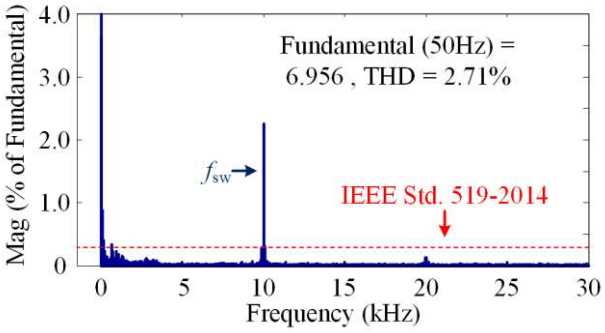

(b) Spectrum of i_{cga}

Figure 3.28 Experimental (a) waveforms and (b) spectrum of i_{cga} of the *LCL*-filtered power converter.

across the trap inductor and trap capacitor. As noted, v_{ct} registers a large amplitude, which can be as high as the DC-link voltage (200 V), and therefore the trap capacitor should be designed with a high-voltage capability. Since the harmonics around f_{sw} are almost removed, the THD of i_{cga} decreases to 1.26%, indicating the superior filtering performance of *LT-C-L* filters. It should be commented that the efficiency of *LT-C-L*-filtered power converters is similar to that of *LCL*-filtered power converters [94].

3.5 State of the Art Passive Power Filters

With the proposals of several advanced passive power filters in recent years, it is of importance to summarize the state of the art passive filters and benchmark them. To this end, this section gives a comprehensive review of the newly materialized passive filters and compares them in terms of filter topologies,

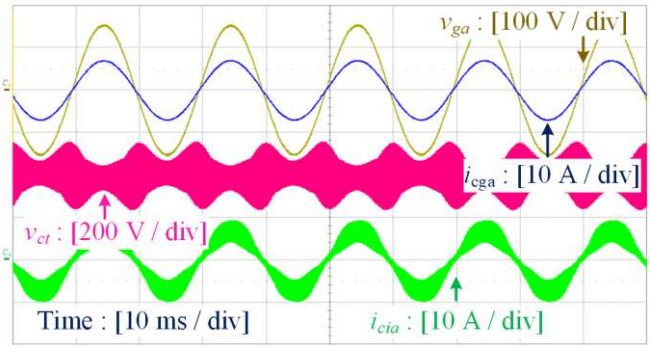

(a) Waveforms

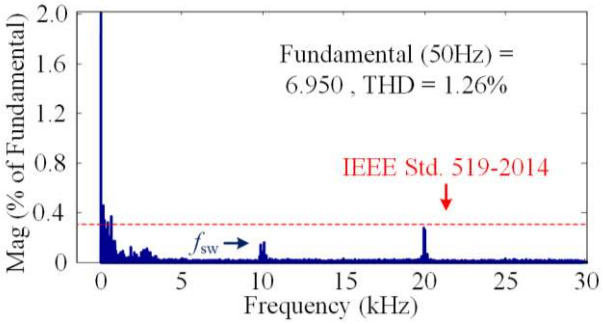

(b) Spectrum of i_{cga}

Figure 3.29 Experimental (a) waveforms and (b) spectrum of i_{cga} of the *LT-C-L*-filtered power converter.

filtering performances, and their robustness. It is concluded that the *LT-C-L* filter can be the most promising trap filter from the comparison results.

3.5.1 Filter Topologies

Figure 3.30 illustrates the topologies of state of the art passive power filters, where the grid impedance is not shown here for simplicity, and its effect will be considered wherever necessary. It is identified that all the passive filters are composed of filter inductors and capacitors. Figure 3.30(a) demonstrates the well-known third-order *LCL* filter, where two filter inductors and one filter capacitor are incorporated. Except for the *LCL* filter, the other passive filters in Figure 3.30 contain *LC*-traps, i.e. series-resonant and/or parallel-resonant *LC*-traps.

As the simplest trap filter, the series *LC*-trap alone forms a series *LC* filter, as depicted in Figure 3.30(b). This filter is mainly used in replacement of the

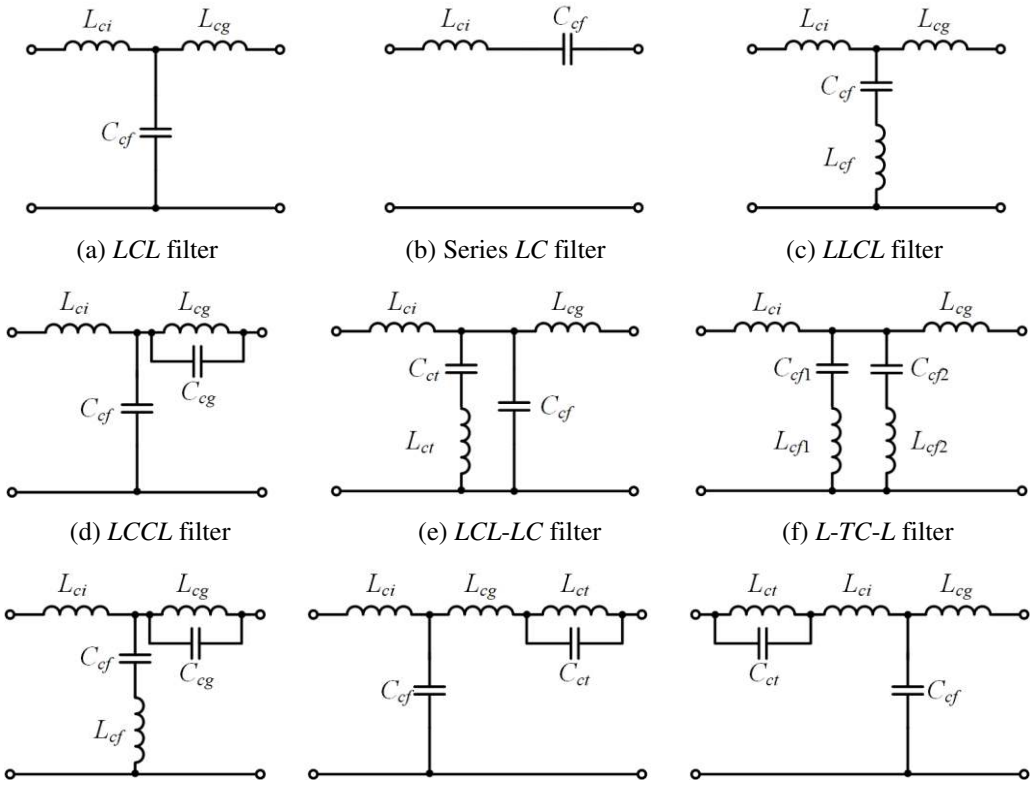

(a) *LCL* filter (b) Series *LC* filter (c) *LLCL* filter

(d) *LCCL* filter (e) *LCL-LC* filter (f) *L-TC-L* filter

(g) *SPRLCL* filter (h) *L-C-TL* filter (i) *LT-C-L* filter

Figure 3.30 Schematic diagrams of state of the art passive filters.

conventional *L* filter for DSTATCOM and APF applications, where the large voltage drop across the trap capacitor is out of phase with the grid voltage, and thus reducing the voltage and power ratings of power converters [95, 96]. To introduce a sufficiently large voltage drop, the capacitance C_{cf} should be large enough. Accordingly, a relatively low trap frequency, e.g. the 7th harmonic frequency in [96], is to be expected. As a result, the series *LC* filter only provides moderate attenuation to switching harmonics. Moreover, as the trap frequency is located within the control bandwidth, the employment of series *LC* filters makes the controller design very challenging [97].

Figure 3.30(c) presents the topology of *LLCL* filters [57]. As mentioned earlier, the *LLCL* filter features a trap characteristic at the switching frequency by inserting an additional small trap inductor into the filter capacitor branch loop of the *LCL* filter [98, 99]. It allows a significant reduction of filter inductances [57].

According to the duality relationship between series resonance and parallel

resonance, a small trap capacitor can be added in parallel and resonated with the grid-side inductor of an *LCL* filter, forming the *LCCL* filter, as presented in Figure 3.30(d). Since the trap capacitor is usually smaller and cheaper than the trap inductor, *LCCL* filters are more cost-effective than *LLCL* filters [93]. Additionally, it is noted from Figure 3.4 that the *LLCL* filter exhibits poor attenuation in the high frequency range. In contrast, the *LCCL* filter performs strong attenuation at high frequencies as well as the *LCL* filter if the grid inductance is taken into consideration under weak grid conditions, and this is a further advantage of *LCCL* filters [93].

To improve the high-frequency attenuation ability of *LLCL* filters, an extra capacitor can be further involved in an *LLCL* filter to construct the *LCL-LC* filter, as depicted in Figure 3.30(e) [100, 101]. Also, the *LCL-LC* filter can be interpreted as a combination of an *LCL* filter and a series *LC*-trap. This filter is of great interest and will be further analyzed in the following subsections.

As mentioned before, the *L-TC-L* filter contains more than one series *LC*-traps, as duplicated in Figure 3.30(f) [83, 88, 102, 103]. These traps are often tuned at the switching frequency and its multiples for trapping of harmonics. Despite performing excellent attenuation around trap frequencies, the *L-TC-L* filter is very complicated even with only two *LC*-traps, not to mention the inclusion of an addition filter capacitor just as that in *LCL-LC* filters, which is capable of improving attenuation in the high-frequency range [83].

Combining the series-resonant *LC*-trap of *LLCL* filters and parallel-resonant *LC*-trap of *LCCL* filters, together with the converter-side inductor, one can obtain the *SPRLCL* filter, as has been illustrated in Figure 3.30(g) and detailed in Section 3.3 [61]. It should be remembered that the *SPRLCL* filter saves one trap inductor as compared with the *L-TC-L* filter. However, the *SPRLCL* filter also suffers from poor attenuation at frequencies above the double switching frequency.

Figure 3.30(h) shows the schematic diagram of *L-C-TL* filters, which can be interpreted as a combination of an *LCL* filter and a parallel *LC*-trap in the grid-side [104, 105]. In terms of filter topologies, the *L-C-TL* filter is the same as the

LCCL filter with an inductive grid impedance. Therefore, the *L-C-TL* filter also possesses a high attenuation ability in the high-frequency range.

Once the parallel *LC*-trap of *L-C-TL* filters is shifted from the grid-side to the converter-side, it is possible to derive the *LT-C-L* filter, as shown in Figure 3.30(i) [94]. Referring back to Figure 3.24, the *LT-C-L* filter is observed to exhibit strong attenuation in the high-frequency band as well as the trapping characteristic at the switching frequency.

Among all state of the art passive filters given in Figure 3.30, the series *LC* filter having only two filter components is the simplest one. However, the series *LC* filter is application specific, which deters its widespread adoptions. In contrast, the *LCL* filter containing three filter components eclipses the single inductor *L* filter in many applications, and it is still an area of ongoing research, but it performs no harmonic trapping at the switching frequency. As fourth-order filters, the *LLCL* and *LCCL* filters incorporate their respective *LC*-traps, and hence featuring very strong attenuation around the switching frequency. The *LCL-LC*, *L-C-TL*, and *LT-C-L* filters are fifth-order filters evolved from the *LLCL* and *LCCL* filters for better high-frequency harmonic attenuation. The *SPRLCL* and *L-TC-L* filters contain at least two *LC*-traps, leading to complicated filter structures, and the respective filter orders are more than five and six, respectively. Because of their complexity, they will no longer be the research focus in the following analysis. In addition, the series *LC* filter in Figure 3.30(b) will not be further analyzed due to its narrow applications and poor high-frequency attenuation.

3.5.2 Filtering Performances

One important criterion to evaluate passive filters is the high-frequency attenuation ability. The modulation of power converters generates voltage harmonics, and these voltage harmonics seen by individual filters are the same as long as the modulation method and converter topology remain unchanged. However, the switching harmonics in the grid-injected currents of the power

converters filtered by different passive filters will differ, which depend on the attenuation ability of each filter, as determined by their plant models $G_{plant}(s)$.

Figure 3.31 draws the Bode diagrams of $G_{plant}(s)$ of the passive filters in Figure 3.30 except for the series *LC* filter, *SPRLCL* filter, and *L-TC-L* filter, whose total inductance and capacitance are designed to be identical. One important criterion of passive filters refers to the high-frequency attenuation ability. It is determined by the high-frequency roll-off rate, which can be further derived from the difference between the degrees of filter plant numerator and denominator. For instance, the degrees of the numerator and denominator of $G_{plant\_LCL}(s)$ are 0 and 3, respectively, as can be obtained from (2-30). Therefore, the high-frequency roll-off rate of *LCL* filters is calculated to be $(0 - 3) \times 20 = -60$ dB/dec (decade), which is in consistence with Figure 3.31.

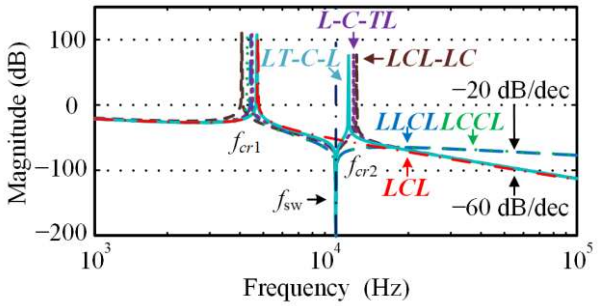

Figure 3.31 Bode diagrams of $G_{plant}(s)$ of power converters with state of the art passive filters.

Similarly, it is derived that the roll-off rate of single inductor *L* filters is −20 dB/dec. The derivation applies equally well to other passive filters. It is noted from Figure 3.31 that *LLCL* and *LCCL* filters have the same high-frequency roll-off rate (i.e. −20 dB/dec) as that of *L* filters. However, it should be emphasized that the *LCCL* filter also exhibits a −60 dB/dec roll-off rate under inductive grid impedance scenarios [93]. In comparison, the *LCL-LC* filter, *L-C-TL* filter, and *LT-C-L* filter feature a −60 dB/dec roll-off rate as that of *LCL* filters, indicating their superior filtering performances. Note that new resonant peaks appear when power converters are filtered by these three passive filters. Additionally, despite not shown in Figure 3.31, the roll-off rates of series *LC* filter, *SPRLCL* filter, and *L-TC-L* filter are calculated as −20 dB/dec [94]. From the above analysis, the

LCL-LC filter, *L-C-TL* filter, and *LT-C-L* filter are desirable in terms of high-frequency attenuation, and therefore they will be analyzed henceforth.

As stated, the prime criterion for evaluating the attenuation ability of passive filters is the content of switching harmonics in the grid current. Nevertheless, converter current harmonics may also be used to evaluate the filtering performance, as a low converter current THD often translates into low converter power losses and/or small current ripples.

Figure 3.32 presents the Bode diagrams of the transfer functions from the converter voltage to the converter current of *LCL-LC* filter, *L-C-TL* filter, and *LT-C-L* filter, where the filter parameters are formulated in Table 3-7.

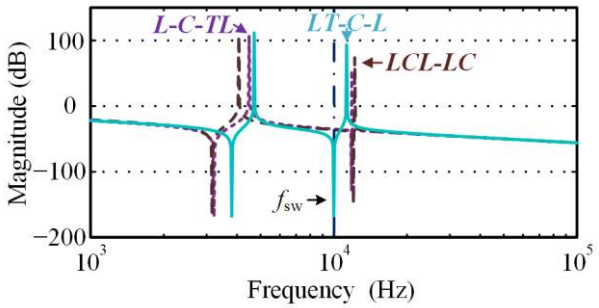

Figure 3.32 Bode diagrams of the transfer functions from the converter voltage to the converter current of *LCL-LC*-, *L-C-TL*-, and *LT-C-L*-filtered power converters.

Table 3-7 Filter parameters of state of the art trap filters.

Symbol	Values of *LCL-LC* filter	Values of *L-C-TL* filter	Values of *LT-C-L* filter
L_{ci} (mH)	1.0	1.0	1.0
C_{cf} (μF)	2.5	2.5	2.5
L_{cg} (mH)	0.7	0.7	0.7
L_{ct} (mH)	0.25	0.25	0.25
C_{ct} (μF)	1.0	1.0	1.0
C_{cd} (μF)	2.5	2.5	2.5
R_{cd} (Ω)	1.0	1.0	1.0

It is clear that only the *LT-C-L* filter performs strong attenuation to converter current harmonics around the switching frequency f_{sw}. This can be understandable, as the parallel *LC*-trap of *LT-C-L* filters can prevent the

switching frequency harmonics from following through the converter branch loop. In contrast, the *LCL-LC* filter bypasses the switching frequency harmonics from the converter branch loop to the series *LC*-trap and prevents them from being injected into the power grid, and therefore the converter current still contains considerable harmonics. Similarly, the *L-C-TL* filter employs a parallel *LC*-trap to block the switching frequency harmonics from entering the grid, and hence the harmonics also exist in the converter current. Due to the salient trap feature of *LT-C-L* filters at f_{sw} in Figure 3.32, the relevant converter current THD can be significantly reduced, as will be validated later.

3.5.3 Filter Robustness

The filtering performances of passive filters may be greatly influenced by grid conditions. In the above analysis, it is assumed that the power grid is stiff and modelled to be an ideal voltage source. However, such an assumption is no longer valid under weak grid conditions, where the short circuit ratio is relatively small, and the grid impedance may vary in a wide range [106]. To yield the worst stability case, the power grid can be simplified into a series connection of an ideal voltage source and a grid inductor. Furthermore, when multiple power converters are operated in parallel for power sharing, the equivalent grid inductance seen by individual power converters will be in proportional to the number of power converters. That is, the effect of the grid impedance will be magnified as the number of power converters increases [107, 108].

Figure 3.33 illustrates the Bode diagrams of $G_{plant}(s)$ of *LCL-LC*-, *L-C-TL*-, and *LT-C-L*-filtered power converters under a weak power grid featuring a grid inductance L_s of 3 mH. As compared with Figure 3.31, Figure 3.33 demonstrates that the second resonance frequencies in the cases of *LCL-LC* filter and *LT-C-L* filter remain almost unchanged. In contrast, the shifted second resonant peak of the *L-C-TL* filter may be triggered by the switching frequency harmonics. The reason for such differences is essentially about the locations of *LC*-traps. As the *LC*-trap of the *L-C-TL* filter appears in the grid-side, it will unavoidably be

affected by the grid inductance. The opposite is true for the other two filters. In this sense, it can be concluded that the *L-C-TL* filter is sensitive to grid impedance variations.

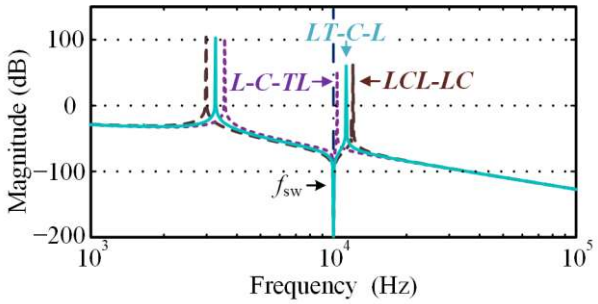

Figure 3.33 Bode diagrams of $G_{plant\_LCL\text{-}LC}(s)$, $G_{plant\_L\text{-}C\text{-}TL}(s)$, and $G_{plant\_LT\text{-}C\text{-}L}(s)$ under a weak grid with L_s = 3 mH.

For the Bode diagrams of $G_{plant}(s)$ analyzed previously, the magnitudes of resonant peaks are far greater than 0 dB. If the phases of $G_{plant}(s)$ around the resonance frequencies range from $-(2n + 1) \times 180^\circ$ to $-(2n - 1) \times 180^\circ$, where n is a positive integer, negative phase margins will be expected. For minimum-phase systems, negative phase margins will make the current control unstable [24]. To avoid the potential instability issue, the resonant peaks should be well damped either passively, i.e. through physical resistors and other passive components, or actively – through control algorithms emulating physical resistors and/or other passive dampers.

Although the active damping technique gets rid of the power losses associated with passive dampers, they may only stabilize the system in specific frequency regions, beyond which the damping effect is no longer valid or optimal [23, 52, 109-112]. Moreover, active damping normally necessitates extra voltage/current sensors, which bring in additional costs and complexity [113-117]. Although the active damping without any sensors is feasible, it is achieved at the expense of increased system complexity and sensitivity [118].

Instead, the passive damping technique can be realized simply and reliably at the expense of a small fraction of power losses [98, 99, 119-122]. Ideally, the passive damping technique should only damp resonant peaks without changing the magnitude or phase responses of $G_{plant}(s)$ at other frequencies. This can be

done in an easy way by paralleling a damping resistor with the filter capacitor branch loop. However, the power loss introduced by the damping resistor is intolerable.

Alternatively, a capacitor can be added in series with the damping resistor to form a series *RC* damper, which performs satisfactory damping to resonant peaks with negligible power losses [122, 123]. Due to the effectiveness and simplicity of series *RC* dampers, they are increasingly being adopted in the literature and employed in this section [84, 94, 123]. By following the design process proposed in [123], the parameters of series *RC* dampers are designed to be $C_{cd} = C_{cf} = 2.5$ μF and $R_{cd} = 1.0$ Ω, where C_{cd} and R_{cd} represent the damping capacitor and resistor, respectively. Taking series *RC* dampers into consideration, one can replot the Bode diagrams of $G_{\text{plant}}(s)$ of *LCL-LC*- and *LT-C-L*-filtered power converters in Figure 3.34.

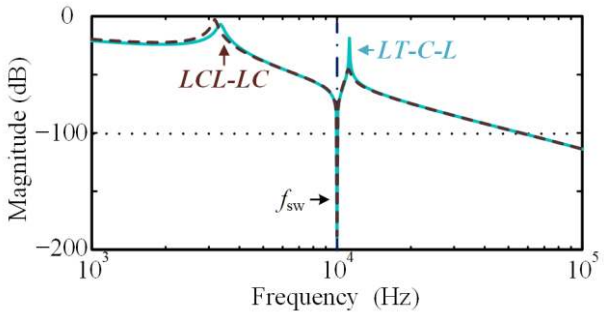

Figure 3.34 Bode diagrams of $G_{\text{plant\_LCL-LC}}(s)$ and $G_{\text{plant\_LT-C-L}}(s)$ with series *RC* dampers.

Noticeably, the resonant peaks of both filters are effectively attenuated below 0 dB. As compared with Figure 3.31, Figure 3.34 shows that the second resonance frequency of *LT-C-L* filters hardly varies, while that concerning *LCL-LC* filters dramatically reduces. Hence, the *LT-C-L* filter performs better robustness than the *LCL-LC* filter against the *RC* damper in terms of resonance frequency drifts. The reason is that the parallel *LC*-trap of *LT-C-L* filters is in the converter-side, while the series *LC*-trap of *LCL-LC* filters is directly paralleled with the *RC* damper. Since the *RC* damper may shift the second resonance frequency of *LCL-LC* filters, the design of filter elements and damper becomes intertwined and inflexible [100]. In contrast, the *LT-C-L* filter greatly simplifies

the design of the second resonance frequency, particularly when the magnetic integration technique is involved.

From the above analysis, the *LT-C-L* filter exhibits high robustness against the grid impedance and passive damper. However, its attenuation around the switching frequency may compromise if the parameters of the parallel *LC*-trap are inaccurate. For demonstration, Figure 3.35 displays the Bode diagrams of $G_{\text{plant\_ LT-C-L}}(s)$ with the ±40% variations of the trap inductance L_{ct}. Notice that a 40% change of L_{ct} will greatly deteriorate the harmonic trapping characteristic of *LT-C-L* filters at f_{sw} or even tend to magnify the switching frequency harmonics due to the overlap of the second resonance frequency and f_{sw}. The high sensitivity to *LC*-trap components may also cause troubles for other trap filters. One exception is the *SPRLCL* filter designed with method III, which can be robust to trap inductors and capacitors, as has been detailed in Section 3.3.

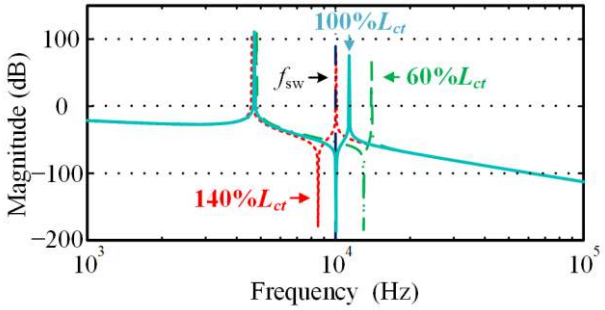

Figure 3.35 Bode diagrams of $G_{\text{plant\_LT-C-L}}(s)$ with the ±40% variations of the trap inductance L_{ct}.

3.5.4 Experimental Verification

This subsection aims to experimentally benchmark the state of the art passive filters based on the filter parameters given in Table 3-7. Figure 3.36 illustrates the experimental spectra of the converter currents i_{cia} of *LCL-LC* and *LT-C-L*-filtered power converters under a stiff power grid. As compared with the *LCL-LC* filter, the *LT-C-L* filter performs much better attenuation around the switching frequency f_{sw}. As a result, the converter current THD is dramatically reduced from 38.09% to 21.18%, thereby validating the excellent filtering performance of *LT-C-L* filters.

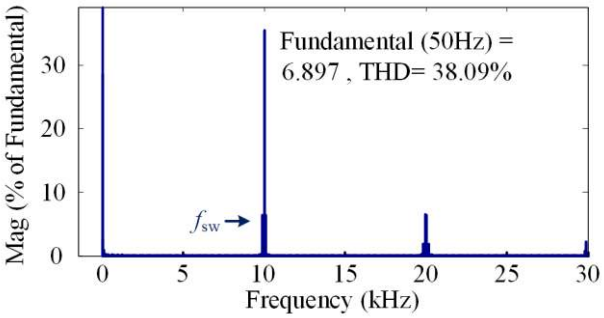

(a) *LCL-LC* filter

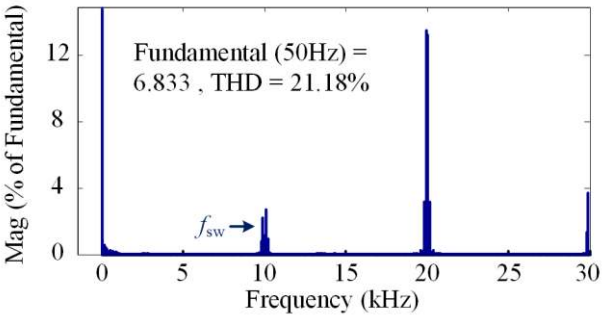

(b) *LT-C-L* filter

Figure 3.36 Experimental spectra of i_{cia} of (a) *LCL-LC*- and (b) *LT-C-L*-filtered power converters.

Referring back to Figure 3.33, the second resonance frequency of *L-C-TL* filters is shifted towards the switching frequency under a weak grid condition, and this may further magnify the switching frequency harmonics. To illustrate this point, the experimental spectra of the converter current i_{cia} and grid current i_{cga} of *L-C-TL*- and *LT-C-L*-filtered power converters under a weak grid condition are given in Figure 3.37 and Figure 3.38, respectively. As correctly predicted by the theoretical analysis, a large current spike in the case of the *L-C-TL* filter is noted to appear around f_{sw}. Due to its significantly large magnitude, the current spike of i_{cia} cannot be successfully blocked by the parallel *LC*-trap of the *L-C-TL* filter in the grid-side, leading to an observable current spike in the spectrum of i_{cga}, as noticed from Figure 3.38(a). The current spike of i_{cga} obviously violates the grid code requirement. In contrast, the *LT-C-L* filter performs high robustness against the grid impedance. Under the same weak grid condition, the *LT-C-L* filter maintains its strong attenuation at f_{sw}. As a result, both the converter and

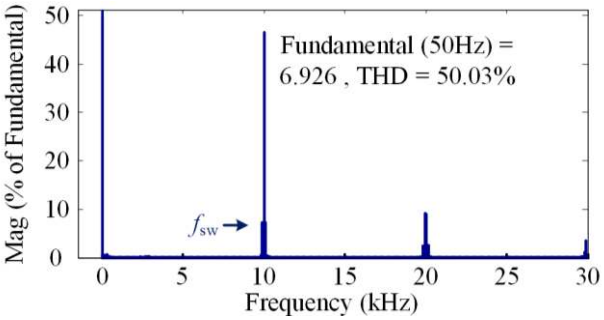

(a) *L-C-TL* filter

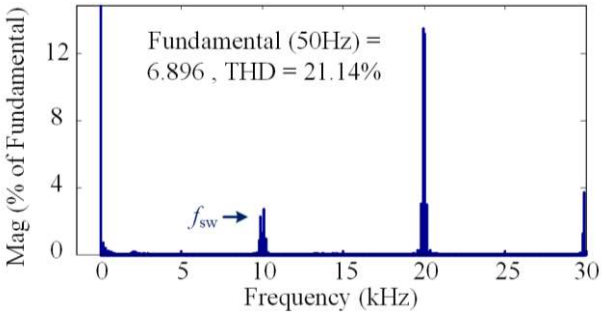

(b) *LT-C-L* filter

Figure 3.37 Experimental spectra of i_{cia} of (a) *L-C-TL*- and (b) *LT-C-L*-filtered power converters under a weak grid with L_s = 3 mH.

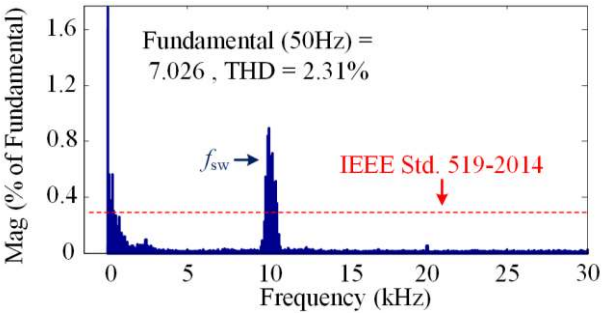

(a) *L-C-TL* filter

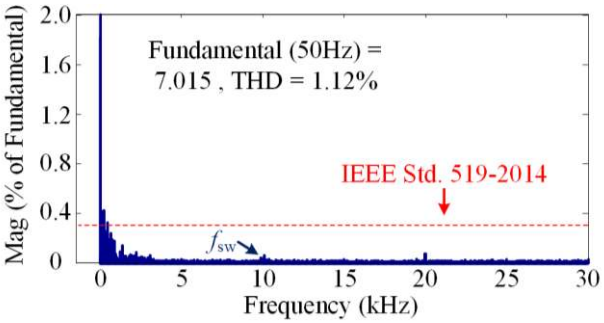

(b) *LT-C-L* filter

Figure 3.38 Experimental spectra of i_{cga} of (a) *L-C-TL*- and (b) *LT-C-L*-filtered power converters under a weak grid with L_s = 3 mH.

grid current THDs are reduced due to the increased attenuation contributed by the grid inductance. These experimental results are in alignment with the analysis provided in this section.

Table 3-8 summarizes the main characteristics of state of the art passive filters, where the "roll-off rates" column refers to the stiff grid condition. Additionally, the robustness of trap filters only concerns about the influence of grid impedances on switching harmonic trapping characteristics. From the experimental results and theoretical analysis, it can be safely concluded that the *LT-C-L* filter is the most promising trap filter in terms of filter topology, filtering performance, and robustness.

Table 3-8 Main characteristics of state of the art passive power filters.

Filter types	Additional components	Filter orders	Trap frequencies	Roll-off rates (dB/dec)	Robustness against L_s
LCL	−	3	−	−60	−
Series *LC*	−	2	7^{th} harmonic	−20	N
LLCL	Trap inductor	4	f_{sw}	−20	Y
LCCL	Trap capacitor	4	f_{sw}	−20	Y
LCL-LC	*LC*-trap	5	f_{sw}	−60	Y
L-TC-L	*LC*-traps	≥ 6	f_{sw}, $2f_{sw}$, …	−20	Y
SPRLCL	Trap inductor and capacitor	≥ 5	f_{sw} and $2f_{sw}$	−20	Y
L-C-TL	*LC*-trap	5	f_{sw}	−60	N
LT-C-L	*LC*-trap	5	f_{sw}	−60	Y

3.6 Summary

This chapter has introduced several advanced passive power filters to resolve the ever-challenging harmonic issue in more-electronics power systems. As compared with the well-known *LCL* filter, these advanced passive filters feature additional series- and/or parallel-resonant *LC*-traps, better harmonic attenuation abilities, smaller filter sizes, and lower costs. To be specific, the magnetic integrated *LLCL* filter can be implemented by a properly designed integrated *LCL* filter without the inclusion of any trap inductor. Therefore, the magnetic

integrated *LLCL* filter yields both the benefits of strong attenuation and high-power density. As the *SPRLCL* filter contains a series-resonant *LC*-trap and a parallel-resonant *LC*-trap, it can be flexibly designed to either simultaneously trap the switching frequency and double switching frequency harmonics or exhibit high robustness against filter parameter variations. The *LT-C-L* filter consists of an *LCL* filter and a parallel-resonant *LC*-trap in the converter-side. Through the comprehensive comparisons of state of the art passive filters, the *LT-C-L* filter is concluded to be the most promising trap filter in terms of filter topology, filtering performance, and robustness.

Chapter 4 Converter-Level Stability Improvement through Impedance Reshaping of Power Converters

This chapter first introduces the background of converter-level instability issues, accompanied by their cutting-edge solutions, in more-electronics power systems. Specifically, improper controller designs, time-delays, resonances arising from high-order passive filters, interactions among multiple power converters, and weak grids could be responsible for converter-level instability issues. This is continued by the exploration of one specific instability issue, namely the instability issue due to PLLs under weak grids. After analysing the effect of PLLs on the current control of power converters, this chapter reveals the relevant instability issue. The instability is caused by the inclusion of PLLs that shapes the *q*-axis converter impedance as a negative resistance in the low-frequency band. To tackle the instability issue, a simple yet effective impedance controller directly relating the *q*-axis voltage to the *q*-axis current reference is further proposed. It reshapes the *q*-axis converter impedance as a positive resistance in the low-frequency band, thereby addressing the instability issue due to PLLs. Finally, a summary providing concluding remarks is given.

4.1 Background and Introduction

Stable operations are of high priority in more-electronics power systems. In general, instability issues can be categorized into converter-level and system-level instability issues. The converter-level instability refers to the unstable operations of specific power converters. Once the problematic power converters are removed from more-electronics power systems, the instability will disappear. In contrast, the system-level instability corresponds to the large-scale instability in the whole power system. It is characterized by excessive frequency and/or voltage deviations, which are simultaneously experienced by a large amount of equipment and devices. Since the converter-level instability, without being properly and promptly treated, may develop into the system-level instability, this

chapter first investigates the converter-level instability, while the system-level instability will be explored in the next chapter.

4.1.1 Sources of Instability Issues

Table 4-1 presents a classification of the instability sources in more-electronics power systems, where the instability sources fall into the sub-fundamental ($< f_{ref}$), near fundamental ($\approx f_{ref}$), fundamental to switching ($>> f_{ref}$ and $<< f_{sw}$), and around and beyond switching frequency ranges ($\geq f_{sw}$) in terms of the time-scale. It is known that different controls feature different control bandwidths and time-scales. Moreover, instability issues can be caused by different controls (e.g. current control or voltage control). Therefore, instability issues are claimed to occur on different time-scales [124]. Note that the system-level instability due to the improper control of frequency/active power and voltage/reactive power is mainly located in the sub-fundamental frequency range. In contrast, the converter-level instability can be found in the entire frequency range covering from below f_{ref} to above f_{sw}.

Table 4-1 Classification of the instability sources in more-electronics power systems.

Frequency ranges (fundamental/switching frequency f_{ref}/f_{sw})	Instability sources
$< f_{ref}$	Frequency/active power control, voltage/reactive power control, DC-link voltage control, AC voltage control, grid synchronization (PLLs), time-delays, converter interactions, weak grids
$\approx f_{ref}$	DC-link voltage control, AC voltage control, grid synchronization (PLLs), time-delays, converter interactions, weak grids
$>> f_{ref}$ and $<< f_{sw}$	AC current control, time-delays, filter resonances, converter interactions, weak grids
$\geq f_{sw}$	PWM generators, filter resonances

The converter-level instability can be caused by improper controller designs (including the DC-link voltage control, AC voltage control, PLL control, AC current control, and PWM generators [125-130]), time-delays, resonances arising from high-order passive filters, interactions among multiple power converters, and weak grids [94, 106-108, 131-135]. These factors often interact with each other and collectively influence the system stability. Ideally, power converters should be designed to be stable under all the operating conditions. However, in practice, it is difficult to accurately predict all the operating conditions of power converters as well as ensure the stable control under these scenarios. As a result, the linear converter control is normally designed according to a predetermined operating point or an operating range of power converters [45, 116, 136].

As discussed in Sections 2.3 and 2.4, with the knowledge of system plant models, power converters can be flexibly and optimally designed. However, even though plant models are given, improper controller designs may still lead to the system instability. Referring to Figure 2.18, a proportional gain K_{cp} greater than 15.1 will destabilize the control of *LCL*-filtered power converters due to the unstable poles outside the unity circle.

It should be recognized that time-delays may also significantly affect the system stability [137-140]. Generally, time-delays are harmful to the system stability owning to the associated phase lag. However, time-delays may also improve the system stability in certain applications, e.g. the *LC*-filtered VCCs with the single-loop voltage control, where a proper phase lag is desired in terms of the stability margin [127].

Since the controllers of power converters are tuned based on specific system operating conditions, the change of system operations may make the initially properly designed power converters unstable. For example, as mentioned in Chapter 3, the parametric changes of filter components dramatically shift the resonance frequencies of high-order passive filters, and this may further induce the instability, because the stable converter control can only be guaranteed under the specific ranges of resonance frequencies. The research with regards to the

instability due to filter resonances has been extensively documented in the literature [23, 24, 52, 109, 111, 112].

In addition to filter resonances, the interactions among multiple power converters may also destabilize the converter control. In this case, multiple power converters are inter-dependent because of the coupling through common paths. One such example is the coupling via the grid impedance for multiple paralleled power converters [141]. As described in Chapter 3, because the voltage drop across the grid impedance increases linearly as the number of power converters increases, the equivalent grid impedance seen by individual power converters increases proportionally as the number of power converters grows. Consequently, power converters may fail to operate stably when paralleled, even if their individual operations show no sign of instabilities [107, 108, 141-143]. It is worth mentioning that the circuiting currents or powers among multiple power converters pose little threat to the system stability. However, such undesirable currents or powers may overstress the semiconductors of power converters and bring in additional power losses [82, 144, 145].

It is well known that power converters may become unstable under weak grid conditions [94, 106, 146, 147]. As stated, weak grids are characterized by large and variable grid impedances. Note that large grid impedances do not necessarily translate into the deteriorated stability margins of power converters. However, as grid impedances may vary in a wide range, it is difficult to ensure that grid impedances always contribute positively to the system stability [106]. In fact, grid impedances often provoke instability concerns. Specifically, they may interact with the converter control in a wide frequency range, shift the filter resonance frequencies, and/or aggravate the coupling effect among multiple power converters [54, 106, 107]. In this sense, weak grids may challenge the stable operations of power converters.

4.1.2 Solutions to Instability Issues

After the sources of instability issues are discussed, solutions can be formulated

accordingly. First, the modification of controller designs is often the most straightforward way to address instability issues. For instance, reducing the bandwidths of DC-link voltage control, AC voltage control, PLL control, and AC current control may possibly resolve the respective instability issues [126]. However, this is often achieved with the sacrifice of system dynamics, as narrow control bandwidths usually mean low control speeds. Novel control schemes are continuously being proposed to address various types of instability issues [41, 124].

The time-delays arising from the control signal transportations from the central controller to the controllers of individual power converters can be eliminated through decentralized control schemes [69, 70]. The decentralized control establishes a rule for individual power converters to follow without communications, e.g. the frequency droop control. Through this way, a global objective, e.g. the active power sharing, can be automatically achieved by all the participators [13]. In addition, as analysed in Section 2.3, the time-delays associated with the digital controllers of power converters may also introduce the instability. In this case, analog controllers can be used to partially replace digital controllers for the reduction of time-delays [138]. Also, the mitigation of time-delays through faster control signal calculations and reference updates is another promising research direction [140].

To tackle the instability issue due to filter resonances, one possibility is to robustly design passive filter parameters. In this case, the parametric variations of passive filters are considered in the design stage so that power converters will operate stably in the presence of resonance frequency drifts. For example, the resonance frequency of the converter-side inductance and filter capacitance of the *LCL*-filtered power converters with the single-loop gird-current-feedback control can be assigned to be above one sixth of the sampling frequency (f_s / 6) [53, 61]. In this way, the stable operation of power converters is always guaranteed regardless of gird conditions. Another solution lies in the employment of passive dampers [84, 121]. As elaborated in Section 3.5, the passive dampers

consisting of resistors and other passive elements are capable of damping the filter resonance and fixing the resonance instability issue. The above-mentioned solutions, in conjunction with various active damping techniques, have been extensively explored in the literature [23, 24, 34, 148, 149].

In addition to the modification of control algorithms, the active damper serves as an alternative solution to the instability issue, which is caused by the interactions among multiple power converters [135]. The active damper is essentially a CCC regulated to behave as physical resistors at the resonance frequencies formed by multiple power converters. It shares almost the same control structure as APFs, as detailed in [135]. By injecting or absorbing a certain amount of current harmonics, the active damper exhibits great attenuation to converter resonances, and thus helping alleviate the instability issue. Research along the direction of the instability due to converter interactions is still active [107, 141, 142].

Although extensive research works attempt to get rid of the adverse effects due to weak grids, operating power converters stably under weak grids remains to be a challenging task [54, 94, 106, 128, 147]. As mentioned, grid impedances may interact with the converter control (e.g. the DC-link voltage control, AC voltage control, PLL control, and AC current control), shift filter resonances, and aggravate the coupling among multiple power converters. As such, many instability issues should be blamed for weak grids. However, it is difficult to accurately predict grid impedances in real time, as the voltages or currents of gird impedances cannot be easily measured by individual power converters [146]. Moreover, grid impedances may vary in a wide range as system operating conditions change, which further complicates the compensation of grid impedances [106]. Therefore, the instability issues concerning weak grids are normally treated separately. For instance, the filter resonance issue under weak grids is investigated in [115, 147]. References [108, 142] explore the filter resonance and converter interaction issues under weak grids. More research efforts should be attached to the instability issues due to weak grids.

Recently, the instability issue formed by the lumped effect of grid synchronization (i.e. PLLs) and weak grids is pointed out by [25, 26]. It is reported that the wide control bandwidth of PLLs may destabilize the converter control under weak grids. However, the PLL control is increasingly implemented with wider control bandwidths and faster control speeds for better grid synchronization. Consequently, effective solutions to this instability issue are quite necessary. In light of this, an impedance controller capable of addressing the instability issue due to PLLs under weak grids is proposed. The main contents in this section can be found in the author's paper [128].

4.2 Phase-Locked-Loops (PLLs)

The grid synchronization of power converters necessitates the information of grid voltages, which is normally obtained and provided by PLLs. To investigate the instability issue due to PLLs under weak grids, an *L*-filtered three-phase power converter is employed, and its schematic and control block diagrams are illustrated in Figure 2.14 and Figure 2.16, respectively. However, the figures should be slightly modified from the following perspectives. First, the weak power grid is modelled as a series connection of ideal voltage sources v_x ($x = a$, b, c) and grid inductances L_s rather than the ideal voltage sources, and then v_{gx} ($x = a$, b, c) represent the total voltages of v_x ($x = a$, b, c) and voltages across L_s. Additionally, the effect of PLLs should be included in Figure 2.16, as will be detailed. In Figure 2.14, the measured grid voltages and converter currents are transformed into the corresponding *dq*-frame variables through the transformation matrix in (2-6). Remember that (2-6) can be further expressed as the multiplication of an *abc* to $\alpha\beta$ transformation matrix $T_{\alpha\beta/abc}$ and an $\alpha\beta$ to *dq* transformation matrix $T_{dq/\alpha\beta}$, i.e.

$$T_{\alpha\beta/abc} = 2/3\begin{bmatrix} 1 & -1/2 & -1/2 \\ 0 & \sqrt{3}/2 & -\sqrt{3}/2 \end{bmatrix}, \tag{4-1}$$

$$T_{dq/\alpha\beta}(t) = \begin{bmatrix} \cos\theta_o(t) & \sin\theta_o(t) \\ -\sin\theta_o(t) & \cos\theta_o(t) \end{bmatrix}, \tag{4-2}$$

where θ_o denotes the phase angle of grid voltages, and the 0-aixs components are ignored here.

4.2.1 PLL Modelling

Figure 4.1 presents the structure of a typical synchronous reference frame PLL, where the PLL loop filter, i.e. the PI controller $G_{\text{pll\_pi}}(z)$, and the voltage-controlled oscillator, viz. the integrator $G_{\text{pll\_}i}(z)$, collectively adjust the PLL phase angle θ_{pll} to attenuate the PLL q-axis voltage v_{gq_pll}, and thus making θ_{pll} track θ_o [49]. In steady state, $\theta_{\text{pll}} = \theta_o$ and $v_{gq\_\text{pll}} = 0$ are satisfied. The discrete controllers $G_{\text{pll\_pi}}(z)$ and $G_{\text{pll\_}i}(z)$ are expressed as

$$G_{\text{pll\_pi}}(z) = K_{\text{pll\_}p} + \frac{K_{\text{pll\_}i} T_s (z+1)}{2(z-1)}, \tag{4-3}$$

$$G_{\text{pll\_}i}(z) = \frac{T_s (z+1)}{2(z-1)}, \tag{4-4}$$

where $K_{\text{pll\_}p}$ and $K_{\text{pll\_}i}$ denote the proportional and integral gains of the PLL control, respectively.

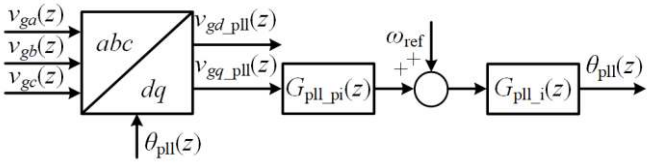

Figure 4.1 Structure of PLLs.

Under small perturbations, the relationship between perturbed PLL phase angle $\Delta\theta_{\text{pll}}$ and q-axis voltage Δv_{gq_pll} can be represented by the following small-signal transfer function:

$$G_{\text{pll\_ol}}(z) = \frac{\Delta\theta_{\text{pll}}(z)}{\Delta v_{gq\_\text{pll}}(z)} = G_{\text{pll\_pi}}(z) G_{\text{pll\_}i}(z), \tag{4-5}$$

which is also the PLL control loop gain. Moreover, the *abc* to *dq* transformation in Figure 4.1 can be mathematically described by (2-6), where θ_o should be replaced by θ_{pll}. It should be emphasized that the *abc* to *dq* transformations of system plants and PLLs are different. Although $\theta_o = \theta_{\text{pll}}$ can be satisfied in steady state, in the face of perturbations and system dynamics, the PLL phase angle θ_{pll}

will deviate from the grid voltage phase angle θ_o. To account for the phase angle difference as well as evaluate its effect on the converter control, the transformation matrices mapping the two frames with regards to θ_o and θ_{pll} are further defined as

$$\begin{aligned} T_{dq\_\text{pll}/dq}(t) &= \begin{bmatrix} \cos\Delta\theta_{\text{pll}}(t) & \sin\Delta\theta_{\text{pll}}(t) \\ -\sin\Delta\theta_{\text{pll}}(t) & \cos\Delta\theta_{\text{pll}}(t) \end{bmatrix}, \\ T_{dq/dq\_\text{pll}}(t) &= T_{dq\_\text{pll}/dq}{}^{-1}(t) = \begin{bmatrix} \cos\Delta\theta_{\text{pll}}(t) & -\sin\Delta\theta_{\text{pll}}(t) \\ \sin\Delta\theta_{\text{pll}}(t) & \cos\Delta\theta_{\text{pll}}(t) \end{bmatrix}, \end{aligned} \tag{4-6}$$

where $T_{dq\_\text{pll}/dq}$ denotes the transformation matrix from the plant dq-frame (corresponding to θ_o) to the PLL dq-frame (corresponding to θ_{pll}), while T_{dq/dq_pll} represents the transformation matrix achieving the opposite purpose. In addition, $\Delta\theta_{\text{pll}} = \theta_{\text{pll}} - \theta_o$ stands for the perturbed PLL phase angle.

Ignoring the high-order terms, (4-6) can be linearized into

$$T_{dq\_\text{pll}/dq}(t) \approx \begin{bmatrix} 1 & \Delta\theta_{\text{pll}}(t) \\ -\Delta\theta_{\text{pll}}(t) & 1 \end{bmatrix}, T_{dq/dq\_\text{pll}}(t) \approx \begin{bmatrix} 1 & -\Delta\theta_{\text{pll}}(t) \\ \Delta\theta_{\text{pll}}(t) & 1 \end{bmatrix}. \tag{4-7}$$

Using (4-7), the dq-frame PLL voltages can be expressed in terms of the dq-frame grid voltages through $T_{dq\_\text{pll}/dq}$ as

$$\begin{bmatrix} v_{gd\_\text{pll}}(t) \\ v_{gq\_\text{pll}}(t) \end{bmatrix} = \begin{bmatrix} 1 & \Delta\theta_{\text{pll}}(t) \\ -\Delta\theta_{\text{pll}}(t) & 1 \end{bmatrix} \begin{bmatrix} v_{gd}(t) \\ v_{gq}(t) \end{bmatrix}. \tag{4-8}$$

Perturbing (4-8) on both sides, it yields

$$\begin{bmatrix} V_{g\_\text{ref}} + \Delta v_{gd\_\text{pll}}(t) \\ \Delta v_{gq\_\text{pll}}(t) \end{bmatrix} = \begin{bmatrix} 1 & \Delta\theta_{\text{pll}}(t) \\ -\Delta\theta_{\text{pll}}(t) & 1 \end{bmatrix} \begin{bmatrix} V_{g\_\text{ref}} + \Delta v_{gd}(t) \\ \Delta v_{gq}(t) \end{bmatrix}, \tag{4-9}$$

where V_{g_ref} stands for the grid voltage reference. Rearranging (4-9) in the z-domain and collecting terms, one obtains

$$\begin{bmatrix} \Delta v_{gd\_\text{pll}}(z) \\ \Delta v_{gq\_\text{pll}}(z) \end{bmatrix} \approx \begin{bmatrix} \Delta v_{gd}(z) \\ -V_{g\_\text{ref}}\Delta\theta_{\text{pll}}(z) + \Delta v_{gq}(z) \end{bmatrix}, \tag{4-10}$$

where the products of perturbed variables are ignored for simplicity. It is noted that V_{g_ref} only appears in the q-axis, because the steady-state values of v_{gq} and v_{gq_pll} are zero.

Substitution of the second equation of (4-10) into (4-5), the closed-loop PLL transfer function from Δv_{gq} to $\Delta\theta_{\text{pll}}$ can be derived as

$$G_{\text{pll\_cl}}(z)=\frac{\Delta\theta_{\text{pll}}(z)}{\Delta v_{gq}(z)}=\frac{G_{\text{pll\_ol}}(z)}{1+G_{\text{pll\_ol}}(z)V_{g\_\text{ref}}}. \tag{4-11}$$

It is clear from (4-11) that the PLL control formulates a path for spreading the disturbance of the *q*-axis voltage to the PLL phase angle, as observed from Figure 4.2, which shows the block diagram of the small-signal model of PLLs.

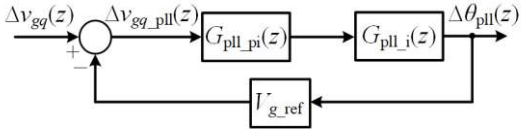

Figure 4.2 Block diagram of the small-signal model of PLLs.

4.2.2 Effect of PLLs

As the PLL phase angle θ_{pll} is involved in the *abc*/*dq* and *dq*/*abc* transformation matrices, all the transformations will inevitably be influenced by the phase angle disturbance $\Delta\theta_{\text{pll}}$. Referring back to Figure 2.14, the converter currents i_{cgx} ($x = a$, b, c) should be measured and then transformed from the *abc*-frame into the *dq*-frame before being regulated by the current controller. Therefore, the *dq*-frame currents i_{cgd} and i_{cgq} will be affected by the phase angle disturbance $\Delta\theta_{\text{pll}}$. This effect can be formulated as

$$\begin{bmatrix}\Delta i_{cgd\_\text{pll}}(z)\\ \Delta i_{cgq\_\text{pll}}(z)\end{bmatrix}\approx\begin{bmatrix}I_{cgq\_\text{ref}}\Delta\theta_{\text{pll}}(z)+\Delta i_{cgd}(z)\\ -I_{cgd\_\text{ref}}\Delta\theta_{\text{pll}}(z)+\Delta i_{cgq}(z)\end{bmatrix}, \tag{4-12}$$

where $\Delta i_{cgd\_\text{pll}}$ and $\Delta i_{cgq\_\text{pll}}$ denote the perturbed converter currents in the PLL *dq*-frame, and I_{cgd_ref} and I_{cgq_ref} represent the *d*- and *q*-axis converter current references, respectively. Equations (4-12) indicate that the PLL phase angle disturbance $\Delta\theta_{\text{pll}}$ will be further propagated into the current control. When power converters are operated with a unity power factor, the disturbance will only be seen in the *q*-axis due to the term $-I_{cgd\_\text{ref}}\Delta\theta_{\text{pll}}(z)$. For STATCOM and DSTATCOM applications where only reactive currents are required, the *d*-axis current control will be disturbed by the term $I_{cgq\_\text{ref}}\Delta\theta_{\text{pll}}(z)$. In the following

discussions, the effect of PLLs on the converter control in the case of unity power factor operations will be elaborated.

In addition to the transformation matrix for converter current measurements, another matrix changing the *dq*-frame variables back into their *abc*-frame counterparts is necessary for duty ratio updates. The effect of this matrix can be equivalently expressed in terms of the converter voltages using T_{dq/dq_pll} as

$$\begin{bmatrix} \Delta v_{\mathrm{inv}d}(z) \\ \Delta v_{\mathrm{inv}q}(z) \end{bmatrix} \approx \begin{bmatrix} \Delta v_{\mathrm{inv}d\_\mathrm{pll}}(z) \\ V_{g\_\mathrm{ref}} \Delta\theta_{\mathrm{pll}}(z) + \Delta v_{\mathrm{inv}q\_\mathrm{pll}}(z) \end{bmatrix}, \tag{4-13}$$

where $\Delta v_{\mathrm{inv}d}$ and $\Delta v_{\mathrm{inv}q}$ refer to the perturbed converter voltages in the plant *dq*-frame, and $\Delta v_{\mathrm{inv}d\_\mathrm{pll}}$ and $\Delta v_{\mathrm{inv}q\_\mathrm{pll}}$ designate the perturbed converter voltages in the PLL *dq*-frame, respectively. Notice that there is only one additional term $V_{g\_\mathrm{ref}}\Delta\theta_{\mathrm{pll}}(z)$ appearing in the *q*-axis, because the steady-state values of *q*-axis voltages are zero.

From the above analysis, there are two additional terms to be included in the *q*-axis when the PLL effect is taken into consideration. For better illustration, the block diagram of the *q*-axis current control is shown in Figure 4.3, where $G_{\mathrm{plant}}(z)$ denotes the system plant, as expressed in (2-32). Moreover, the current controller $G_{cc}(z)$ is implemented as a PI controller:

$$G_{cc}(z) = K_{cp} + \frac{K_{ci}T_s(z+1)}{2(z-1)}, \tag{4-14}$$

where K_{cp} and K_{ci} denote the proportional and integral gains, respectively.

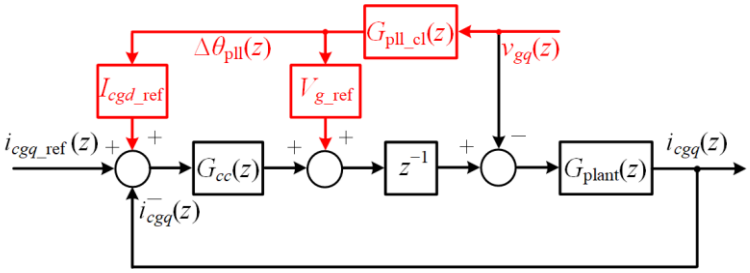

Figure 4.3 Block diagram of the *q*-axis current control including the PLL effect.

Since the PLL mainly affects the *q*-axis current control, the *d*-axis current control remains unchanged in Figure 2.16(b). From Figure 4.3, the closed-loop current control transfer function can be derived as (2-34), i.e.:

$$G_{c\_\mathrm{cl}}(z)=\frac{i_{cgq}(z)}{i_{cgq\_\mathrm{ref}}(z)}=\frac{G_{cc}(z)z^{-1}G_{\mathrm{plant}}(z)}{1+G_{cc}(z)z^{-1}G_{\mathrm{plant}}(z)}. \tag{4-15}$$

The system and control parameters are tabulated in Table 4-2 and Table 4-3, respectively, where a large grid inductance L_s of 10 mH is employed to emulate the weak grid. Based on these parameters, the Bode diagram of the current control closed-loop transfer function $G_{c\_\mathrm{cl}}(z)$ as a function of the current control proportional gain K_{cp} is plotted in Figure 4.4. As observed, $G_{c\_\mathrm{cl}}(z)$ features a unity magnitude gain and a zero phase shift within its control bandwidth, namely $G_{c\_\mathrm{cl}}(z) \approx 1$ in the low-frequency band, thereby indicating the effectiveness of current tracking. As K_{cp} increases, the resonance at around 1.5 kHz becomes more noticeable, implying that the maximum value of K_{cp} should be limited. Additionally, it should be commented that the integral gain K_{ci} mainly affects $G_{c\_\mathrm{cl}}(z)$ in the sub-synchronous frequency range, i.e. $f << f_{\mathrm{ref}}$, and therefore the Bode diagram of $G_{c\_\mathrm{cl}}(z)$ in Figure 4.4 is predominantly determined by K_{cp}.

Table 4-2 System parameters of power converters for testing the impedance controller.

Description	Symbol	Value
Filter inductance	L_c	2 mH
Grid inductance	L_s	10 mH
Grid resistance	R_s	0 Ω
Active power reference	P_{c_ref}	0.6 kW
DC-link voltage reference	$V_{\mathrm{cdc\_ref}}$	250 V
Grid voltage reference	V_{g_ref}	100 V
Converter current reference	I_{cgd_ref}	4 A
Fundamental frequency	f_{ref}	50 Hz
Switching/sampling frequency	$f_{\mathrm{sw}}/f_{\mathrm{s}}$	10 kHz

Table 4-3 Control parameters of power converters for testing the impedance controller.

Description	Symbol	Value
PLL control proportional gain	K_{pll_p}	15
PLL control integral gain	K_{pll_i}	300
Current control proportional gain	K_{cp}	15
Current control integral gain	K_{ci}	300
Impedance control gain	K_{qf}	−0.1

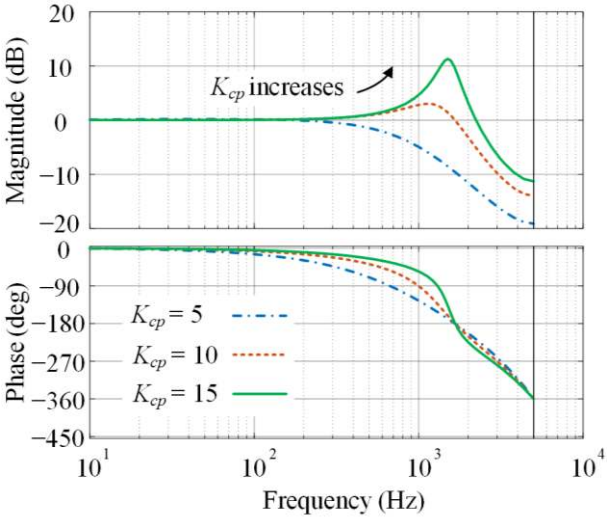

Figure 4.4 Bode diagram of $G_{c\_cl}(z)$ as a function of K_{cp}.

The transfer function from the perturbed q-axis grid voltage Δv_{gq} to the perturbed q-axis converter current Δi_{cgq} can be derived from Figure 4.3 as

$$G_{vgq\_cl}(z) = \frac{\Delta i_{cgq}(z)}{\Delta v_{gq}(z)} = G_{vgq\_pll}(z) + G_{vgq\_plant}(z), \tag{4-16}$$

where $G_{vgq\_pll}(z)$ and $G_{vgq\_plant}(z)$ are expressed as

$$G_{vgq\_pll}(z) = G_{c\_cl}(z)G_{pll\_cl}(z)\left[I_{cgd\_ref} + \frac{V_{g\_ref}}{G_{cc}(z)} \right], \tag{4-17}$$

$$G_{vgq\_plant}(z) = \frac{-G_{plant}(z)}{1 + G_{cc}(z)z^{-1}G_{plant}(z)}. \tag{4-18}$$

Note that $G_{vgq\_pll}(z)$ accounts for the effect of the PLL on the converter control, and it is an important part of $G_{vgq\_cl}(z)$. Furthermore, $G_{vgq\_cl}(z)$ and the q-axis converter impedance $Z_{cq}(z)$ have a reciprocal relationship:

$$Z_{cq}(z) = \frac{-1}{G_{vgq\_cl}(z)} = \frac{-\Delta v_{gq}(z)}{\Delta i_{cgq}(z)}, \tag{4-19}$$

where the minus sign is caused by the definition of current directions in Figure 2.14. Relating (4-17) to (4-19), it is noted that the PLL also influences the q-axis converter impedance.

To see this, Figure 4.5 illustrates the Bode diagram of the q-axis converter impedance $Z_{cq}(z)$ as a function of the PLL control proportional gain K_{pll_p}. As

seen, $Z_{cq}(z)$ registers a negative resistor behavior in the low-frequency band, where the magnitude is almost constant while the phase shift is around −180 degrees [26, 150]. Such a negative resistor region may pose instability concerns to the converter control, as will be detailed in the next section. Moreover, the negative resistive region enlarges as $K_{\text{pll\_}p}$ increases. Notice that a large $K_{\text{pll\_}p}$ is equivalent to a wide PLL control bandwidth, and the integral gain of the PLL control $K_{\text{pll\_}i}$ has a negligible influence on $Z_{cq}(z)$ in Figure 4.5.

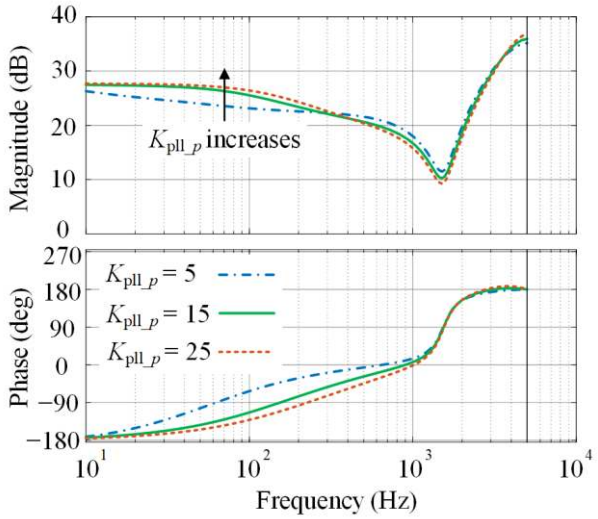

Figure 4.5 Bode diagram of $Z_{cq}(z)$ as a function of $K_{\text{pll\_}p}$.

4.3 Instability Issue due to PLLs

Generally, the instability issues in more-electronics power systems can be analysed and addressed through two methodologies, i.e. the state-space method and impedance criterion [124]. Before investigating the instability issue due to PLLs, this section briefly introduces the two methodologies.

4.3.1 Introduction of Impedance Criterion

In conventional power systems, the state-space method serves as the primary choice for stability analysis and controller synthesis [13]. Using this method, the dynamics of every component in power systems are modelled, and then collectively formulated into state-space models. Through matrix operations, the

system stability can be evaluated by the characteristic equations and eigenvalues, i.e. the modes, of state-space models. Moreover, the effect of each input or state on a specific mode can be quantified. To overcome instability issues, controllers are designed in such a manner that the modes can be allocated with predetermined values or regions. Alternatively, controllers can be optimized according to certain norms. For highly nonlinear systems, Lyapunov functions may be defined and utilized to judge the system stability. The benefits of the state-space method can be summarized as the accurate description of system internal behaviours, analysis and synthesis of multi-input, multi-output, and nonlinear systems, and inclusion of initial conditions. Due to these attractive features, the state-space method is well suited for complex systems with multiple control objectives.

In contrast, the impedance criterion is a transfer function-based method belonging to the classic control theory [40, 151]. The impedance criterion is originally proposed by Middlebrook to assess the stability of DC-DC converters [152]. By calculating the ratio of the filter impedance to the converter impedance, which is also the loop gain, the stability of DC-DC power converters can then be evaluated according to the Nyquist stability criterion. Due to its simplicity and effectiveness, the interest on the impedance criterion has expanded ever since. Later, it is transplanted into AC systems [41]. To ensure fixed system operating points for impedance derivations, AC systems are modelled in the synchronous *dq*-frame rather than the natural *abc*-frame, based on which the system stability can be further judged [41]. The impedance criterion is beneficial in terms of its simplicity and maturity. Moreover, the direct measurements of converter impedances without system models are also feasible. In this sense, power converters are interpreted as black boxes, whose dynamics are only reflected in their grid-connected terminals [124]. The impedance criterion is an ideal tool for the converter-level stability analysis and controller synthesis, where power converters are simplified into the corresponding Thevenin or Norton equivalent circuits, and then the circuit theory can be used for stability evaluation. As such,

the instability issue due to PLLs is investigated through the impedance criterion, as will be disclosed next.

4.3.2 Stability Analysis

According to Figure 4.3, the Norton equivalent circuit of power converters in the z-domain is depicted in Figure 4.6, where $G_{c\_cl}(z)$ and $Z_{cq}(z)$ are expressed in (4-15) and (4-19), respectively. $Z_s(z)$ models the grid impedance, including both the grid inductance and resistance, expressed as

$$Z_s(z) = \frac{T_s}{L_s(z-1)} + R_s, \tag{4-20}$$

where L_s and R_s denote the grid inductance and resistance, respectively.

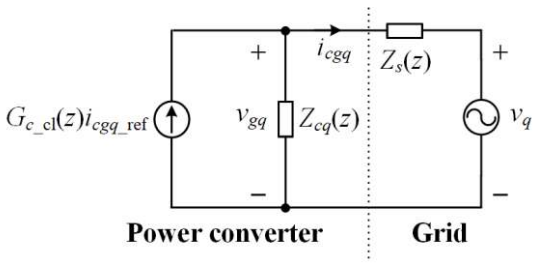

Figure 4.6 Norton equivalent circuit of power converters.

In Figure 4.6, there are one dependent current source and one independent voltage source. According to the superposition principle, the grid current i_{cgq} can be derived by activating only one source at a time and then superposing their effects. First, with the voltage source v_q disabled, one part of the grid current is derived as

$$i_{cgq1}(z) = \frac{G_{c\_cl}(z)i_{cgq\_ref}(z)}{1 + Z_s(z)/Z_{cq}(z)}. \tag{4-21}$$

Afterwards, the voltage source is activated, meanwhile the current source is treated as an open circuit. The remaining part of i_{cgq} can be derived as

$$i_{cgq2}(z) = \frac{-v_q(z)/Z_{cq}(z)}{1 + Z_s(z)/Z_{cq}(z)}. \tag{4-22}$$

The system will be stable if and only if all the poles of i_{cgq1} and i_{cgq2} are inside the unity circle. To ensure the system stability, power converters should first be

internally stable under stiff grid conditions. After substituting $Z_s(z) = 0$ into (4-21) and (4-22), one can notice that i_{cgq1} and i_{cgq2} reduce to $G_{c\_cl}(z)$ and $1 / Z_{cq}(z)$, respectively. Figure 4.7 and Figure 4.8 present the pole-zero maps of $G_{c\_cl}(z)$ and $1 / Z_{cq}(z)$, respectively. Note that $1 / Z_{cq}(z)$ contains a zero outside the unity circle, yet all the poles of $G_{c\_cl}(z)$ and $1 / Z_{cq}(z)$ are stable.

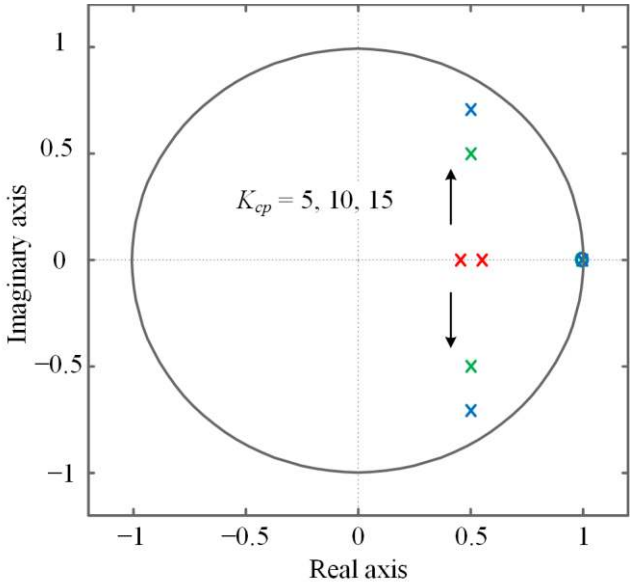

Figure 4.7 Pole-zero maps of $G_{c\_cl}(z)$ as a function of K_{cp}.

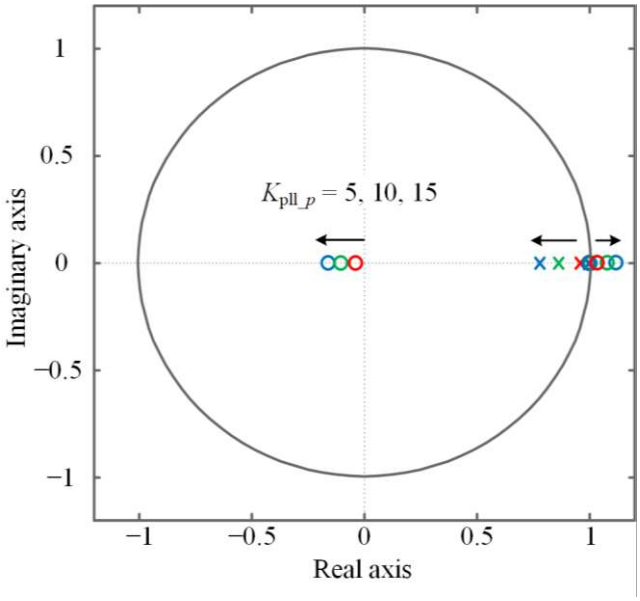

Figure 4.8 Pole-zero maps of $1 / Z_{cq}(z)$ as a function of K_{pll_p}.

Under this condition, the system stability can be further evaluated by the denominators of i_{cgq1} and i_{cgq2}. It is apparent from (4-21) and (4-22) that the

denominators are mainly determined by the ratio of the grid impedance to the converter impedance $Z_s(z) / Z_{cq}(z)$. The impedance criterion says that if the phase margin of $Z_s(z) / Z_{cq}(z)$ at the crossover frequency, where $|Z_s(z) / Z_{cq}(z)| = 0$ dB, is positive, the system will be stable, otherwise the instability issue will be expected [152]. Equivalently, $|Z_s(z) / Z_{cq}(z)| < 0$ dB at all the ±180° crossings can be translated into the stable current control.

For illustration, Figure 4.9 draws the Bode diagrams of $Z_s(z) / Z_{cq}(z)$ as functions of PLL proportional gain $K_{\text{pll\_}p}$, grid inductance L_s, and grid resistance

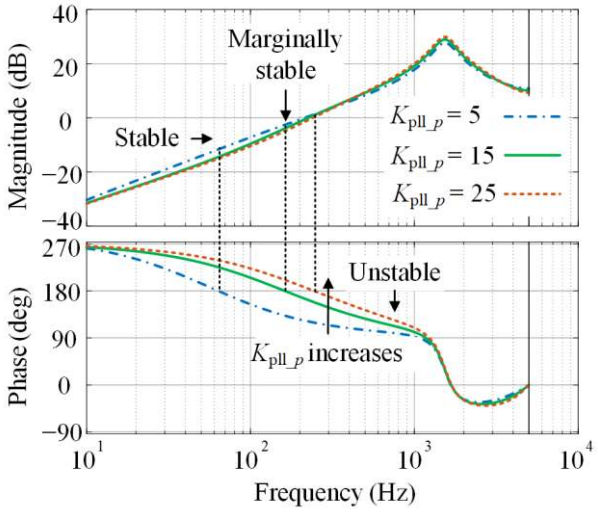

(a) Various $K_{\text{pll\_}p}$

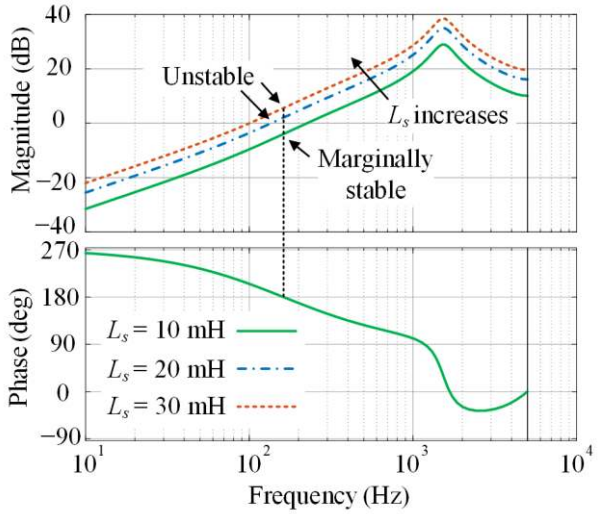

(b) Various L_s

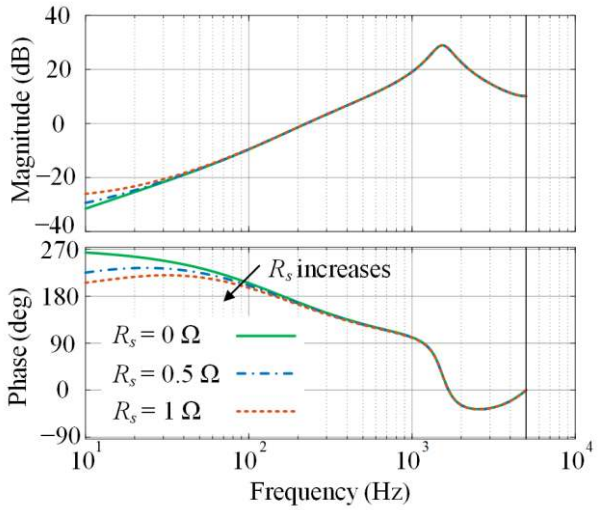

(c) Various R_s

Figure 4.9 Bode diagrams of $Z_s(z) / Z_{cq}(z)$ as functions of (a) $K_{\text{pll\_}p}$, (b) L_s, and (c) R_s.

R_s. As $K_{\text{pll\_}p}$ or L_s increases, the current control gradually becomes unstable, thereby confirming that the instability is due to the improper PLL design or the large grid inductance. This is because increasing $K_{\text{pll\_}p}$ will widen the negative resistance region of the q-axis converter impedance $Z_{cq}(z)$ (see Figure 4.5), and the -180° phase lag of $Z_{cq}(z)$ becomes a 180° phase lead in $Z_s(z) / Z_{cq}(z)$. It is clear from Figure 4.9(a) that the enlarged phase lead region shifts the 180° crossing frequency rightwards, where the magnitude of $Z_s(z) / Z_{cq}(z)$ tends to exceed 0 dB, and thus leading to the unstable current control. Alternatively, the increment of L_s shifts the magnitude curve of $Z_s(z) / Z_{cq}(z)$ upwards, which deteriorates the gain margin and system stability. As noticed from Figure 4.9(c), the grid resistance R_s mainly influences the low-frequency gain and phase, but it only slightly affects the magnitude and phase around the crossover frequency. To this end, R_s will be ignored in the following analysis. Additionally, although the marginally stable cases in Figure 4.9 are noted to have positive margins, the stability margins are relatively small, and hence these cases are considered to be marginally stable.

4.4 Stability Improvement through Impedance Reshaping

The above analysis indicates that a wide bandwidth of the PLL control, i.e. a large $K_{\text{pll\_}p}$, is harmful to the system stability due to the enlarged negative

resistance region of the q-axis converter impedance, particularly under severe weak grids. Therefore, a straightforward solution to the instability issue is reducing $K_{\text{pll\_}p}$. However, the reduction of $K_{\text{pll\_}p}$ will lead to poor system dynamics, as will be demonstrated.

4.4.1 Fundamental Principle

It is highly desirable if the q-axis converter impedance can be reshaped as a positive resistance in the low-frequency band. Referring to Figure 4.4, the closed-loop current control transfer function $G_{c\_\text{cl}}(z)$ is observed to have a positive resistance region featuring a unity gain and a zero phase shift within its bandwidth. Such an observation implies that $Z_{cq}(z)$ may be reshaped as desired through the help of $G_{c\_\text{cl}}(z)$. This objective can be achieved by relating the q-axis voltage v_{gq} to the q-axis current reference i_{cgq_ref} through the proposed impedance controller. Figure 4.10 depicts the block diagram of the current control including the proposed impedance controller, where $G_{qf}(z)$ denotes its transfer function. Remember that the transfer function from i_{cgq_ref} to i_{cgq} is $G_{c\_\text{cl}}(z)$. Therefore, the proposed impedance controller essentially modifies the converter impedance by introducing an additional branch loop consisting of $G_{qf}(z)G_{c\_\text{cl}}(z)$. Once the impedance controller is incorporated, $G_{vgq\_\text{cl}}(z)$, namely the negative reciprocal of $Z_{cq}(z)$, changes into

$$G_{vgq\_\text{cl}}(z)=\frac{\Delta i_{cgq}(z)}{\Delta v_{gq}(z)}=G_{vgq\_\text{pll}}(z)+G_{vgq\_\text{plant}}(z)+G_{vgq\_qf}(z), \tag{4-23}$$

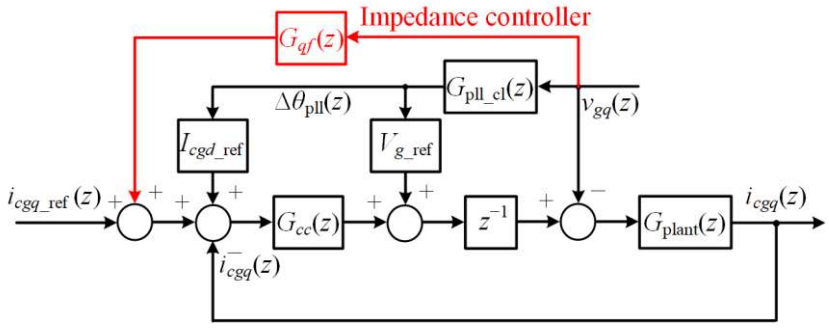

Figure 4.10 Block diagram of the q-axis current control with the proposed impedance controller.

where $G_{vgq\_pll}(z)$ and $G_{vgq\_plant}(z)$ are given in (4-17) and (4-18), respectively. $G_{vgq\_qf}(z)$ models the effect of the impedance controller on the current control, which can be derived as

$$G_{vgq\_qf}(z) = G_{qf}(z)G_{c\_cl}(z). \tag{4-24}$$

As mentioned, $G_{vgq\_cl}(z) \approx 1$ can be satisfied in the low-frequency band. Therefore, it can be derived from (4-24) that $G_{vgq\_qf}(z) \approx G_{qf}(z)$. Hence, $G_{qf}(z)$ can be simply implemented as a proportional controller with a gain of K_{qf} in order to affect $G_{vgq\_cl}(z)$ as a positive resistor do. Recalling that the relationship between converter impedance $Z_{cq}(z)$ and $G_{vgq\_cl}(z)$ is a negative reciprocal in (4-19), K_{qf} should be negative so that $Z_{cq}(z)$ will be reshaped as a positive resistance in the low-frequency band.

4.4.2 Design of Impedance Controller

It is noted that from (4-23) that the impedance controller and PLL introduce $G_{vgq\_qf}(z)$ and $G_{vgq\_pll}(z)$, respectively. Ideally, $G_{vgq\_qf}(z)$ and $G_{vgq\_pll}(z)$ should completely cancel out with each other so that the instability concern due to PLLs can be totally addressed. Mathematically, this objective can be expressed as

$$G_{vgq\_pll}(z) + G_{vgq\_qf}(z) = 0. \tag{4-25}$$

Substitution of (4-17) and (4-24) into (4-25), the ideal impedance controller can be derived as

$$G_{qf}(z) = -G_{pll\_cl}(z)\left[I_{cgd\_ref} + \frac{V_{g\_ref}}{G_{cc}(z)} \right]. \tag{4-26}$$

In the low-frequency band, which is of interest, (4-26) can be simplified into

$$K_{qf} = -\left(\frac{I_{cgd\_ref}}{V_{g\_ref}} + \frac{1}{K_{cp}}\right), \tag{4-27}$$

from which the proportional gain K_{qf} can be readily derived. Substituting of the relevant parameter values in Table 4-2 and Table 4-3 into (4-27), $K_{qf} = -0.1$ is obtained and documented in Table 4-3.

Figure 4.11 compares the ideal impedance controller in (4-26) and the simplified impedance controller in (4-27). It reveals that the proportional gain K_{qf} can be a good approximation of $G_{qf}(z)$ in the low-frequency band, which covers the negative resistance region in Figure 4.5. Implementing the impedance controller as a proportional controller will greatly simplify the controller design process, as can be referred to (4-27).

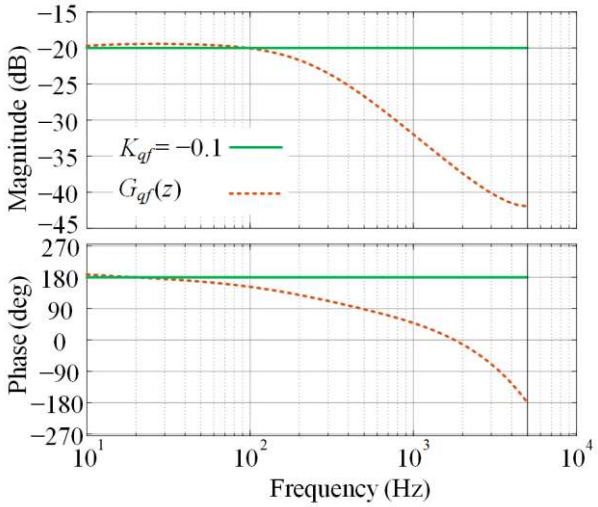

Figure 4.11 Bode diagrams of ideal and simplified impedance controllers $G_{qf}(z)$ and K_{qf}.

4.4.3 Impedance Reshaping and Stability Improvement

With the proposed impedance controller, Figure 4.12 illustrates the Bode diagrams of the reshaped converter impedance $Z_{cq}(z)$ as functions of PLL control proportional gain $K_{\text{pll\_}p}$ and impedance control gain K_{qf}. It is obvious from Figure 4.12(a) that $Z_{cq}(z)$ features a positive resistance region, where an almost constant magnitude and a zero phase shift can be seen, regardless of $K_{\text{pll\_}p}$. As observed, there is a strong correlation between positive resistance region and K_{qf}. Specifically, the positive resistance region expands as $|K_{qf}|$ increases, as verified by Figure 4.12(b).

Further on, the reshaped impedance $Z_{cq}(z)$ dramatically changes the Bode diagrams of the impedance ratio $Z_s(z) / Z_{cq}(z)$, as validated by Figure 4.13, where the stable current control can always be ensured. It is confirmed that the positive resistance feature of $Z_{cq}(z)$ contributes to the stability improvement.

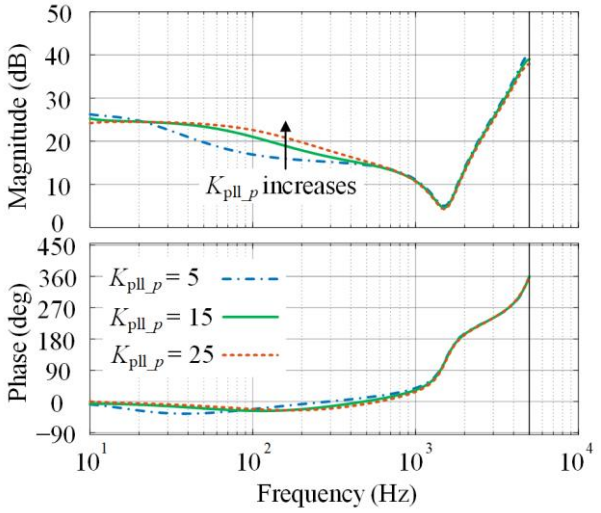

(a) Various K_{pll_p}

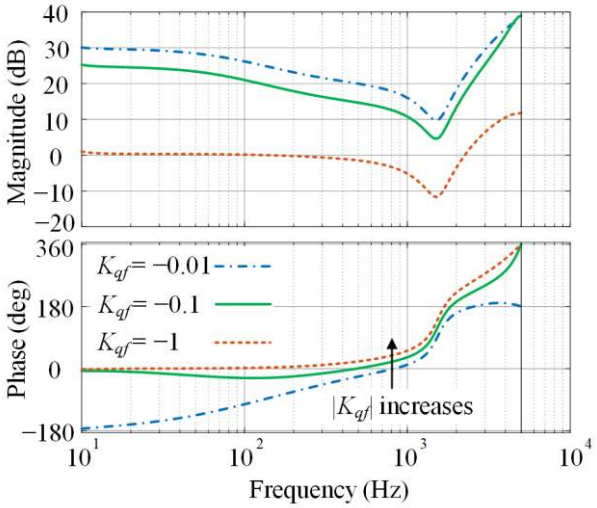

(b) Various K_{qf}

Figure 4.12 Bode diagrams of $Z_{cq}(z)$ as functions of K_{pll_p} and K_{qf} with the impedance controller.

To effectively reject high-frequency noises, it is necessary to incorporate low-pass filters (LPFs) into PLLs. When a first-order LPF having a cut-off frequency of 1000 Hz is accounted, the Bode diagrams of $Z_s(z)$ / $Z_{cq}(z)$ without and with the proposed impedance controller are depicted in Figure 4.14. It is noted from Figure 4.14(a) that the inclusion of the PLL filter deteriorates the system stability, where the marginally stable case turns into the unstable case. Fortunately, both cases can be stabilized by the proposed impedance controller, as evidenced by Figure 4.14(b).

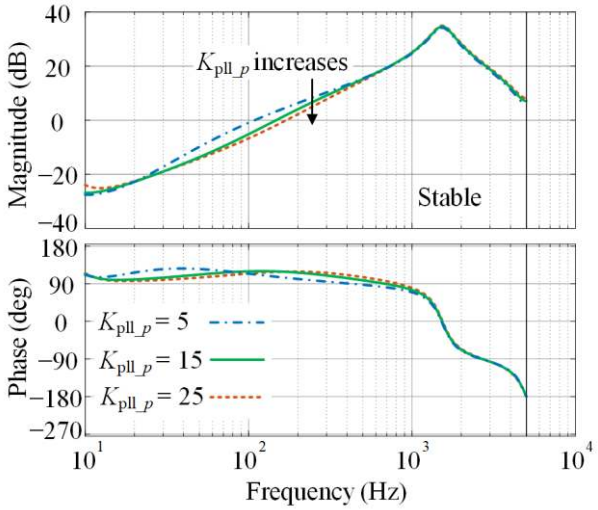

(a) Various K_{pll_p}

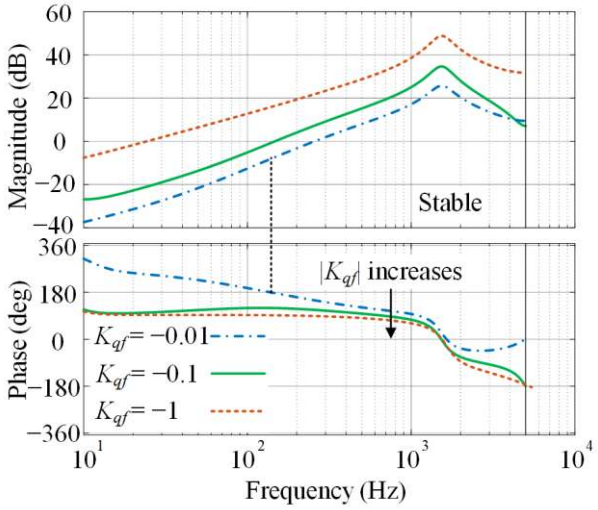

(b) Various K_{qf}

Figure 4.13 Bode diagrams of $Z_s(z)$ / $Z_{cq}(z)$ as functions of K_{pll_p} and K_{qf} with the impedance controller.

4.4.4 Simulation and Experimental Verifications

To illustrate the effectiveness of the proposed impedance controller on addressing the instability issue due to PLLs, simulation and experimental results of the three-phase grid-connected power converters with the system and control parameters listed in Table 4-2 and Table 4-3, respectively, are presented in this subsection. The simulation models were developed under the Matlab/Simulink

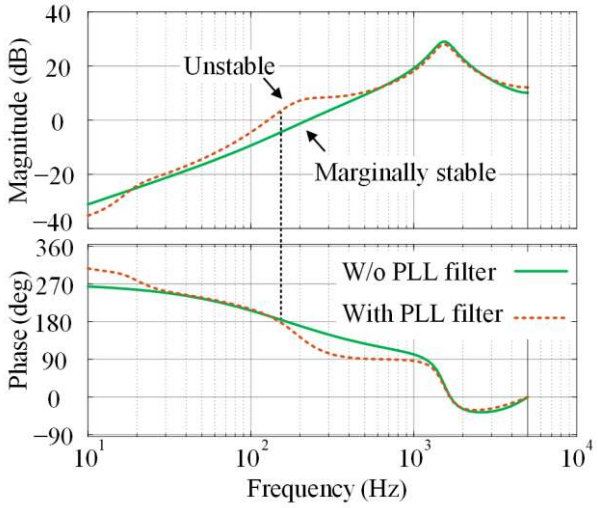

(a) Without impedance controller

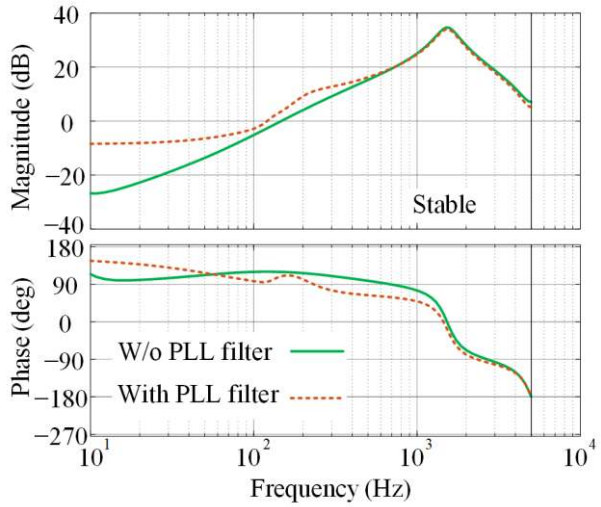

(b) With impedance controller

Figure 4.14 Bode diagrams of $Z_s(z)$ / $Z_{cq}(z)$ including the PLL filter (a) without and (b) with the proposed impedance controller.

environment. The experiments were conducted on the more-electronics power system shown in Figure 2.1, where the weak power grid was emulated by the VCC, namely the VSG, together with the external inductors inserted between VCC and CCCs.

The dynamic simulation results of grid currents i_{cgx} ($x = a, b, c$) and PLL q-axis voltage v_{gq_pll} are illustrated in Figure 4.15, where the power converter is designed to be unstable without enabling the proposed impedance controller. When the

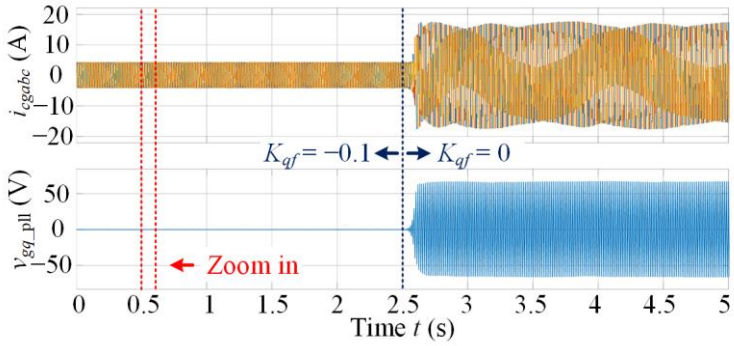

(a) Overall view

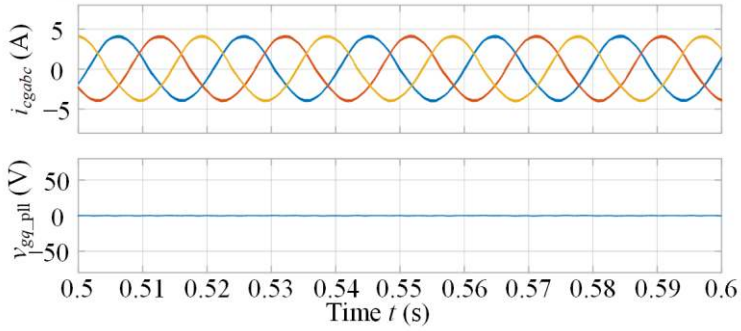

(b) Zoom-in view

Figure 4.15 Simulation results of grid currents i_{cgx} ($x = a, b, c$) and PLL q-axis voltage v_{gq_pll} during system dynamics.

impedance controller is activated, i.e. $K_{qf} = -0.1$, the power converter operates stably with a negligible PLL q-axis voltage v_{gq_pll}. As predicted, once the impedance controller is disabled at t = 2.5 s, i.e. $K_{qf} = 0$, the system becomes unstable. In this case, v_{gq_pll} features a considerably large magnitude, indicating that the instability issue is due to the PLL.

Under the same testing condition, the experimental results of grid currents i_{cgx} ($x = a, b, c$) and PLL q-axis voltage v_{gq_pll} are presented in Figure 4.16. Once again, the instability issue appears after letting $K_{qf} = 0$. To protect semiconductor devices, the power converter stops working when the converter currents go beyond 15 A, and therefore i_{cgx} ($x = a, b, c$) and v_{gq_pll} eventually reach zero. The simulation and experimental studies agree well with the theoretical analysis provided in the previous sections.

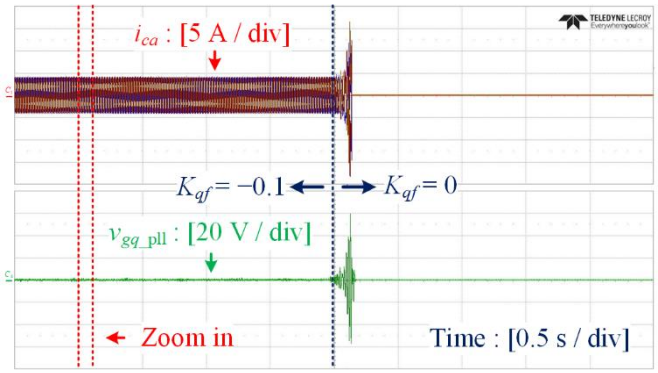

(a) Overall view

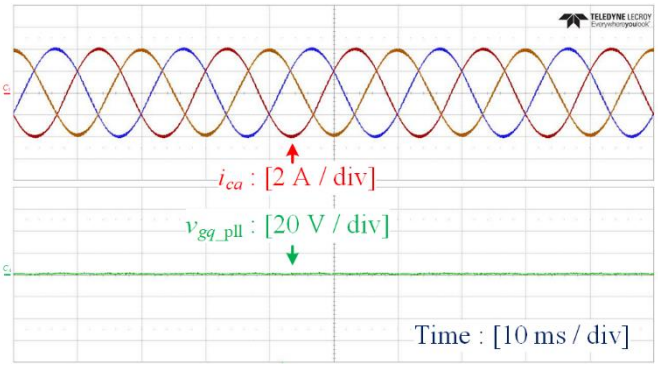

(b) Zoom-in view

Figure 4.16 Experimental results of grid currents i_{cgx} (x = a, b, c) and PLL q-axis voltage v_{gq_pll} during system dynamics.

As discussed, an alternative solution to the instability issue due to PLLs under weak grids is reducing the PLL control bandwidth or the PLL control proportional gain K_{pll_p}. However, the reduction of K_{pll_p} only narrows the negative resistance region of the converter impedance rather than reshaping it as a positive resistance in the low-frequency band (see Figure 4.5). In this regard, the solution of reducing K_{pll_p} may only partially alleviate the instability issue instead of completely addressing it. In contrast, the proposed impedance controller reshapes the converter impedance as a positive resistance in the low-frequency band, thereby overcoming the instability issue theoretically.

In addition, system dynamics deteriorate as K_{pll_p} reduces, because narrow control bandwidths often lead to the slow reference tracking and poor disturbance rejection. To clearly illustrate the drawback of reducing K_{pll_p}, Figure 4.17 presents the simulation results of v_{gq_pll} during system startups with K_{pll_p} = 1 and

$K_{\text{pll\_}p}$ = 15, where the system is put into operation at t = 0.25 s. It is clear by comparing Figure 4.17(a) and Figure 4.17(b) that v_{gq_pll} experiences more oscillations and slow dynamics in the case of a small $K_{\text{pll\_}p}$ = 1, and the case of a large $K_{\text{pll\_}p}$ = 15 can get rid of these adverse results. Therefore, it is concluded that the reduction of $K_{\text{pll\_}p}$ improves the system stability at the expense of system dynamics. In contrast, the proposed impedance controller is superior as it preserves the system stability without any sacrifice of PLL designs. This conclusion can be further experimentally verified by Figure 4.18, where the experimental results are in alignment with the simulation results. The above simulation and experimental results clearly demonstrate the correctness of the theoretical analysis and the superiority of the proposed impedance controller.

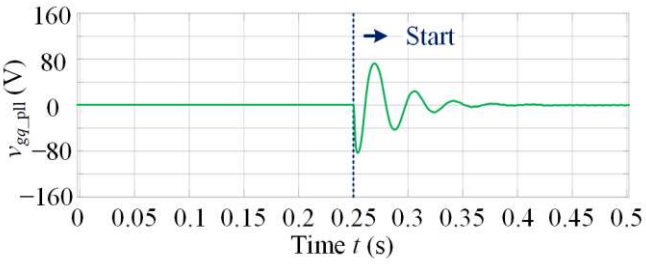

(a) $K_{\text{pll\_}p}$ = 1

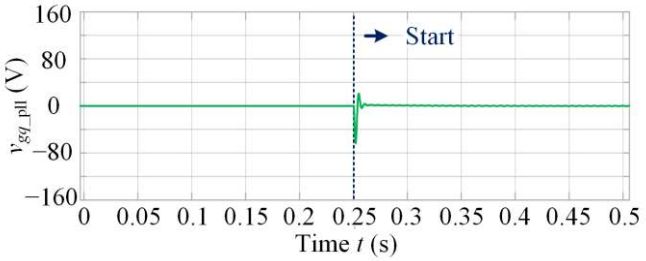

(b) $K_{\text{pll\_}p}$ = 15

Figure 4.17 Simulation results of PLL q-axis voltages v_{gq_pll} during system startups with (a) $K_{\text{pll\_}p}$ = 1 and (b) $K_{\text{pll\_}p}$ = 15.

4.5 Summary

This chapter has briefly reviewed the sources of converter-level instability issues in more-electronics power systems, including improper controller designs,

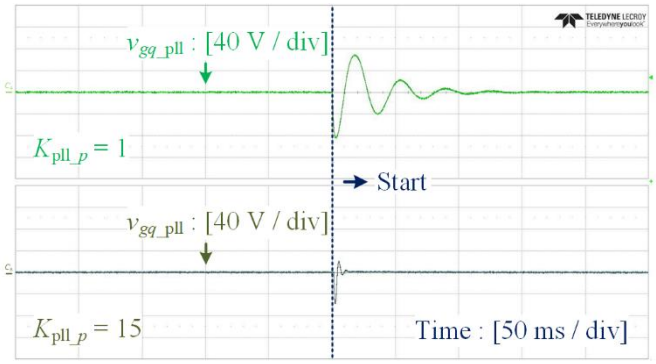

Figure 4.18 Experimental results of PLL q-axis voltages v_{gq_pll} during system startups with the upper trace K_{pll_p} = 1 and lower trace K_{pll_p} = 15.

time-delays, filter resonances, interactions among multiple power converters, and weak grids. Accordingly, the commonly adopted solutions to instability issues have been introduced. It is found that the instability issue due to PLLs under weak grids has so far not been well addressed. Through the system modelling and analysis, this instability issue is known to be caused by the negative resistance region in the low-frequency band of the q-axis converter impedance. To tackle the instability issue, an impedance controller directly relating the q-axis voltage to the q-axis current reference has been proposed. Since the q-axis current reference approximately equals to the q-axis current in the low-frequency band, the proposed impedance controller reshapes the q-axis converter impedance as a positive resistance in the low-frequency band, and thus overcoming the instability issue due to PLLs, as verified by the simulation and experimental results.

Chapter 5 System-Level Frequency Stability Improvement by Distributed Virtual Inertia and VSGs

This chapter focuses on the system-level frequency stability of more-electronics power systems. It begins with the introduction of the lack of inertia issue. This is followed by the analysis of the inertia effect on the frequency regulation. It is identified that the lack of inertia challenges the frequency regulation in terms of frequency nadir and rate of change of frequency (RoCoF). As such, two approaches are proposed for inertia enhancement. The first approach is to employ the proposed grid-connected power converters with the distributed virtual inertia. By proportionally relating the grid frequency and DC-link voltages of power converters, their DC-link capacitors become energy buffers and can generate the virtual inertia according to system demands. The second approach lies in the use of VSGs. To facilitate the implementation of VSGs, the hybrid ESS (HESS) consisting of a battery and an ultracapacitor is proposed. In the HESS, the ultracapacitor tackles the fast-varying power due to inertia emulation while the battery handles the long-term power fluctuations required by the remaining parts of VSGs. Through these approaches, the significant improvements of frequency nadir and RoCoF can be expected, resulting in a further improvement of the system-level frequency stability.

5.1 Background and Introduction

As discussed, the system-level control mainly refers to the frequency and voltage control. The grid frequency is a fundamental indicator of the active power balance between generation and demand, and the reactive power imbalance makes the grid voltage amplitude deviate from its nominal value [13]. Furthermore, the frequency or voltage will drop if the demanded power exceeds the generated power, and vice versa. Therefore, the system-level control is essentially the regulation of active and reactive powers. In more-electronics power systems, grid-interfaced power converters are normally operated with

unity power factor operations to avoid unnecessary reactive power flows, except for STATCOMs or DSTATCOMs and APFs, whose reactive power outputs are intended to help balance the system-level reactive power. Therefore, fewer pressing concerns about reactive power are introduced by power electronics in more-electronics power systems. In contrast, the frequency control or active power balance is considered to be more of a concern, as will be discussed.

5.1.1 Challenge of Inertia Reduction

Many power system operators treat the frequency control as a high-priority area, because the grid frequency should always be tightly regulated to avoid the frequency instability [153-156]. The operations of generating units at low-frequencies may mechanically overstress turbine blades or overheat boilers due to the reduced outputs of pumps and fans [13]. Therefore, under-frequency protective relays are incorporated in the generating units to trip them off under excessive frequency drops. As a result, the improper frequency control may cause a large-scale tripping of generating units, which will further aggravate the imbalance between generation and demand, and thus leading to cascading failures or even grid collapses [13]. To avoid such disasters, various international grid codes prescribe standards on the acceptable frequency ranges, as given in Table 5-1, where the normal operating frequency bands set long-term allowable frequency variation ranges and operational frequency tolerance bands limit instantaneous frequency changes [157]. It should be remarked that the thresholds of under-frequency load shedding are prescribed by several grid codes, e.g. 49.7 Hz by the Singapore grid code [155]. Under normal operating conditions, the grid frequency should never touch these thresholds. In the face of contingencies, i.e. severe frequency events, non-critical loads may be partially tripped to assist the active power balance at the expense of additional operating costs. Figure 5.1 sketches a frequency response curve following a generator tripping event, where the primary frequency control arrests the fast frequency decline, and then the secondary frequency control restores the frequency to its nominal value [13].

Note that the minimum frequency, i.e. the frequency nadir, must be maintained within the frequency bands prescribed by grid codes.

Table 5-1 International grid standards on frequency control.

Country/Region	Australia [158]	Europe [159]	North America [154]	Singapore [155]
Nominal frequencies (Hz)	50	50	60	50
Normal operating frequency bands (Hz)	Interconnected system: ±0.15 Islanded system: ±0.5	±0.2	Targeted frequency band: Eastern Interconnection: ±0.018 Western Interconnection: ±0.0228 Texas Interconnection: ±0.030 Quebec Interconnection: ±0.021	±0.2
Operational frequency tolerance bands (Hz)	±1 Extreme frequency tolerance band: 47−52	±0.8	Under-frequency load shedding: Eastern Interconnection: 59.5 Western Interconnection: 59.5 Texas Interconnection: 59.3 Quebec Interconnection: 58.5	Under-frequency load shedding: 49.7

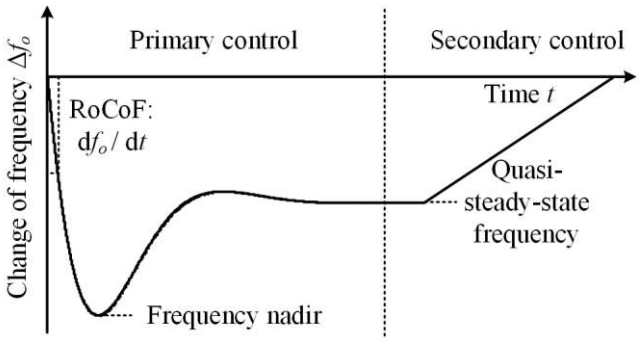

Figure 5.1 Frequency response curve following a generator tripping event.

In addition to the frequency nadir, the rate of change of frequency, i.e. the RoCoF (see Figure 5.1), should also be tightly regulated. Otherwise, the tripping of generators and catastrophic results as those due to excessive frequency deviations may also happen. The reason is that the protective relays for high RoCoF events are also necessary in generating units to avoid the risks of generator pole slipping under excessive RoCoF levels, e.g. 1.5 Hz/s to 2 Hz/s (over a 500 ms rolling window) [153]. Besides, the anti-islanding protective relays are based on RoCoF levels, for example in the Ireland/North Ireland jurisdiction [153]. Therefore, excessive RoCoF levels may trigger anti-islanding protections. To prevent generating units from tripping, the requirements on the

RoCoF withstand capabilities of generators are prescribed by various grid codes, as formulated in Table 5-2, where more stringent requirements are to be expected in the near future. From the above discussions, RoCoF levels should be maintained low enough for the compliance of grid codes.

Table 5-2 International grid standards on the RoCoF withstand capabilities of generators.

Country/ region	Australia [160]	Great Britain [156]	Ireland/North Ireland [161]
Current requirement	Automatic access standard: ±4 Hz/s for 0.25 s, minimum access standard: ±1 Hz/s for 1 s	0.125 Hz/s for 0.5 s	0.5 Hz/s for 0.5 s
Future requirement	Non-synchronous systems: ±4 Hz/s for 0.25 s & ±3 Hz/s for 1 s, Synchronous systems: automatic access standard: ±4 Hz/s for 0.25 s & ±3 Hz/s for 1 s, minimum access standard: ±1 Hz/s for 1 s	New synchronous units and non-synchronous units: 1 Hz/s for 0.5 s Incumbent synchronous units: 0.5 Hz/s for 0.5 s	1 Hz/s for 0.5 s

In conventional power systems, synchronous generators are responsible for the frequency regulation. Returning to Figure 5.1, the frequency nadir and RoCoF are mainly determined by the primary frequency control provided by synchronous generators, and the primary frequency control is further contributed by two parts – the frequency droop and power system inertia. The concept of the frequency droop, paired with its effect, has been detailed in Section 2.5. The power system inertia refers to the per unit kinetic energy stored in the rotors of synchronous generators and turbines [13], which can be defined as

$$H = \frac{E_{\text{gen}}}{VA_{\text{base}}} = \frac{J\omega_{m\text{ref}}{}^{2}}{2VA_{\text{base}}}, \tag{5-1}$$

where E_{gen} denotes the rated kinetic energy of synchronous generators, J represents the combined moment of inertia of synchronous generators and turbines, $\omega_{m\text{ref}}$ stands for the rated angular velocity of rotors, VA_{base} refers to the rated power of synchronous generators, and H designates the inertia coefficient, which is defined to quantitatively evaluate the inertia of synchronous generators. The effect of inertia or H can be described as follows. Since the speeds of synchronous generator rotors synchronize with the grid frequency, the rotors autonomously slow down under low-frequency events. This will deliver a short

burst of the kinetic energy stored in the rotors, and thus helping to balance the power mismatch between generation and demand as well as to slow down the frequency change, and the opposite is true for the case of over-frequency events. Figure 5.2 visualizes the effect of inertia on the frequency regulation under a low-frequency event, where both the frequency change Δf_o and RoCoF $\mathrm{d}f_o/\mathrm{d}t$ can be improved through the increment of H, thereby showing the positive effect of inertia on the frequency regulation. It is reported that typical values of H are 5 s for gas-fired generators, 3.5 s for coal-fired generators, 4 s for nuclear generators, and 3 s for hydraulic generators [13, 153].

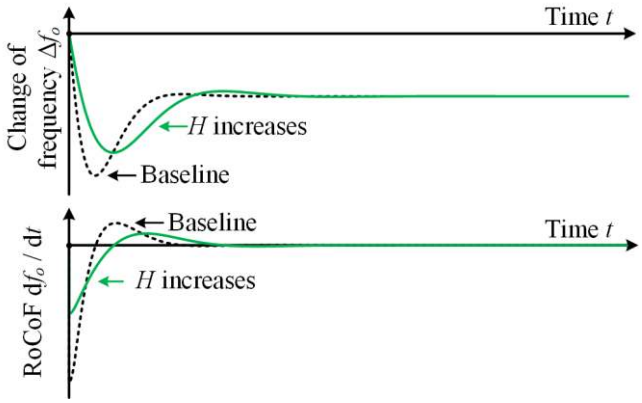

Figure 5.2 Effect of inertia under a low-frequency event.

In more-electronics power systems, synchronous generators are gradually being replaced by power electronics-interfaced renewable generators due to the large-scale deployment of renewable energies. However, different from synchronous generators, power electronic converters feature no kinetic energy or inertia. Even though wind turbines have rotors and the associated kinetic energies, the speeds of wind turbines are normally decoupled from the grid frequency by power converters for a better control of rotor speeds [5, 162]. Therefore, no inertia can be naturally expected from renewable generation systems. As the trend of renewable integration proceeds, the power system inertia continues to reduce [163, 164]. The lack of inertia issue has already challenged the frequency stability and reliability of small-scale power systems, e.g. the Ireland and Great Britain power systems [156, 161], in terms of excessive frequency nadir (< 49 Hz) and RoCoF levels (> 0.5 Hz/s). For larger power systems with AC

interconnections, the inertia shortage will become a concern sooner or later. As tabulated in Table 5-2, several power system operators attempt to alleviate the negative effects of high RoCoF levels due to the lack of inertia issue by enhancing the RoCoF withstand capabilities of generators. However, the RoCoF testing of generators costs a fortune (US $1.5M per combined cycle gas turbine estimated by GE [153]), which remains as a large obstacle for the widespread adoption of this approach. Moreover, the approach cannot improve the RoCoF or inertia, and therefore it is unlikely to completely address the inertia reduction challenge. Alternatively, great efforts should be attached to inertia enhancement techniques.

5.1.2 Inertia Enhancement Techniques

As synchronous generators are inertia sources, it is possible to enhance the power system inertia through the employment of additional synchronous generators in more-electronics power systems. One example lies in the use of synchronous condensers, which are essentially synchronous generators without prime movers or loads. Normally, synchronous condensers are used for reactive power compensation and voltage control, while they may also serve as inertia suppliers. The typical inertia coefficient H of synchronous condensers is reported to be 2.1 s [153]. However, high operating and maintenance costs stand as their major drawbacks.

Through the dedicated control of rotor speeds, wind turbines can release or absorb the kinetic energy as synchronous generators do during frequency events [165]. In this way, the emulated inertia, or known as the virtual inertia, can be expected from wind turbines. The inertial responses contributed by wind turbines have already been proven and made mandatory in Hydro-Quebec [153]. However, the inertia emulated by wind turbines in Hydro-Quebec is still different from the inertia generated by synchronous generators [153]. This is because wind turbines feature a speed-recovery period after the inertial power injection during low-frequency events, and an improper speed-recovery will cause a second frequency dip [166]. The speed-recovery is no longer necessary with the curtailment of wind

power at the expense of non-trivial opportunity costs in the spilled energy [162]. Other techniques for the enhancement of power system inertia and frequency stability will be elaborated in the following sections.

5.2 Influence of Inertia on Frequency Regulation

Before investigating the proposed inertia enhancement methods, this section will quantitatively analyse the influence of inertia on the frequency regulation. This part mainly follows the author's paper [167].

5.2.1 Frequency Regulation Framework

Figure 5.3 depicts the simplified schematic diagram of a single-area power system, where P_g denotes the power generated by synchronous generators or VSGs in more-electronics power systems, P_c stands for the power released by grid-connected power converters, P_l designates the power absorption of frequency-independent resistive loads, and P_d refers to the power consumed by frequency-dependent loads, e.g. induction motors. The power versus frequency relationships of individual equipment are also provided in Figure 5.3, where the

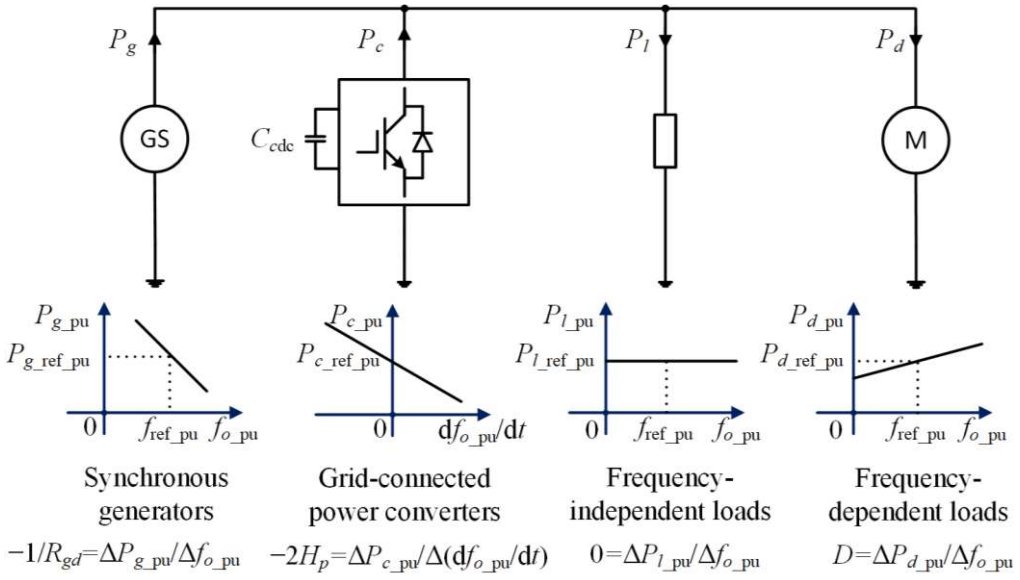

Figure 5.3 Simplified schematic diagram of a single-area power system (GS: synchronous generators and M: motors).

frequency droop characteristic of synchronous generators can be clearly observed, and R_{gd} represents the frequency droop coefficient. Moreover, it is noted that the per unit power absorbed by grid-connected power converters P_{c_pu} varies as a function of the per unit RoCoF $\mathrm{d}f_{o\_pu}$ / $\mathrm{d}t$, and this is intended to generate the virtual inertia with an inertia coefficient H_p, as will be detailed. Without activating the virtual inertia control, P_{c_pu} is assumed to be a constant $P_{c\_ref\_pu}$, as the variability of renewable generation is lumped together with the load change. The frequency-independent loads absorb a fixed amount of power regardless of the grid frequency. In contrast, the frequency-dependent loads consume more power as the frequency increases, thereby providing a degree of damping to the frequency regulation, and the damping coefficient D is used to evaluate the damping effect, as has been defined in Table 2-5.

Figure 5.4 presents the block diagram of a typical frequency regulation framework, where $G_{gt}(s)$ models the speed governor and reheat turbine [13]. Recapping that the frequency and active power control of VSGs in Figure 2.21 follows Figure 5.4, and therefore the corresponding parameters are the same. To this end, $G_{gt}(s)$ can be referred to (2-35), where the parameter values are documented in Table 2-5. The well-known swing equation, which mathematically describes the electromechanical behaviour of synchronous generators, can be obtained from Figure 5.4 as

$$\Delta P_{\mathrm{in\_pu}}(s) - \Delta P_{l\_\mathrm{pu}}(s) = 2Hsf_{o\_\mathrm{pu}}(s) + D\Delta f_{o\_\mathrm{pu}}(s), \tag{5-2}$$

where the inertia coefficient H is defined in (5-1).

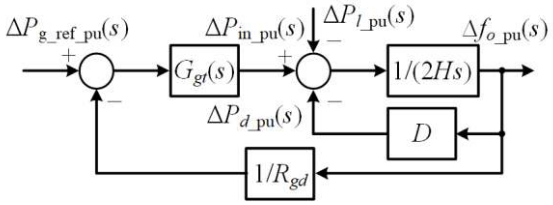

Figure 5.4 Block diagram of the frequency regulation framework.

5.2.2 Influence of Inertia

This subsection aims to quantitatively analyze the influence of inertia on the

frequency regulation. For analysis, the transfer function from ΔP_{l_pu} to Δf_{o_pu} is derived after substituting $G_{gt}(s)$ in (2-35) into Figure 5.4 as

$$G_{Pf}(s)=\frac{\Delta f_{o\_\mathrm{pu}}(s)}{\Delta P_{l\_\mathrm{pu}}(s)}=\frac{-R_{gd}(1+sT_G)(1+sT_{\mathrm{CH}})(1+sT_{\mathrm{RH}})}{(2Hs+D)(1+sT_G)(1+sT_{\mathrm{CH}})(1+sT_{\mathrm{RH}})R_{gd}+sF_{\mathrm{HP}}T_{\mathrm{RH}}+1}, \quad (5\text{-}3)$$

where the time constant of the reheater T_{RH} is much greater than the other time constants according to Table 2-5.

Figure 5.5 depicts the pole-zero map of $G_{Pf}(s)$ as a function of the inertia coefficient H. As H increases, the poles P_3 and P_4 gradually approach and tend to cancel out the zeros Z_2 and Z_3, leaving the conjugate poles P_1 and P_2 as the dominant poles, which together with the zero Z_1, will determine the dynamics of the grid frequency during frequency events. Therefore, it is possible to simplify $G_{Pf}(s)$ as a transfer function comprising the zero Z_1 and poles P_1 and P_2:

$$G_{Pf}(s)=\frac{\Delta f_{o\_\mathrm{pu}}(s)}{\Delta P_{l\_\mathrm{pu}}(s)}=\frac{-R_{gd}(1+sT_{\mathrm{RH}})}{(2Hs+D)(1+sT_{\mathrm{RH}})R_{gd}+sF_{\mathrm{HP}}T_{\mathrm{RH}}+1}, \quad (5\text{-}4)$$

where the dynamics associated with the time constants T_G and T_{CH} are ignored.

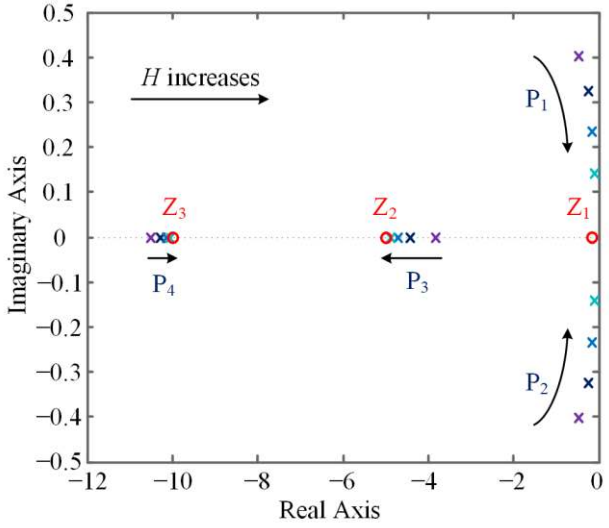

Figure 5.5 Pole-zero map of $G_{Pf}(s)$ as a function of H (H = 5, 10, 20, and 50).

After some manipulation, (5-4) becomes

$$G_{Pf}(s)=\frac{\Delta f_{o\_\mathrm{pu}}(s)}{\Delta P_{l\_\mathrm{pu}}(s)}=G_0\frac{s+z_1}{s^2+2\zeta\omega_n s+\omega_n{}^2}, \quad (5\text{-}5)$$

where the coefficients are expressed as

$$G_0 = \frac{-1}{2H}, z_1 = \frac{1}{T_{\mathrm{RH}}}, \omega_n = \sqrt{\frac{DR_{gd}+1}{2HR_{gd}T_{\mathrm{RH}}}}, \zeta = \frac{2HR_{gd} + DR_{gd}T_{\mathrm{RH}} + F_{\mathrm{HP}}T_{\mathrm{RH}}}{4HR_{gd}T_{\mathrm{RH}}\omega_n}, \quad (5\text{-}6)$$

where ω_n and ζ denote the undamped natural angular frequency and damping ratio, respectively. Figure 5.6 illustrates the 3% step-up responses of $G_{Pf}(s)$ in (5-3) and (5-4) as a function of H. It is apparent that the frequency nadir rises with the increment of H. Moreover, the frequency differences between original and simplified $G_{Pf}(s)$ cases are always less than the 10% maximum frequency deviations, thereby confirming the effectiveness of the model simplification.

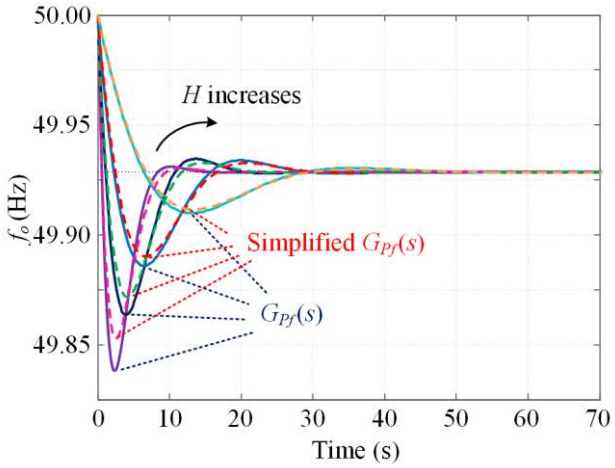

Figure 5.6 Responses of $G_{Pf}(s)$ as a function of H (H = 5, 10, 20, and 50) under a 3% step-up load change.

To quantify the dependence of several important performance indices on the inertia coefficient H, the per unit grid frequency f_{o_pu} under a step-up load change is derived from Figure 5.4 and expressed in the s-domain as

$$\begin{aligned} f_{o\_\mathrm{pu}}(s) &= \underbrace{f_{\mathrm{ref}\_\mathrm{pu}}(s)}_{\text{Reference}} + \underbrace{\frac{G_{Pf}(s)}{s}}_{\text{Change}} \\ &= \frac{1}{s} + G_0 \left\{ \begin{array}{l} \dfrac{1}{\omega_d} \cdot \dfrac{\omega_d}{(s+\zeta\omega_n)^2 + \omega_d^{\,2}} + \dfrac{z_1}{\omega_n^{\,2}} \cdot \\ \left[\dfrac{1}{s} - \dfrac{s+\zeta\omega_n}{(s+\zeta\omega_n)^2 + \omega_d^{\,2}} - \dfrac{\zeta\omega_n}{\omega_d} \cdot \dfrac{\omega_d}{(s+\zeta\omega_n)^2 + \omega_d^{\,2}} \right] \end{array} \right\}, \end{aligned} \quad (5\text{-}7)$$

where $f_{\mathrm{ref}\_\mathrm{pu}}(s) = 1 / s$ and $G_{Pf}(s) / s$ represent the transfer functions of per unit frequency reference and frequency change, respectively. ω_d denotes the damped

angular frequency, which can be expressed as a function of ω_n and ζ:

$$\omega_d = \omega_n \sqrt{1-\zeta^2}. \tag{5-8}$$

Through the inverse Laplace transformation of (5-7), the time domain expression of f_{o_pu} is derived as

$$f_{o\_\text{pu}}(t) = 1 + G_0 \left[\frac{z_1}{\omega_n^{\,2}} - e^{-\zeta\omega_n t} A \sin(\omega_d t + \beta) \right], \tag{5-9}$$

where A and β are expressed as

$$A = \sqrt{(\frac{z_1}{\omega_n^{\,2}})^2 + (\frac{-z_1\zeta + \omega_n}{\omega_n \omega_d})^2}, \beta = \arctan\left[\frac{\omega_d z_1}{(z_1\zeta - \omega_n)\omega_n} \right]. \tag{5-10}$$

With the time domain expression of f_{o_pu}, several important performance indices concerning the frequency regulation can be further derived. By differentiating (5-9) on both sides with respect to time, it yields the expression of the RoCoF $\mathrm{d}f_{o\_\text{pu}} / \mathrm{d}t$:

$$\frac{\mathrm{d}f_{o\_\text{pu}}(t)}{\mathrm{d}t} = G_0 \left[\zeta\omega_n e^{-\zeta\omega_n t} A \sin(\omega_d t + \beta) - e^{-\zeta\omega_n t} A \omega_d \cos(\omega_d t + \beta) \right]. \tag{5-11}$$

Let (5-9) equal zero, the peak time t_{peak} is derived as

$$t_{\text{peak}} = \frac{1}{\omega_d} \left[\arctan(\frac{\sqrt{1-\zeta^2}}{\zeta}) - \beta + \pi \right]. \tag{5-12}$$

Replacing t in the right-hand side of (5-9) by t_{peak}, one obtains the peak frequency, i.e. the frequency nadir $f_{o\_\text{peak\_pu}}$,

$$f_{o\_\text{peak\_pu}} = 1 + \frac{G_0 z_1}{\omega_n^{\,2}} + G_0 e^{-\zeta\omega_n t_{\text{peak}}} A \sqrt{1-\zeta^2}, \tag{5-13}$$

where the first two terms collectively represent the quasi-steady-state frequency (see Figure 5.1). It can be denoted as $f_{o\_\text{qss\_pu}}$ and expressed as

$$f_{o\_\text{qss\_pu}} = 1 + \frac{G_0 z_1}{\omega_n^{\,2}} = 1 - \frac{R_{gd}}{DR_{gd} + 1}, \tag{5-14}$$

where the second equation is satisfied by substituting the relevant parameters in (5-6) into the first equation of (5-14). It is obvious that the inertia coefficient H

has no effect on the quasi-steady-state frequency $f_{o\_qss\_pu}$, as verified by Figure 5.6. However, H greatly affects the RoCoF and frequency nadir according to (5-6), (5-11), and (5-13). An alternative performance index to the frequency nadir is the frequency overshoot $f_{o\sigma}$. Using (5-13) and (5-14), $f_{o\sigma}$ can be derived as

$$f_{o\sigma} = \left| \frac{f_{o\_qss\_pu} - f_{o\_peak\_pu}}{f_{o\_qss\_pu}} \right| \times 100\% = \left| \frac{e^{-\zeta\omega_n t_{peak}} A\sqrt{1-\zeta^2}\,\omega_n^{\,2}}{2H\omega_n^{\,2} - z_1} \right| \times 100\%. \quad (5\text{-}15)$$

Moreover, the settling time t_s, i.e. the time for the grid frequency to reach and stay within the 2% quasi-steady-state frequency error band, can be derived with (5-9) and (5-14) as

$$\left| \frac{f_{o\_pu}(t_s) - f_{o\_qss\_pu}}{1 - f_{o\_qss\_pu}} \right| = 2\% \Rightarrow t_s = -\frac{1}{\zeta\omega_n} \ln\left(\frac{0.02 z_1}{A\omega_n^{\,2}}\right). \quad (5\text{-}16)$$

Using (5-11) − (5-16), Figure 5.7 plots the frequency regulation performance

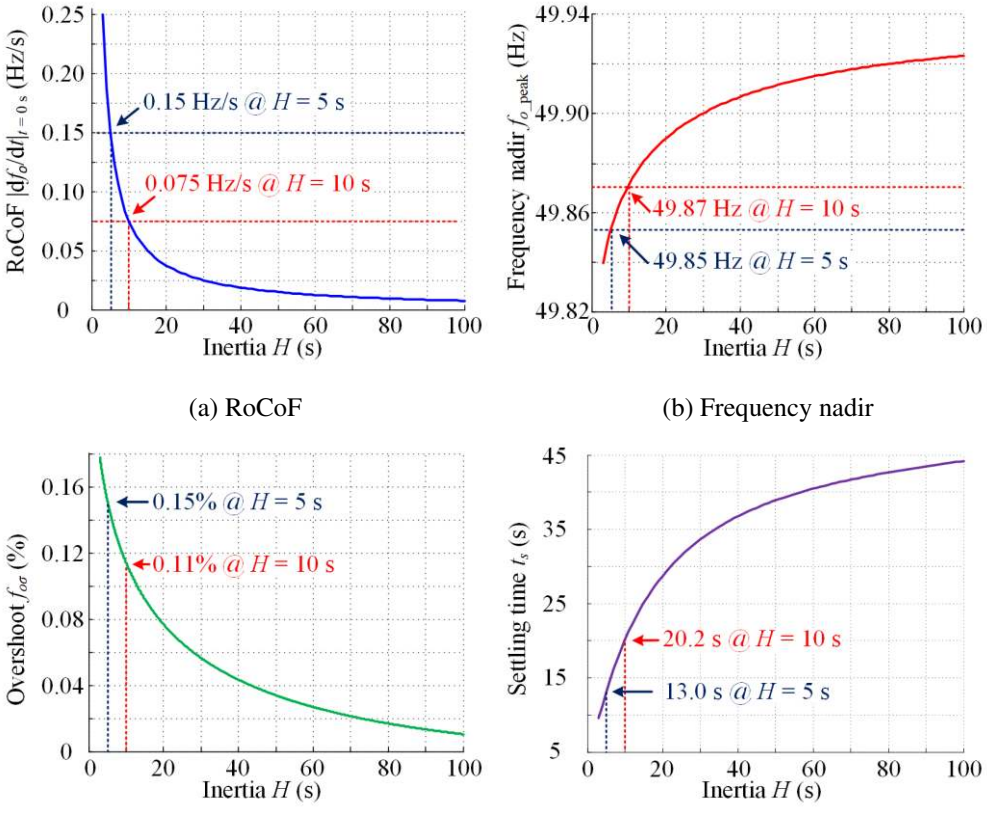

(a) RoCoF (b) Frequency nadir

(c) Overshoot (d) Settling time

Figure 5.7 Frequency regulation performance indices (a) RoCoF, (b) frequency nadir, (c) overshoot, and (d) settling time as a function of H under a 3% step-up load change.

indices as a function of H under a 3% step-up load change, where the performance indices are expressed in real values. It is noted from Figure 5.7(a) that the RoCoF drops as H increases. Figure 5.7(b) confirms that the frequency nadir improves with the increment of H. These curves validate the effectiveness of inertia in suppressing the RoCoF and frequency deviation. Not surprisingly, a small frequency overshoot is to be expected in the case of a large H in Figure 5.7(c). However, increasing H will slow down the dynamics of the frequency regulation and extend the frequency restoration, and this is the biggest drawback of increasing inertia, as verified by Figure 5.7(d). Therefore, a trade-off between frequency nadir/RoCoF and settling time is necessary when designing the inertia coefficient H. In general, increasing H is helpful for the frequency stability of power systems, as it improves the frequency nadir and RoCoF [168-170]. As such, the following sections aim to enhance the power system inertia. Note that the performance indices derived in this section, accompanied by Figure 5.7, serve as the theoretical basis for the design and enhancement of inertia.

5.3 Power Converters with Distributed Virtual Inertia

As discussed, the increment of inertia helps improve the frequency stability and frequency regulation of more-electronics power systems. To increase the power system inertia, this section proposes one effective approach − the distributed virtual inertia provided by grid-connected power converters. Returning to Figure 2.1, either constant voltage sources or capacitors can be connected to the DC-links of grid-connected power converters. When power converters are fed by capacitors, the DC-link capacitors show great promise to provide a certain amount of inertia upon system demands, as will be disclosed.

5.3.1 Fundamental Principle

For conventional synchronous generators, the associated inertia constant H has been given in (5-1). It represents the per unit kinetic energy stored in the rotors of synchronous generators and turbines. Similar to synchronous generators, DC-

link capacitors also store energy, and therefore they have the potential for inertia emulation. Following the definition of H, one can define the inertia coefficient of DC-link capacitors H_{cap} as

$$H_{\text{cap}} = \frac{E_{\text{cap}}}{VA_{\text{base}}} = \frac{C_{\text{cdc}} V_{\text{cdc\_ref}}^{\ 2}}{2VA_{\text{base}}}, \tag{5-17}$$

where C_{cdc} and $V_{\text{cdc\_ref}}$ denote the DC-link capacitance and DC-link voltage reference, respectively.

Figure 5.8 shows the inertia mapping between synchronous generators and DC-link capacitors, where the mechanical angular velocity and electrical angular frequency (denoted as ω_o) are equal for synchronous generators with one pair of poles. The same is true for their respective references (represented as ω_{ref}). It can be observed from Figure 5.8 that the angular frequency ω_o and DC-link voltage v_{cdc} play similar roles in determining the respective inertia coefficients H and H_{cap}, as H and H_{cap} vary in proportional to the squares of ω_{ref} and $V_{\text{cdc\_ref}}$, respectively. This observation implies that the DC-link capacitor can release or absorb energy in a similar way as synchronous generators do if the DC-link voltage v_{cdc} and grid frequency f_o (note that $\omega_o = 2\pi f_o$) are directly related. Through this way, the emulated inertia or virtual inertia can be expected from grid-connected power converters.

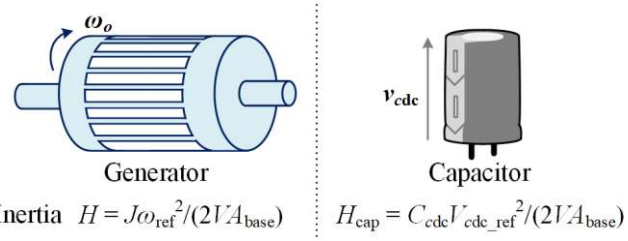

Figure 5.8 Inertia mapping between synchronous generators and DC-link capacitors.

Figure 5.9 illustrates the overall structure of the grid-connected power converters with the distributed virtual inertia, where the CCCs are employed as examples, and PWM refers to the pulse-width modulator. The inner-loop current controller aims to regulate the dq-frame grid currents i_{cgd} and i_{cgq} following their references i_{cgd_ref} and i_{cgq_ref}, which has been well designed in Section 2.4. However, in this case, as the DC-link is no longer fed by a constant voltage source,

the DC-link voltage should be regulated by the outer-loop voltage controller to ensure linear modulations and not to overstress semiconductor devices. The voltage controller is implemented as a PI controller, which controls the DC-link voltage v_{cdc} to track its reference v_{cdc_ref} through the change of the d-axis current reference i_{cgd_ref}, meanwhile the q-axis current reference i_{cgq_ref} depends on the requirement of reactive power compensation. In addition to the voltage and current controllers, the proposed virtual inertia controller linking the grid frequency change Δf_g and the DC-link voltage change Δv_{cdc_ref} through a transfer function $G_{fv}(s)$ is added. It modifies the DC-link voltage during frequency events so that the DC-link capacitor will release or absorb energy for inertia emulation. It should be emphasized that the proposed control scheme only utilizes the DC-link capacitors of power converters, without employing any additional energy storage units. Since the DC-link capacitors are always necessary in grid-connected power converters for DC-link voltage support and harmonic filtering, the proposed control scheme puts no extra burden on hardware designs [18, 75, 171, 172]. Additionally, it is noted from Figure 5.9 that the grid frequency f_g is measured and detected from the grid voltages v_{gabc} by the PLL. Other methods for faster grid frequency detections, such as frequency-locked-loops [173], are also possible. In this part, PLL dynamics are ignored so that $f_g = f_o$ is satisfied.

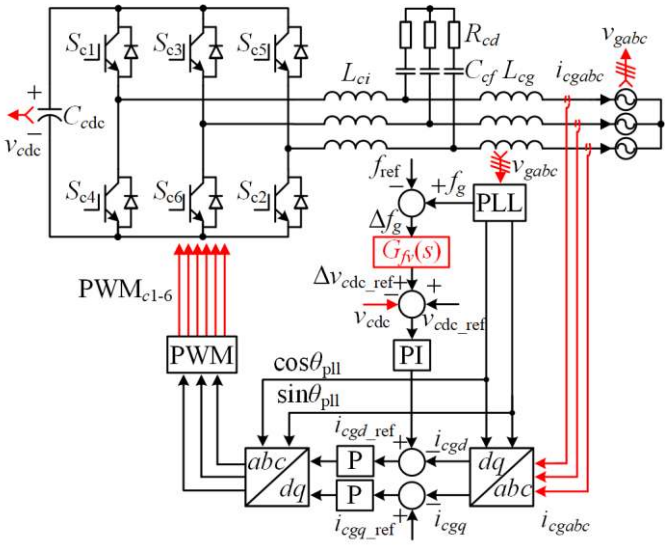

Figure 5.9 Overall structure of grid-connected power converters with distributed virtual inertia.

5.3.2 Analysis of Virtual Inertia

Without considering the proposed virtual inertia control, Figure 5.10 gives the block diagram of the voltage and current controllers of grid-connected power converters in the *s*-domain. The *s*-domain model rather than the mixed *s*- and *z*-domain model is involved, because the frequency regulation of power systems mainly covers the sub-fundamental frequency band, and the *s*-domain is sufficiently accurate in such a low-frequency band. For the same reason, the time-delays due to the calculations and updates of modulation signals are ignored.

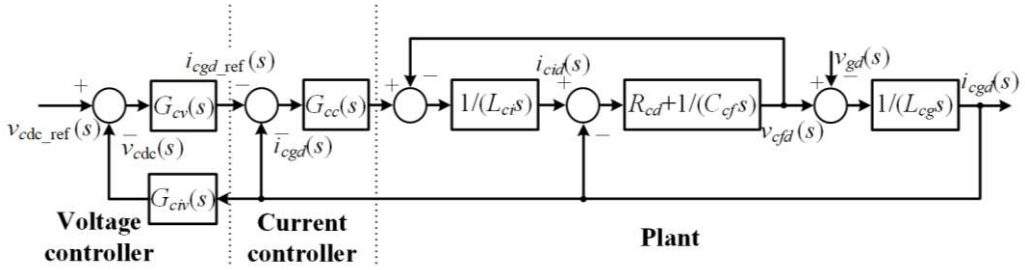

Figure 5.10 Block diagram of the voltage and current controllers of grid-connected power converters in the *s*-domain.

In Figure 5.10, the current controller $G_{cc}(s)$ and voltage controller $G_{cv}(s)$ are implemented as a P controller and a PI controller, respectively. Notice that the minus sign of the current reference i_{cgd_ref} is due to the definition of current directions in Figure 5.9. In addition, $G_{civ}(s)$ denotes the transfer function from the grid-injected current to the DC-link capacitor voltage. Under the assumption of lossless power conversions, $G_{civ}(s)$ can be derived based on the active power balance between AC and DC sides of power converters as

$$G_{civ}(s) = \frac{-3V_{g\_ref}}{2V_{cdc\_ref}C_{cdc}s}, \tag{5-18}$$

where the parameter values can be found in Table 2-4. Note that the damping resistor R_{cd} has been incorporated in the experiments, yet it may also be removed if necessary. Under this condition, the plant model $G_{plant}(s)$ can be referred to (2-30). Using (2-30), the closed-loop transfer function of the current control can be expressed as

$$G_{c\_cl}(s)=\frac{i_{cgd}(s)}{i_{cgd\_ref}(s)}=\frac{G_{cc}(s)G_{plant}(s)}{1+G_{cc}(s)G_{plant}(s)}. \tag{5-19}$$

Furthermore, the closed-loop voltage control transfer function is derived as

$$G_{v\_cl}(s)=\frac{v_{cdc}(s)}{v_{cdc\_ref}(s)}=\frac{G_{c\_cl}(s)G_{cv}(s)}{1+G_{c\_cl}(s)G_{cv}(s)G_{civ}(s)}, \tag{5-20}$$

whose response time normally lies in the range of tenths of seconds [141].

By enabling the proposed virtual inertia control, the frequency regulation framework is changed into Figure 5.11, where an additional branch loop connecting the per unit grid frequency change Δf_{o_pu} to the per unit converter output power change ΔP_{c_pu} appears.

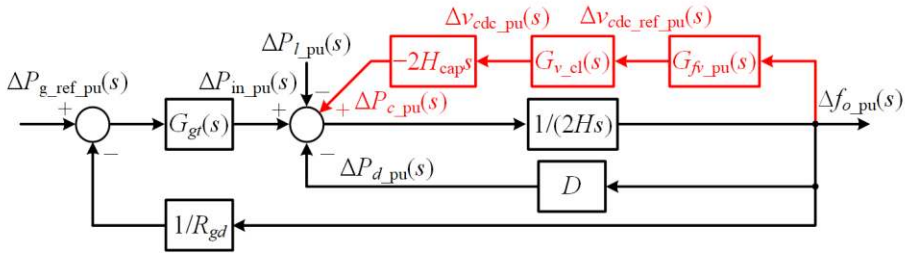

Figure 5.11 Frequency regulation framework with the virtual inertia control.

There are three transfer functions associated with this additional branch loop. The first one is the proposed virtual inertia controller $G_{fv\_pu}(s)$, which links the grid frequency to the DC-link voltage reference. It should be remarked that $G_{fv\_pu}(s)$ is the per unit form controller, and thus it should be scaled before being used to replace $G_{fv}(s)$ in Figure 5.9. The second transfer function $G_{v\_cl}(s)$ models the closed-loop voltage control, as expressed in (5-20). The third transfer function $-2H_{cap}s$ mathematically describes the relationship between DC-link voltage and converter output power. Such a relationship can be derived as follows. Under a DC-link voltage perturbation Δv_{cdc}, the capacitor will release a certain amount of energy ΔE_c, which can be written as

$$\Delta E_c(t)=C_{cdc}V_{cdc\_ref}{}^2/2-C_{cdc}\left[V_{cdc\_ref}+\Delta v_{cdc}(t)\right]^2/2\approx -C_{cdc}V_{cdc\_ref}\Delta v_{cdc}(t), \tag{5-21}$$

where the high-order term pertaining to the square of Δv_{cdc} is ignored. Differentiating (5-21) on both sides, it yields

$$\Delta P_c(t) = \frac{\mathrm{d}\Delta E_c(t)}{\mathrm{d}t} = -C_{c\mathrm{dc}} V_{c\mathrm{dc\_ref}} \frac{\mathrm{d}\Delta v_{c\mathrm{dc}}(t)}{\mathrm{d}t}. \tag{5-22}$$

Upon normalizing, (5-22) becomes

$$\Delta P_{c\_\mathrm{pu}}(t) = -\frac{C_{c\mathrm{dc}} V_{c\mathrm{dc\_ref}}{}^2}{VA_{\mathrm{base}}} \cdot \frac{\mathrm{d}\Delta v_{c\mathrm{dc\_pu}}(t)}{\mathrm{d}t} = -2H_{\mathrm{cap}} \frac{\mathrm{d}\Delta v_{c\mathrm{dc\_pu}}(t)}{\mathrm{d}t}, \tag{5-23}$$

where the second equation is satisfied after substituting H_{cap} in (5-17) into (5-23). Rearranging (5-23) in the s-domain, one obtains

$$\frac{\Delta P_{c\_\mathrm{pu}}(s)}{\Delta v_{c\mathrm{dc\_pu}}(s)} = -2H_{\mathrm{cap}} s, \tag{5-24}$$

which is exactly the third transfer function mentioned before.

By closing the forward path $1 / (2Hs)$ through the feedback loop introduced by the virtual inertia control in Figure 5.11, the swing equation is reshaped as

$$\Delta P_{\mathrm{in\_pu}}(s) - \Delta P_{l\_\mathrm{pu}}(s) = 2[H + \underbrace{H_{\mathrm{cap}} G_{v\_\mathrm{cl}}(s) G_{fv\_\mathrm{pu}}(s)}_{\text{Virtual Inertia}}] s f_{o\_\mathrm{pu}}(s) + D\Delta f_{o\_\mathrm{pu}}(s), \tag{5-25}$$

where the second term of the equivalent inertia coefficient $H_{\mathrm{cap}} G_{v\_\mathrm{cl}}(s) G_{fv\_\mathrm{pu}}(s)$ quantifies the degree of inertia enhancement, and it is defined as the virtual inertia coefficient $H_p(s)$, i.e.

$$H_p(s) = H_{\mathrm{cap}} G_{v\_\mathrm{cl}}(s) G_{fv\_\mathrm{pu}}(s). \tag{5-26}$$

Note that the DC-link voltage control features much faster dynamics as compared with the frequency control, and therefore the closed-loop voltage control $G_{v\_\mathrm{cl}}(s)$ can be simplified into one when analyzing the effect of the virtual inertia control. In order to obtain a constant inertia coefficient H_p, the virtual inertia controller $G_{fv\_\mathrm{pu}}(s)$ should be implemented as a P controller with a gain K_{fv_pu} according to (5-26). Referring to Figure 5.9, the virtual inertia control gain K_{fv} equals the ratio of $\Delta v_{c\mathrm{dc\_ref}}$ to Δf_g or Δf_o, whereupon the relevant per unit variables have the following relationship:

$$K_{fv\_\mathrm{pu}} = \frac{\Delta V_{c\mathrm{dc\_max}} / V_{c\mathrm{dc\_ref}}}{\Delta f_{\mathrm{max}} / f_{\mathrm{ref}}}, \tag{5-27}$$

where $\Delta V_{c\mathrm{dc\_max}}$ and Δf_{max} denote the maximum acceptable voltage change and frequency change, respectively. $V_{c\mathrm{dc\_ref}}$ and f_{ref} are employed here to normalize

the voltage change and frequency change, respectively. Through the proposed virtual inertia control, the DC-link voltage v_{cdc} is confined to [($V_{cdc\_ref} - \Delta V_{cdc\_max}$ / 2), ($V_{cdc\_ref} + \Delta V_{cdc\_max}$ / 2)], where the minimum voltage ($V_{cdc\_ref} - \Delta V_{cdc\_max}$ / 2) is designed to ensure the linear modulations of power converters, and it can be improved through the injection of a third-order harmonic term into the modulation references [19]. In contrast, the maximum voltage ($V_{cdc\_ref} + \Delta V_{cdc\_max}$ / 2) depends on the voltage capabilities of semiconductors and DC-link capacitor.

Substitution of (5-17), (5-27), and $G_{v\_cl}(s)$ = 1 into (5-26), the virtual inertia coefficient can be reorganized as

$$H_p = \frac{C_{cdc} V_{cdc\_ref} \Delta V_{cdc\_max} f_{ref}}{2VA_{base} \Delta f_{max}}, \tag{5-28}$$

where the virtual inertia coefficient H_p is noted to be mainly determined by the DC-link capacitance C_{cdc}, rated DC-link voltage V_{cdc_ref}, and maximum acceptable voltage change ΔV_{cdc_max} under a certain power rating VA_{base} and a ratio of the frequency change $\Delta f_{max} / f_{ref}$.

According to the system and control parameters formulated in Table 5-3 and Table 5-4, respectively, VA_{base} = 1 kVA, Δf_{max} = 0.2 Hz, and f_{ref} = 50 Hz are

Table 5-3 System parameters for testing the distributed virtual inertia.

Description	Symbol	Value
Filter capacitance	C_{cf}	5 μF
Grid filter inductance	L_{cg}	1 mH
Converter filter inductance	L_{ci}	1 mH
Damping resistor	R_{cd}	1 Ω
DC-link capacitance	C_{cdc}	2.82 mF
DC-link voltage reference	V_{cdc_ref}	400 V
Maximum voltage change	ΔV_{cdc_max}	36 V
Grid voltage reference (rms)	V_{g_ref}	110 V
Fundamental frequency	f_{ref}	50 Hz
Maximum frequency change	Δf_{max}	0.2 Hz
Power rating	VA_{base}	1 kVA
Switching/sampling frequency	f_{sw}/f_s	10 kHz

Table 5-4 Control parameters for testing the distributed virtual inertia.

Description	Symbol	Value
Frequency droop coefficient	R_{gd}	0.05
Speed governor coefficient	T_G	0.1 s
Turbine HP coefficient	F_{HP}	0.3 s
Time constant of main inlet volumes	T_{CH}	0.2 s
Time constant of reheater	T_{RH}	7.0 s
Damping coefficient	D	1
Synchronous generators inertia coefficient	H	5 s
Capacitor inertia coefficient	H_{cap}	0.225 s
Virtual inertia control gain	$K_{fv}/K_{fv\_\mathrm{pu}}$	180/22.5
Virtual inertia coefficient	H_p	5 s

satisfied. Under this condition, Figure 5.12 plots the virtual inertia coefficient H_p as functions of DC-link capacitance $C_{c\mathrm{dc}}$, DC-link voltage reference $V_{c\mathrm{dc\_ref}}$, and maximum acceptable voltage change $\Delta V_{c\mathrm{dc\_max}}$. It is obvious that H_p increases linearly with the increment of $C_{c\mathrm{dc}}$, $V_{c\mathrm{dc\_ref}}$, and $\Delta V_{c\mathrm{dc\_max}}$. Additionally, power converters have the potential to generate larger virtual inertia than the inertia provided by synchronous generators (H normally ranges from 2 s to 10 s [13, 174]). However, this is achieved under the scenarios of large DC-link capacitances, DC-link voltages, and/or voltage deviations, which challenge the design of power converters in terms of cost, size, and control. Therefore, it is recommended to emulate only an appropriate amount of inertia for frequency stability enhancement.

5.3.3 Design of Virtual Inertia

After the analysis of virtual inertia, this subsection further presents the design procedure of virtual inertia. Figure 5.13 illustrates a design flowchart of virtual inertia, where the requirements of frequency regulation performance indices, such as the RoCoF and frequency nadir, are used as inputs, while the DC-link capacitance $C_{c\mathrm{dc}}$, DC-link voltage reference $V_{c\mathrm{dc\_ref}}$, and its maximum allowable change $\Delta V_{c\mathrm{dc\_max}}$ serve as outputs. With the knowledge of targeted RoCoF and

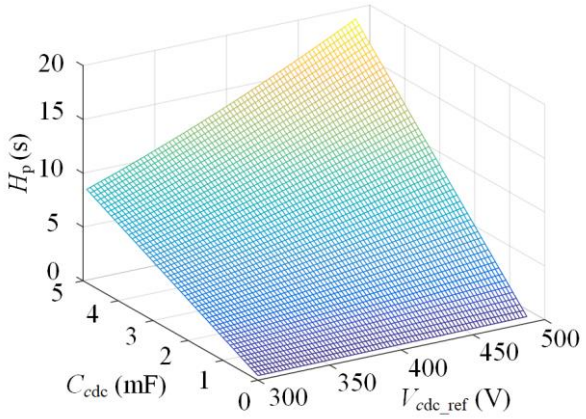

(a) Variations of C_{cdc} and V_{cdc_ref} ($\Delta V_{cdc\_max} = 0.15V_{cdc\_ref}$)

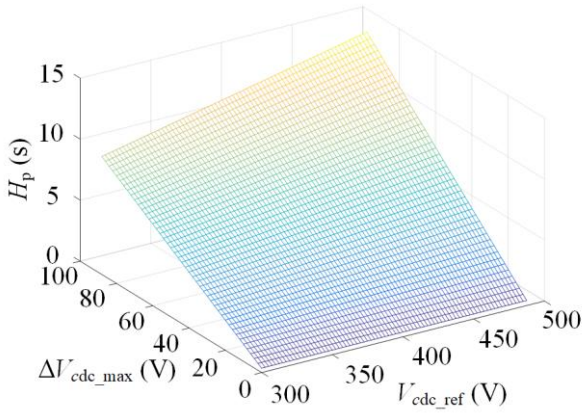

(b) Variations of ΔV_{cdc_max} and V_{cdc_ref} (C_{cdc} = 2.82mF)

Figure 5.12 Plots of the virtual inertia coefficient H_p as functions of (a) C_{cdc} and V_{cdc_ref} and (b) ΔV_{cdc_max} and V_{cdc_ref}.

and frequency nadir, the required inertia coefficient $H + H_p$ can be specified based on Figure 5.7. Furthermore, the virtual inertia coefficient H_p can be readily obtained if H is given. Referring to the system parameters VA_{base}, f_{ref}, and Δf_{max}, the design parameters C_{cdc}, V_{cdc_ref}, and ΔV_{cdc_max} can be determined according to Figure 5.12. If the design result gives rise to an overmodulation, the design parameters and/or performance indices should be modified.

5.3.4 Simulation and Experimental Verifications

The simulations were conducted under the Matlab/Simulink environment to

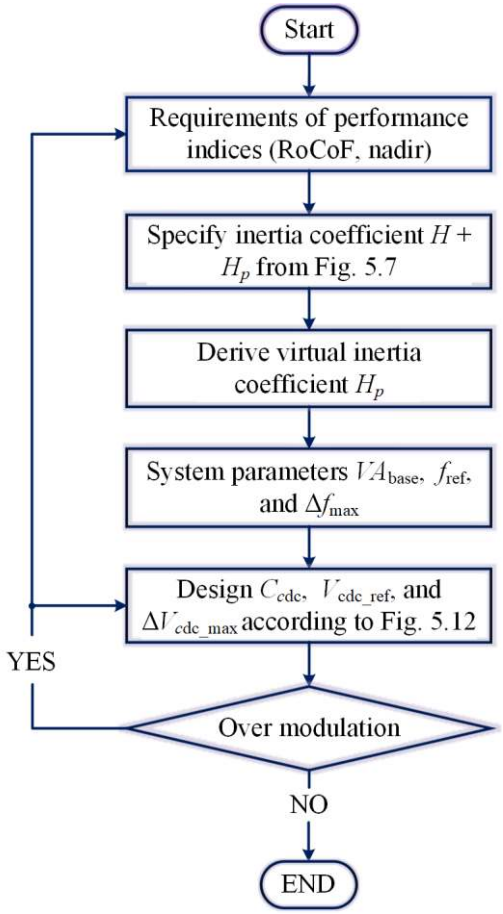

Figure 5.13 Design flowchart of virtual inertia.

illustrate the benefits of the proposed virtual inertia control. According to Table 5-3, the virtual inertia coefficient H_p is calculated to be 5 s, which is identical to the inertia coefficient of the synchronous generator, as listed in Table 5-4. Stated another way, it is possible to replace synchronous generators with power converter-interfaced renewable generators without any inertia reduction. In this sense, the proposed approach can be a promising solution to the lack of inertia issue faced by more-electronics power systems.

Figure 5.14 illustrates the simulation waveforms of grid frequency f_o and DC-link voltage v_{cdc} during a 3% step-up load change. As shown, in the face of this low-frequency event, the case without the virtual inertia control registers a frequency nadir f_{o_peak} of 49.84 Hz and a maximum frequency deviation of 0.16 Hz. In contrast, the frequency nadir and maximum frequency deviation are improved to 49.86 Hz and 0.14 Hz, respectively, after the proposed virtual inertia

control is employed. In other words, a 12.5% improvement of the frequency nadir can be expected with the proposed method. Moreover, the RoCoF $|\mathrm{d}f_o / \mathrm{d}t|_{t=0\,\mathrm{s}}$ is observed to decrease from 0.150 Hz/s to 0.075 Hz/s, representing a 50% enhancement of the RoCoF. It should be emphasized that these performance indices can be further improved through the design of the virtual inertia coefficient H_p if necessary. During the frequency event, the DC-link voltage v_{cdc} varies in proportional to the frequency f_o for inertia emulation. Upon reaching quasi-steady-state, the frequency and voltage are fixed at 49.93 Hz and 387 V, respectively. Such errors can be further corrected by the secondary frequency

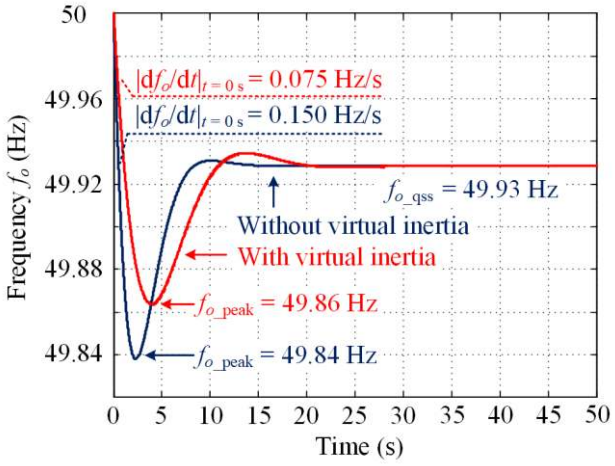

(a) Frequency f_o

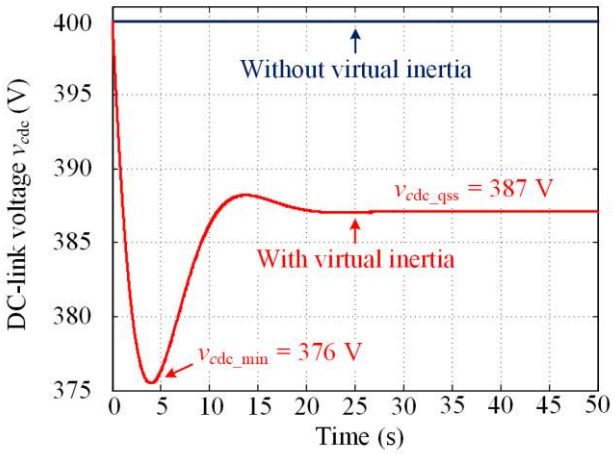

(b) DC-link voltage v_{cdc}

Figure 5.14 Simulation waveforms of (a) frequency f_o and (b) DC-link voltage v_{cdc} with and without the distributed virtual inertia under a 3% step-up load change.

control, whose effect has been verified in Figure 2.23.

Figure 5.15 presents the changes of output energy ΔE_c and power ΔP_c during the same frequency event of a 3% step-up load change. Obviously, the power converter with the distributed virtual inertia outputs energy in support of the frequency regulation during frequency dynamics. After the support, its power change restores. In this sense, the proposed virtual inertia control will not interfere with the normal operations of power converters.

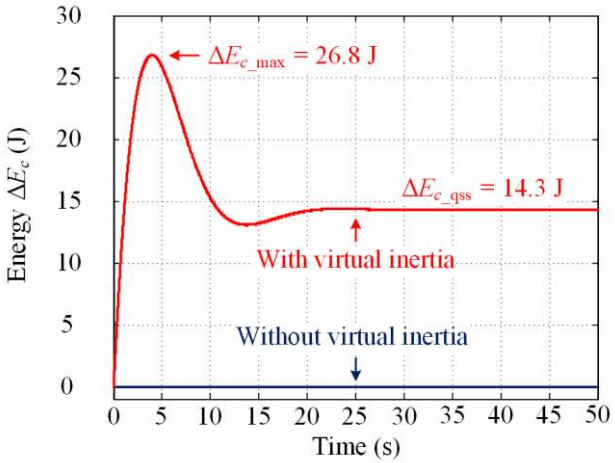

(a) Energy change ΔE_c

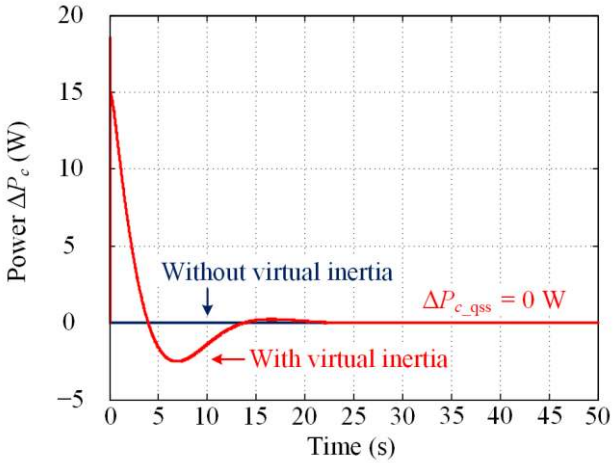

(b) Power change ΔP_c

Figure 5.15 Simulation waveforms of (a) energy change ΔE_c and (b) power change ΔP_c with and without the distributed virtual inertia under a 3% step-up load change.

In contrast, Figure 5.16 presents the simulation waveforms of frequency f_o and DC-link voltage v_{cdc} under a 3% step-down load change. In this case, the

frequency climbs up during the frequency event, and a positive quasi-steady-state frequency f_{o_qss} is to be observed. Without the distributed virtual inertia, the frequency peaks at 50.16 Hz. This value is improved to be 50.14 Hz when the virtual inertia control is activated. Once again, a 50% improvement of the RoCoF from 0.150 Hz/s to 0.075 Hz/s can be noticed. During the frequency event, the DC-link voltage v_{cdc} changes in proportional to the frequency for generating the virtual inertia.

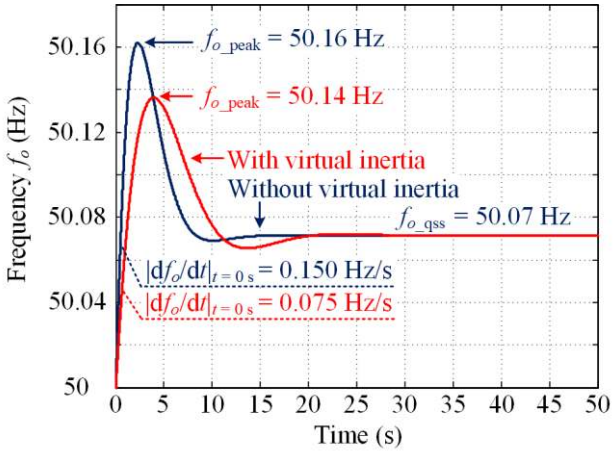

(a) Frequency f_o

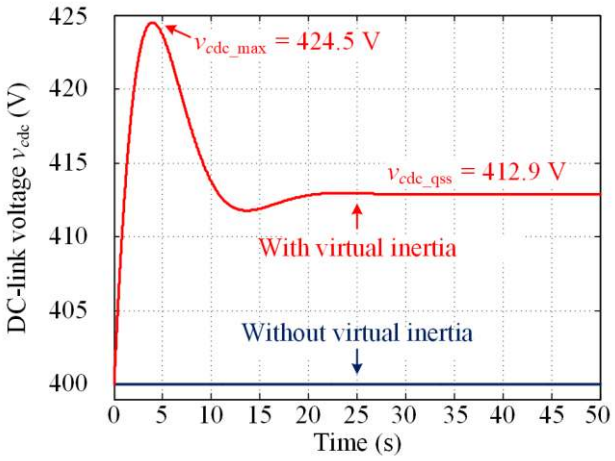

(b) DC-link voltage v_{cdc}

Figure 5.16 Simulation waveforms of (a) frequency f_o and (b) DC-link voltage v_{cdc} with and without the distributed virtual inertia under a 3% step-down load change.

The relevant waveforms of output energy change ΔE_c and power change ΔP_c are given in Figure 5.17. During the over-frequency event, the power converter

absorbs energy and power from the grid for balancing the generation and demand. Once the frequency event settles down, the converter power change returns to zero.

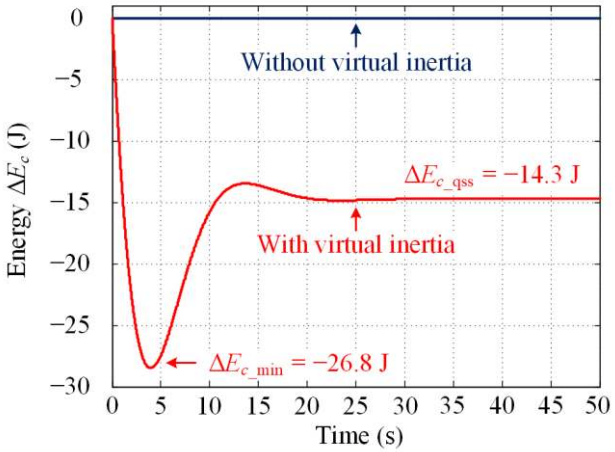

(a) Energy change ΔE_c

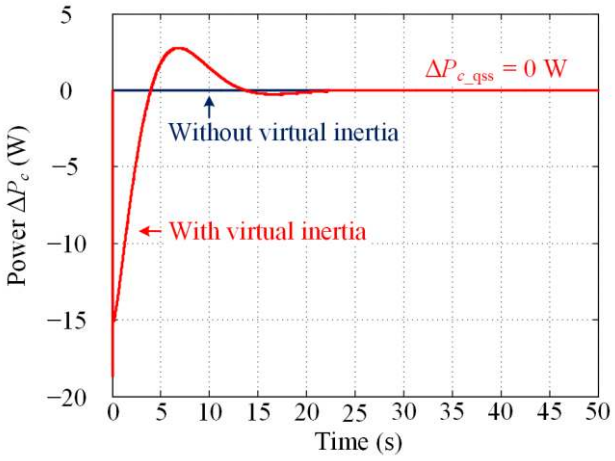

(b) Power change ΔP_c

Figure 5.17 Simulation waveforms of (a) energy change ΔE_c and (b) power change ΔP_c with and without the distributed virtual inertia under a 3% step-down load change.

To further validate the correctness of simulation results, experiments were carried out with the system and control parameter values given in Table 5-3 and Table 5-4, respectively. Remember that the VSG is employed in replacement of the conventional synchronous generator for the frequency regulation, and the design of VSGs has been discussed in Chapter 2. Other VSG designs with similar frequency control objectives can be found in [37, 65, 175-177]. With the help of

the VSG, the improvement of the frequency regulation by grid-connected power converters can be verified.

Figure 5.18 provides the experimental waveforms of the power converters with and without the proposed distributed virtual inertia when they are subjected to a 3% step-up load change. Similar to Figure 5.14, the proposed virtual inertia control contributes to the improvement of the frequency stability. Specifically, the frequency nadir and RoCoF increase from 49.83 Hz and 0.150 Hz/s to 49.86 Hz and 0.075 Hz/s, respectively, thereby validating the effectiveness of the distributed virtual inertia. Note that the DC-link voltage varies in proportional to the frequency for inertia emulation.

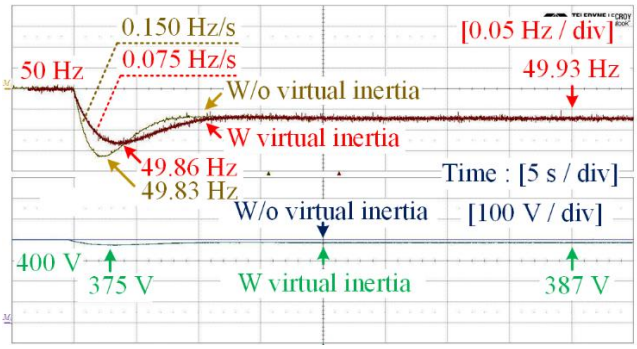

Figure 5.18 Experimental waveforms of frequency f_o (top) and DC-link voltage v_{cdc} (bottom) with and without the distributed virtual inertia under a 3% step-up load change.

Figure 5.19 sketches the experimental waveforms of energy change and power change of power converters in the presence of a 3% step-up load change. In accordance with Figure 5.15, the power converter the virtual inertia contributes additional power only before the frequency reaches its quasi-steady-state.

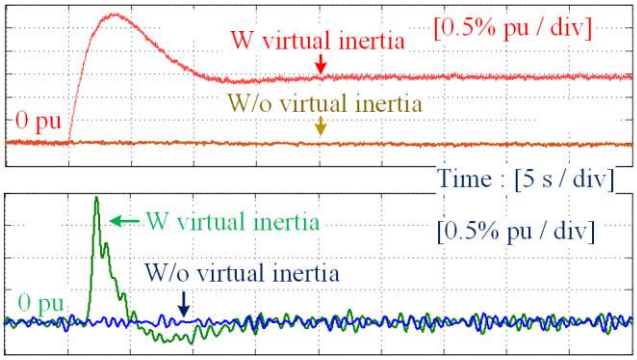

Figure 5.19 Experimental waveforms of energy change ΔE_c (top) and power change ΔP_c (bottom) with and without the distributed virtual inertia under a 3% step-up load change.

Figure 5.20 shows the experimental waveforms of frequency f_o and DC-link voltage v_{cdc} under a 3% step-down load change. In response to the frequency rise, the DC-link voltage increases proportionally. As a result, the frequency peak and RoCoF are improved from 50.16 Hz and 0.150 Hz/s to 50.13 Hz and 0.075 Hz/s, respectively. The corresponding waveforms of energy change ΔE_c and power change ΔP_c are illustrated in Figure 5.21. From the above analysis, the simulation and experimental results agree with the predicted results given in Section 5.2, thereby indicating the effectiveness of the proposed inertia analysis method in predicting the values of performance indices. The slight differences among predicted, simulation, and experimental results may be caused by the errors due to model simplification (see Figure 5.6) and signal measurements.

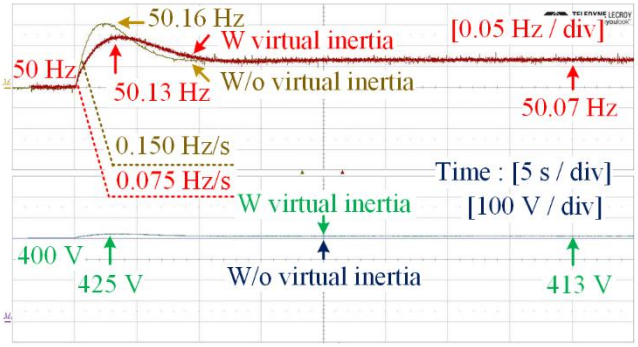

Figure 5.20 Experimental waveforms of frequency f_o (top) and DC-link voltage v_{cdc} (bottom) with and without the distributed virtual inertia under a 3% step-down load change.

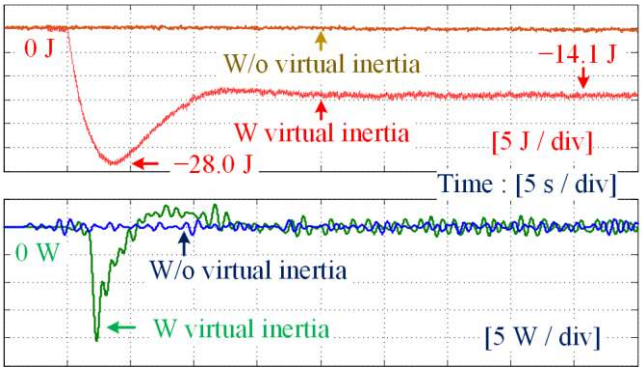

Figure 5.21 Experimental waveforms of energy change ΔE_c (top) and power change ΔP_c (bottom) with and without the distributed virtual inertia under a 3% step-down load change.

So far, the effectiveness of the proposed distributed virtual inertia has been demonstrated. It is capable of improving the frequency nadir and RoCoF during frequency events. Furthermore, the design parameters of virtual inertia has been

identified. Through the change of design parameters, the virtual inertia is flexibly designed. The proposed virtual inertia control can be easily implemented without changing of hardware. Under the cases where the virtual inertia emulated by DC-link capacitors is insufficient, ultracapacitors can be further incorporated and used as inertia suppliers, as detailed in the next section.

5.4 VSGs with Hybrid Energy Storage Systems (HESSs)

Another possibility for inertia enhancement is the virtual inertia contributed by VSGs. It is known that VSGs are expected to regulate the grid frequency in replacement of conventional synchronous generators in future more-electronics power systems. Therefore, they should contribute the power system inertia and provide inertial responses during frequency events. However, unlike synchronous generators, VSGs are essentially power converters without kinetic energy storage. In order to absorb and deliver energy as synchronous generators do, VSGs should incorporate energy storage systems (ESSs). Nevertheless, the implementation and coordination control of ESSs in VSGs have not been covered in the literature. To fill this gap, this section proposes the HESS including a battery and an ultracapacitor for VSGs to achieve the frequency regulation. The most salient feature of the proposed HESS lies in that the ultracapacitor automatically tackles the fast-changing power due to inertia emulation while the battery compensates for the long-term power fluctuations required by the remaining parts of VSGs. In doing so, the proposed HESS allows the reductions of battery power fluctuation and changing rate. This part includes the author's paper in [178].

5.4.1 System Implementation

As discussed in Chapter 2, the most popular implementation of VSGs is a VCC fed by an ideal DC voltage source in Figure 2.3. Based on this configuration, the previous research works on VSGs only focus on the controller designs and rarely touches the practical implementations of VSGs [37, 63, 66, 176, 177, 179]. In

these research works, the power required by all the control loops of VSGs is provided by the ideal voltage source, which is certainly not the real case. To implement the frequency regulation, VSGs should inject or absorb a certain amount of energy during frequency events. This means that the ESSs capable of storing and releasing energy should be included in VSGs.

For selection of energy storage units in ESSs, it is highly desirable that high-energy density units and high-power density units can be used together so that the system lifetime can be extended without any significant compromise on the system cost. One such example is the battery/ultracapacitor HESS, where the battery features a high-energy density while the ultracapacitor is characterized by a high-power density [9, 10, 32, 180]. Through low-/high-pass filters, the low-frequency power command can be extracted and applied to the battery control, while the high-frequency power command is assigned to the ultracapacitor control. Although filters are effective in terms of power allocation, it is difficult to design the cut-off frequency of such filters, and it is typically determined through trial and error [9, 32].

In order to get rid of the difficulties associated with filter designs, this section proposes a novel approach for power allocation. Specifically, the high-frequency power fluctuations due to inertia emulation are allocated to the ultracapacitor. In contrast, the low-frequency power fluctuations required by the remaining parts of the VSG control, i.e. the frequency droop and reheat turbine, are handled by the battery. Through this approach, one can fully utilize the benefits of both battery and ultracapacitor to realize a practical VSG system. Moreover, since the VSG controllers are designed following the standard frequency regulation framework, there are clear physical meanings related to the key parameters of the VSG control, such as the inertia coefficient H. This in turn greatly facilitates the design of the HESS, as the proposed HESS is designed following the model and control of VSGs, and the power references of ultracapacitor and battery are derived from inertia emulation and the remaining parts of the VSG control rather than conventional low- or high-pass filters, respectively.

Figure 5.22 illustrates the schematic diagram of the proposed VSG system, where the battery/ultracapacitor (UC) HESS is intended to regulate the grid voltages and frequency, while the renewable generation system operates in the MPPT mode to optimize the energy yield. In the HESS, the ultracapacitor is placed in the DC-link of a three-phase inverter, while the battery is tied to the ultracapacitor through a DC-DC power converter (a boost converter here). Such an implementation of HESSs allows the simplification of the battery management system due to the low battery voltage, and other potential configurations for HESS implementations can be found in [180]. The system parameters are tabulated in Table 5-5.

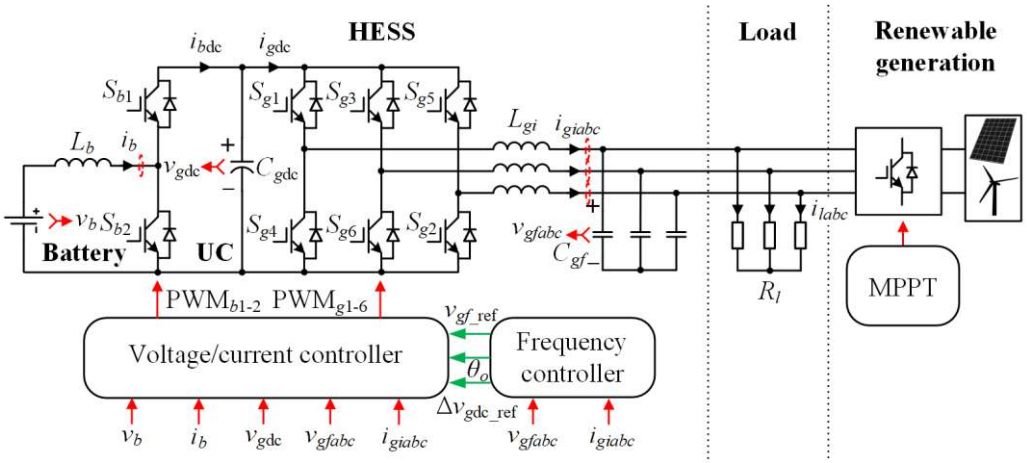

Figure 5.22 Schematic diagram of the proposed VSG system (UC: ultracapacitor).

Table 5-5 System parameters of the proposed VSG system.

Description	Symbol	Value
AC filter capacitance	C_{gf}	50 μF
AC filter inductance	L_{gi}	1 mH
AC voltage reference (rms)	V_{gf_ref}	110 V
DC-link voltage reference	V_{gdc_ref}	400 V
DC-link capacitance	C_{gdc}	3.76 mF
DC filter inductance	L_b	5.6 mH
Battery voltage reference	V_{b_ref}	250 V
Maximum DC-link voltage change	ΔV_{gdc_max}	27 V
Maximum frequency change	Δf_{max}	0.2 Hz
Power rating	VA_{base}	1 kVA
Switching/sampling frequency	f_{sw}/f_s	10 kHz

5.4.2 Control Structure

In Figure 5.22, the voltage/current controller aims to tightly regulate the grid voltages v_{gfx} ($x = a, b, c$) as well as the DC-link voltage v_{gdc}, i.e. the ultracapacitor voltage, whose references are provided by the frequency controller. In accordance with these two control objectives, the voltage/current controller is separated into two parts, namely the AC and DC voltage/current controllers, and each part is tasked at one control objective. The AC voltage/current controller performs the regulation of grid voltages v_{gfx} ($x = a, b, c$) according to their amplitude reference v_{gf_ref} and phase angle reference θ_o. This controller has been carefully designed in Section 2.3 with the relevant control block diagram shown in Figure 2.5 and control parameters listed in Table 2-4, respectively.

In contrast, the DC voltage/current controller is intended to control the DC-link voltage v_{gdc}. It features a cascaded control structure, consisting of an inner current-loop and an outer voltage-loop. Figure 5.23 illustrates the block diagram of the DC voltage/current controller, where $G_{bv}(z)$ and $G_{bc}(z)$ denote the voltage controller and current controller, respectively. D_b represents the quiescent duty ratio of the boost converter, and $D_b' = 1 - D_b$ stands for the compliment duty ratio. The DC voltage/current controller can be designed following the guidelines provided in the second part of [20], and the relevant control parameters are formulated in Table 5-6. It should be highlighted that the voltage reference is flexibly adjusted by the frequency controller through a term Δv_{gdc_ref}. By doing so, the ultracapacitor will automatically absorb or release the power required by inertia emulation, as will be detailed.

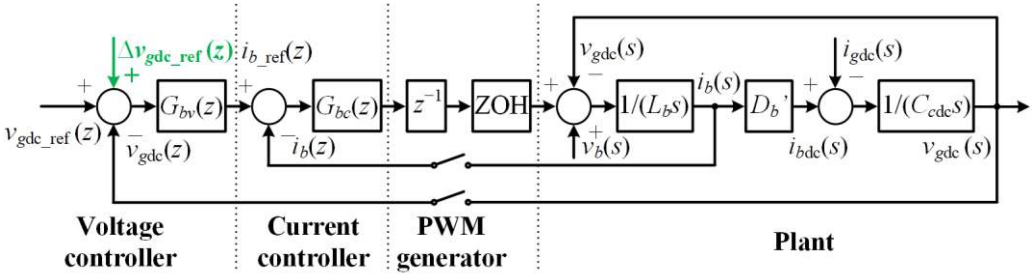

Figure 5.23 Block diagram of the DC voltage/current controller of HESSs.

Table 5-6 Control parameters of the DC voltage/current controller of HESSs.

Description	Symbol	Value
Voltage proportional gain	K_{bvp}	0.1
Voltage integral gain	K_{bvi}	1
Current proportional gain	K_{bcp}	30
Quiescent duty ratio	D_b	0.375
Quiescent compliment duty ratio	D_b'	0.625

The structure of the frequency controller in Figure 5.22 mainly follows that of Figure 2.21. The difference lies in that the frequency controller presented here provides the DC-link voltage reference change $\Delta v_{g\text{dc\_ref}}$ in addition to the voltage amplitude reference v_{gf_ref} and phase angle θ_o. The DC-link voltage reference change $\Delta v_{g\text{dc\_ref}}$ will be sent to the DC voltage/current controller after being calculated by the frequency controller. Figure 5.24 details the block diagram of the proposed frequency controller, where the transformations between per unit and real parameters are explicitly shown. As mentioned, $G_{gt}(s)$ models the dynamics of speed governor and reheat turbine, and its expression can be found in (2-35). The definitions of control parameters, together with their values, are tabulated in Table 5-7. Heightened attention should be attached to the proportional gain K_{fv_pu}, which directly links the grid frequency f_o (note that f_o = f_g in the situation of an ideal frequency measurement) to the DC-link voltage reference $v_{g\text{dc\_ref}}$ for inertia emulation. By following the virtual inertia concept proposed in the previous section, the DC-link capacitor, namely the ultracapacitor, can be exploited to generate the virtual inertia when its voltage is proportionally related to the grid frequency. In consequence, the power allocation between ultracapacitor and battery can be achieved, as will be explained in the next subsection.

5.4.3 Power Management Scheme

Figure 5.25 presents the block diagram of the frequency regulation framework of the proposed VSG system. Since the frequency regulation is mainly related to

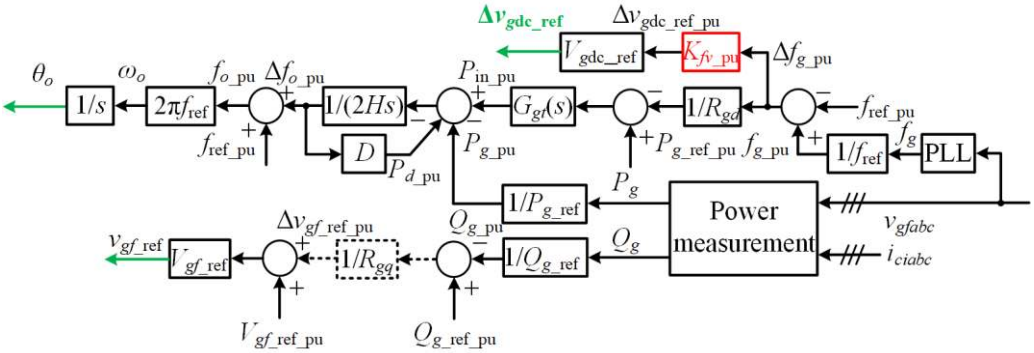

Figure 5.24 Block diagram of the frequency controller of HESSs.

Table 5-7 Control parameters of the frequency controller of HESSs.

Description	Symbol	Value
Frequency droop coefficient	R_{gd}	0.05
Reactive power droop coefficient	R_{gq}	20
Speed governor coefficient	T_G	0.1 s
Turbine HP coefficient	F_{HP}	0.3 s
Time constant of main inlet volumes	T_{CH}	0.2 s
Time constant of reheater	T_{RH}	7.0 s
Inertia coefficient	H	5 s
Damping coefficient	D	1
Virtual inertia control gain	$K_{fv}/K_{fv\_\mathrm{pu}}$	133/16.6
Ultracapacitor inertia coefficient	H_{uc}	0.3 s
Virtual inertia coefficient	H_p	5 s
Active power reference	P_{g_ref}	1 kW
Reactive power reference	Q_{g_ref}	0 Var
Fundamental frequency	f_{ref}	50 Hz

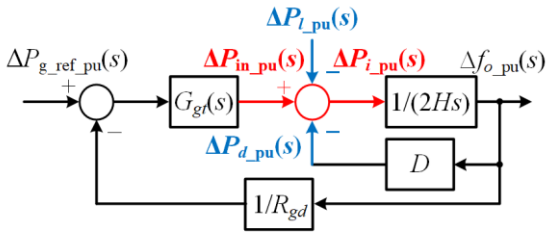

Figure 5.25 Block diagram of the frequency regulation framework of the proposed VSG system.

the active power control, the blocks associated with the reactive power control are ignored in this subsection. Notice that the proposed frequency regulation framework is identical to the standard frequency regulation framework shown in

Figure 5.4. This can be understandable as the proposed VSG is expected to regulate the grid frequency as conventional synchronous generators do. However, it should be highlighted that the focus here is on the power allocation rather than the frequency regulation.

Referring to the power summing node in Figure 5.25, one can obtain the swing equation, which has been given in (5-2) and is reorganized as follows:

$$\Delta P_{\text{in\_pu}}(s) - \Delta P_{l\_\text{pu}}(s) - \Delta P_{d\_\text{pu}}(s) = \Delta P_{i\_\text{pu}}(s), \tag{5-29}$$

where $\Delta P_{\text{in\_pu}}$ denotes the VSG input power change. ΔP_{l_pu} represents the power change caused by the resistive loads and RESs, which equals the VSG output power change ΔP_{g_pu} here because there are no physical frequency-dependent loads in the testing system, and their effects are emulated by the VSG for simplicity. ΔP_{d_pu} stands for the power change of frequency-dependent loads. ΔP_{i_pu} designates the power change required for inertia emulation. According to Figure 5.25, ΔP_{d_pu} and ΔP_{i_pu} can be further expressed as

$$\Delta P_{d\_\text{pu}}(s) = D\Delta f_{o\_\text{pu}}(s), \tag{5-30}$$

$$\Delta P_{i\_\text{pu}}(s) = 2Hs\Delta f_{o\_\text{pu}}(s). \tag{5-31}$$

Substituting of (5-30) and (5-31) into (5-29) and rearranging it yields

$$\underbrace{\Delta P_{\text{in\_pu}}(s)}_{\text{Battery}} + \underbrace{\left[-2Hs\Delta f_{o\_\text{pu}}(s)\right]}_{\text{Ultracapacitor}} = \underbrace{\Delta P_{l\_\text{pu}}(s) + D\Delta f_{o\_\text{pu}}(s)}_{\text{Loads and RESs}}, \tag{5-32}$$

where the power changes in the left-hand side should be supplied by the VSG to balance the load and RES power changes in the right-hand side in real time.

Returning to Figure 5.25, in the face of a sudden load change ΔP_{l_pu}, the VSG will increase its input power such that $\Delta P_{\text{in\_pu}} = -G_{gt}(s)\Delta f_{o\_\text{pu}} / R_{gd}$ provided that the power reference is fixed, i.e. $\Delta P_{g\_\text{ref\_pu}} = 0$. In steady state, $\Delta P_{\text{in\_pu}} = -\Delta f_{o\_\text{pu}} / R_{gd}$ is satisfied. It should be noted that there is a large reheat turbine time constant T_{RH} associated with $G_{gt}(s)$, and thus the VSG input power $P_{\text{in\_pu}}$ changes very slowly during transients. As the battery features a higher-energy density and a lower-power density as compared with the ultracapacitor, the slowly changing power $\Delta P_{\text{in\_pu}}$ is allocated to the battery, or

$$\Delta P_{\text{bat\_pu}}(s) = \Delta P_{\text{in\_pu}}(s) = -\frac{G_{gt}(s)\Delta f_{o\_\text{pu}}(s)}{R_{gd}}, \tag{5-33}$$

where $\Delta P_{\text{bat\_pu}}$ denotes the per unit battery power change. In contrast, the power change ($-2Hs\Delta f_{\text{o\_pu}}$) or $-\Delta P_{i\_\text{pu}}$ required by inertia emulation varies very fast, as it incorporates a differential operator, thereby indicating that the relevant power changes in proportional to the time-derivative of the grid frequency. In light of the high-power density feature of ultracapacitors, the fast-changing power is assigned to the ultracapacitor, i.e.

$$\Delta P_{\text{uc\_pu}}(s) = -\Delta P_{i\_\text{pu}}(s) = -2Hs\Delta f_{o\_\text{pu}}(s). \tag{5-34}$$

where $\Delta P_{\text{uc\_pu}}$ represents the per unit ultracapacitor power change. The principle of power allocation is shown vividly in Figure 5.26, where the power imbalance introduced by the changes of RESs and loads will be compensated by the changes of battery and ultracapacitor powers, as mathematically described by (5-32).

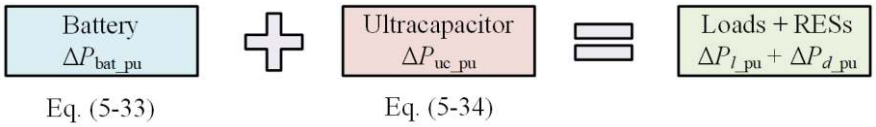

Figure 5.26 Principle of power allocation according to (5-32).

As stated, the ultracapacitor is expected to generate or absorb the required power for inertia emulation after its per unit voltage $v_{g\text{dc\_pu}}$ and grid frequency f_{o_pu} are proportionally linked through the proportional control gain K_{fv_pu} in Figure 5.24. Therefore, the virtual inertia contributed by the ultracapacitor can be derived following the same procedure as given in the previous section. Recalling (5-17), the ultracapacitor inertia coefficient H_{uc} can be defined as

$$H_{\text{uc}} = \frac{E_{\text{uc}}}{VA_{\text{base}}} = \frac{C_{g\text{dc}}V_{g\text{dc\_ref}}{}^2}{2VA_{\text{base}}}, \tag{5-35}$$

where E_{uc} refers to the energy stored in the ultracapacitor, and the remaining parameters can be found in Table 5-5. Similar to (5-23), under a DC-link voltage perturbation, the per unit power released by the ultracapacitor is

$$\Delta P_{\text{uc\_pu}}(t) = -2H_{\text{uc}}\frac{\text{d}\Delta v_{g\text{dc\_pu}}(t)}{\text{d}t}, \tag{5-36}$$

Substitution of $\Delta v_{g\text{dc\_pu}} = K_{fv\_\text{pu}}\Delta f_{o\_\text{pu}}$ into (5-36), it yields

$$\Delta P_{\text{uc\_pu}}(t) = -2H_{\text{uc}}K_{fv\_\text{pu}}\frac{\text{d}\Delta f_{o\_\text{pu}}(t)}{\text{d}t}, \tag{5-37}$$

where the term $H_{\text{uc}}K_{fv\_\text{pu}}$ denotes the virtual inertia coefficient. To generate a desired virtual inertia coefficient $H_p = H_{\text{uc}}K_{fv\_\text{pu}}$, K_{fv_pu} is designed to be

$$K_{fv\_\text{pu}} = \frac{2H_p VA_{\text{base}}}{C_{g\text{dc}}V_{g\text{dc\_ref}}^{\ 2}}, \tag{5-38}$$

The relationships of virtual inertia coefficient H_p and several design parameters can be referred to Figure 5.12. According to the parameter values listed in Table 5-5 and Table 5-7, the virtual inertia coefficient H_p and synchronous inertia coefficient H are both designed to be 5 s.

5.4.4 Experimental Verification

To illustrate the benefits of the proposed VSG with the HESS, experiments were conducted based on the system schematic diagram shown in Figure 5.22. Figure 5.27 illustrates the steady-state experimental results of the proposed VSG system. As predicted, the AC grid voltages v_{gfx} (x = a, b, c) feature clean sinusoidal waveforms, thereby demonstrating the effectiveness of the AC voltage/current controller. The currents following through the resistive loads i_{lx} (x = a, b, c) share the same waveforms as the AC grid voltages v_{gfx} except for the scaled magnitudes. In addition, the ripples in the DC inductor current i_b can be effectively attenuated by the output LC filter of the boost converter, leading to a DC-link voltage $v_{g\text{dc}}$ with negligible ripples. The stable DC-link voltage clearly shows the feasibility of the DC voltage/current controller.

Figure 5.28 sketches the experimental waveforms of frequency f_o and DC-link voltage $v_{g\text{dc}}$ of the proposed VSG system under a 3% step-up load change. It is clear that the VSG performs the frequency regulation in the same way as conventional synchronous generators do. During the frequency event, $v_{g\text{dc}}$ varies in proportional to f_o such that the power is delivered for inertia emulation. Their minimum values are found to be 377 V and 49.83 Hz, respectively. Note that the

quasi-steady-state frequency and voltage can be restored if the secondary frequency control is incorporated, as detailed in Section 2.5.

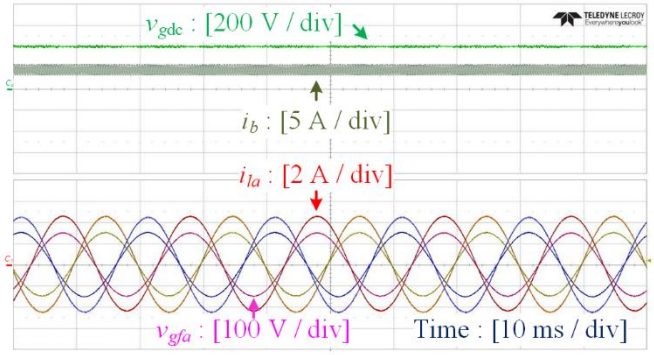

Figure 5.27 Steady-state experimental results of the proposed VSG system.

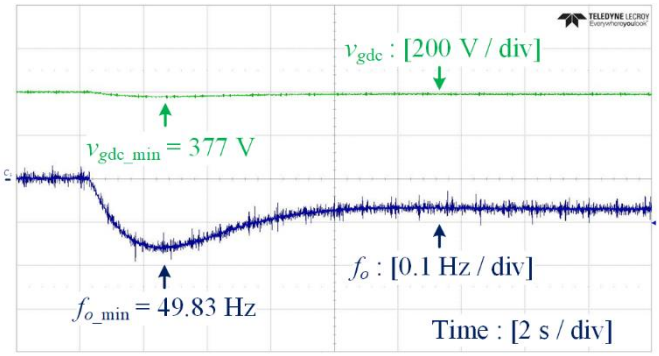

Figure 5.28 Experimental waveforms of frequency f_o and ultracapacitor voltage v_{gdc} of the proposed VSG system under a 3% step-up load change.

In accordance with the frequency and DC-link voltage responses, the changes of battery and ultracapacitor powers are further visualized in Figure 5.29, where the effective power allocation can clearly be observed. In the face of the step-up load change, the ultracapacitor immediately increases its power output to help balance the power mismatch, and this illustrates the effect of virtual inertia. In contrast, the battery power climbs up slowly and balances the load change as the frequency dynamics settle down. Note that inertia emulation requires a very fast change of the output power during frequency events, which may negatively influence the battery lifetime without the help of the ultracapacitor.

Figure 5.30 presents the power response waveforms of the proposed VSG system under an intermittent RES output. In this situation, the ultracapacitor compensates high-frequency power fluctuations. Thanks to the help of the

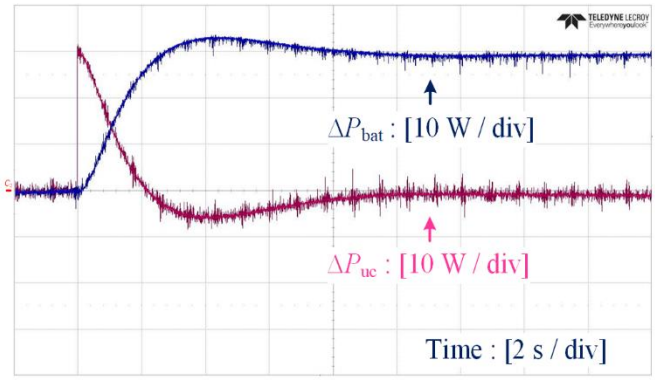

Figure 5.29 Experimental waveforms of battery power change ΔP_{bat} and ultracapacitor power change ΔP_{uc} of the proposed VSG system under a 3% step-up load change.

ultracapacitor, battery power fluctuations, together with their changing rates, can be dramatically reduced. Note that the extent of power fluctuation reductions depends on the virtual inertia, which can be flexibly designed by either changing the ultracapacitor inertia coefficient H_{uc} or the proportional gain K_{fv_pu}. These experimental results coincide with the previous theoretical analysis.

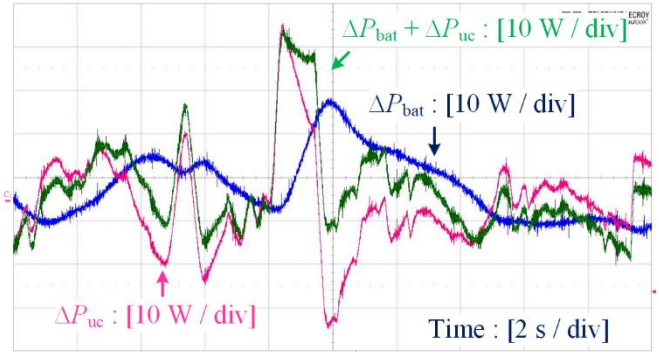

Figure 5.30 Experimental waveforms of the battery power change ΔP_{bat} and ultracapacitor power change ΔP_{uc} of the proposed VSG system under an intermittent RES output.

5.5 Summary

This chapter has investigated the system-level frequency stability of more-electronics power systems, particularly for the lack of inertia issue, and proposed the distributed virtual inertia and VSGs with HESSs for inertia and stability enhancement. Through the analysis of the inertia effect, it is identified that the increment of inertia greatly helps the frequency regulation in terms of frequency

nadir and RoCoF. As such, two approaches have been proposed for inertia enhancement. The first approach lies in the use of grid-connected power converters for providing the distributed power system inertia. By proportionally linking the grid frequency and DC-link voltages of grid-connected power converters, the DC-link capacitors of power converters can absorb and release power in a similar way as the rotors of synchronous generators do. As a result, the emulated inertia can be expected from grid-connected power converters. The second approach implements the frequency regulation and power management of VSGs by the HESS consisting of a battery and an ultracapacitor. In the HESS, the ultracapacitor voltage varies in proportional to the grid frequency. In this way, the ultracapacitor tackles the short-term power fluctuations for inertia emulation, and the battery handles the long-term power fluctuations required by the remaining parts of the VSG. In consequence, battery power fluctuations, along with their changing rates, can be dramatically reduced. These approaches greatly improve the frequency nadir and RoCoF, leading to a better system-level frequency stability.

Chapter 6 Conclusion and Future Research

This chapter concludes the major contributions of this thesis and provides the recommendations for future research with regards to the power quality and stability improvement of more-electronics power systems. The conclusion of this thesis is listed below:

- The proposed advanced passive filters − the magnetic integrated *LLCL* filter, *SPRLCL* filter, and *LT-C-L* filter allow effective harmonic filtering and power quality enhancement with small filter sizes;
- The converter-level instability issue arising from PLLs under weak grids can be resolved by reshaping the *q*-axis impedance of power converters through the proposed impedance controller;
- It is possible to significantly improve the system-level frequency stability through the use of distributed virtual inertia by grid-connected power converters and VSGs with HESSs;

After emerging challenges and opportunities in more-electronics power systems are identified, this chapter further points out the future research directions as follows:

- Grid support by power converters under adverse grid conditions;
- Converter-level instability issues due to the grid support, e.g. the active power support, reactive power support, and virtual inertia control;
- System-level stability improvement using the inertia emulated by energy storage units, such as batteries and flywheels;

6.1 Conclusion

This thesis analyzes and addresses several power quality and instability issues introduced by power electronics in more-electronics power systems. Through extensive theoretical analyses and experimental verifications, the conclusion can be readily obtained as follows.

The proposed advanced passive filters are effective solutions to the ever-challenging current harmonic issue in more-electronics power systems. In addition to an *LCL* filter, these advanced passive filters contain additional series- and/or parallel-resonant *LC*-traps. They feature strong harmonic attenuation, small filter sizes, and low costs. Specifically, the magnetic integrated *LLCL* filter is implemented by an integrated *LCL* filter by designing the trap frequency at the switching frequency. Without the employment of any trap inductor, it yields the benefits of both *LLCL* filter and magnetic integration, i.e. strong attenuation and high-power density. The *SPRLCL* filter contains two *LC*-traps (one series-resonant trap and one parallel-resonant trap). These traps can be flexibly designed to either simultaneously trap the switching frequency and double switching frequency harmonics or exhibit high robustness against filter parameter variations. The *LT-C-L* filter is a combination of an *LCL* filter and a converter-side parallel-resonant *LC*-trap. The *LT-C-L* filter is concluded to be the most promising trap filter in terms of filter topology, filtering performance, and robustness.

The converter-level instability issue arising from PLLs under weak grids can be addressed by reshaping the *q*-axis converter impedance. Through the impedance criterion, it is found that the instability issue due to PLLs under weak grids is caused by the negative resistance region in the low-frequency band of the *q*-axis converter impedance. As a solution, the impedance controller directly relating the *q*-axis voltage to the *q*-axis current reference has been proposed. For a properly designed current controller, the *q*-axis current reference is approximately equal to the *q*-axis current in the low-frequency band. Therefore, the proposed impedance controller helps to reshape the *q*-axis converter impedance as a positive resistance in the low-frequency band, and thus overcoming the converter-level instability issue due to PLLs.

The system-level frequency stability can be greatly improved by the distributed virtual inertia contributed by grid-connected power converters and VSGs. After the inertia effect is analyzed, it is revealed that the frequency regulation,

characterized by the frequency nadir and RoCoF, can be improved as the inertia increases. In this sense, the improvement of the frequency stability translates into the increment of inertia. To enhance the inertia, grid-connected power converters are exploited to generate the distributed virtual inertia through the dedicated control. By proportionally linking the grid frequency and DC-link voltages of grid-connected power converters, the DC-link capacitors of power converters can emulate the rotors of synchronous generators. In this way, the power required for inertia emulation can be expected from grid-connected power converters. Another possibility for inertia enhancement comes from VSGs. With the proposed HESS consisting of a battery and an ultracapacitor included in VSGs, the power management of VSGs can be implemented. In the HESS, the ultracapacitor tackles the short-term power fluctuations for inertia emulation, and the battery handles the long-term power fluctuations required by the remaining parts of the VSG. Through the proposed power allocation scheme, battery power fluctuations, along with their changing rates, can be significantly reduced.

6.2 Future Research

Power converters with conventional control objectives, e.g. the AC current control, AC voltage control, and DC-link voltage control, have been extensively analyzed and well-studied in the literature [22, 38, 39, 181-184]. In accordance with these control objectives, numerous topologies of power converters have also been proposed to reduce loss and cost as well as improve efficiency, power density, and reliability of power converters [79, 172, 185-193]. Research works along the trajectory of achieving conventional control objectives are still going on, mainly related to the control of multiple power converters.

As discussed, power converters are increasingly expected to provide grid support functions, such as the active power support, reactive power support, and inertia control. Such grid support functions may significantly modify the control and operations of future more-electronics power systems [194, 195] [31, 64, 196-199]. On one hand, there are great opportunities of enhancing the system-level

stability using the grid support by power converters. On the other hand, the grid support may change the modeling and control of power converters. Therefore, it is recommended to further explore and tackle the issues due to the grid support by power converters.

6.2.1 Grid Support under Adverse Grid Conditions

As mentioned in Chapter 3, power quality issues can be largely categorized into voltage and current quality issues. Furthermore, voltage quality issues comprise voltage sags/swells, unbalances, and harmonics, and current quality issues include the reactive current, current harmonics, and unbalances. This thesis mainly focuses on the reactive current and current harmonic issues. However, it should be emphasized that voltage quality issues will act as a barrier for power converters to provide the grid support.

Unless being properly regulated, power converters with grid support functions may possibly aggravate voltage distortions and unbalances under adverse grid conditions. Although voltage quality issues can be resolved by DVRs and UPQCs, these solutions feature considerable capital and operating costs, and hence it is impractical to deploy DVRs and UPQCs in a large-scale [16, 17]. Instead, it is highly desirable if individual power converters can provide grid support functions and meanwhile address grid voltage issues without employing any additional equipment. To achieve this purpose, the accurate measurements of electrical parameters, such as the grid frequency and voltage amplitude, should be guaranteed, based on which effective grid support schemes are also necessary.

Normally, PLLs are employed for signal measurements. Under distorted and unbalanced grid conditions, the detected frequency and voltage signals will be inaccurate, which further translate into incorrect power references and in turn cause the distortions of grid-injected currents. As solutions, the modified PLLs capable of accurately measuring the grid frequency and voltage amplitude under adverse grid conditions are proposed [51, 173, 200]. However, there is always a trade-off between signal accuracy and detection speed. In this sense, fast and

accurate signal measurement methods are required, which necessitate further investigations.

With the knowledge of electrical parameters, it is necessary to further explore grid support schemes. When providing the grid support, power converters should never be overloaded. Moreover, their operations should always positively contribute to the system stability and power quality rather than in the opposite way. In the case of short-term grid faults, power converters should stay in grid-connection and perform fault ride-through, otherwise the system-level instability may arise because of the sudden loss of power support [30, 162]. In the presence of long-term grid faults, it is a must for power converters to protect themselves and promptly disconnect from the power grid [195]. It remains a challenging task for power converters to provide the grid support while ensuing the above objectives, and hence grid support schemes should be further investigated.

6.2.2 Converter-Level Instability Issues due to Grid Support

As discussed in Chapter 4, the sources of converter-level instability issues are found to be improper controller designs (including the DC-link voltage control, AC voltage control, PLL control, AC current control, and PWM generators), time-delays, resonances arising from high-order passive filters, interactions among multiple power converters, and weak grids. This thesis concentrates on the instability issue due to the PLL control under weak grids, where grid support functions are excluded from the converter control. When power converters are supposed to provide grid support functions, new types of instability issues will appear. The mechanisms behind these instability issues as well as their solutions serve as future research directions.

In the presence of large time-delays, the provision of active power support may destabilize the power converter control [201]. Such time-delays can originate from the signal transmissions between central controller and controllers of individual power converters. To overcome this type of instability, one solution lies in the elimination of time-delays using decentralized control schemes [70].

However, the decentralized control may be unfavourable in terms of system cost and energy optimization. Alternatively, the converter control may be well designed so that power converters can provide the stable active power support even when large time-delays are present. Considering the uncertainty feature of time-delays, robust controllers may be applied to ensure stable operations of individual power converters [202]. The design of robust controllers for the active power support can be a future research direction.

The concept of the distributed virtual inertia contributed by grid-connected power converters has been introduced in Section 5.3. According to the relevant discussions and experimental results, the distributed virtual inertia generated by grid-connected power converters offers a degree of the inertia control in more-electronics power systems. Therefore, the virtual inertia is concluded to be a promising way of supporting the frequency regulation and system stability. However, the virtual inertia control may induce instability issues to the grid-connected power converters under weak grid conditions. The underlying principle of this instability issue, in combination with its solutions, will be thoroughly investigated in the future.

In parallel with the active power support and virtual inertia control, the reactive power support may also pose a threat to the stability of power converters under weak grid conditions. Since the potential instability issues due to the virtual inertia control and reactive power support occur in the converter-level, they may possibly be addressed through the modification of the converter control. The relevant control schemes will be the future research focus.

6.2.3 Virtual Inertia Support by Energy Storage Units

As stated in Chapter 5, the system-level stability mainly includes two aspects − the frequency stability and voltage stability. This thesis targets at the improvement of the frequency stability through the enhancement of inertia. To increase the inertia, two methods have been proposed. Specifically, the first method refers to the distributed virtual inertia emulated by the DC-link capacitors

of power converters. For the second method, the virtual inertia comes from the ultracapacitors of VSGs. It should be emphasized that many other energy storage units in addition to capacitors and ultracapacitors are also potential inertia suppliers. Therefore, the exploitation of virtual inertia supported by other energy storage units, such as batteries, should be further investigated.

Different from capacitors and ultracapacitors, batteries have almost fixed voltages (in a normal state of charge), and therefore battery voltages cannot easily be changed in proportional to the grid frequency for inertia emulation. However, it is still possible for batteries to absorb and deliver power in the same way as synchronous generators do through the dedicated control, and thus resulting in the production of virtual inertia [203]. Harvesting the virtual inertia from batteries is another research direction in the future.

In addition to AC more-electronics power systems, DC power systems are also showing great promise due to its benefits of simplicity and low-cost [33, 204]. Moreover, hybrid AC/DC more-electronics power systems combining the advantages of both AC and DC power systems receive a growing popularity recently [205-209]. The concept of virtual inertia may also be transplanted from AC systems into DC and hybrid AC/DC systems. In these cases, the virtual inertia design process as well as energy storage sizing scheme may become very different from those given in Chapter 5, particularly when the interaction between AC and DC systems are taken into consideration. In this regard, the virtual inertia support by energy storage in DC and hybrid AC/DC more-electronics power systems may be further explored.

Author's Publications

Journal Papers:

1. **J. Fang**, H. Li, Y. Tang, and F. Blaabjerg, "Distributed power system virtual inertia implemented by grid-connected power converters," ***IEEE Trans. Power Electron.***, vol. 33, no. 10, pp. 8488−8499, Oct. 2018.
2. **J. Fang**, X. Li, H. Li, and Y. Tang, "Stability improvement for three-phase grid-connected converters through impedance reshaping in quadrature-axis," ***IEEE Trans. Power Electron.***, vol. 33, no. 10, pp. 8365−8375, Oct. 2018.
3. **J. Fang**, Y. Tang, H. Li, and X. Li, "A battery/ultracapacitor hybrid energy storage system for implementing the power management of virtual synchronous generators," ***IEEE Trans. Power Electron.***, vol. 33, no. 4, pp. 2820−2824, Apr. 2018.
4. **J. Fang**, X. Li, X. Yang, and Y. Tang, "An integrated trap−*LCL* filter with reduced current harmonics for grid-connected converters under weak grid conditions," ***IEEE Trans. Power Electron.***, vol. 32, no. 11, pp. 8446–8457, Nov. 2017.
5. **J. Fang**, X. Yang, L. Zhang, and Y. Tang, "An optimal digital pulse-width-modulated dither technique to enhance the resolution of high frequency power converters," ***IEEE Trans. Power Electron.*,** vol. 32, no. 9, pp. 7222–7232, Sep. 2017.
6. **J. Fang**, H. Li, and Y. Tang, "A magnetic integrated *LLCL* filter for grid-connected voltage-source converters," ***IEEE Trans. Power Electron*.**, vol. 32, no. 3, pp. 1725–1730, Mar. 2017.
7. **J. Fang**, G. Xiao, X. Yang, and Y. Tang, "Parameter design of a novel series-parallel-resonant *LCL* filter for single-phase half-bridge active power filters," ***IEEE Trans. Power Electron.***, vol. 32, no. 1, pp. 200–217, Jan. 2017.

Conference Papers:

8. **J. Fang**, X. Li, Y. Tang, and H. Li, "Design of virtual synchronous generators with enhanced frequency regulation and reduced voltage distortions", in *Proc. IEEE APEC*, pp. 1412–1419, San Antonio, TEXAS, USA, 4–8 Mar. 2018.
9. **J. Fang**, X. Li, Y. Tang, and H. Li, "Power management of virtual synchronous generators through using hybrid energy storage systems", in *Proc. IEEE APEC*, pp. 1407–1411, San Antonio, TEXAS, USA, 4–8 Mar. 2018.

10. **J. Fang**, R. Zhang, H. Li, and Y. Tang, “Inertia enhancement by gird-connected power converters with frequency-locked-loops for frequency derivative estimation,” in *Proc. PESGM 2018*, Portland, Oregon, USA, 5–9 Aug. 2018.

11. **J. Fang**, X. Li, Y. Tang, and H. Li, “Improvement of frequency stability in power electronics-based power systems,” in *Proc. ACEPT*, pp. 1–6, Singapore, 24–26 Oct. 2017. (**Best Paper Award**).

12. **J. Fang,** X. Li, and Y. Tang, “Grid-connected power converters with distributed virtual power system inertia,” in *Proc. IEEE ECCE*, pp. 4267–4273, Cincinnati, Ohio, USA, 1–5 Oct. 2017.

13. **J. Fang**, X. Li, and Y. Tang, "A novel *LCL*-filtered single-phase half-bridge distributed static compensator with DC-link filter capacitors and reduced passive component parameters", in *Proc. IEEE APEC*, pp. 3279–3285, Tampa, Florida, USA, 26–30 Mar. 2017.

14. **J. Fang**, X. Li, and Y. Tang, “A review of passive power filters for voltage-source converters,” in *Proc. ACEPT*, pp. 1–6, Singapore, 25–27 Oct. 2016.

15. **J. Fang**, L. Zhang, Y. Tang, and X. Yang, “An optimal digital pulse-width-modulated dither technique to enhance the resolution of wide bandgap device-based high frequency power converters,” in *Proc. IPEMC 2016 – ECCE Asia*, pp. 589–596, Hefei, China, 22–25 May 2016.

16. Y. Tang, **J. Fang**, X. Li, and H. Li, “Reshaping quadrature-axis impedance of three-phase grid-connected converters for low-frequency stability improvement,” in *Proc. IPEC 2018 – ECCE Asia*, Niigata, Japan, 20–24 May 2018.

17. K. Guo, **J. Fang**, and Y. Tang, “Autonomous DC-link voltage restoration for grid-connected power converters providing virtual inertia,” in *Proc. IEEE ECCE*, Portland, Oregon, USA, 23–27 Sep. 2018.

References

[1] H. Farhangi, "The path of the smart grid," *IEEE Power Energy Mag.,* vol. 8, pp. 18-28, Jan./Feb. 2010.

[2] S. M. Amin and B. F. Wollenberg, "Toward a smart grid," *IEEE Power Energy Mag.,* vol. 8, pp. 114-122, Apr. 2008.

[3] J. G. Kassakian and T. M. Jahns, "Evolving and emerging applications of power electronics in systems," *IEEE J. Emerging Sel. Topics Power Electron,* vol. 1, pp. 47-58, Jun. 2013.

[4] *REN21*, *Paris, France, "Renewables 2017 global status report."* (2017). [Online]. Available: http://www.ren21.net

[5] Z. Chen, J. M. Guerrero, and F. Blaabjerg, "A review of the state of the art of power electronics for wind turbines," *IEEE Trans. Power Electron.,* vol. 24, pp. 1859-1875, Aug. 2009.

[6] F. Blaabjerg, R. Teodorescu, M. Liserre, and A. V. Timbus, "Overview of control and grid synchronization for distributed power generation systems," *IEEE Trans. Ind. Electron.,* vol. 53, pp. 1398-1409, Oct. 2006.

[7] J. P. Barton and D. G. Infield, "Energy storage and its use with intermittent renewable energy," *IEEE Trans. Energy Conv.,* vol. 19, pp. 441-448, Jun. 2004.

[8] P. F. Frack, P. E. Mercado, M. G. Molina, E. H. Watanabe, R. W. De Doncker, and H. Stagge, "Control strategy for frequency control in autonomous microgrids," *IEEE J. Emerging Sel. Topics Power Electron,* vol. 3, pp. 1046-1055, Dec. 2015.

[9] C. Jian and A. Emadi, "A new battery/ultracapacitor hybrid energy storage system for electric, hybrid, and plug-in hybrid electric vehicles," *IEEE Trans. Power Electron.,* vol. 27, pp. 122-132, Jan. 2012.

[10] A. Khaligh and L. Zhihao, "Battery, ultracapacitor, fuel Cell, and hybrid energy storage systems for electric, hybrid electric, fuel cell, and plug-in hybrid electric vehicles: state of the art," *IEEE Trans. Veh. Technol.,* vol. 59, pp. 2806-2814, Jul. 2010.

[11] M. Yilmaz and P. T. Krein, "Review of battery charger topologies, charging power levels, and infrastructure for plug-in electric and hybrid vehicles," *IEEE Trans. Power Electron.,* vol. 28, pp. 2151-2169, May 2013.

[12] R. C. Dugan, M. F. McGranaghan, S. Santoso, and H. W. Beaty, *Electrical power systems quality*. 2 Penn Plaza, New York, NY, USA: McGraw-Hill, 2003.

[13] P. Kundur, *Power system stability and control*. New York, NY, USA: Mograw-Hill, 1994.

[14] *IEEE recommended practices and requirements for harmonic control in electric power systems*, IEEE Standard 519−2014, 2014.

[15] H. Akagi, "New trends in active filters for power conditioning," *IEEE Trans. Ind. Appl.,* vol. 32, pp. 1312-1322, Nov./Dec. 1996.

[16] Y. W. Li, D. M. Vilathgamuwa, F. Blaabjerg, and P. C. Loh, "A robust control scheme for medium-voltage-level DVR implementation," *IEEE Trans. Ind. Electron.,* vol. 54, pp. 2249-2261, Aug. 2007.

[17] V. Khadkikar, "Enhancing electric power quality using UPQC: a comprehensive overview," *IEEE Trans. Power Electron.,* vol. 27, pp. 2284-2297, May 2012.

[18] B. Singh, B. N. Singh, A. Chandra, K. Al-Haddad, A. Pandey, and D. P. Kothari, "A review of three-phase improved power quality AC–DC converters," *IEEE Trans. Ind. Electron.,* vol. 51, pp. 641-660, Jun. 2004.

[19] D. G. Holmes and T. A. Lipo, *Pulse width modulation for power converters: principles and practive*. Hoboken, NJ: Wiley, 2003.

[20] R. W. Erickson and D. Maksimovic, *Fundamentals of power electronics*. 233 Spring Street, New York, NY, USA: Springer, 2001.

[21] D. Pan, X. Ruan, C. Bao, W. Li, and X. Wang, "Magnetic integration of the *LCL* filter in grid-connected inverters," *IEEE Trans. Power Electron.,* vol. 29, pp. 1573-1578, Apr. 2014.

[22] D. N. Zmood and D. G. Holmes, "Stationary frame current regulation of PWM inverters with zero steady-state error," *IEEE Trans. Power Electron.,* vol. 18, pp. 814-822, May 2003.

[23] S. G. Parker, B. P. McGrath, and D. G. Holmes, "Regions of active damping control for LCL Filters," *IEEE Trans. Ind. Appl.,* vol. 50, pp. 424-432, Jan./Feb. 2014.

[24] D. Pan, X. Ruan, C. Bao, W. Li, and X. Wang, "Capacitor-current-feedback active damping with reduced computation delay for improving robustness of *LCL*-type grid-connected inverter," *IEEE Trans. Power Electron.,* vol. 29, pp. 3414-3427, Jul. 2014.

[25] D. Dong, B. Wen, D. Boroyevich, P. Mattavelli, and Y. Xue, "Analysis of phase-locked loop low-frequency stability in three-phase grid-connected power converters considering impedance interactions," *IEEE Trans. Ind. Electron.,* vol. 62, pp. 310-321, Jan. 2015.

[26] K. M. Alawasa, Y. A. R. I. Mohamed, and W. Xu, "Active mitigation of subsynchronous interactions between PWM voltage-source converters and power networks," *IEEE Trans. Power Electron.,* vol. 29, pp. 121-134, Jan. 2014.

[27] K. M. Alawasa and Y. A. R. I. Mohamed, "A simple approach to damp SSR in series-compensated systems via reshaping the output admittance of a nearby VSC-based system," *IEEE Trans. Ind. Electron.,* vol. 62, pp. 2673-2682, May 2015.

[28] B. Wen, D. Boroyevich, R. Burgos, P. Mattavelli, and Z. Shen, "Analysis of D-Q small-signal impedance of grid-tied Inverters," *IEEE Trans. Power Electron.,* vol. 31, pp. 675-687, Jan. 2016.

[29] H. Akagi, Y. Kanazawa, and A. Nabae, "Instantaneous reactive power compensators comprising switching devices without energy storage components," *IEEE Trans. Ind. Appl.,* vol. 20, pp. 625-630, May/Jun. 1984.

[30] Y. Yang, F. Blaabjerg, and H. Wang, "Low-voltage ride-through of single-phase transformerless photovoltaic inverters," *IEEE Trans. Ind. Appl.,* vol. 50, pp. 1942-1952, May/Jun. 2014.

[31] I. Serban and C. Marinescu, "Control strategy of three-phase battery energy storage systems for frequency support in microgrids and with uninterrupted supply of local loads," *IEEE Trans. Power Electron.,* vol. 29, pp. 5010-5020, Sep. 2014.

[32] H. Zhou, T. Bhattacharya, D. Tran, T. S. T. Siew, and A. M. Khambadkone, "Composite energy storage system involving battery and ultracapacitor with dynamic energy management in microgrid applications," *IEEE Trans. Power Electron.,* vol. 26, pp. 923-930, Mar. 2011.

[33] J. M. Guerrero, J. C. Vasquez, J. Matas, L. G. de Vicuna, and M. Castilla, "Hierarchical control of droop-controlled AC and DC microgrids—a general approach toward standardization," *IEEE Trans. Ind. Electron.,* vol. 58, pp. 158-172, Jan. 2011.

[34] X. Wang, F. Blaabjerg, and W. Wu, "Modeling and analysis of harmonic stability in an AC power-electronics-based power system," *IEEE Trans. Power Electron.,* vol. 29, pp. 6421-6432, Dec. 2014.

[35] H.-P. Beck and R. Hesse, "Virtual synchronous machine," presented at the *Proc. 9th Int. Conf. Elect. Power Qual. Util. (EPQU)*, 2007, pp. 1–6.

[36] J. Driesen and K. Visscher, "Virtual synchronous generators," presented at the *Proc. IEEE Power Energy Soc.Gen. Meeting—Convers. Del. Elect. Energy 21st Century*, Jul. 2008, pp. 1-3.

[37] M. Guan, W. Pan, J. Zhang, Q. Hao, J. Cheng, and X. Zheng, "Synchronous generator emulation control strategy for voltage source converter (VSC) stations," *IEEE Trans. Power Syst.,* vol. 30, pp. 3093-3101, Nov. 2015.

[38] J. Rocabert, A. Luna, F. Blaabjerg, and P. Rodríguez, "Control of power converters in AC microgrids," *IEEE Trans. Power Electron.,* vol. 27, pp. 4734-4749, Nov. 2012.

[39] A. V. Timbus, M. Liserre, R. Teodorescu, P. Rodriguez, and F. Blaabjerg, "Evaluation of current controllers for distributed power generation systems," *IEEE Trans. Power Electron.,* vol. 24, pp. 654-664, 2009.

[40] B. Wen, D. Dong, D. Boroyevich, R. Burgos, P. Mattavelli, and Z. Shen, "Impedance-based analysis of grid-synchronization stability for three-phase paralleled converters," *IEEE Trans. Power Electron.,* vol. 31, pp. 26-38, Jan. 2016.

[41] J. Sun, "Small-signal methods for AC distributed power systems a–review," *IEEE Trans. Power Electron.,* vol. 24, pp. 2545-2554, Nov. 2009.

[42] J. Fang, X. Li, Y. Tang, and H. Li, "Design of virtual synchronous generators with enhanced frequency regulation and reduced voltage distortions," presented at the *Proc. IEEE APEC*, pp. 1412–1419, San Antonio, TEXAS, USA, 4–8 Mar. 2018.

[43] S. Buso and P. Miattavelli, *Digital control in power electronics, 2nd edition*. San Rafael, CA, USA: Morgan and Claypool, 2015.

[44] D. M. Van de Sype, K. De Gusseme, F. M. L. L. De Belie, A. P. Van den Bossche, and J. A. Melkebeek, "Small-signal z-domain analysis of digitally controlled converters," *IEEE Trans. Power Electron.,* vol. 21, pp. 470-478, Mar. 2006.

[45] Z. Kai, K. Yong, X. Jian, and C. Jian, "Direct repetitive control of SPWM inverter for UPS purpose," *IEEE Trans. Power Electron.,* vol. 18, pp. 784-792, May 2003.

[46] S. Jiang, D. Cao, Y. Li, J. Liu, and F. Z. Peng, "Low-THD, fast-transient, and cost-effective synchronous-frame repetitive controller for three-phase UPS inverters," *IEEE Trans. Power Electron.,* vol. 27, pp. 2994-3005, Jun. 2012.

[47] A. García-Cerrada, O. Pinzón-Ardila, V. Feliu-Batlle, P. Roncero-Sánchez, and P. García-González, "Application of a repetitive controller for a three-phase active power filter," *IEEE Trans. Power Electron.,* vol. 22, pp. 237-246, Jan. 2007.

[48] A. G. Yepes, F. D. Freijedo, J. Doval-Gandoy, O. López, J. Malvar, and P. Fernandez-Comesaña, "Effects of discretization methods on the performance of resonant controllers," *IEEE Trans. Power Electron.,* vol. 25, pp. 1692-1712, 2010.

[49] S. Chung, "A phase tracking system for three phase utility interface inverters," *IEEE Trans. Power Electron.,* vol. 15, pp. 431-438, May 2000.

[50] M. Karimi-Ghartemani and M. R. Iravani, "A method for synchronization of power electronic converters in polluted and variable-frequency environments," *IEEE Trans. Power Syst.,* vol. 19, pp. 1263-1270, Aug. 2004.

[51] M. Karimi-Ghartemani, "A novel three-phase magnitude-phase-locked loop system," *IEEE Trans. Circuits Syst. I, Fundam. Theory Appl,* vol. 53, pp. 1792-1802, Aug. 2006.

[52] J. Wang, J. D. Yan, L. Jiang, and J. Zou, "Delay-dependent stability of single-loop controlled grid-connected inverters with *LCL* filters," *IEEE Trans. Power Electron.,* vol. 31, pp. 743-757, Jan. 2016.

[53] Y. Tang, W. Yao, P. C. Loh, and F. Blaabjerg, "Design of *LCL*-filters with *LCL* resonance frequencies beyond the Nyquist frequency for grid-connected converters," *IEEE J. Emerging Sel. Topics Power Electron,* vol. 4, pp. 3-14, Mar. 2016.

[54] X. Li, J. Fang, Y. Tang, and X. Wu, "Robust design of *LCL* filters for single-current-loop controlled grid-connected power converters with unit PCC voltage feedforward," *IEEE J. Emerging Sel. Topics Power Electron,* vol. 6, pp. 54-72, Mar. 2018.

[55] J. Wang, J. D. Yan, and L. Jiang, "Pseudo-derivative-feedback current control for three-phase grid-connected inverters with *LCL* filters," *IEEE Trans. Power Electron.,* vol. 31, pp. 3898-3912, May 2016.

[56] M. Liserre, F. Blaabjerg, and S. Hansen, "Design and control of an *LCL*-filter-based three-phase active rectifier," *IEEE Trans. Ind. Appl.,* vol. 41, pp. 1281-1291, Sep./Oct. 2005.

[57] W. Wu, Y. He, and F. Blaabjerg, "An *LLCL* power filter for single-phase grid-tied inverter," *IEEE Trans. Power Electron.,* vol. 27, pp. 782-789, Feb. 2012.

[58] Y. Tang, P. C. Loh, P. Wang, F. H. Choo, F. Gao, and F. Blaabjerg, "Generalized design of high performance shunt active power filter with output *LCL* filter," *IEEE Trans. Ind. Electron.,* vol. 59, pp. 1443-1452, Mar. 2012.

[59] Q. Liu, L. Peng, Y. Kang, S. Tang, D. Wu, and Y. Qi, "A novel design and optimization method of an *LCL* filter for a shunt active power filter," *IEEE Trans. Ind. Electron.,* vol. 61, pp. 4000-4010, Aug. 2014.

[60] K. Jalili and S. Bernet, "Design of *LCL* filters of active-front-end two-level voltage-source converters," *IEEE Trans. Ind. Electron.,* vol. 56, pp. 1674-1689, May 2009.

[61] J. Fang, G. Xiao, X. Yang, and Y. Tang, "Parameter design of a novel series-parallel-resonant *LCL* filter for single-phase half-bridge active power filters," *IEEE Trans. Power Electron.,* vol. 32, pp. 200-217, Jan. 2017.

[62] J. Fang, X. Li, and Y. Tang, "A novel *LCL*-filtered single-phase half-bridge distributed static compensator with DC-link filter capacitors and reduced passive component parameters," presented at the *Proc. IEEE APEC*, pp. 3279–3285, Tampa, Florida, USA, 26–30 Mar. 2017.

[63] Q. Zhong and G. Weiss, "Synchronverters: inverters that mimic synchronous generators," *IEEE Trans. Ind. Electron.,* vol. 58, pp. 1259-1267, Apr. 2011.

[64] Y. G. Rebours, D. S. Kirschen, M. Trotignon, and S. Rossignol, "A survey of frequency and voltage control ancillary services—part I technical features," *IEEE Trans. Power Syst.,* vol. 22, pp. 350-357, Feb. 2007.

[65] Q.-C. Zhong, P.-L. Nguyen, Z. Ma, and W. Sheng, "Self-synchronized synchronverters: inverters without a dedicated synchronization unit," *IEEE Trans. Power Electron.,* vol. 29, pp. 617-630, Feb. 2014.

[66] M. A. Torres L, L. A. C. Lopes, L. A. Moran T, and J. R. Espinoza C, "Self-tuning virtual synchronous machine: a control strategy for energy storage systems to support dynamic frequency control," *IEEE Trans. Energy Conv.,* vol. 29, pp. 833-840, Dec. 2014.

[67] J. Alipoor, Y. Miura, and T. Ise, "Power system stabilization using virtual synchronous generator with alternating moment of inertia," *IEEE J. Emerging Sel. Topics Power Electron,* vol. 3, pp. 451-458, Jun. 2015.

[68] K. De Brabandere, B. Bolsens, J. Van den Keybus, A. Woyte, J. Driesen, and R. Belmans, "A voltage and frequency droop control method for parallel inverters," *IEEE Trans. Power Electron.,* vol. 22, pp. 1107-1115, Jul. 2007.

[69] J. M. Guerrero, J. Matas, L. Garcia de Vicuna, M. Castilla, and J. Miret, "Decentralized control for parallel operation of distributed generation inverters using resistive output impedance," *IEEE Trans. Ind. Electron.,* vol. 54, pp. 994-1004, Apr. 2007.

[70] J. M. Guerrero, M. Chandorkar, T.-L. Lee, and P. C. Loh, "Advanced control architectures for intelligent microgrids—part I: decentralized and hierarchical control," *IEEE Trans. Ind. Electron.,* vol. 60, pp. 1254-1262, Apr. 2013.

[71] J. He and Y. W. Li, "Generalized closed-loop control schemes with embedded virtual impedances for voltage source converters with *LC* or *LCL* filters," *IEEE Trans. Power Electron.,* vol. 27, pp. 1850-1861, Apr. 2012.

[72] J. M. Guerrero, L. Hang, and J. Uceda, "Control of distributed uninterruptible power supply systems," *IEEE Trans. Ind. Electron.,* vol. 55, pp. 2845-2859, Aug. 2008.

[73] J. M. Guerrero, L. GarciadeVicuna, J. Matas, M. Castilla, and J. Miret, "A wireless controller to enhance dynamic performance of parallel inverters in distributed generation systems," *IEEE Trans. Power Electron.,* vol. 19, pp. 1205-1213, Sep. 2004.

[74] H. Fujita and H. Akagi, "The unified power quality conditioner: the Integration of series- and shunt-active filters," *IEEE Trans. Power Electron.,* vol. 13, pp. 315-322, Mar. 1998.

[75] B. Singh, B. N. Singh, A. Chandra, K. Al-Haddad, A. Pandey, and D. P. Kothari, "A review of single-phase improved power quality AC-DC converters," *IEEE Trans. Ind. Electron.,* vol. 50, pp. 962-981, Oct. 2003.

[76] V. Khadkikar and A. Chandra, "A new control philosophy for a unified power quality conditioner (UPQC) to coordinate load-reactive power demand between shunt and series inverters," *IEEE Trans. Power Del.,* vol. 23, pp. 2522-2534, Oct. 2008.

[77] F. Peng, J.-S. Lai, J. W. McKeever, and J. VanCoevering, "A multilevel voltage-source inverter with separate DG sources for SVG," *IEEE Trans. Ind. Appl.,* vol. 32, pp. 1130-1138, Sep./Oct. 1996.

[78] B. Singh, P. Jayaprakash, D. P. Kothari, A. Chandra, and K. Al Haddad, "Comprehensive study of DSTATCOM configurations," *IEEE Trans. Ind. Informat.,* vol. 10, pp. 854-870, May 2014.

[79] H. Akagi, "Classification, terminology, and application of the modular multilevel cascade converter (MMCC)," *IEEE Trans. Power Electron.,* vol. 26, pp. 3119-3130, Nov. 2011.

[80] J. M. Guerrero, J. C. Vasquez, J. Matas, M. Castilla, and L. G. de Vicuna, "Control strategy for flexible microgrid based on parallel line-interactive UPS systems," *IEEE Trans. Ind. Electron.,* vol. 56, pp. 726-736, Mar. 2009.

[81] Y. Liang, "A new type of STATCOM based on cascading voltage-source inverters with phase-shifted unipolar SPWM.pdf," *IEEE Trans. Ind. Appl.,* vol. 35, pp. 1118-1123, Sep./Oct. 1999.

[82] D. Perreault, K. Sato, R. L. Selders, Jr., and J. G. Kassakian, "Switching-ripple-based current sharing for paralleled power converters," *IEEE Trans. Circuits Syst. I, Fundam. Theory Appl,* vol. 46, pp. 1264-1274, Oct. 1999.

[83] J. Xu, J. Yang, J. Ye, Z. Zhang, and A. Shen, "An *LTCL* filter for three-phase grid-connected converters," *IEEE Trans. Power Electron.,* vol. 29, pp. 4322-4338, Aug. 2014.

[84] R. N. Beres, X. Wang, M. Liserre, F. Blaabjerg, and C. L. Bak, "A review of passive power filters for three-phase grid-connected voltage-source converters," *IEEE J. Emerging Sel. Topics Power Electron.,* vol. 4, pp. 54-69, Mar. 2016.

[85] X. Li, J. Fang, P. Lin, and Y. Tang, "Active magnetic decoupling for improving the performance of integrated *LCL*-filters in grid-connected converters," *IEEE Trans. Ind. Electron.,* in press.

[86] Y. Liu, K. See, K. Tseng, R. Simanjorang, and J.-S. Lai, "Magnetic integration of three-phase LCL filter with delta-yoke composite core," *IEEE Trans. Power Electron.,* vol. 32, pp. 3835-3843, Jun. 2016.

[87] J. Fang, H. Li, and Y. Tang, "A magnetic integrated *LLCL* filter for grid-connected voltage source converters," *IEEE Trans. Power Electron.,* vol. 32, pp. 1725-1730, Mar. 2017.

[88] X. Li, P. Lin, and Y. Tang, "Magnetic integration of *LTL* filter with two *LC*-traps for grid-connected power converters," *IEEE J. Emerging Sel. Topics Power Electron,* in press.

[89] G. Gohil, L. Bede, R. Teodorescu, T. Kerekes, and F. Blaabjerg, "Optimized integrated harmonic filter inductor for dual-converter fed open-end transformer topology," *IEEE Trans. Power Electron.,* vol. 32, pp. 1818-1831, Mar. 2016.

[90] *Ferrites and Accessories, EPCOS Data Book*, TDK Inc., Munich, Germany, 2013.

[91] *Digikey Electronics Co. Ltd, MN, USA, "Ferrite Cores."* (2016). [Online]. Available: http://www.digikey.com/product-search/en/magnetics-transformer-inductor-components/ferrite-cores

[92] J. Fang, X. Li, and Y. Tang, "A review of passive power filters for voltage-source converters," presented at the *Proc. ACEPT*, pp. 1–6, Singapore, 25–27 Oct. 2016.

[93] J. Fang, G. Xiao, and Y. Zhang, " An LCCL filter and its application to a half-bridge APF," presented at the *Proc. ICPE 2015–ECCE Asia*, pp. 2566–2573, Seoul, Korea, 1–5 Jun. 2015.

[94] J. Fang, X. Li, X. Yang, and Y. Tang, "An integrated trap-*LCL* filter with reduced current harmonics for grid-connected converters under weak grid conditions," *IEEE Trans. Power Electron.,* vol. 32, pp. 8446-8457, Jan. 2017.

[95] S. Srianthumrong and H. Akagi, "Medium-voltage transformerless ac/dc power conversion system consisting of a diode rectifier and a shunt hybrid filter," *IEEE Trans. Ind. Appl.,* vol. 39, pp. 874-882, May/Jun. 2003.

[96] R. Inzunza and H. Akagi, "A 6.6-kV transformerless shunt hybrid active filter for installation on a power distribution system," *IEEE Trans. Power Electron.,* vol. 20, pp. 893-900, Jul. 2005.
[97] X. Wang, Y. Pang, P. C. Loh, and F. Blaabjerg, "A series-*LC*-filtered active damper with grid disturbance rejection for AC power-electronics-based power systems," *IEEE Trans. Power Electron.,* vol. 30, pp. 4037-4041, Aug. 2015.
[98] Y. Liu, W. Wu, Y. He, Z. Lin, F. Blaabjerg, and H. S.-H. Chung, "An efficient and robust hybrid damper for *LCL*- or *LLCL*-based grid-tied inverter with strong grid-side harmonic voltage effect rejection," *IEEE Trans. Ind. Electron.,* vol. 63, pp. 926-936, Feb. 2016.
[99] W. Wu, Y. Sun, M. Huang, X. Wang, H. Wang, F. Blaabjerg*, et al.*, "A robust passive damping method for *LLCL*-filter-based grid-tied inverters to minimize the effect of grid harmonic voltages," *IEEE Trans. Power Electron.,* vol. 29, pp. 3279-3289, Jul. 2014.
[100] X. Zhang, H. Zhu, H. Li, and C. Yu, "An *LCL-LC* filter for grid-connected converter: topology, parameter, and analysis," *IEEE Trans. Power Electron.,* vol. 30, pp. 5067-5077, Sep. 2015.
[101] W. Wu, Y. Sun, Z. Lin, Y. He, M. Huang, F. Blaabjerg*, et al.*, "A modified *LLCL* filter with the reduced conducted EMI noise," *IEEE Trans. Power Electron.,* vol. 29, pp. 3393-3402, Jul. 2014.
[102] W. Wu, Y. He, Z. Lin, F. Blaabjerg, and H. S.-H. Chung, "A simple differential mode EMI suppressor for the *LLCL*-filter-based single-phase grid-tied transformerless inverter," *IEEE Trans. Ind. Electron.,* vol. 62, pp. 4141-4147, Jul. 2015.
[103] M. Sanatkar-Chayjani and M. Monfared, "Stability analysis and robust design of *LCL* with multituned traps filter for grid connected converters," *IEEE Trans. Ind. Electron.,* vol. 63, pp. 6823-6834, Nov. 2016.
[104] W. Wu, Y. Sun, Z. Lin, T. Tang, F. Blaabjerg, and H. S.-H. Chung, "A new *LCL*-filter with In-series parallel resonant circuit for single-phase grid-tied inverter," *IEEE Trans. Ind. Electron.,* vol. 61, pp. 4640-4644, Sep. 2014.
[105] X. Wang, M. Huang, H. Bai, P. C. Loh, and F. Blaabjerg, "Influence of modulation method on using *LC*-traps with single-phase voltage source inverters," presented at the *Proc. 17th ECPE*, pp. 1–9, Geneva, Switzerland, 8–10 Sep. 2015.
[106] M. Liserre, R. Teodorescu, and F. Blaabjerg, "Stability of photovoltaic and wind turbine grid-connected inverters for a large set of grid impedance values," *IEEE Trans. Power Electron.,* vol. 21, pp. 263-272, Jan. 2006.
[107] J. L. Agorreta, M. Borrega, J. López, and L. Marroyo, "Modeling and control of N-paralleled grid-connected inverters with *LCL* filter coupled due to grid impedance in PV plants," *IEEE Trans. Power Electron.,* vol. 26, pp. 770-785, Mar. 2011.

[108] J. He, Y. W. Li, D. Bosnjak, and B. Harris, "Investigation and active damping of multiple resonances in a parallel-inverter-based microgrid," *IEEE Trans. Power Electron.,* vol. 28, pp. 234-246, Jan. 2013.
[109] X. Li, X. Wu, Y. Geng, X. Yuan, C. Xia, and X. Zhang, "Wide damping region for *LCL*-type grid-connected inverter with an improved capacitor-current-feedback method," *IEEE Trans. Power Electron.,* vol. 30, pp. 5247-5259, Sep. 2015.
[110] M. Huang, X. Wang, P. C. Loh, and F. Blaabjerg, "Active damping of *LLCL*-filter resonance based on *LC*-trap voltage or current feedback," *IEEE Trans. Power Electron.,* vol. 31, pp. 2337-2346, Mar. 2016.
[111] X. Wang, F. Blaabjerg, and P. C. Loh, "Virtual *RC* damping of *LCL*-filtered voltage source converters with extended selective harmonic compensation," *IEEE Trans. Power Electron.,* vol. 30, pp. 4726-4737, Sep. 2015.
[112] C. Zou, B. Liu, S. Duan, and R. Li, "Influence of delay on system stability and delay optimization of grid-connected inverters with *LCL* filters," *IEEE Trans. Ind. Informat.,* vol. 10, pp. 1775-1784, Aug. 2014.
[113] J. Dannehl, F. W. Fuchs, S. Hansen, and P. B. Thøgersen, "Investigation of active damping approaches for PI-based current control of grid-connected pulse width modulation converters with *LCL* filters," *IEEE Trans. Ind. Appl.,* vol. 46, pp. 1509-1517, Jul./Aug. 2010.
[114] J. Dannehl, F. W. Fuchs, and P. B. Thogersen, "PI state space current control of grid-connected PWM converters with *LCL* filters," *IEEE Trans. Power Electron.,* vol. 25, pp. 2320-2330, Sep. 2010.
[115] L. A. Maccari, J. R. Massing, L. Schuch, C. Rech, H. Pinheiro, R. C. L. F. Oliveira*, et al.*, "LMI-based control for grid-connected converters with *LCL* filters under uncertain parameters," *IEEE Trans. Power Electron.,* vol. 29, pp. 3776-3785, Jul. 2014.
[116] D. Pan, X. Ruan, C. Bao, W. Li, and X. Wang, "Optimized controller design for *LCL*-type grid-connected inverter to achieve high robustness against grid-impedance variation," *IEEE Trans. Ind. Electron.,* vol. 62, pp. 1537-1547, Mar. 2015.
[117] D. Yang, X. Ruan, and H. Wu, "Impedance shaping of the grid-connected inverter with *LCL* filter to improve its adaptability to the weak grid condition," *IEEE Trans. Power Electron.,* vol. 29, pp. 5795-5805, Nov. 2014.
[118] A. Kahrobaeian and Y. A.-R. I. Mohamed, "Robust single-loop direct current control of *LCL*-filtered converter-based DG units in grid-connected and autonomous microgrid modes," *IEEE Trans. Power Electron.,* vol. 29, pp. 5605-5619, Oct. 2014.
[119] R. N. Beres, X. Wang, F. Blaabjerg, M. Liserre, and C. L. Bak, "Optimal design of high-order passive-damped filters for grid-connected applications," *IEEE Trans. Power Electron.,* vol. 31, pp. 2083-2098, Mar. 2016.

[120] J. Muhlethaler, M. Schweizer, R. Blattmann, J. W. Kolar, and A. Ecklebe, "Optimal design of *LCL* harmonic filters for three-phase PFC rectifiers," *IEEE Trans. Power Electron.,* vol. 28, pp. 3114-3125, Jul. 2013.
[121] R. Peña-Alzola, M. Liserre, F. Blaabjerg, R. Sebastián, J. Dannehl, and F. W. Fuchs, "Analysis of the passive damping losses in *LCL*-filter-based grid converters," *IEEE Trans. Power Electron.,* vol. 28, pp. 2642-2646, 2013.
[122] W. Wu, Y. He, T. Tang, and F. Blaabjerg, "A new design method for the passive damped *LCL* and *LLCL* filter-based single-phase grid-tied inverter," *IEEE Trans. Ind. Electron.,* vol. 60, pp. 4339-4350, Oct. 2013.
[123] P. Channegowda and V. John, "Filter optimization for grid interactive voltage source inverters," *IEEE Trans. Ind. Electron.,* vol. 57, pp. 4106-4114, Dec. 2010.
[124] X. Wang and F. Blaabjerg, "Harmonic stability in power electronic based power systems: concept, modeling, and analysis," *IEEE trans. Smart Grid,* in press.
[125] L. Harnefors, M. Bongiorno, and S. Lundberg, "Input-admittance calculation and shaping for controlled voltage-source converters," *IEEE Trans. Ind. Electron.,* vol. 54, pp. 3323-3334, Dec. 2007.
[126] L. Harnefors, "Analysis of subsynchronous torsional interaction with power electronic converters," *IEEE Trans. Power Syst.,* vol. 22, pp. 305-313, Feb. 2007.
[127] X. Wang, P. C. Loh, and F. Blaabjerg, "Stability analysis and controller synthesis for single-loop voltage-controlled VSIs," *IEEE Trans. Power Electron.,* vol. 32, pp. 7394-7404, Sep. 2017.
[128] J. Fang, X. Li, H. Li, and Y. Tang, "Stability improvement for three-phase grid-connected converters through impedance reshaping in quadrature-axis," *IEEE Trans. Power Electron.,* in press.
[129] D. G. Holmes, T. A. Lipo, B. P. McGrath, and W. Y. Kong, "Optimized design of stationary frame three phase AC current regulators," *IEEE Trans. Power Electron.,* vol. 24, pp. 2417-2426, Nov. 2009.
[130] L. Harnefors, R. Finger, X. Wang, H. Bai, and F. Blaabjerg, "VSC input-admittance modeling and analysis above the nyquist frequency for passivity-based stability assessment," *IEEE Trans. Ind. Electron.,* vol. 64, pp. 6362-6370, Aug. 2017.
[131] C. Bao, X. Ruan, X. Wang, W. Li, D. Pan, and K. Weng, "Step-by-step controller design for *LCL*-type grid-connected inverter with capacitor-current-feedback active-damping," *IEEE Trans. Power Electron.,* vol. 29, pp. 1239-1253, Mar. 2014.
[132] S. Guoqiao, X. Dehong, C. Luping, and Z. Xuancai, "An improved control strategy for grid-connected voltage source inverters with an LCL filter," *IEEE Trans. Power Electron.,* vol. 23, pp. 1899-1906, Jul. 2008.
[133] L. Harnefors, A. G. Yepes, A. Vidal, and J. Doval-Gandoy, "Passivity-based controller design of grid-connected VSCs for prevention of

electrical resonance instability," *IEEE Trans. Ind. Electron.,* vol. 62, pp. 702-710, Feb. 2015.

[134] Y. Tang, P. C. Loh, P. Wang, F. H. Choo, and F. Gao, "Exploring inherent damping characteristic of *LCL*-filters for three-phase grid-connected voltage source inverters," *IEEE Trans. Power Electron.,* vol. 27, pp. 1433-1443, Mar. 2012.

[135] X. Wang, F. Blaabjerg, M. Liserre, Z. Chen, J. He, and Y. Li, "An active damper for stabilizing power-electronics-based AC systems," *IEEE Trans. Power Electron.,* vol. 29, pp. 3318-3329, Jul. 2014.

[136] D. Yang, X. Ruan, and H. Wu, "A real-time computation method with dual sampling mode to improve the current control performance of the *LCL*-type grid-connected inverter," *IEEE Trans. Ind. Electron.,* vol. 62, pp. 4563-4572, Jul. 2015.

[137] D. Maksimovic and R. Zane, "Small-signal discrete-time modeling of digitally controlled PWM converters," *IEEE Trans. Power Electron.,* vol. 22, pp. 2552-2556, Nov. 2007.

[138] Y. F. Liu, E. Meyer, and X. Liu, "Recent developments in digital control strategies for DC/DC switching power converters," *IEEE Trans. Power Electron.,* vol. 24, pp. 2567-2577, Nov. 2009.

[139] J. Ma, X. Wang, F. Blaabjerg, L. Harnefors, and W. Song, "Accuracy analysis of the zero-order hold model for digital pulsewidth modulation," *IEEE Trans. Power Electron.,* in press.

[140] X. Zhang, J. W. Spencer, and J. M. Guerrero, "Small-signal modeling of digitally controlled grid-connvected inverters with *LCL* filters," *IEEE Trans. Ind. Electron.,* vol. 60, pp. 3752-3765, Sep. 2013.

[141] C. Wan, M. Huang, C. K. Tse, and X. Ruan, "Effects of interaction of power converters coupled via power grid: a design-oriented study," *IEEE Trans. Power Electron.,* vol. 30, pp. 3589-3600, Jul. 2015.

[142] M. Lu, X. Wang, P. Loh, and F. Blaabjerg, "Resonance interaction of multi-parallel grid-connected inverters with *LCL*–filter," *IEEE Trans. Power Electron.,* vol. 32, pp. 894-899, Feb. 2017.

[143] R. Turner, S. Walton, and R. Duke, "Stability and bandwidth implications of digitally controlled grid-connected parallel inverters," *IEEE Trans. Ind. Electron.,* vol. 57, pp. 3685-3694, Nov. 2010.

[144] D. Zhang, F. Wang, R. Burgos, R. Lai, and D. Boroyevich, "Impact of interleaving on AC passive components of paralleled three-phase voltage-source converters," *IEEE Trans. Ind. Appl.,* vol. 46, pp. 1042-1054, May/Jun. 2010.

[145] Z. Ye, D. Boroyevich, J.-Y. Choi, and F. C. Lee, "Control of circulating current in two parallel three-phase boost rectifiers," *IEEE Trans. Power Electron.,* vol. 17, pp. 609-615, Sep. 2002.

[146] M. Liserre, F. Blaabjerg, and R. Teodorescu, "Grid impedance estimation via excitation of *LCL*-type-filter resonance," *IEEE Trans. Ind. Appl.,* vol. 43, pp. 1401-1407, Sep./Oct. 2007.

[147] X. Li, J. Fang, Y. Tang, X. Wu, and Y. Geng, "Capacitor-voltage feedforward with full delay compensation to improve weak grids adaptability of *LCL*-filtered grid-connected converters for distributed generation systems," *IEEE Trans. Power Electron.,* vol. 33, pp. 749-764, Feb. 2018.

[148] J. Dannehl, M. Liserre, and F. W. Fuchs, "Filter-based active damping of voltage source converters with *LCL* filter," *IEEE Trans. Ind. Electron.,* vol. 58, pp. 3623-3633, Aug. 2011.

[149] J. Dannehl, C. Wessels, and F. W. Fuchs, "Limitations of voltage-oriented PI current control of grid-connected PWM rectifiers with *LCL* filters," *IEEE Trans. Ind. Electron.,* vol. 56, pp. 380-388, Feb. 2009.

[150] B. Wen, D. Boroyevich, R. Burgos, P. Mattavelli, and Z. Shen, "Small-signal stability analysis of three-phase AC systems in the presence of constant power loads based on measured *d-q* frame impedances," *IEEE Trans. Power Electron.,* vol. 30, pp. 5952-5963, Oct. 2015.

[151] J. Sun, "Impedance-based stability criterion for grid-connected inverters," *IEEE Trans. Power Electron.,* vol. 26, pp. 3075-3078, Nov. 2011.

[152] R. D. Middlebrook, "Input filter considerations in design and application switching regulators," presented at the *IEEE Ind. Appl. Soc.*, pp. 366–382,1976.

[153] *Australia Energy Market Operator*, *Melbourne, VIC, Australia, "International review of frequency control adaptation."* (2017). [Online]. Available: http://www.aemo.com.au

[154] *North American Electric Reliability Corporation, North Tower, GA, United States of America, "Balancing and frequency control"* (2011). [Online]. Available: http://www.nerc.com

[155] *Energy Market Authority, SG, Singapore, "Transmission code"* (2017). [Online]. Available: http://www.ema.gov.sg

[156] *National Grid, London, ENG, United Kingdom*, *"The grid code."* (2017). [Online]. Available: http://www.nationalgrid.com

[157] *North American Electric Reliability Corporation, North Tower, GA, United States of America, "Reliability standards for the bulk eleectric systems os north America"* (2017). [Online]. Available: http://www.nerc.com

[158] *Australia Energy Market Commission*, *Sydney, NSW, Australia, "The frequency operating standard."* (2017). [Online]. Available: http://www.aemc.gov.au

[159] *European Network of Transmission System Operators for Electricity*, *Brussels, BRL, Belgium, "P1−Policy 1: load-frequency control and performance."* (2017). [Online]. Available: http://www.entsoe.eu.

[160] *Australia Energy Market Operator*, *Melbourne, VIC, Australia, "Electricity rule change proposal."* (2017). [Online]. Available: http://www.aemo.com.au

[161] *RoCoF modification proposal – TSOs' recommendations*, EirGrid/SONI, Ballsbridge, DUB, Ireland, 2012.

[162] F. Blaabjerg and M. Ke, "Future on power electronics for wind turbine systems," *IEEE J. Emerging Sel. Topics Power Electron,* vol. 1, pp. 139-152, Sep. 2013.
[163] Y. Liu, S. You, J. Tan, Y. Zhang, and Y. Liu, "Frequency response assessment and enhancement of the U.S. power grids towards extra-high photovoltaic generation penetrations – an industry perspective," *IEEE Trans. Power Syst.,* in press.
[164] Y. Liu, S. You, and Y. Liu, "Study of wind and PV frequency control in U.S. power grids—EI and TI case studies," *IEEE Power Energy Technol. Syst. J.,* vol. 4, pp. 65-73, Aug. 2017.
[165] J. Morren, S. W. H. de Haan, W. L. Kling, and J. A. Ferreira, "Wind turbines emulating inertia and supporting primary frequency control," *IEEE Trans. Power Syst.,* vol. 21, pp. 433-434, Feb. 2006.
[166] K. Liu, Y. Qu, H.-M. Kim, and H. Song, "Avoiding frequency second dip in power unreserved control during wind power rotational speed recovery," *IEEE Trans. Power Syst.,* in press.
[167] J. Fang, H. Li, Y. Tang, and F. Blaabjerg, "Distributed power system virtual inertia implemented by grid-connected power converters," *IEEE Trans. Power Electron.,* in press.
[168] M. Arani and S. El, "Implementing virtual inertia in DFIG-based wind power generation," *IEEE Trans. Power Syst.,* vol. 28, pp. 1373-1384, May 2013.
[169] S. Eftekharnejad, V. Vittal, G. T. Heydt, B. Keel, and J. Loehr, "Small signal stability assessment of power systems with increased penetration of photovoltaic generation: a case study," *IEEE Trans. Sustain. Energy* vol. 4, pp. 960-967, Oct. 2013.
[170] J. W. Ingleson and E. Allen, "Tracking the eastern interconnection frequency governing characteristic," presented at the *Proc. IEEE PESGM*, pp. 1-6, Providence, RI, USA, 25–29 Jul. 2010.
[171] H. Wang and F. Blaabjerg, "Reliability of capacitors for DC-Link applications in power electronic converters—an overview," *IEEE Trans. Ind. Appl.,* vol. 50, pp. 3569-3578, Sep./Oct. 2014.
[172] Y. Xue, L. Chang, S. B. Kjaer, J. Bordonau, and T. Shimizu, "Topologies of single-phase inverters for small distributed power generators: an overview," *IEEE Trans. Power Electron.,* vol. 19, pp. 1305-1314, Sep. 2004.
[173] P. Rodríguez, A. Luna, R. S. Muñoz-Aguilar, I. Etxeberria-Otadui, R. Teodorescu, and F. Blaabjerg, "A stationary reference frame grid synchronization system for three-phase grid-connected power converters under adverse grid conditions," *IEEE Trans. Power Electron.,* vol. 27, pp. 99-112, Jan. 2012.
[174] G. Delille, B. Francois, and G. Malarange, "Dynamic frequency control support by energy storage to reduce the impact of wind and solar generation on isolated power system's inertia," *IEEE Trans. Sustain. Energy,* vol. 3, pp. 931-939, Oct. 2012.

[175] Y. Hirase, K. Sugimoto, K. Sakimoto, and T. Ise, "Analysis of resonance in microgrids and effects of system frequency stabilization using a virtual synchronous generator," *IEEE J. Emerging Sel. Topics Power Electron,* vol. 4, pp. 1287-1298, Dec. 2016.

[176] J. Liu, Y. Miura, and T. Ise, "Comparison of dynamic characteristics between virtual synchronous generator and droop control in inverter-based distributed generators," *IEEE Trans. Power Electron.,* vol. 31, pp. 3600-3611, May 2016.

[177] H. Wu, X. Ruan, D. Yang, X. Chen, W. Zhao, Z. Lv*, et al.*, "Small-signal modeling and parameters design for virtual synchronous generators," *IEEE Trans. Ind. Electron.,* vol. 63, pp. 4292-4303, Jul. 2016.

[178] J. Fang, Y. Tang, H. Li, and X. Li, "A battery/ultracapacitor hybrid energy storage system for implementing the power management of virtual synchronous generators," *IEEE Trans. Power Electron.,* vol. 33, pp. 2820-2824, Apr. 2018.

[179] J. A. Suul, S. Darco, and G. Guidi, "Virtual synchronous machine-based control of a single-phase bi-directional battery charger for providing vehicle-to-grid services," *IEEE Trans. Ind. Appl.,* vol. 52, pp. 3234-3244, Jul./Aug. 2016.

[180] S. M. Lukic, C. Jian, R. C. Bansal, F. Rodriguez, and A. Emadi, "Energy storage systems for automotive applications," *IEEE Trans. Ind. Electron.,* vol. 55, pp. 2258-2267, Jun. 2008.

[181] M. G. Villalva, J. R. Gazoli, and E. R. Filho, "Comprehensive approach to modeling and simulation of photovoltaic arrays," *IEEE Trans. Power Electron.,* vol. 24, pp. 1198-1208, May 2009.

[182] F. Blaabjerg and M. Ke, "Power electronics converters for wind turbine systems," *IEEE Trans. Ind. Appl.,* vol. 48, pp. 708-719, Mar./Apr. 2012.

[183] Y. Tang, P. C. Loh, P. Wang, and F. H. Choo, "One-cycle-controlled three-phase PWM rectifiers with improved regulation under unbalanced and distorted input-voltage conditions," *IEEE Trans. Power Electron.,* vol. 25, pp. 2786-2796, Nov. 2010.

[184] R. C. N. Pilawa-Podgurski and D. J. Perreault, "Submodule integrated distributed maximum power point tracking for solar photovoltaic applications," *IEEE Trans. Power Electron.,* vol. 28, pp. 2957-2967, Jun. 2013.

[185] S. B. Kjaer, J. K. Pedersen, and F. Blaabjerg, "A review of single-phase grid-connected inverters for photovoltaic modules," *IEEE Trans. Ind. Appl.,* vol. 41, pp. 1292-1306, Sep./Oct. 2005.

[186] G. R. Walker and P. C. Sernia, "Cascaded DC–DC converter connection of photovoltaic modules," *IEEE Trans. Power Electron.,* vol. 19, pp. 1130-1139, Jul. 2004.

[187] L. Quan and P. Wolfs, "A review of the single phase photovoltaic module integrated converter topologies with three different DC link configurations," *IEEE Trans. Power Electron.,* vol. 23, pp. 1320-1333, May 2008.

[188] P. Fang Zheng, "Z-source inverter," *IEEE Trans. Ind. Appl.,* vol. 39, pp. 504-510, Mar./Apr. 2003.
[189] Y. Tang, F. Blaabjerg, P. C. Loh, C. Jin, and P. Wang, "Decoupling of fluctuating power in single-phase systems through a symmetrical half-bridge circuit," *IEEE Trans. Power Electron.,* vol. 30, pp. 1855-1865, Apr. 2015.
[190] Y. Tang, W. Yao, P. C. Loh, and F. Blaabjerg, "Highly reliable transformerless photovoltaic inverters with leakage current and pulsating power elimination," *IEEE Trans. Ind. Electron.,* vol. 63, pp. 1016-1026, Feb. 2016.
[191] Y. Tang and F. Blaabjerg, "A component-minimized single-phase active power decoupling circuit with reduced current stress to semiconductor switches," *IEEE Trans. Power Electron.,* vol. 30, pp. 2905-2910, Jun. 2015.
[192] J. Rodriguez, J.-S. Lai, and F. Z. Peng, "Multilevel inverters: a survey of topologies, controls and applications," *IEEE Trans. Ind. Electron.,* vol. 49, pp. 724-738, Aug. 2002.
[193] S. Kouro, M. Malinowski, K. Gopakumar, J. Pou, L. G. Franquelo, W. Bin*, et al.*, "Recent advances and industrial applications of multilevel converters," *IEEE Trans. Ind. Electron.,* vol. 57, pp. 2553-2580, Aug. 2010.
[194] A. F. Hoke, M. Shirazi, S. Chakraborty, E. Muljadi, and D. Maksimovic, "Rapid active power control of photovoltaic systems for grid frequency support," *IEEE J. Emerging Sel. Topics Power Electron,* vol. 5, pp. 1154-1163, Sep. 2017.
[195] F. Blaabjerg, Y. Yang, D. Yang, and X. Wang, "Distributed power-generation systems and protection," *Proc. IEEE,* vol. 105, pp. 1311-1331, Jul. 2017.
[196] W. Wu, Y. Chen, A. Luo, L. Zhou, X. Zhou, L. Yang*, et al.*, "A virtual inertia control strategy for DC microgrids analogized with virtual synchronous machines," *IEEE Trans. Ind. Electron.,* in press.
[197] J. Zhu, C. D. Booth, G. P. Adam, A. J. Roscoe, and C. G. Bright, "Inertia emulation control strategy for VSC-HVDC transmission systems," *IEEE Trans. Power Syst.,* vol. 28, pp. 1277-1287, May 2013.
[198] W. Wang, Y. Li, Y. Cao, U. Hager, and C. Rehtanz, "Adaptive droop control of VSC-MTDC system for frequency support and power sharing," *IEEE Trans. Power Syst.,* vol. 33, pp. 1264-1274, Mar. 2018.
[199] L. Xiong, F. Zhuo, F. Wang, X. Liu, Y. Chen, M. Zhu*, et al.*, "Static synchronous generator model: a new perspective to investigate dynamic characteristics and stability issues of grid-tied PWM inverter," *IEEE Trans. Power Electron.,* vol. 31, pp. 6264-6280, Sep. 2016.
[200] P. Rodriguez, J. Pou, J. Bergas, J. I. Candela, R. Burgos, and D. Boroyevich, "Decoupled double synchronous reference frame PLL for power converters control," *IEEE Trans. Power Electron.,* vol. 22, pp. 584-592, Mar. 2007.

[201] J. Fang, X. Li, Y. Tang, and H. Li, "Improvement of frequency stability in power electronics-based power systems," presented at the *Proc. ACEPT*, pp. 1–6, Singapore, 24–26 Oct. 2017.
[202] T. Kerdphol, F. S. Rahman, Y. Mitani, M. Watanabe, and S. Kufeoglu, "Robust virtual inertia control of an islanded microgrid considering high penetration of renewable energy," *IEEE Access,* vol. 6, pp. 625-636, Feb. 2018.
[203] J. Fang, R. Zhang, Y. Tang, and H. Li, "Inertia enhancement by grid-connected power converters with frequency-locked-loops for frequency derivative estimation," presented at the *Proc. PESGM*, Portland, Oregon, USA, 5–9 Aug. 2018.
[204] C. Jin, P. Wang, J. Xiao, Y. Tang, and F. H. Choo, "Implementation of hierarchical control in DC microgrids," *IEEE Trans. Ind. Electron.,* vol. 61, pp. 4032-4042, Aug. 2014.
[205] P. C. Loh, D. Li, J. Chai, and F. Blaabjerg, "Autonomous operation of hybrid microgrid with AC and DC subgrids," *IEEE Trans. Power Electron.,* vol. 28, pp. 2214-2223, May 2013.
[206] A. Gupta, S. Doolla, and K. Chatterjee, "Hybrid AC-DC microgrid: systematic evaluation of control strategies," *IEEE trans. Smart Grid,* in press.
[207] F. Nejabatkhah and Y. Li, "Overview of power management strategies of hybrid AC/DC microgrid," *IEEE Trans. Power Electron.,* vol. 30, pp. 7072-7089, Dec. 2015.
[208] P. C. Loh, D. Li, Y. K. Chai, and F. Blaabjerg, "Autonomous control of interlinking converter with energy storage in hybrid AC–DC microgrid," *IEEE Trans. Ind. Appl.,* vol. 49, pp. 1374-1382, May/Jun. 2013.
[209] X. Liu, P. Wang, and P. C. Loh, "A hybrid AC/DC microgrid and its coordination control," *IEEE trans. Smart Grid,* vol. 2, pp. 278-286, Jun. 2011.